



Muhammad Abubakar, MSc

Design and Analysis of New Control Strategies for Stability Enhancement of a Micro-Grid under Various Operating Modes

DOCTORAL THESIS

to achieve the university degree of
Doktor der technischen Wissenschaften

submitted to

Graz University of Technology

Supervisor

Ao. Univ.-Prof. Dipl.-Ing. Dr. techn. Herwig Renner
Institute of Electrical Power Systems

External Reviewer

Univ.Prof. Dipl.-Ing. Dr.sc.techn. Bernd Klöckl
Energy Systems and Networks, TU Vienna

Graz/Austria, October 2024

AFFIDAVIT

I declare that I have authored this thesis independently, that I have not used other than the declared sources/resources, and that I have explicitly indicated all material which has been quoted either literally or by content from the sources used. The text document uploaded to TUGRAZonline is identical to the present doctoral thesis.

Date, Signature

ACKNOWLEDGEMENT

This dissertation is submitted for the degree of philosophy doctor at Graz University of Technology (TUG) in Graz/Austria. The research presented herein is conducted in the field of converter's control schemes and enhancement of the micro-grid's stability. The research and this thesis were composed during my stay at the Institute of Electrical Power Systems (IEAN) at Graz University of Technology.

My special thanks go to Ao. Univ. Prof. Dipl.-Ing. Dr. techn. Herwig Renner and Univ.-Prof. DDipl. Ing. Dr. techn. Robert Schürhuber, who not only gave me the opportunity to conduct my dissertation on this interesting and exciting topic but also supported me during this time and helped me with their guidance and commitment. Moreover, I am thankful to them for the faith they had placed in me and the scope they had given me for new ideas that contributed significantly to the success of this work. I also like to thank Univ.Prof. Dipl.-Ing. Dr.sc.techn. Bernd Klöckl for being the external reviewer and his conscientious review as well as his helpful comments and advice on this dissertation.

This research is funded by the Higher Education Commission (HEC), Pakistan and supported by the Austria's Agency for Education and Internationalisation (OeAD). I also thank my funding and partner agencies for having faith on me and providing me this opportunity to work on this exciting topic. I would also like to thank Univ.-Prof. Dr. Thomas Kienberger, Montanuniversität Leoben for sharing the data of Generic European Network. I also like to thank my colleagues, fellow Ph.D. students and friends, who helped me with their creative ideas, and discussions.

Lastly, I would be remiss in not mentioning my family, especially my parents, brother, sisters, and children. Their belief in me has kept my spirits and motivation high during this process. They always supported and encouraged me throughout my life and have, therefore, made this work possible. I would like to pay special thanks to my spouse, Nazish, for her support and immeasurable patience during my doctorate and also during the writing of this thesis. Thank you for always being able to rely on you and always believing to be able to do so in the future.

Graz, October 2024

Muhammad Abubakar

ABSTRACT

The concept of micro-grid (MG) got more attention in recent times due to the paradigm shift from centralized power systems to the localized power systems that are dedicated for a specific service area. It has its own electrical power sources and loads. It can operate in standalone/islanded mode, or it can also be connected to the main power network-called grid connected mode. Due to the growing CO₂ emissions and the availability of renewable energy sources in a specific geographical location, converter based renewable energy sources are mostly used as power sources for the MG. Thus, the response of the converters defines the response of the MG in different operating conditions. Broadly, the converter's control schemes are divided into two categories, i.e., grid following control (GFL) and grid forming control (GFM)- both having their own merits and demerits. The size, location, ratio of GFM to GFL based power, and the total power capacity of the MG are the important factors while designing the MG.

With the advantages of the MG, there are also stability challenges associated with the operation of the MG due to the low inertia and low fault current levels. The stability of the MG can be categorized into small and large signal stability for frequency, voltage, and converter-driven stability. In grid connected mode, the small signal stability is not important as it is primarily controlled by the external grid, but the large signal stability is important. However, in the islanded mode, as there is no external grid available, thus both the small and large signal stabilities are important. Additionally, to deal with the negative effects of the large penetration of the converter-based sources into the power system, some standards are defined which discuss the required response from the converters in particular situations. The response of the grid-connected MG is monitored at its point of connection (POC). Thus, the MG also needs to meet these requirements in grid-connected mode.

The stability of the MG is largely decided by the control schemes of the connected converters. There are several standard control schemes discussed in the literature for the GFL and GFM. However, due to the limited network strength of MG, some modifications in these control schemes are important to achieve stable operation. Thus, the first part of this thesis discusses the improved control schemes for GFL and GFM converters to achieve a robust response in different operating conditions. It also presents a performance comparison of the conventional GFL scheme and the improved one to quantify the degree of improvement in different operating conditions. The major focus is to achieve a stable response, ensure the safe operation of the converter, maximize the utility of current handling capability, and improve the voltage uniformity in case of unbalanced faults. Similarly, the GFM control scheme is modified to achieve stable response from weak to stiff grid connections, improve the converter-driven stability in case of faults with limited current handling capability, and achieve smooth transition from different modes of operation.

In the second part of this thesis, the impact of different control schemes on the calculations of the short circuit power in a multi-converter system is discussed. Moreover, the key parameters for the design and stable operation of the MG are also discussed along with the detailed stability analysis in both modes of operation. Some recommendations are presented for the selection of the location, type, size, and ratio of GFM to GFL based power for designing the MG. The key objective is to achieve a stable response from MG in all operating conditions while ensuring the current limits of the converters and improving the reliability of the service. The design of the load management system and its features are also discussed. Finally, the outcomes of the detailed stability studies in both operating modes are presented.

KURZFASSUNG

Das Konzept des Mikronetzes (MG) hat in jüngster Zeit aufgrund des Paradigmenwechsels von zentralisierten Stromversorgungssystemen zu lokalen Stromversorgungssystemen, die für einen bestimmten Versorgungsbereich bestimmt sind, zunehmend an Bedeutung gewonnen. Es verfügt über eigene Stromquellen und Verbraucher. Es kann im Inselmodus betrieben werden oder auch an das öffentliche Verbundnetz angeschlossen werden, was als netzgekoppelter Modus bezeichnet wird. Aufgrund der steigenden CO₂-Emissionen und der Verfügbarkeit erneuerbarer Energiequellen an einem bestimmten geografischen Standort werden als Energiequellen für das MG meist umrichterbasierte erneuerbare Energiequellen verwendet. Das Verhalten der Umrichter bestimmt somit das Verhalten des MG in unterschiedlichen Betriebszuständen. Im Großen und Ganzen sind die Steuerungsschemata des Konverters in zwei Kategorien unterteilt, nämlich netzgeführte Umrichter (grid following, GFL) und netzbildende Umrichter (grid forming, GFM), die beide ihre jeweiligen Vor- und Nachteile haben. Auch die Nennleistung, der Anschlusspunkt im Netz und das Verhältnis von GFL und GFM zur Gesamtleistungskapazität sind bei der Gestaltung des MG wichtig.

Neben den Vorteilen des MG sind mit dem Betrieb des MG aufgrund der geringen Trägheit und der niedrigen Fehlerströme auch Stabilitätsprobleme verbunden. Die Stabilität des MG kann in Kleinsignal- und Großsignalstabilität hinsichtlich Frequenz und Spannung eingeteilt werden. Im netzgekoppelten Modus ist die Kleinsignalstabilität nicht wichtig, da sie hauptsächlich vom externen Netz gesteuert wird, aber die Großsignalstabilität ist wichtig. Da jedoch im Inselmodus kein externes Netz verfügbar ist, sind sowohl beide Stabilitätsuntersuchungen wichtig. Zusätzlich wird die Reaktion der netzgekoppelten MG an ihrem Anschlusspunkt (Point of Connection, POC) überwacht. Um möglichen destabilisierenden Auswirkungen einer hohen Durchdringung konverterbasierter Quellen in das Stromnetz entgegenzuwirken, wurden einige Standards definiert, in denen die erforderliche Reaktion der Konverter in bestimmten Situationen vorgegeben werden.

Die Stabilität des MG wird maßgeblich durch die Regelkonzepte der angeschlossenen Umrichter bestimmt. In der Literatur werden einige Standardkontrollschemaschemata für GFL und GFM diskutiert. Aufgrund der begrenzten Kurzschlussleistung im MG sind jedoch einige Änderungen an diesen Steuerungsschemata wichtig, um einen stabilen Betrieb zu erreichen. Daher werden im ersten Teil dieser Arbeit die verbesserten Steuerungsschemata für GFL- und GFM-Umrichter analysiert, um eine robuste Reaktion unter verschiedenen Betriebsbedingungen zu erreichen. Außerdem wird das Verhalten des herkömmlichen GFL-Schemas und des verbesserten Schemas verglichen, um den Grad der Verbesserung unter verschiedenen Betriebsbedingungen zu quantifizieren. Das Hauptaugenmerk liegt darauf, ein stabiles Betriebsverhalten zu erreichen, den sicheren Betrieb des Umrichters zu gewährleisten, die Ausnutzung der möglichen Stromgrenzen zu optimieren und die Symmetrie der

Spannung bei unsymmetrischen Fehlern zu verbessern. In ähnlicher Weise wird das GFM-Steuerungsschema modifiziert, um eine stabile Reaktion sowohl in schwachen als auch in steifen Netzen zu erreichen, die transiente Stabilität bei Fehlern mit begrenzter Stromverarbeitungsfähigkeit zu verbessern und einen reibungslosen Übergang von verschiedenen Betriebsmodi zu erreichen.

Im zweiten Teil dieser Arbeit werden die Schlüsselparameter für das Design und den stabilen Betrieb des MG sowie die detaillierte Stabilitätsanalyse in beiden Betriebsmodi diskutiert. Es werden auch einige Regeln für die Auswahl des Standorts, des Typs, der Größe und des Verhältnisses der GFL-basierten Leistung zur GFM-basierten Leistung für die Gestaltung des MG besprochen. Das Hauptziel besteht darin, eine stabile Reaktion von MG unter allen Betriebsbedingungen zu erreichen, gleichzeitig die Einhaltung der Stromgrenzen der Umrichter sicherzustellen und damit die Zuverlässigkeit im Betrieb zu verbessern. Abschließend werden detaillierte Stabilitätsstudien in beiden Betriebsmodi diskutiert.

CONTENTS

ACKNOWLEDGEMENT	III
ABSTRACT	IV
KURZFASSUNG	VI
CONTENTS.....	VIII
LIST OF ABBREVIATIONS.....	XII
LIST OF SYMBOLS.....	XV
1. INTRODUCTION	1
1.1 OBJECTIVES AND SUMMARY OF THE WORK	3
1.2 THESIS OUTLINE.....	4
1.3 LIST OF PUBLICATIONS	4
2. LITERATURE REVIEW	6
2.1 OVERVIEW OF MICRO-GRID	7
2.1.1 <i>Definition of Micro-grid</i>	9
2.1.2 <i>Major Components of Micro-grid</i>	10
2.1.3 <i>Benefits of Micro-grid</i>	11
2.1.4 <i>Classifications of Micro-grid</i>	12
2.1.5 <i>Control of Micro-grid</i>	15
2.1.6 <i>Micro-grid Challenges</i>	17
2.2 STABILITY OF MICRO-GRID	19
2.2.1 <i>Classification of Micro-grid Stability</i>	21
2.2.2 <i>Review of Stability Improvement Studies</i>	23
2.3 OVERVIEW OF CONVERTER'S CONTROL SCHEMES	24
2.3.1 <i>Review of Grid Following Converter</i>	25
2.3.2 <i>Review of Grid Forming Converter</i>	31
2.4 POTENTIAL TEST NETWORKS FOR MICRO-GRID	36
2.4.1 <i>IEEE 34 Bus System</i>	36
2.4.2 <i>Generic European Network</i>	37
2.4.3 <i>European LV Distribution Network</i>	38
3. GRID FOLLOWING CONTROL SCHEME	39
3.1 LCL FILTER DESIGN	40
3.2 MATHEMATICAL EXPRESSIONS FOR DIFFERENT REFERENCE FRAMES	42
3.3 MODELING AND PERFORMANCE ANALYSIS OF CONVENTIONAL GFL SCHEME	46

3.3.1 Phase Locked Loop (PLL)	46
3.3.2 Reference Current Calculations	48
3.3.3 Current Limiter and Priority Current Injection	50
3.3.4 Current Controller and Compensation	50
3.3.5 Exemplary Performance Analysis of Conventional GFL Scheme	55
3.3.6 Possible Improvements in Conventional GFL Scheme	60
3.4 DESIGN OF A NOVEL CONTROL SCHEME FOR GFL	61
3.4.1 Achieving Reference Powers at POC in Normal Conditions	61
3.4.2 Sequence Extraction.....	63
3.4.3 Fault Detection.....	70
3.4.4 Reference Current Calculation.....	74
3.4.5 Current Limitation and Priority.....	77
3.4.6 Inner Current Controller.....	86
3.5 PERFORMANCE ANALYSIS OF IMPROVED GFL CONTROL SCHEME	89
3.5.1 Performance in Normal Conditions.....	90
3.5.2 Performance in LVRT Conditions	91
3.6 FURTHER IMPROVEMENTS	101
3.6.1 Optimal Angle for the Negative Sequence Current Phasor to Achieve Minimum VUF.....	101
3.6.2 Minimization of Real Power Oscillations.....	105
3.7 TAKE AWAYS FROM MODELING AND ANALYSIS OF GFL	111
4. GRID FORMING CONTROL SCHEME	113
4.1 CONVENTIONAL SYNCHRONVERTER CONTROL SCHEME	113
4.1.1 Performance Analysis of Conventional GFM Scheme.....	114
4.1.2 Possible Improvements in Conventional GFM Scheme	118
4.2 DESIGN OF AN ENHANCED GFM SCHEME.....	119
4.2.1 Synchronization.....	119
4.2.2 Enhanced Real Power-Frequency Control.....	126
4.2.3 Enhanced Reactive Power-Voltage Control	130
4.2.4 Priority Injection Schemes.....	135
4.2.5 Current Limitation and Current Control.....	139
4.3 PERFORMANCE ANALYSIS OF IMPROVED GFM CONTROL SCHEME	143
4.3.1 Small Signal Stability	144
4.3.2 Large Signal Stability.....	147
4.4 TAKE AWAYS FROM MODELING AND ANALYSIS OF GFM	153
5. STABILITY OF MULTI-CONVERTER SYSTEMS	156
5.1 SHORT CIRCUIT RATIO	156
5.1.1 SCP of GFM in Small Disturbances	157

5.1.2 SCP of GFM in Large Disturbances.....	161
5.2 ANALYSIS OF MULTI-CONVERTER SYSTEM	162
5.2.1 GFM Vs Grid	164
5.2.2 GFL and Grid	165
5.2.3 GFL and GFM	166
5.2.4 Connection of Multiple GFMs	169
5.2.5 Simultaneous Connection of GFL and GFM with the Grid	172
5.3 TAKE AWAYS FROM THE MULTI-CONVERTER SYSTEMS' ANALYSIS	174
6. ANALYSIS OF A MICRO GRID	175
6.1 SELECTION OF TEST NETWORK	175
6.2 SELECTION OF SIZE, LOCATION, AND TYPE OF THE CONVERTERS FOR EACH FEEDER	177
6.2.1 Selection of Converters for Residential Feeder	178
6.2.2 Selection of Converters for Commercial Feeder	180
6.3 PROCEDURE FOR BLACK START	181
6.4 INITIALIZATION PROCESS OF THE RESIDENTIAL MG	182
6.5 LOAD MANAGEMENT SYSTEM FOR RESIDENTIAL MG	186
6.6 STABILITY ANALYSIS OF THE RESIDENTIAL MICRO-GRID IN ISLANDED MODE	191
6.6.1 Small Signal Stability	191
6.6.2 Large Signal Stability.....	193
6.7 ANALYSIS OF THE RESIDENTIAL MG IN GRID-CONNECTED MODE	204
6.7.1 Smooth Connection/disconnection to the Grid.....	204
6.7.2 Large Signal Stability in Grid Connected Mode.....	207
6.8 TAKE AWAYS FROM MG'S ANALYSIS.	212
7. DISCUSSION AND CONCLUSION	213
7.1 GENERAL CONCLUSIONS.....	213
7.2 SPECIFIC CONCLUSIONS ADDRESSING THE FORMULATED RESEARCH QUESTIONS	214
7.3 FUTURE RECOMMENDATIONS	216
REFERENCES	I
APPENDICES	VII
A. DATA FOR GENERIC EUROPEAN NETWORK	VII
B. DATA FOR EUROPEAN LV DISTRIBUTION NETWORK.....	XI
C. DERIVATION OF TRANSFER FUNCTION FOR LCL FILTER	XIII
D. PERFORMANCE OF LCL FILTER	XIV
E. LINEARIZATION AND LAPLACE TRANSFORMATION OF DIFFERENTIAL EQUATIONS	XVII

F. STATIONARY REFERENCE FRAME COMPONENTS IN UNBALANCED CONDITIONS	XVIII
G. POSITIVE AND NEGATIVE SEQUENCE COMPONENTS IN STATIONARY REFERENCE FRAME	XIX
H. DERIVATION OF DSM FOR SEQUENCE EXTRACTION.....	XX
I. DERIVATION OF SSB BASED FAULT DETECTION METHOD	XXI
J. DERIVATION OF SBS BASED FAULT DETECTION METHOD	XXII
K. EXPRESSIONS FOR REAL AND REACTIVE POWER IN UNBALANCED CONDITIONS.....	XXIII
L. DERIVATION FOR MAGNITUDE OF RESULTANT CURRENT PHASOR	XXV
M. DERIVATION OF LINE CURRENT EXPRESSIONS IN TERM OF SEQUENCE COMPONENTS.....	XXVI
N. DERIVATION OF SCP FOR ISLANDED GFM IN CASE OF SMALL DISTURBANCES.....	XXVII
O. NUMERICAL EXAMPLE FOR THE CALCULATION OF SCR IN MULTI-CONVERTER SYSTEM	XXIX
P. BLOCK DIAGRAM FOR INNER CURRENT CONTROLLER WITH VOLTAGE LOOP.....	XXX

LIST OF ABBREVIATIONS

$\alpha\beta$	stationary reference frame.
AC	alternating current.
BCI	balanced current injection.
CB	circuit breaker.
CCT	critical clearing time.
CHP	combined heat and power.
CIG	converter-interfaced generation.
CIGRE	international council on large electric systems.
CSNS	component-wise sequence numeric summation.
DC	direct current.
DCC	direct current control.
DES	distributed energy sources.
DFIG	doubly fed induction generator.
DG	distributed generation.
DLG	double line to ground.
DQ	synchronous rotating reference frame.
DR	damping resistor.
DS	distributed sources.
DSM	delay sample method.
DSVS	detailed sequence vector summation.
EMS	energy management system.
EU	European union.
FC	fuzzy control.
FOGI	first order generalized integrator.
FFT	fast Fourier transform.
GC	grid connected.
GCR	grid code recommendations.
GFL	grid following control.
Gel	grid feeding converter.
GFM	grid forming control.
GSL	grid supporting control.
GTO	gate turn-off.
HV	high voltage.
IDSM	improved delay sample method.
IEEE	institute of electrical and electronics engineers.

IGBT	insulated-gate bipolar transistor.
LC	local control.
LFC	load frequency control.
L-L	line to line.
LPF	low pass filter.
LV	low voltage.
LVRT	low voltage ride through.
MB	main breaker.
MC	multi-converter.
MCS	multi-converter system.
MG	micro-grid.
MPPT	maximum power point tracking.
MRPF	minimum real power fluctuation.
MV	medium voltage.
NC	normal conditions.
NZE	net zero emission.
OAI	optimum angle injection.
OH	overhead line.
OV	over voltage.
pf	power factor.
PI	proportional-integral controller.
PLL	phase locked loop.
POC	point of connection.
PR	proportional resonant controller.
PV	photovoltaics.
PWM	pulse width modulation.
QPR	quasi-proportional resonant controller.
RES	renewable energy source.
RMS	root mean square.
RQ	research question.
SBS	sequence-based scheme.
SCC	short circuit current.
SCP	short circuit power.
SCR	short circuit ratio.
SD	standard deviation.
SEP	stable equilibrium point.
SFCL	superconducting fault current limiter.

SG	synchronous generator.
SLG	single line to ground.
SoC	state of charge.
SOGI	second order generalized integrator.
SRF-PLL	synchronous reference frame phase locked loop.
SSB	simple sequence based.
SSR	sub-synchronous resonance.
SSVS	simplified sequence vector summation.
SVPWM	space vector pulse width modulation.
STATCOM	static synchronous compensator.
THD	total harmonic distortion.
Tr	transformer.
UG	underground cable.
VSC	voltage source converter.
VSG	virtual synchronous generator.
VUF	voltage unbalance factor.

LIST OF SYMBOLS

Symbol	Description
X^*	To denote the reference value for any parameter (i.e., X here)
X^{**}	To denote the reference value for any parameter (i.e., X here) after applying its limits
$ X $	To denote the magnitude of any complex parameter (i.e., X here)
ΔX	To denote the change in value of any parameter (i.e., X here)
X_o	To denote the initial value for any parameter (i.e., X here)
$X_{\alpha\beta}$	To denote any phasor (i.e., X here) in stationary reference frame
X_{abc}	To denote any phasor (i.e., X here) in 'abc' reference frame
X_{adj}	To denote the adjusted values for any parameter (i.e., X here)
X_b	To denote any base parameter (i.e., X here)
$X_{c,vc}$	To denote the current control and voltage control parameters respectively (i.e., X here)
X_{dq}	To denote any phasor (i.e., X here) in rotating reference frame
X_{dc}	To denote the dc side parameter (i.e., X here)
$X_{g,f,tr}$	To denote any parameter (i.e., X here) of grid, filter, and transformer respectively
$X_{GFL,GFM}$	To denote any parameter (i.e., X here) of grid following converter and grid forming converter respectively
X_{L-L}	To denote line-to-line value of any parameter (i.e., X here)
$X_{LV,HV}$	To denote any parameter (i.e., X here) on the LV and HV side of the transformer respectively.
$X_{OL,CL}$	To denote any open loop and closed loop transfer function (i.e., X here) respectively
X_{max}	To denote the maximum value of any parameter (i.e., X here)
X_{poc}	Measured parameter (i.e., X here) at POC
$X_{p,n}$	To denote any parameter (i.e., X here) for the positive or negative sequence respectively
X_{res}	To denote any parameter (i.e., X here) related to the resonance
X_{sc}	To denote any parameter (i.e., X here) related to the short circuit
X_{tot}	To denote summation value of any parameter (i.e., X here)
X_1	To denote any parameter (i.e., X here) of LCL filter on converter's side
X_2	To denote any parameter (i.e., X here) of LCL filter on grid's side
X_2^g	To denote summation of any parameter (i.e., X here) of grid, transformer and LCL filter's parameter on grid's side
X^{lim}	To denote the limit of any parameter (i.e., X here)
X^T	To denote the orthogonal of a parameter (i.e., X here)
C	Capacitance
C_F	Capacitance of the filter
D_p	Droop coefficient for real power control

D_q	Droop coefficient for reactive power control
D_ω	Droop coefficient for frequency
D_V	Droop coefficient for voltage
e	Internal three phase voltage for GFM
f	Frequency
f_c	Critical frequency
f_{con}	Converter's frequency
f_{cut}	Cutoff frequency
f_s	Sampling frequency
f_{sw}	Switching frequency
G_{DR}	Damping resistor's gain
G_p	Proportional gain for frequency correction
H	For presenting Transfer function
I	Current phasor's magnitude
i	Line current phasor
i_l	Converter's side current
i_c	Line current phasor passing through capacitor of the LCL filter
i_g	Measured current on converter's side of POC
j	To represent imaginary component
J	Moment of inertia
$k_{p,n}$	Proportional gain for the positive and negative sequence currents injection, in LVRT, respectively
K	gain
K_i	Integral gain of the controller
K_p	Proportional gain of the controller
L_F	Inductance of the filter
L	Inductance
M_{jif}	Output of Q-V control for synchronverter
p	Real power
P_L	Real power of the load
$p_{p,n}$	Real power of positive and negative sequence respectively
\tilde{P}	Real power fluctuation component in unbalanced conditions
p^{lim}	Limit for the real power decided by the priority injection scheme
p^{rated}	Rated real power of the converter
Q	Quality factor
Q_L	Reactive power of the load
q	Reactive power

$q_{p,n}$	Reactive power of positive and negative sequence respectively
\tilde{q}	Reactive power fluctuation component in unbalanced conditions
R	Resistance
R_d	Damping resistor
S	Aparant power
T_e	Electrical torque
T_{on}	On-time delay
T_{off}	Off-time delay
T_m	Mechanical torque
T_s	Sampling time
τ_{PLL}	Time constant for the PLL controller
ζ	Damping constant
v, u	Voltage phasor
v_{dc}	DC link voltage
v_c	Voltage across the filter's capacitance
v_{fb}	Feedback voltage
v_i	Voltage phasor on the terminal of the converter (before filter)
V	Voltage phasor's magnitude
$\omega, \dot{\theta}$	Angular frequency
ω_c	Critical angular frequency
ω_i	Bandwidth of inner current controller
ω_v	Bandwidth of inner voltage controller
ω_{cut}	Cutoff angular frequency
ω_n	Natural oscillation frequency
ω_{PLL}	Angular frequency assessed by the PLL
X	Reactance
X/R	Reactance to resistance ratio
z	Discrete domain operator
Z	Impedance
θ	Angle
θ_{PLL}	Voltage angle assessment by the PLL
θ_v	Initial angle of the voltage phasor
θ_i	Initial angle of the current phasor
θ_{vpn}	Angle between positive and negative sequence voltage phasors

1. INTRODUCTION

In recent years, the increasing demand of energy and the lesser availability of fossil resources lead to vast research and development for more sustainable and alternative electrical resources. Globally, the renewable energy sources (RES) are gaining a larger share in the total generation of electricity. Apart from sustainability, the increasing share of RES is also helping in reducing the environmental pollution as the power plants have major share in it [1, 2].

Micro-grid (MG) is an expanding energy sector which shows the shift from centralized power systems towards the localized power systems. It is designed for a specific geographical location e.g., communities, campuses, factories, etc. Most of the distributed generation (DG) for the MG is based on the RES. It can operate in both grid-connected and islanded mode. With the islanding operation capability, it can enhance the reliability of service for its connected loads if any disturbance occurs on the grid's side. MGs are not only efficient, low cost and eco-friendly, but they also enhance the stability of the external power grid with their grid-connected mode. The sources connected in a MG can be centrally controlled which mainly adjusts the reference powers for each converter based on the operating conditions. It helps to control the MG effectively and optimally as all the information is passed to a centralized control unit. However, a centralized controller needs the extra communication lines, and the communication delays must also be taken into consideration. Moreover, due to centralized controller and involved communication protocols, it also lowers energy security as it is prone to cyber-attacks. Some distributed controls are also proposed which don't need a centralized control unit and no communication protocols are required between the converters. Thus, it improves the energy security of MG, but the optimal operation of the converters may be compromised.

The classification of stability of MG is somewhat different than the one for conventional power systems. The stability of MG can be classified into short-term and long-term stability [3]. Based on the disturbance, the MG stability can be categorized as small- and large signal stability where the small signal refers to the change in operating conditions in which the converter's current limit is not reached and the large signal stability is referred to the transients. Based on the control design and parameter tuning, the small signal stability can be both short term and long term. The small and large signal stabilities are important for voltage, frequency, and converter-driven stability where the converter-driven stability refers to the stability issues related to the slow interactions of the power-electronic devices with the other power electronic devices or with the electromechanical dynamics of the synchronous generator (SG). It primarily deals with the power oscillations of the converters due to wrong angle assessment by grid following control (GFL) based converter or the out of synchronous operation of the grid forming control (GFM) based converter. It also includes the un-damped power

oscillations in case of large penetration of the converter-based power sources without proper tuning of the control parameters.

The stable operation of the MG in different operating conditions is of utmost importance for the reliability of the system. Due to the limited power reserves, and most of them are of converter-based RES, the inertia of the system is too small, which makes the system responsive to even small changes in the operating conditions. Thus, small signal stability is important for the islanded MG. Moreover, due to the limited current injection capability of the converters, the fault current levels are largely reduced which poses serious challenges for the large signal stability and for timely fault detection. Unlike the conventional power system, the MG with 100 % converter-based sources has no directly connected synchronous generators, thus no rotor angle stability is defined but the newly defined slow interaction converter -driven stability is important as it deals with the phase locked loop (PLL) stability of GFL and ensures the synchronization of the GFM (angle stability). Converter-driven stability is important along with voltage and frequency stability in case of large disturbances. In case of unintentional shift from grid-connected to islanded mode, the short-term stability of MG is under serious question due to the operation of each converter at different stable equilibrium point (SEP).

The GFL scheme, as the name suggests, follows the grid, and injects the reference real and reactive powers. In case of faults, the grid operators demand some additional reactive power for the voltage support, thus, it is important to detect the faulty conditions timely and accurately and inject the reactive power accordingly. Moreover, selective voltage support is demanded in unbalanced faults, thus the GFL scheme should be able to inject the negative sequence current in such conditions. The stability of the GFL is highly affected by the stable operation of the PLL (for angle estimation) and the speed of the inner current controller. The stability of PLL comes under the umbrella of the converter-driven stability which is quite low for the weak grids due to the introduction of the negative admittance by the PLL in parallel to the network's admittance.

On the other hand, GFM can form the grid and maintain the voltage and frequency by itself. It can be modeled with a controlled voltage source and has the black start capability. Depending upon the dc side storage, it can also introduce virtual inertia to the system. GFM is normally stable in weaker grids and faces some stability issues in strong grid connections. Due to the voltage source behavior, GFM offers natural response of a three-phase voltage source against any disturbance in different operating conditions. Converter-driven stability of GFM is important in the perspective of large signal stability as it ensures the synchronization of the GFM with the grid/MG. Moreover, for enhanced stability, it is important for the GFM to ensure smooth connection/disconnection with the power network.

1.1 Objectives and Summary of the Work

Even though the MG is considered as a potential solution for the growing electrical systems, it faces some technical challenges which need to be analyzed and addressed for enhanced reliability of the future power systems. Due to the large penetration of the converter-based generation in the MG, it is important to improve the control schemes of the converters to enhance the stability of the MG. Thus, in the first part, this thesis presents improved schemes for the GFL and GFM to offer stable operation in different operating conditions. To improve the converter-driven stability i.e., PLL stability, a reference current adjustment scheme is introduced which can be activated in grid connected mode and deactivated in islanded operation of the MG to limit the effect of the negative admittance introduced by the PLL. Better schemes for sequence extraction and fault detection are also discussed. Moreover, the improved GFL scheme offers flexible current controls, and ensures the maximum utilization of the converter's current handling capability. Some comparative studies confirm that better voltage uniformity and minimum real power oscillations can be achieved by properly calculating the reference currents in case of unbalanced conditions. The GFM scheme is modified to enhance the converter-driven stability related to the maximum power transfer capability of the voltage source in case of voltage dips. It ensures the synchronization in different operating conditions, especially in case of frequency dips when converter is already operating at its maximum real power. In such scenarios, the conventional GFM scheme results in out of synchronous operation.

In the second part of this thesis, the analysis of multi-converter system (MCS) is performed to discuss the impact of different control schemes on the calculation of the short circuit power. This also helps to define some recommendations for the converter's connection to ensure stable operation. In the second part, the recommendations for the design of the MG are also discussed along with some recommendations for the load management system to enhance the small signal stability of the MG. Finally, the small and large signal stabilities are analyzed for the designed MG under different modes of operation. It is important to mention here that the stable operation of the MG under various operating modes is of primary interest in this thesis. The type and unit cost of the dc sources are not considered in this work; thus, the general benefits of the MG are not discussed explicitly but some of the benefits can be verified from this work.

The objectives of this thesis are mainly divided into two categories. As the converter-based power sources are the building blocks for the MG, thus the first category deals with the design of flexible control schemes. The research questions under this category are given below.

RQ1: How to achieve a stable response of GFL, ensuring and maximizing the utility of current limit of the converter and prioritizing certain current components?

RQ2: How to enhance the voltage uniformity and minimize real power oscillations in case of unbalanced faults?

RQ3: How to design a unified GFM scheme for weak to stiff grid connections ensuring synchronization in fault and post fault conditions?

The second category deals with research questions related to the design of the MG to achieve its stable operation. These questions are given below.

RQ4: What is the impact of different converter's control schemes on the short circuit power?

RQ5: What should be the ratio of GFM to GFL based power for stable operation of the MG?

RQ6: What should be the characteristics of the load management system for the smooth operation of the MG?

To test the performance of the newly developed control schemes, the small and large signal stabilities of the designed MG are analyzed in different modes of operation.

1.2 Thesis Outline

The thesis outline is given below.

- **Chapter 2** presents the literature review regarding the MG, its classifications, challenges, and the types of stability. It also provides an overview regarding different control schemes for converter control, their fundamental operating principles, the stated advancements, and limitations in their operations. Some potential networks for MG are also discussed in this chapter.
- **Chapter 3** discusses the design of the conventional and improved GFL schemes. It also presents performance comparison between different reference current calculation schemes, priority injection schemes and current limitation schemes.
- **Chapter 4** presents the conventional and improved design for the GFM schemes along with their performance in different operating conditions.
- **Chapter 5** investigates multi-converter systems. It presents the calculations of the short circuit power of the converters in case of small and large disturbances. It also discusses some important recommendations for the converter's connection.
- **Chapter 6** discusses different factors in the design of the MG. It also discusses the load management system for the MG to ensure smooth operation in different conditions. Moreover, the detailed stability analysis is performed for the islanded, and grid connected operations.
- **Chapter 7** summarizes the thesis. It also presents specific findings related to the research questions and discusses some future recommendations.

1.3 List of Publications

This research has resulted in the following publications.

- I. M. Abubakar, H. Renner, and R. Schürhuber. (2023), "Development of a Novel Control Scheme to Achieve the Minimum Unbalance Factor and Real Power Fluctuations under Asymmetrical Faults", *Energies* 16(22), DOI: [10.3390/en16227511](https://doi.org/10.3390/en16227511).
- II. M. Abubakar, H. Renner, and R. Schürhuber, "Development of a Novel Control Scheme for Grid-Following Converter under Asymmetrical Faults", *Energies*, vol. 16, p. 1276, 2023, DOI: [10.3390/en16031276](https://doi.org/10.3390/en16031276).
- III. M. Abubakar, P. Hackl, H. Renner, and R. Schürhuber, "Investigation of Optimal Share of Active and Reactive Current Injection in Negative Sequence in Case of Unbalanced Faults in Grid Following Converter", *CIGRE B4 Colloquium 2023, Vienna, Austria, 2023*.
- IV. M. Abubakar, H. Akbari, and H. Renner, "Development of Reference Current Calculation Scheme for Grid-Side Converter during Unbalanced Faults", *2022 Second International Conference on Sustainable Mobility Applications, Renewables and Technology (SMART), 2022*, pp. 1-9, DOI: [10.1109/smart55236.2022.9990338](https://doi.org/10.1109/smart55236.2022.9990338).

The author has also published the following article during the Ph.D. study.

- V. M. Abubakar, B. Hussain, M. M. Majeed, and D. Ali, "Enhancement of Rotor Angle Stability with Superconducting Fault Current Limiter", *2022 International Conference on Recent Advances in Electrical Engineering & Computer Sciences (RAEE & CS), 2022*, pp. 1-6, DOI: [10.1109/raeecs56511.2022.9954579](https://doi.org/10.1109/raeecs56511.2022.9954579).

The author has also co-authored the following article during the Ph.D. study.

- VI. M. A. Shoaib, A. Q. Khan, S. T. Gul, G. Mustafa, M. Abid, M. Abubakar, et al., "Fault location in meshed power networks by using hybrid sparse current and voltage measurements along with RSFCL", *Electric Power Systems Research*, vol. 225, p. 109789, 2023/12/01/ 2023, DOI: [10.1016/j.epsr.2023.109789](https://doi.org/10.1016/j.epsr.2023.109789).

2. LITERATURE REVIEW

Due to the different measures taken to control the global warming, e.g., net zero emission (NZE) 2050, the share of renewable energy is increasing in the global electricity generation. It helps to reduce CO₂ emissions and to keep the average temperature rise below 1.5°C. In 2023, the renewable based electricity generation capacity jumped up to 507 GW which is 50 % higher than its previous value. There are different factors responsible for such trends e.g., recent technological advances, energy policy announcements, energy security issues, and higher costs for conventional energy sources etc. Figure 2.1 shows the increase in the capacity of renewable based electricity generation in the coming years [4].

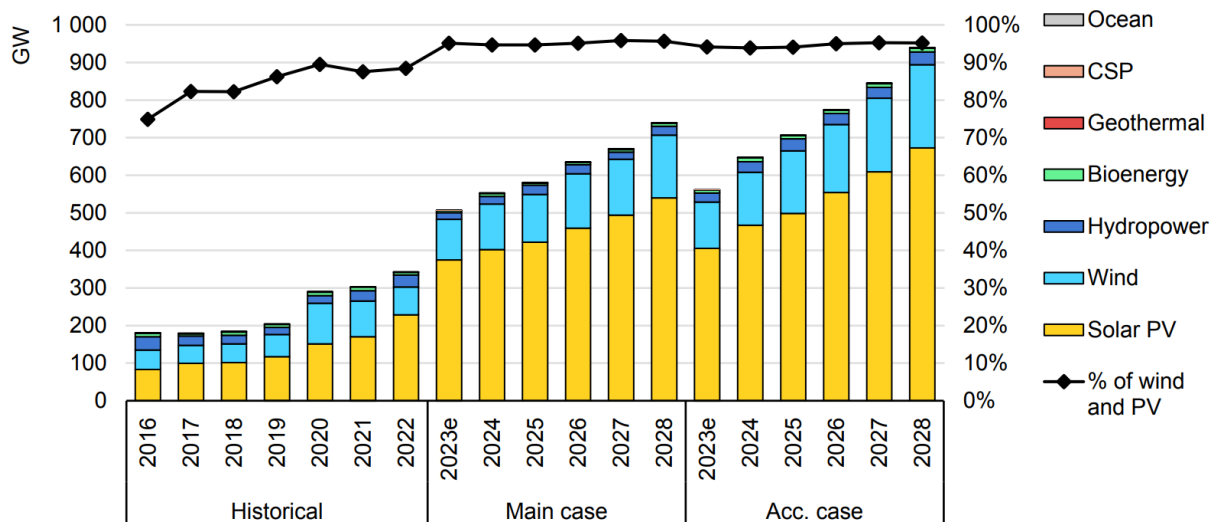


Figure 2.1: Capacity addition of different renewable electricity technologies, Ref. [4]

Due to the regional energy security issues, revised energy policies by different countries, and the fast completion of the onshore wind power projects, a rapid increase in the total capacity of different renewable electricity generation technologies, is expected in 2023 and 2024 which can be 15 % higher than its normal trend. To cut the share in CO₂ emission, different countries announced their energy policies. Austria sets a target of 100 % renewable-based electricity supply (national balance) by 2030 which means that there will be a net increase of 22-27 TWh of renewable electricity across all technologies [1]. Similarly, the European Union (EU) planned to double the share of solar and wind electricity by 2025 and to triple it till 2030 [2].

From Figure 2.1, it is clear that among different renewable technologies, photovoltaics (PV) and wind have the major share of installed electricity generation capacity. The large and small-scale PV systems result in 2/3 of the global increase in renewable electricity generation. Due to direct current (DC) power generation, the PV systems need the DC/AC converters to connect with the alternating current (AC) power system. Most of the new converters are voltage source converter (VSC) due to its reactive power control capability. As far as the performance of the VSC is concerned, the control scheme is more influencing than its topology. Thus, different control schemes for the converters will be discussed in

this thesis. Due to the low inertia and the increased share of converter-based power generation, it poses huge impacts on the stability of the power system. Moreover, due to the decentralized nature of renewable energy sources, a localized power system can also be developed with the help of several renewable energy sources which is termed as micro-grid.

2.1 Overview of Micro-Grid

In the late 20th to early 21st century, the focus of research started to shift to decentralized electrical systems. In [5], the author used the term ‘MicroGrid’ for the isolated power system to provide power to the remote earth station in Antarctica. In [6], the authors introduced the ‘micro-grid’ term for an isolated electrical system having dedicated generation and loads. It is defined as a self-sufficient power system having its own distributed sources (DS), flexible loads, energy storage element(s) and centralized/decentralized controller. In the next five years, different aspects of MG were discussed in several publications. In that period, different challenges of MG such as, control strategies, reliability of distribution system with micro-grids, DC-DC converters, and optimal sizing of DGs etc., were addressed [7-12]. Due to the higher penetration of DSs, the stability of individual DSs and their interactions decide the stability of the MG.

Due to its advantages, such as low costs (investment, maintenance, and operation), ability to integrate RES, and enhanced efficiency with combined heat and power (CHP) cycle, MGs got the attention of the investors. The market of the MG is continuously increasing and same is forecasted for the coming years which is shown in Figure 2.2.

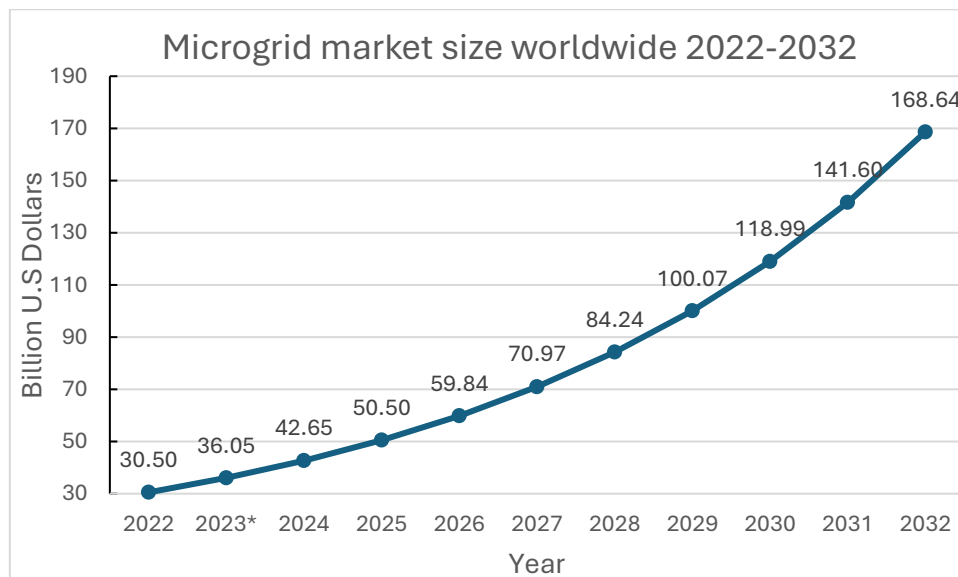


Figure 2.2: Forecasted MG market size worldwide from 2022-2032, Ref. [13]

The expected compound annual growth rate for the MG market is expected to jump from 17.9 % to 18.7 % from 2023 to 2032 which is the indication of huge investments in MGs and market

competitiveness of the MGs. The largest market for the MGs is in North America whereas its growing rate is higher in Asia Pacific [13, 14]. Most of the installed MGs are grid connected e.g., in 2022, about 62 % of the installed MGs were grid connected and 38 % were operated in islanded mode [13].

The details of some of the recently installed MG projects in United States of America (USA) are given in Table 2.1.

Table 2.1: Details of the selected recently installed MGs in USA, Ref. [15]

Project Name	State	Primary Application	Total Capacity (kW)
Village of Boaz	WI	City/Community	250
Ben E. Keith Beverages (Budweiser/Bud Light)	TX	Commercial	1792
Borough of Quakertown Microgrid	PA	City/Community	12500
"Power to Protect" Microgrid	TN	Research Facility	855
City of Dublin Senior Center	CA	Hospital/Healthcare	163
Dublin Wave Waterpark	CA	Commercial	775
Northside Aztlan Community Center	CO	Public Institution	174
Hot Springs Microgrid	NC	City/Community	6400
Indiana National Guard Camp Atterbury	IN	Military	7000
Emory University Campus / Health Sciences Research Building II	GA	College/University	6500
Kaiser Permanente Ontario	CA	Hospital/Healthcare	9000
McKinleyville CSD da'ledik Microgrid Hiller Park Wastewater Treatment Plant	CA	Water Treatment/Utility	1250
The Tradition- Clearfork Senior Living	TX	Other	1344
The Village of Southampton Senior Living	TX	Other	896
Fort Benning	GA	Military	39750
ShopRite Deer Park, NY	NY	Commercial	720
Walmart 00457	TX	Commercial	896
Walmart 02132	LA	Commercial	1344
Walmart 00777	TX	Commercial	896
Walmart 04129	LA	Commercial	1344

The above table shows only few MG projects which are installed in 2023. It shows different applications of the MG including residential, commercial, healthcare, military, and research sectors, etc. It also shows that the power rating of the MG may vary from few kW to several MW. The MGs are installed in almost all the states of USA with major installations in Texas followed by Alaska and New York with total installed MG capacity of 850, 725, and 588 MW respectively [15]. The annual growth in total installed MG capacity and the total MG projects in USA are given in Figure 2.3.

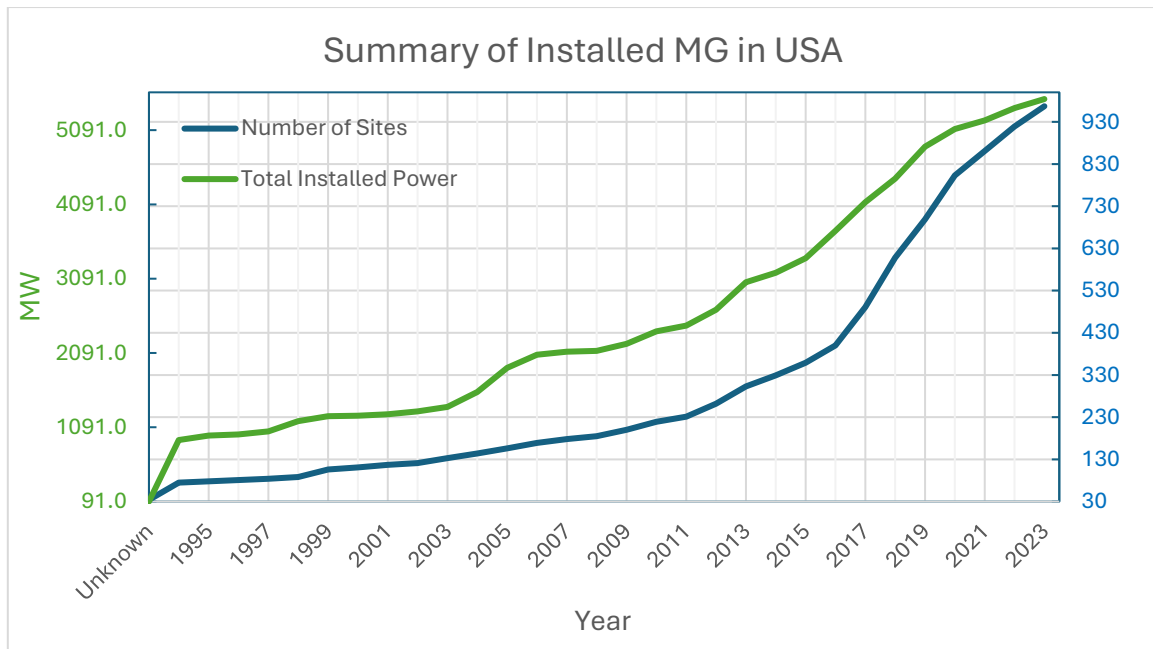


Figure 2.3: Summary of installed MGs in USA, Ref. [15]

The above figure shows a continuously increasing trend in the number of installed MGs projects. Based on these trends and the forecast discussed in Figure 2.2, it is expected that such trends will continue in future with even higher rates.

2.1.1 Definition of Micro-grid

Numerous definitions of micro-grid with two essential conditions were found in the literature that are:

- i. Having its dedicated electrical power sources and loads.
- ii. Could be operated in standalone/islanded and grid-connected mode.

International Council on Large Electric Systems (CIGRE) announced a working group (WG C6.22) for micro-grid (MG) evaluation roadmap. One of the major tasks for this group was to define the MG with respect to the already available definitions [16]. The definition of MG developed by CIGRE working group (WG C6.22) is given below [16].

“Microgrids are electricity distribution systems containing loads and distributed energy resources, (such as distributed generators, storage devices, or controllable loads) that can be operated in a controlled, coordinated way either while connected to the main power network or while islanded.”

The Institute of Electrical and Electronics Engineers (IEEE) defines the MG as given below [17].

“A group of interconnected loads and distributed energy resources with clearly defined electrical boundaries that acts as a single controllable entity with respect to the grid and can connect and disconnect from the grid to enable it to operate in both grid-connected or island modes.”

2.1.2 Major Components of Micro-grid

From the above given definitions, the fundamental components of the MG are listed below.

- i. Distributed Generation
- ii. Distributed Energy Storage
- iii. Loads
- iv. Control Unit

2.1.2.1 Distributed Generation

In MG, the electrical power sources are distributed, and it can be comprised of small size conventional dispatchable sources which can be controlled by the MG controller e.g., diesel, natural gas, and biogas-based synchronous generators (SGs) etc., and intermittent renewable energy sources (RES). These sources offer limited control as the output power can only be regulated if reference power is less than the maximum available power. Most common type of RES for the MG is PV [18, 19].

2.1.2.2 Distributed Energy Storage

The distributed energy storage helps to achieve the load balancing and peak shifting features, but its performance is highly dependent on the actual state of charge (SoC) of the energy storage elements. It not only enhances the small signal stability of the system but also enables to operate the MG economically. It also helps in improving the power quality and reliability of the MG. Distributed energy management system decides the response of different energy storage elements available in a MG [20].

2.1.2.3 Loads

The loads can be classified into different categories. These are briefly discussed in [17] and are given below.

- i. **Critical loads:** as the name suggests, these loads must be served in both grid connected and islanded modes e.g., life saving loads, security systems, etc.
- ii. **Controlled loads:** based on the operating conditions, these loads can be regulated by the load management system.
- iii. **Interruptible loads:** As the name suggests, these loads can be shutdown to balance the generation and load of the MG. Unlike controlled loads, these loads are completely shut down.
- iv. **Dump loads:** These loads are important particularly in islanded operation of the MG. They help to achieve the power balance if there is surplus power, and the curtailment of generation is not possible.

2.1.2.4 Control Unit

MG consists of different layers of control i.e., first, second, and third level control. These control layers can be centralized, de-centralized or distributed. The first level control is normally the de-centralized

control which acts based on the measurements at point of connection (POC). The second level control can be centralized / distributed and is responsible for the energy management of the MG. It defines the output power for the generation units and controls the loads as well. Apart from the controllers, the control unit is comprised off the sensors and the communication network [21].

The general layout diagram of a MG is given in Figure 2.4.



Figure 2.4: General layout of a micro-grid, Ref. [22]

MG can be operated in grid connected or in islanded mode. Based on the situation, it can receive/feed power to the main grid and can help to enhance the reliability of the power system. Several MGs can also be connected to each other to form a flexible and robust power system.

2.1.3 Benefits of Micro-grid

The potential benefits of the MG are majorly discussed in [18] and are given below.

- i. **Enhanced Reliability:** The main advantage of MG is its distributed power sources which allow it to feed the loads if the grid side experiences any disturbance [17, 18, 23].
- ii. **Enhanced Flexibility:** Due to the lower rating and customized control, the MG can be configured to achieve the specific needs of the society. It can be easily reconfigured to change its size or service area [23].
- iii. **Reduced Energy Costs:** Due to the distributed nature of the sources, the overall power losses are less than the conventional power system. Moreover, it can also reduce the demand charges with the help of peak shaving and the local renewable energy sources can provide power at lower rates than the conventional power system [17, 24, 25].
- iv. **Environmental Effect:** MG has a positive impact on the environment as it allows to integrate RESs into the power system. A large share of the total power capacity of a MG is comprised of RESs [26, 27].

- v. **Higher Energy Security:** Different factors affect energy security of the large power systems particularly for the remote areas. These factors include the extreme weather conditions, aging of the equipment, and cyber/physical attacks. Due to the distributed sources of MG, it can provide energy to the remote areas where the main utility is unreliable or expensive and the probability of above mentioned factors is also considerably reduced due to the smaller service area [23, 28].
- vi. **Utility Support:** MG can be operated in grid-connected mode to support the grid in peak load conditions. They can also provide voltage and frequency support in case of contingencies [18, 27].

2.1.4 Classifications of Micro-grid

Based on several parameters, Micro-grids can be classified into different types. In [18], the authors discussed the classification of the MG based on its size, location, application, and sources, etc. The classification of MG is given in Figure 2.5 [18].

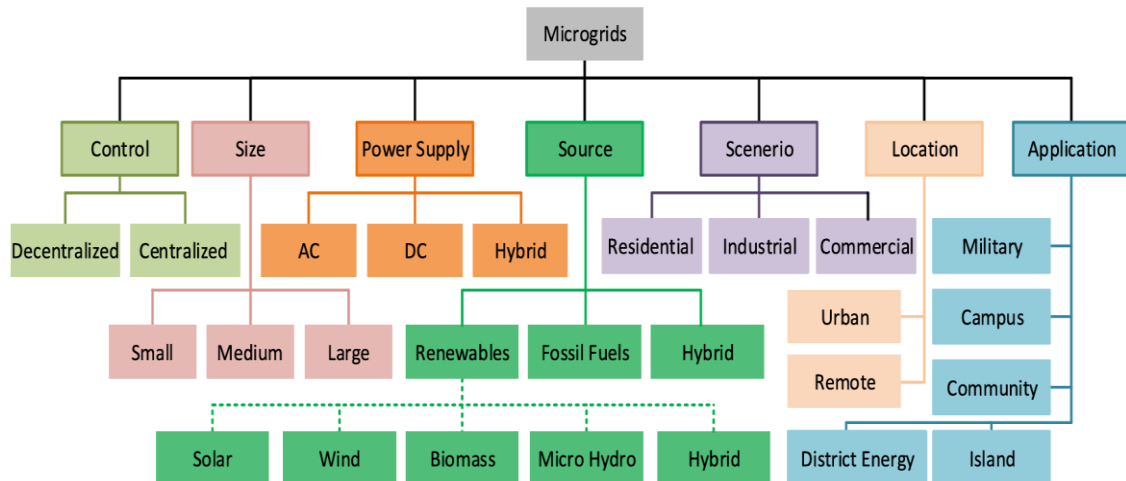


Figure 2.5: Classifications of micro-grid, Ref. [18]

Micro-grids can be classified based on their control hierarchy. The ‘control’ in the above figure refers to the second level control of the MG. In most of the schemes, a centralized second level controller acts as energy management system (EMS) for the MG and calculates the reference power outputs for the generation units based on the measurements at different points, but it is classified as less robust than the decentralized control [29]. Whereas in decentralized control, the first level control of each generating unit regulates its power based on the actual operating conditions at their point of connection (POC). In some papers, distributed controls are also proposed. Each of the control schemes has its own advantages and disadvantages [21, 28].

The MG can be classified into three categories based on its size. The power range for each category largely varies in the literature. Some authors define the power of small MG to be less than 10 kW [19] whereas others consider it to be up to 10 MW [18]. Same is the case for medium and large-scale MGs

which are considered up to 100 MW and 1000 MW respectively if they serve an industrial zone and industrial site respectively [30]. By this comparison, it can be concluded that the MG can be classified based on its capacity, but its range varies largely in different scenarios.

The other important classification is based on the nature of the power sources available in a MG. By definition, the MG may have some dispatchable power units based on the conventional energy sources [16]. Whereas RES-based MGs require energy storage system to ensure the power balance [31]. The RES-based MGs are getting huge attention due to their lower carbon footprints and fast response.

Based on the type of the distribution systems, the MG can be categorized into three different types i.e., AC Micro-grid (AC-MG), DC Micro-grid (DC-MG), and Hybrid Micro-grid (Hyb-MG) [32]. The general layout of AC-MG is discussed in [29] and given in Figure 2.6.

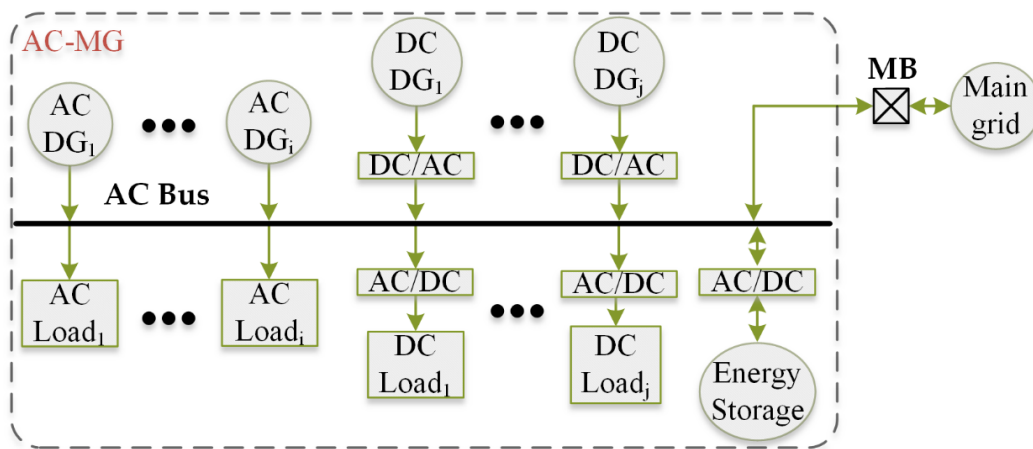


Figure 2.6: General layout of AC micro-grid

The AC-MG can be defined as the MG whose sources and loads are of AC nature at their respective POCs. The AC-MG contains directly connected AC loads, distributed AC power sources, converter-based DC power sources (whose output is AC at their respective POC with the MG), and some converter-based DC loads. The main distribution system is AC in nature. The ‘MB’ in the above figure refers to the main breaker which is controlled by the second level control of the MG. In grid connected mode, AC-MG normally supports the grid in case of voltage and frequency dips but due to the limited power capacity, its impact is limited on the conventional power system. However, in islanded mode, MG needs to regulate its generation based on the frequency and voltage. The AC-MG can be of different arrangements i.e., single phase, three phase with ground, and three phase without ground. Depending upon the nature of the loads, the AC-MG may have different operating frequency than the main grid, in such conditions, it needs to change its operating conditions to synchronize with the main grid. The protection scheme for such a type of MG is somewhat simpler than the protection for the DC-MG but, unlike DC-MG, it also needs to ensure frequency stability [18, 29].

The general layout of DC-MG is given in Figure 2.7.

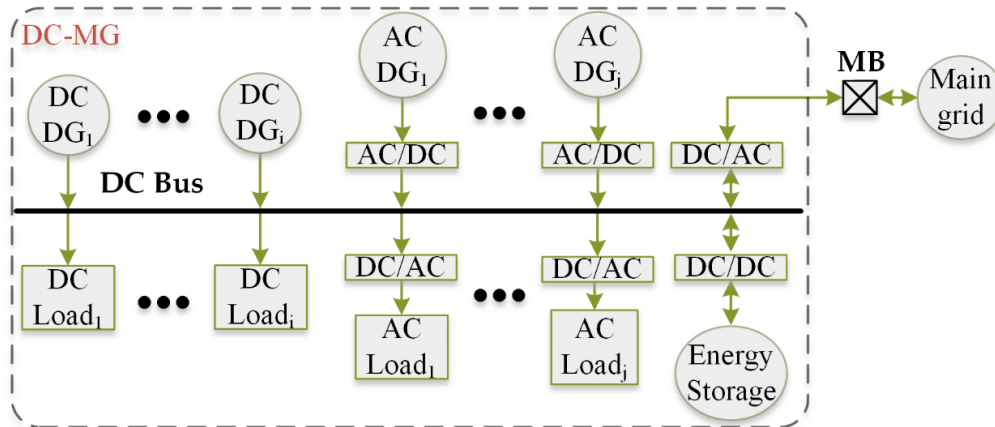


Figure 2.7: General layout of DC micro-grid

As the name suggests, the nature of the sources and loads at their respective POCs is DC. The AC power sources and loads need the AC/DC interface to connect with the DC-MG. It needs an additional power conversion device (DC/AC) for its connection with the main grid. Due to the DC operation, it has simpler second level control as compared to the AC-MG. Keeping in mind that most of the RES are of DC nature, the DC-MG has higher efficiency due to the less power conversions. It also helps to enhance the power quality. Moreover, due to the DC nature of the sources, the synchronization of the power sources in DC-MG is simpler as compared to AC-MG. On the other hand, it has high protection cost due to the DC voltage. Moreover, the DC voltage levels are also not standardized for DC-MG. The DC-MG can have different arrangements i.e., mono-polar, bi-polar, and homo-polar, etc. [19, 29].

The general layout of Hybrid-MG is given in Figure 2.8.

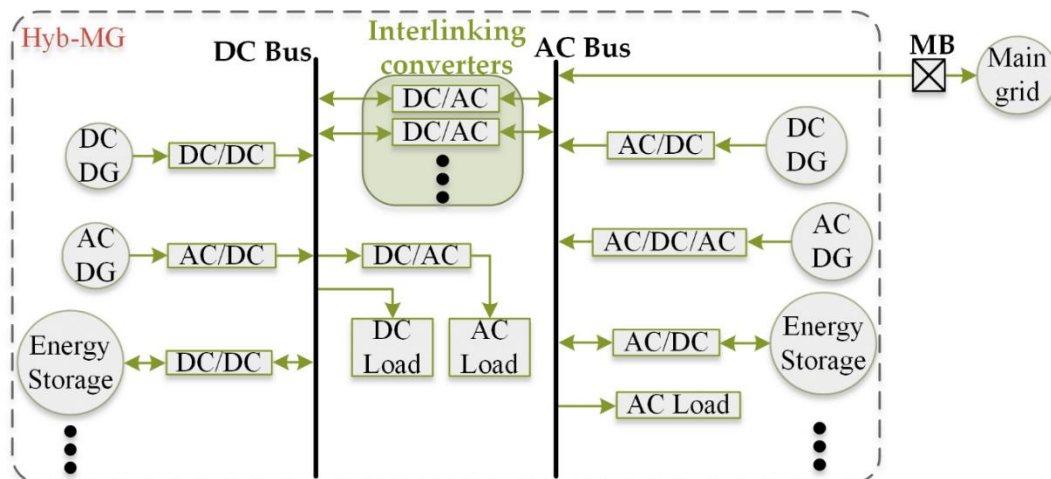


Figure 2.8: General layout of hybrid micro-grid, Ref. [28]

As the name suggests, the Hyb-MG consists of DC and AC power sources and loads. It contains both DC and AC buses. The sources and loads connected with each bus have the same type at their respective POC. It merges the advantages of both the AC-MG and DC-MG. It helps to reduce the unit price by reducing the number of conversion devices and overall power losses in the MG. The interlinking DC/AC converters have bi-directional power flow capability. Both the buses act like sub-MGs of each

type. In normal islanded operation, the sources connected to each bus are responsible for stabilizing the voltage and the interlinking converters help in achieving the overall power balance in the MG. However, due to the complex arrangement, the Hyb-MG needs complex controller and EMS [28, 33]. Different arrangements of Hyb-MG are discussed in [32]. A comparison between different arrangements of the MG is given in Table 2.2.

Table 2.2: Comparison of different types of MG

Factors	AC-MG	DC-MG	Hyb-MG
Better Power Quality	✓	✓✓✓	✓✓
Less Control Complexity	✓✓	✓✓✓	✓
Easy Synchronization of MG's sources	✓	✓✓✓	✓✓
Low Protection Cost	✓✓✓	✓	✓✓

2.1.5 Control of Micro-grid

The MG's control is responsible for its stable operation and defines its response in case of voltage/frequency dips. It is also responsible for smooth transfer between grid-connected to islanded mode and vice versa. It also controls the response of each power source in normal and emergency situations. Normally, the MG control is presented in hierarchical form having first, second and third level control. Each control layer has its own objectives and architecture. The typical hierarchical control layout is presented in Figure 2.9.

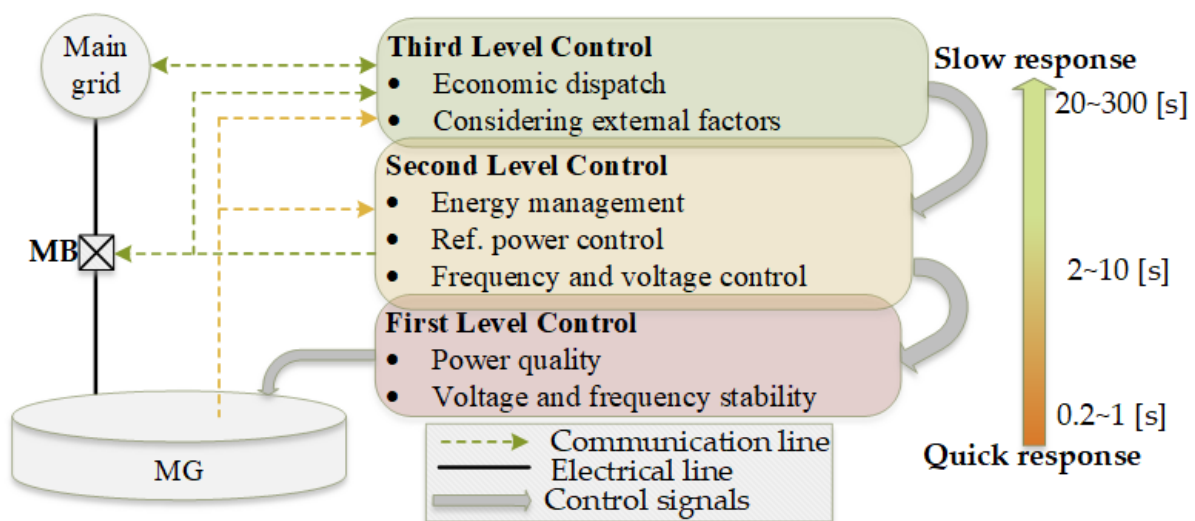


Figure 2.9: Layout of hierarchical control of micro-grid

The first level control is designed for each power generating source in the MG. Depending upon the nature of the primary energy source, there are different schemes for each type. In common, these sources need to be connected through a DC/AC converter. The common control schemes for these converters are grid following and grid forming control schemes. Each of the schemes will be discussed in detail as these are the building blocks for the MG and have a huge impact on the response and stability of the MG in different operating conditions. The first level control is de-centralized, and it responds according

to the operating conditions at POC. It is also responsible for the over current protection of the converter and maintaining the minimum DC link voltage (on the DC side of the converter) [21, 29].

Second level control of MG is also known as energy management system of the MG. It is responsible for secure, reliable, and economical operation of the MG in both grid-connected and islanded mode. It normally controls the reference power of the different sources of MG. It is also responsible for the smooth transitions from grid-connected to islanded mode and vice versa. The second level control can have a centralized controller, distributed controllers, or de-centralized controllers. Each arrangement has its own advantages and disadvantages [21].

In the case of centralized controller, all the measurements at different nodes are passed on to a unified controller which is also connected to the first level controller of each power source. Depending upon the actual conditions, it can regulate the output of the individual sources. It needs communication lines for measurement and control. Thus, the communication delays need to be incorporated while investigating its response in different contingencies. Moreover, it reduces the reliability of the system as the failure of centralized controller leads to system's failure [18].

In distributed control, there are several second level controllers connected to each other through communication channels. Each of the controllers is responsible for some of the sources and loads and it receives the measurements from certain nodes. Such an arrangement helps to improve the reliability and robustness of the system without compromising the advantages of the centralized controller [18].

The decentralized control got more attention of the researchers in recent years due to its relatively higher reliability and low installation cost. In this arrangement, the response of each source is decided based on the local measurements and no communication channels are required. It enhances the reliability of the system, but the drawback lies with the unit cost optimization [28]. Various layouts for the second level control are given in Figure 2.10.

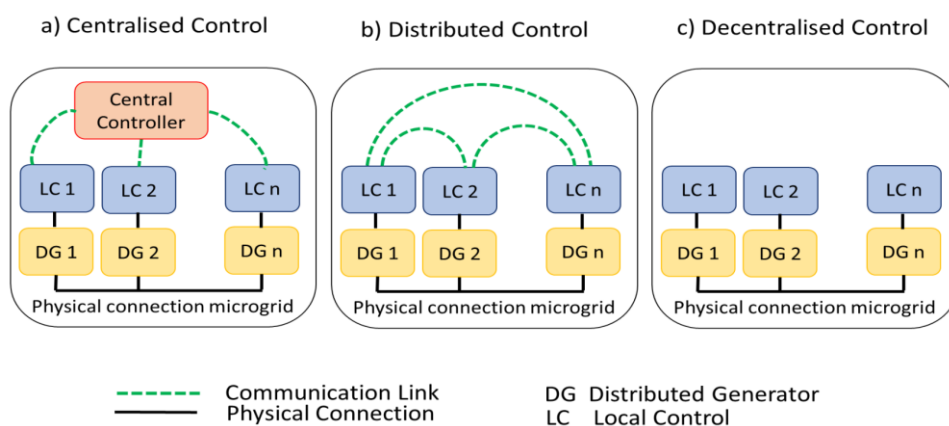


Figure 2.10: Arrangements for second level control, Ref. [34]

The advantages and disadvantages of the three arrangements for the second level control are discussed in [35] and summarized in Table 2.3.

Table 2.3: Comparison of different arrangements for second level control

Factors	Centralized	Distributed	Decentralized
Better Unit Cost Optimization	✓✓✓	✓✓	✓
Less Communication Infrastructure	✓	✓✓	✓✓✓
Better Reliability	✓	✓✓	✓✓✓
Easy Scalability	✓	✓✓	✓✓✓
Less Computation Complexity	✓	✓✓	✓✓✓

The third level control is responsible for the coordination with other MGs or with the external grid. It is responsible for higher economic enhancements considering the external factors. It operates on system's level [28].

2.1.6 Micro-grid Challenges

Although there are many advantages of MG over the conventional power systems. However, there are also some challenges in its implementation. These challenges can be further classified into different categories i.e., technological, economic, and regulatory, etc. Figure 2.11 presents the challenges associated with the implementation of MG.

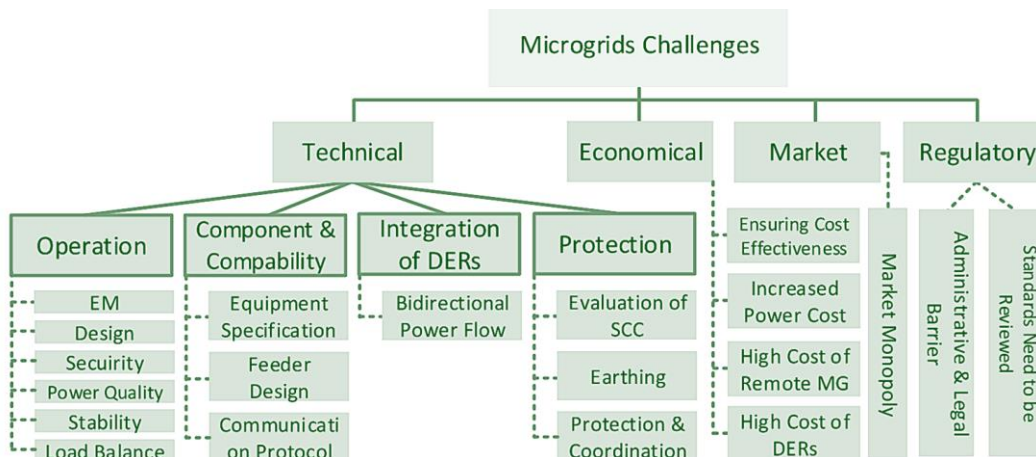


Figure 2.11: Challenges associated with MG, Ref. [18]

2.1.6.1 Technical Challenges

The power balance is an important operational challenge in the islanded MG as in this mode, the power balance needs to be achieved by the MG itself, so it needs to regulate the power of different sources and shedding some of the loads depending upon the actual conditions [18]. The operational challenges also include the start-up issues in islanded mode as the frequency in such scenarios may deviate drastically for few initial cycles and can cause the tripping of the power sources, thus some special controls are required in this period. Due to having intermittent power sources and energy storage elements, their ratio and location need to be carefully decided for efficient energy management. The stability of MG is another important technological challenge which will be discussed in detail in the next section.

Due to the integration of the distributed energy sources (DES), the radial power flow of the distribution system is no longer valid which can pose several issues in protection coordination, voltage control, and fault current calculation. Similarly, addressing some physical challenges related to the infrastructure are also important for the implementation of MG. Such challenges include the designing of feeders of MG and the required communication protocols and infrastructure [18].

Due to the high penetration of converter based intermittent power sources, it is difficult to calculate the short circuit power levels at any node in the MG which impacts the design of protection scheme for the MG [36]. In islanded operation of a MG, the conventional protection scheme may not work properly due to the low short circuit power (SCP). In [28], the adaptive protection scheme is discussed which can adjust the predefined relay settings based on the mode of operation. The earthing is also an important consideration while designing the protection for MG due to the huge diversity in the type of power generating sources [37].

2.1.6.2 Economic Challenges

Even though the costs for power converters were reduced in the past years due to the advancements in the field of semi-conductors but still there are economic challenges associated with the implementation of MG. The unit price of energy can be reduced by carefully regulating the power of each generator, which needs a complex controller to ensure the lower unit cost. Moreover, due to the infrastructure's upgradation, the fixed costs can also be increased specifically for the consumers who don't have net metering. The maintenance costs also need to be accounted for while calculating the economic performance of MG. Lastly, due to the higher initial costs associated with RES, it can be difficult to make huge investments. In such cases, the governments should subsidize the RES so that the NZE could be achieved by 2050 [18].

2.1.6.3 Market Challenges

The other key point is to establish an energy market for the MG energy trade. As the existing market loses control in the case of disconnection from the main grid. In such scenarios, who will decide the energy price for the consumers who are being supplied by the MG? To regulate the energy price in all possible scenarios, the energy market specific to MG should be established [18].

2.1.6.4 Regulatory Challenges

The standards, addressing the integration of RES, its protection and safety, should be revisited with the large penetration of such sources in the power system. The impact of large penetration of such sources in the power system is huge on the stability and protection of the system. There are some standards addressing the integration of MG with the existing distribution system i.e., EREC G59/3-3 and IEEE 1547 but they need to be reviewed with the recent developments in the control schemes of MG. Similarly, the regulations for the MG operation are also missing even though some countries are

encouraging MGs. Such legislations should be done in near future to expand the MGs in existing power system [18].

2.2 Stability of Micro-grid

The stability of a system is its ability to return to the steady state after experiencing a disturbance [38]. The stability of conventional power system can be classified into three categories i.e., voltage, frequency and rotor angle stability [39]. Voltage stability refers to the ability of the power system to achieve a stable voltage at each node after experiencing a disturbance. Similarly, frequency stability is the ability of the power system to achieve a relatively constant frequency after a fault or load change. It is associated with the balance of demand and supply of the real power. The rotor angle stability deals with the synchronization between different generators after experiencing a disturbance. Rotor angle stability can be confirmed if the generators achieve a constant rotor angle after a disturbance. It is an indication of the degree of balance between the electro-magnetic torque of the generator and the mechanical torque [3]. The stability of conventional power system is defined by the dynamic response of the synchronous generators. However, the stability of the modern power system is redefined due to the large penetration of the converter-interfaced generation (CIG). In [40], the authors introduced two new categories for the stability called the converter-driven stability and the resonance stability. The stability classification for the modern power systems is presented in Figure 2.12.

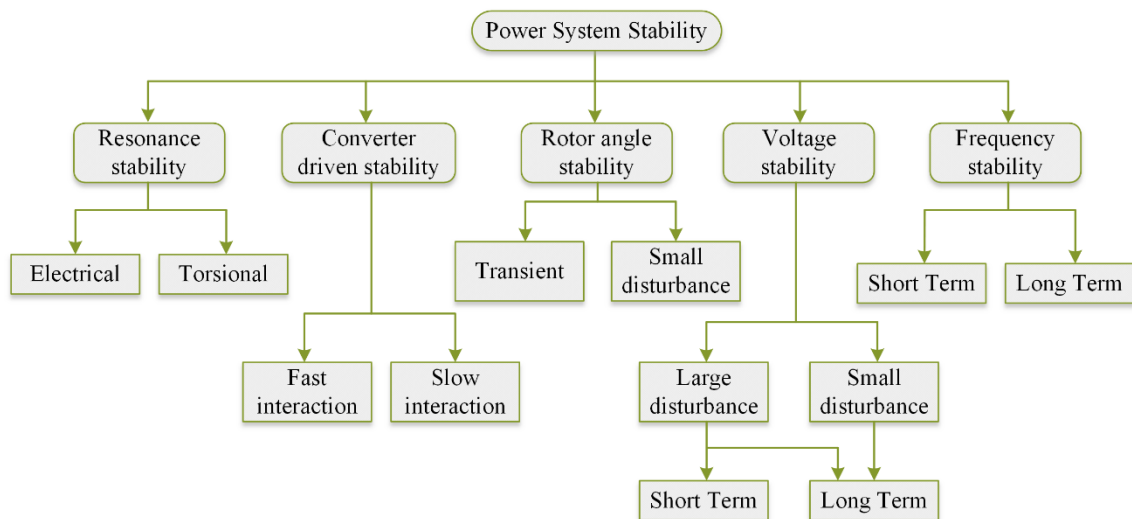


Figure 2.12: Classifications of stability for modern power systems, Ref. [40]

Due to the increased penetration of the series compensation devices in the transmission systems, resonance stability becomes important for the modern power systems. The resonance stability is associated to the sub-synchronous resonance (SSR). The sub-category ‘torsional’ deals with the resonance between the torsional frequencies of the turbine-generator shaft and the series compensation elements of the power network. The other sub-category deals with the resonance between the generator and the series compensation elements of the network. Moreover, due to the different response of the CIGs as compared to the conventional synchronous generators, the converter-driven stability is

introduced for the modern power systems. It deals with the interactions of the CIG control schemes with the electromechanical dynamics of the generators or the electromagnetic transients of the network. The subcategories correspond to the frequency of the oscillations due to such interactions. These interactions may result in the loss of synchronization of CIGs with the rest of the power system [41].

In conventional power system, the major focus of stability studies is on the transmission system whereas the MGs are operated at distribution levels which have higher R/X ratios than the transmission system. The higher R/X ratios result in strong coupling between active power and voltage which has a huge impact on the voltage stability. Moreover, due to the higher share of CIGs in MG, the stability of MG is predominantly decided by the dynamic response of the CIGs. Additionally, due to the low inertia, limited current handling capability, and fast control, the stability of MG is different than that of conventional power system. The stability of the MG is majorly affected by the control schemes of the converters and the type of CIGs. The CIGs can be classified into two major categories e.g., the controlled sources with energy storage elements and the intermittent sources. The intermittent sources (wind and PV) can only be controlled in unidirectional. The converter-based energy storage coupled sources responds quickly to the any variation in the operating conditions to achieve the power balance but the sources without storage are relatively slow unidirectional and depend on the response of their primary energy source. Both types of sources have different control schemes [3].

The converters' control schemes have a huge impact on the stability of the MG. The control schemes normally act very fast in response to a disturbance. The relative bandwidth of different key elements is given in Figure 2.13. The common types of control strategies for converter-based sources are PQ control, V/f control and droop control. The PQ control enables to inject the reference real and reactive power into the system irrespective of the operating conditions. It requires the real time measurement of the voltage's magnitude and its phase angle at POC and acts as a controlled current source. Normally such schemes are also referred to as grid following control schemes. To mimic the behavior of synchronous generator, the droop control schemes are used which regulate the active and reactive power based on the frequency and voltage at POC. They are also referred to as grid forming control schemes. Both schemes will be discussed in detail in the coming sections.

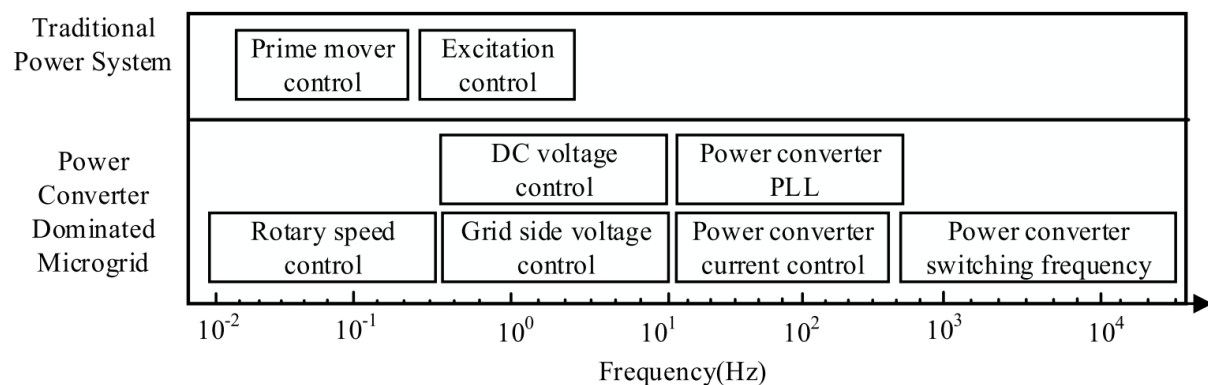


Figure 2.13: Comparison of bandwidth for different systems, Ref. [36]

2.2.1 Classification of Micro-grid Stability

The MG stability can be classified based on its operation mode, type of disturbance, and electrical balance. Based on the last two factors, the stability of the MG can be divided into small disturbance/signal and large disturbance/signal stability. Depending upon the size and characteristics of the RES connected in the MG, the MG stability can be short as well as long term stability [3].

The detailed classification of MG stability is given in Figure 2.14.

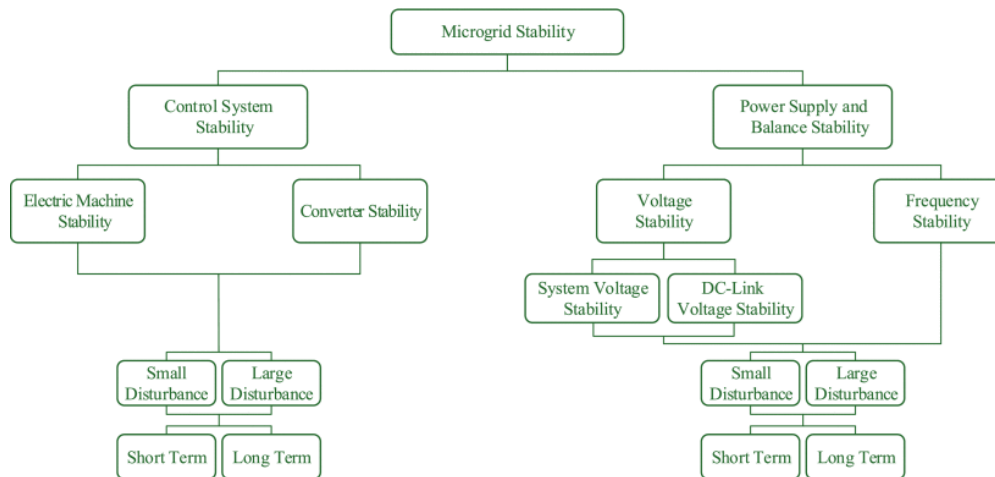


Figure 2.14: Classifications of micro-grid stability, Ref. [38]

In grid-connected mode, the external grid is mainly responsible for the voltage and frequency stability due to the limited power capacity of MG as compared to the main grid. In islanded mode, the MG needs to balance the power in every situation so both the voltage and frequency stabilities are important in this mode of operation.

The small signal stability (also referred as small disturbance stability) corresponds to any disturbance in which the system can be represented through linear set of equations i.e., small load variations with slow ramp or small change in reference values with slow ramp, etc. It can be short-term in grid-connected mode because the converter's response is expected in fraction of seconds subject to the small variations in operating conditions. The optimization of droop gains can enhance the small signal stability. The small signal stability is critical in islanded mode as the MG itself needs to ensure power balance. In such conditions, the small signal stability can vary from short-term to long-term depending upon the type of disturbance and converters' response [3, 38]. It can be investigated both in frequency and time domain. The methods for the analysis of small signal stability are discussed in [29] and presented in Figure 2.15.

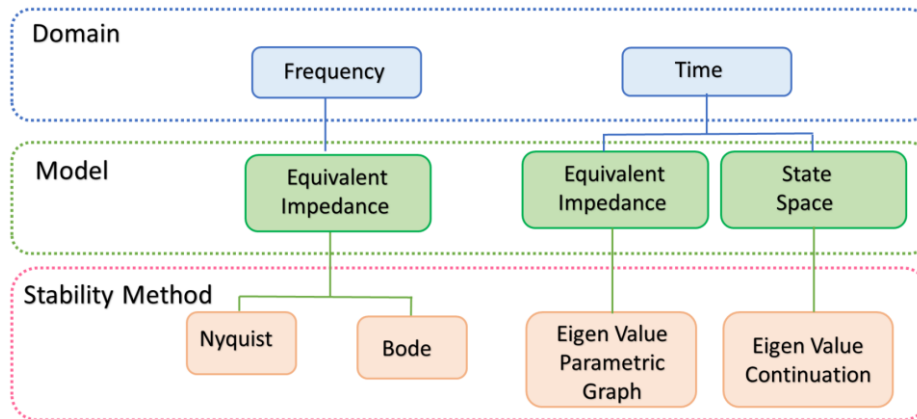


Figure 2.15: Methods for analysis of small signal stability, Ref. [29]

The large signal stability (also referred as large disturbance stability) corresponds to the events in which the system cannot be represented in linear set of equations without compromising its accuracy. Such events include the short circuit faults, component failures, and unplanned transition from grid connected to islanded mode, etc. The response of a DG in any fault scenario is majorly affected by the control scheme and the characteristics of that DG. In case of short circuit faults, the converters may need to respond very quickly to ensure their safety against overcurrent, hence, it is termed as ultra-short term [3]. In islanded operation, the transient stability can range from ultra-short to long term based on the control schemes and the type of primary energy sources [3]. Different analysis techniques for transient stability are discussed in [36] and a comparison is presented in Table 2.4.

Table 2.4: Comparison of transient stability methods, Ref. [36]

Method	Application	Comments
Time-domain simulation	Used in most of industrial methods, also used as standards for testing other methods	Trade-off between simulation time and accuracy, important to find instability criterion.
Lyapunov method	Helps in estimation of stability margin	System's based Lyapunov function, regions of attraction are estimated.
Hybrid method	Online stability analysis	Better performance in analysis of large power systems.
Inverse trajectory	Suitable for relatively small systems	Difficult to use for systems having more state variables.

The control system stability includes the stability issues due to the poor tuning of the control parameters and the undamped power oscillations between different CIGs. The electric machine stability is important for the MG having some SGs as it is associated to the poor tuning of the excitor and governor of the SG. The converter-driven stability is associated to the stable response of the converters in different operating conditions which can be unstable due to the poor tuning of the PLL, fast response of the inner current controllers or the limited maximum possible power transfer between the CIG and the network (based on the control type of the CIG).

2.2.2 Review of Stability Improvement Studies

To improve the stability of MG, several models have been suggested. In [42], a real-time simulation platform is built to study the impact of communication networks on the stability of the system. In [43], a hybrid droop scheme is introduced to enhance the stability of the MG in both grid-connected and islanded mode against the dynamic load variations. The scheme is capable of self-synchronization and the decentralized second level controller is discussed. However, it did not discuss the response in unbalanced conditions and the grid code requirements (GCR) in faulty conditions.

In [44], the authors investigated the response of the conventional frequency droop control for power sharing in islanded MG. The results confirm the better performance of angle droop control over the conventional frequency droop control. However, the problem with the angle droop control is that it can cause instability at MG level. To keep the MG stable, the authors proposed a supplementary control along with the angle droop control. In [45], the authors optimized the control parameters and used the impedance method and Lyapunov's direct method for the small signal stability in islanded mode. The optimization of the control parameters increased the sensitivity of the parameters.

In [46], Load Frequency Control (LFC) is used along with the droop control of the frequency which is modeled with a straight line. The frequency response is better with LFC, but careful correction needs to be done as overcorrection may cause instability. In [47], the authors proposed a new state-space model for the MG in order to study the stability of MG with eigenvalues. For the small signal stability improvement of an islanded MG, an arctan power-frequency droop control method is presented in [48]. In [49], the authors proposed a modified droop control scheme to address the stability under large frequency variations. However, the applicability of this scheme is limited to the GFMs.

Reactive power compensation is also used to enhance the stability. An extra power inverter is used to support the extra reactive power [50]. In [51], the authors introduced the fuzzy-based virtual synchronous generator (VSG) control and compared its performance with the cost function-based inertia and with damping coefficient optimization technique. The proposed scheme enhances the system's inertia in case of large disturbances by introducing a correction term to the reference active power. The summary of some of the papers is tabulated in Table 2.5.

Table 2.5: Summary of some papers

Topic	Study type	Comments	Potential Gaps
Frequency Controlled Inverter Chains [52]	String Stability	Mainly about frequency and power oscillations and to suppress these oscillations when number of inverters are increased.	<ul style="list-style-type: none"> Coupling between voltage and frequency can be considered for LV MG. Study for inductive and resistive lines.
Optimized design for grid forming and grid supporting inverter	Small Signal Stability	Optimized parameters offer better results.	<ul style="list-style-type: none"> Adaptive optimization and sensitivity analysis are missing.

controls (Use virtual Impedance) [45]			
Use of R-SFCL for the improvement of Micro-Grid's Transient Stability [53]	Transient Stability	The voltage across superconducting fault current limiter (SFCL) can be a triggering signal for the switching of the control of master DG.	<ul style="list-style-type: none"> • Can be used to enhance the fault ride through capability of DGs. • Other types of SFCL can also be investigated.
A Fuzzy Based Virtual Synchronous Generator Control [51]	Transient Stability	Fuzzy controller with virtual inertia is designed for stability improvement.	<ul style="list-style-type: none"> • The proposed scheme can be combined with damping coefficient optimization technique to mitigate the delayed response of the latter scheme.

2.3 Overview of Converter's Control Schemes

The response of the first level control of CIGs has a huge impact on the small and large signal stability of the MG. In this section, an overview of different control schemes is presented. The modeling of these control schemes will be discussed in the next chapter.

The converter's control schemes can be broadly divided into two main categories i.e.,

- i. Grid Following Control (GFL)
- ii. Grid Forming Control (GFM)

As the name suggests, the GFL converter follows the grid. It requires the measured frequency and voltage at POC and injects the reference real and reactive power to the system. It can be sub-divided into two categories i.e., grid feeding (GFeL) converter-which feeds constant real and reactive power irrespective of the grid conditions and the grid supporting (GSL) converter which delivers additional power based the actual grid conditions [54]. The GFL converter requires an active ac power source for its operation whereas the GFM mimics the synchronous machine i.e., it can work independently and provides real and reactive power according to the frequency and voltage droop controls. The GFL converter behaves as a controlled current source while the GFM converter behaves as a controlled voltage source. A comparison between GFL and GFM is discussed in [55] which shows that both schemes are duals of each other in many aspects. In [56], a comparison between the GFL and GFM schemes is presented which is given in Table 2.6.

Table 2.6: Comparison of GFL and GFM

GFL Control Scheme	GFM Control Scheme
Needs an active voltage source under normal conditions	Can form the grid itself and maintain the voltage and frequency
Vector control of injected current	Vector control of terminal voltage
Needs a dedicated synchronization unit	Does not need the dedicated synchronization unit
No black-start capability	Black-start capability
Instability threshold exists which means 100 % converter-based generation is not possible	Theoretically can operate stably in 100 % converter-based generation network

2.3.1 Review of Grid Following Converter

GFL requires an active voltage source to operate. It acts as a controlled current source. The control scheme calculates the reference injected current phasor. The inner current controller is designed to ensure the over current limit of the converter. The simplified electrical model of GFL based converter is given in Figure 2.16.

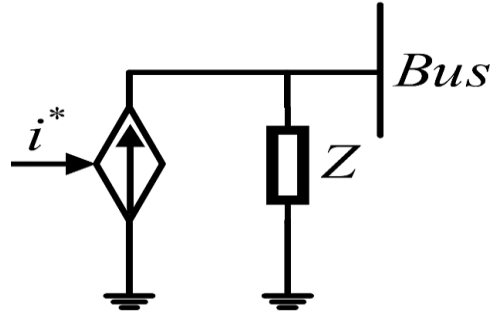


Figure 2.16: Electrical model of GFL based converter, Ref. [36]

In this thesis, the superscript '*' is used for the reference quantities. Furthermore, 'i' and 'Z' stand for current and impedance respectively. The calculation of reference current is dependent on the type of control scheme. In GFEL, the reference current is calculated based on the reference real and reactive power. The reference real power is further limited by the dc link voltage protection and the reference reactive power is limited by the current limit of the converter. In GSL scheme, additional real and reactive powers are injected based on the measured frequency and voltage at POC. Frequency support is possible if an energy storage element is available along with the primary energy source. The general layout for GSL is given in Figure 2.17.

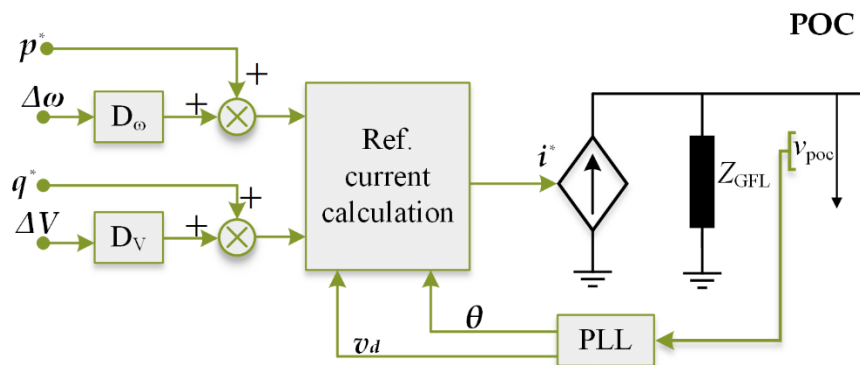


Figure 2.17: Simplified layout of GSL based converter

Where p^* , q^* , $\Delta\omega$, ΔV , i^* , D and Z_{GFL} denotes the reference active power, reference reactive power, difference between reference and measured angular frequency, difference between reference and measured voltage magnitude, reference current phasor, droop gain and line/shunt impedance respectively. 'POC' stands for point of connection and the PLL is the phase locked loop which helps in assessing the magnitude (v_d) and angle (θ) of the voltage phasor at POC. If the droop gains are set to zero, the same arrangement represents the GFEL. The control scheme can be designed in stationary

reference ($\alpha\beta$) frame, synchronously rotating reference (DQ) frame, or in per-phase (abc) frame [57]. The mostly used converter arrangement for the low power MG is the two-level, three-phase, three-leg converter which is unable to inject the zero-sequence component or the power in the three phases in abc -frame can't be controlled independently. Due to the simplicity, the $\alpha\beta$ and DQ frames are normally used for designing the converter's control schemes. DQ-frame requires frequency/phase angle measurement which is measured with the help of phase locked loop (PLL).

The $\alpha\beta$ -frame does not require the frequency information explicitly, so the converter's performance is enhanced due to the absence of PLL. Moreover, its performance in unbalanced conditions is improved as it can be designed without sequence extraction. However, the current calculation scheme is complex due to the coupling of the current components. The proportional resonant (PR) controller can be used as inner current controller instead of simple proportional-integral (PI) controller. Moreover, the current's amplitude limitation and priority current injections are also complex in $\alpha\beta$ -frame as compared to the DQ-frame. By using some filters, the harmonic injection can be controlled. The control scheme layout for GFeL in $\alpha\beta$ -frame is discussed in [58] and given in Figure 2.18.

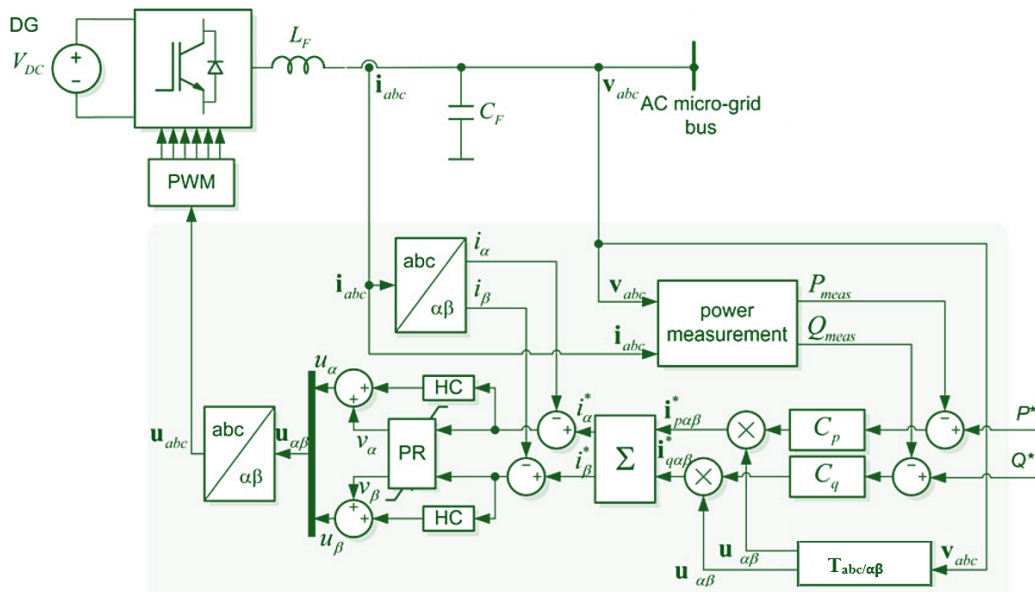


Figure 2.18: Control layout of GFeL in $\alpha\beta$ -frame, Ref. [58]

Where 'HC' stands for harmonic compensator and 'PR' is the proportional resonant controller. The DQ-frame results in simpler expressions for the reference active and reactive components of current. The decoupling of the active and reactive component of current is easy in DQ-frame. Moreover, a PI controller can be used as the inner current controller and the current limitation is comparatively easier in DQ-frame as compared to $\alpha\beta$ -frame. However, the speed and accuracy of PLL affect the overall performance of the control scheme particularly in case of contingencies. The stability criteria of the PLL is discussed in [59]. With the help of PLL, the harmonic injections can be minimized but the stability of PLL decides the stability of the control scheme which may get unstable during transients.

Moreover, its performance in unbalanced conditions is also poor. The comparison summary of DQ and $\alpha\beta$ -frame is presented in Table 2.7.

 Table 2.7: Performance comparison of DQ and $\alpha\beta$ frames

Factors	DQ-frame	$\alpha\beta$ -frame
Simpler expressions for reference current	✓	✗
Decoupled current components	✓	✗
Simplified inner current controller	✓	✗
Inherent active filtering feature	✓	✗
Easy implementation of current limitation	✓	✗
Performance limitations due to PLL	✗	✓
Requirement of sequence extraction in voltage unbalanced conditions	✗	✓
Robust from the perspective of varying grid conditions	✗	✓

The general layout of GFEL, in DQ-frame, is shown in Figure 2.19. The real power injection is decided based on the dc link voltage and the reference reactive power is constant. If there is an extra loop for the terminal voltage deciding the reference reactive current, then the same scheme can be for the GSL.

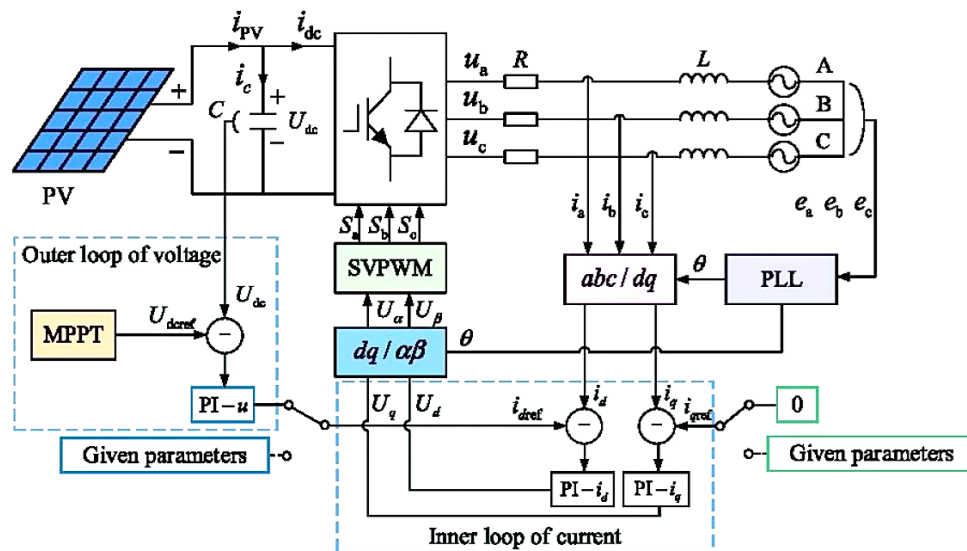


Figure 2.19: General layout of GFL converter, Ref. [60]

Where ‘MPPT’ stands for maximum power point tracking. The real power injection is dependent on the type of primary energy source while the reactive power injection can have various modes both in normal and faulty conditions. In normal operation, the reactive power injection can be based on the actual voltage at POC, reference reactive power in open/closed loop, or based on the desired power factor. Similarly, there can be different requirements for reactive current injection in the faulty conditions. Different reactive current control modes are discussed in IEC 61400-27-1 which are described in Table 2.8.

Table 2.8: Reactive current control modes for wind turbine type-4A, Ref. [61]

M_{qG}	Description	M_{qUVRT}	Description
0	Voltage control	0	Reactive current injection proportional to the voltage dip

1	Closed loop reactive power control	1	Reactive current proportional to the voltage dip plus pre-fault reactive current
2	Open loop reactive power control	2	Reactive current proportional to the voltage dip plus pre-fault reactive current plus some constant reactive current decided by the operator
3	Closed loop power factor control		
4	Open loop power factor control		

Where the M_{qG} represents the reactive power injection modes in normal conditions and the M_{qUVRT} represents the reactive current injection in faulty conditions.

2.3.1.1 Grid Code Requirements for GFL

The low voltage ride through (LVRT) requirement is discussed in [62] and is given in Figure 2.20.

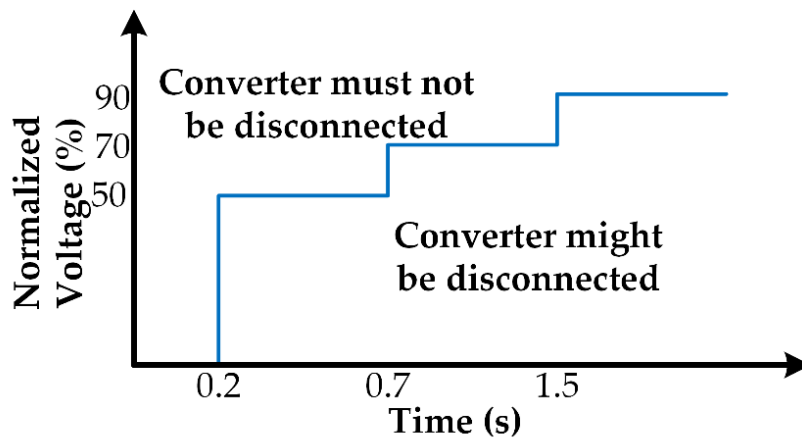


Figure 2.20: LVRT Requirements for converter's connection

The normalized voltage in the above figure is the ratio of minimum line-to-line root mean square (RMS) voltage to the rated line-to-line (L-L) RMS voltage. Initially, LVRT requirement was introduced to avoid the loss of power in case of voltage dips/sags [63]. Due to the ability of VSC to provide reactive power, voltage support is demanded in low voltage (LV) situations from the new generation converters, so the additional reactive current injection is the other requirement along with the minimum connection time. Grid codes are developed which define the required voltage support during such conditions. Such current injection not only helps in the restoration of the voltage, but it also helps in the fault detection. The symmetrical faults are easy to deal with as equal voltage support is required for all the phases, but the selective voltage support is demanded in case of asymmetrical faults which is complex and needs more attention as most of the faults are asymmetric in nature [64]. The reason for providing the selective voltage support is to restore the voltage balancing among different phases. It is possible with the help of negative sequence current injection which should be proportional to the actual negative sequence voltage at POC.

The sequence extraction in real time is a challenging task which increases the complexity and may cause some inaccuracy in the actual current injection. There are different techniques for sequence extraction

in real time having their own merits and demerits. Different algorithms for the real time extraction of the sequence components are discussed in [65-69]. In a three-phase, three-leg converter, zero-sequence injection is not possible, and it is also not demanded in most of the grid codes. Only the positive and negative sequence injections are mostly discussed. German grid codes (VDE-AR-N 4100 and VDE-AR-N 4110) define the range of the proportional constant for reactive current injection in the respective sequence [70] which is shown in Figure 2.21.

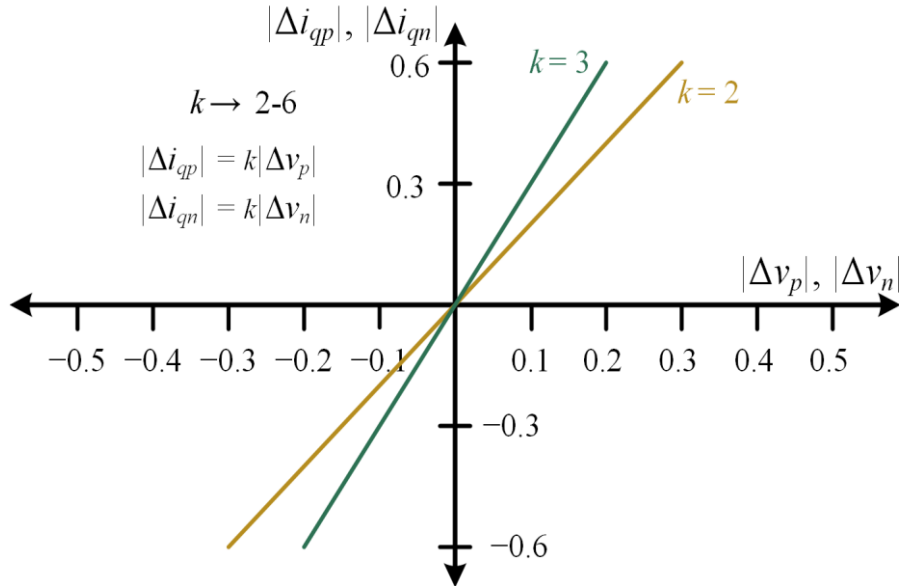


Figure 2.21: Positive and negative sequence reactive current requirements in LVRT conditions

The subscripts ‘ p ’ and ‘ n ’ stand for positive and negative sequence respectively. Moreover, ‘ i_q ’ represents the reactive current component and ‘ k ’ is the proportional gain constant. ‘ Δv ’ represents the voltage dip in the respective sequence and ‘ Δi ’ is the additional current injection in the respective sequence. From the above figure, it is clear that only the reactive current injection in both the sequences is demanded. The negative sequence current injection is also used to limit the real/reactive power oscillations and to mitigate the dc link voltage fluctuations [71]. However, the fulfillment of the current limit of the converter is a challenging task in such conditions. Moreover, due to the limited over-current capability of the converter, a priority injection scheme is also essential to ensure the required converter’s response.

2.3.1.2 Review of GFL Control Schemes

In [71], the authors proposed a reference current calculation scheme for the GFL in unbalanced conditions. The proposed scheme ensures the safe operation of the converter in such conditions, but it involves the angle between the positive and negative sequence voltage phasors which may cause inaccuracy due to the sequence extraction scheme. Moreover, it also uses a dedicated PLL for the negative sequence current injection. Another scheme for the enhancement of LVRT in unbalanced conditions is proposed in [72] but this scheme also involves the true angle between the positive and negative sequence voltage phasors. Most of the authors proposed the current limit schemes for the GFL

in case of unbalanced faults which involves the true angle between the positive and negative sequence voltage phasors which may cause inaccuracy [71-75]. In [76], the authors discussed a control scheme for the offshore wind power plants which injects the negative sequence current to maximize the stable real power injection.

In [77], the authors presented a simplified control scheme for the current limitation. It assumes the in-phase positive and negative sequence current phasors. However, it is unable to ensure the maximum utilization of the converter's current capacity in case of asymmetrical faults and it does not comply with the grid code requirements. In [78], the authors investigated the impact of negative sequence current injection on the voltage unbalance factor (VUF) which is the indication of the degree of uniformity and defined as the ratio of magnitude of negative sequence voltage phasor to the magnitude of the positive sequence voltage phasor ($|v_n|/|v_p|$). However, the current limitation scheme is not discussed. A comparison study is presented in [79] which compares the performance of the negative sequence current injection with different proportional gains.

Even though the grid codes demand the reactive current injection in the negative sequence, a comprehensive study is important to investigate the impact of different current distributions in the negative sequence over the VUF. This is important since the positive and negative sequence phasors rotate with the same frequency, but opposite in direction so the reactive current in the negative sequence may not result into minimum VUF. In [78], the authors presented the impact of non-zero active current injection in the negative sequence over the VUF. However, the magnitude of the negative current phasor is not limited according to the grid code recommendations. Moreover, it also requires the physical parameters of the grid to distribute the negative sequence current phasor into its components. The assessment of these physical parameters in real time is a challenging task. A comparative study between the response of a synchronous generator and a GFL based converter is presented in [80]. It investigates the different values of the proportional gain in the negative sequence. However, this study only involves the reactive current injection in the negative sequence.

In [81], the authors investigated the impact of active current injection in the negative sequence over the stability of PLL. However, it did not discuss the impact on the VUF. In [82], the performance of the GFL is investigated with the active current injection in the negative sequence. However, the impact on the VUF is not investigated and the negative sequence current phasor's magnitude is not calculated according to the GCR. Most of the studies, which involve the investigation of the impact of negative sequence current injection over the VUF, consider only the reactive current injection [71-73, 75, 79]. Moreover, in unbalanced conditions, the fluctuations in both the real and reactive power can't be eliminated simultaneously [83]. In some publications, the authors investigated the impact of negative sequence current injection on the fluctuations of the injected real/reactive power [82-85]. However, they did not investigate its simultaneous effect on the VUF.

2.3.1.3 Identified Research Gaps in GFL Scheme

The above given review identifies some of the research gaps in the GFL control which can enhance its response and make the control more flexible. The potential points are given below.

- Design of a robust sequence extraction scheme.
- Fault detection scheme in terms of sequence voltage phasors.
- Design a flexible control scheme without dedicated PLL for the negative sequence and enabling to easily limit the current amplitudes.
- Design of the priority current injection schemes to prioritize the individual active/reactive components in both the sequences.
- Design of a simpler reference current generation scheme to ensure the safe operation of the converter under unbalanced faults.
- Enhance the performance of the current limitation scheme by utilizing the maximum current capacity of the converter in case of unbalanced faults.
- Investigation of the optimal share of negative sequence current phasor into its components to achieve the minimum VUF.
- Design of a novel control scheme to achieve the minimum real power fluctuations along with the minimum VUF.

2.3.2 Review of Grid Forming Converter

In GFL, the interactions between the synchronization units can cause instability of the system, especially in weak grid conditions [86]. Moreover, the systems with high penetration of GFL can face the issues in the small signal stability [87, 88]. To address this problem, the grid forming control (GFM) schemes are introduced which normally have inherent synchronization unit in the form of power balance that is often termed as power synchronization. Unlike GFL, the GFM based converters can operate in islanded mode. There are several control schemes available for GFM. It acts like a controlled voltage source. The control scheme decides the reference frequency and voltage amplitude. The simplified electrical model of GFM based converter is shown in Figure 2.22.

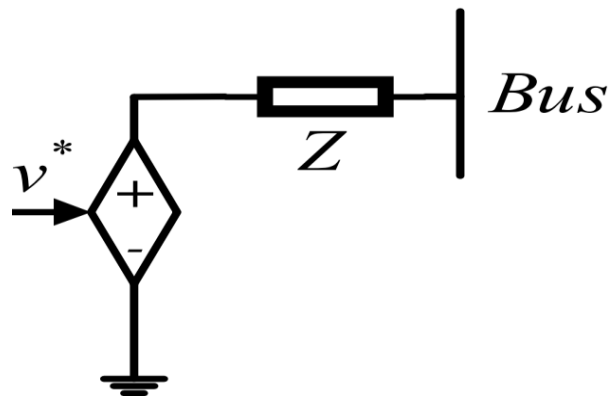


Figure 2.22: Electrical model of GFM based converter, Ref. [36]

It acts like a voltage source behind an impedance. There are different control schemes for the calculation of the reference voltage. The control schemes can be broadly divided into three main categories i.e., droop controls, synchronous machine-based control, and some other controls. These schemes are discussed in [54] and given in Figure 2.23.

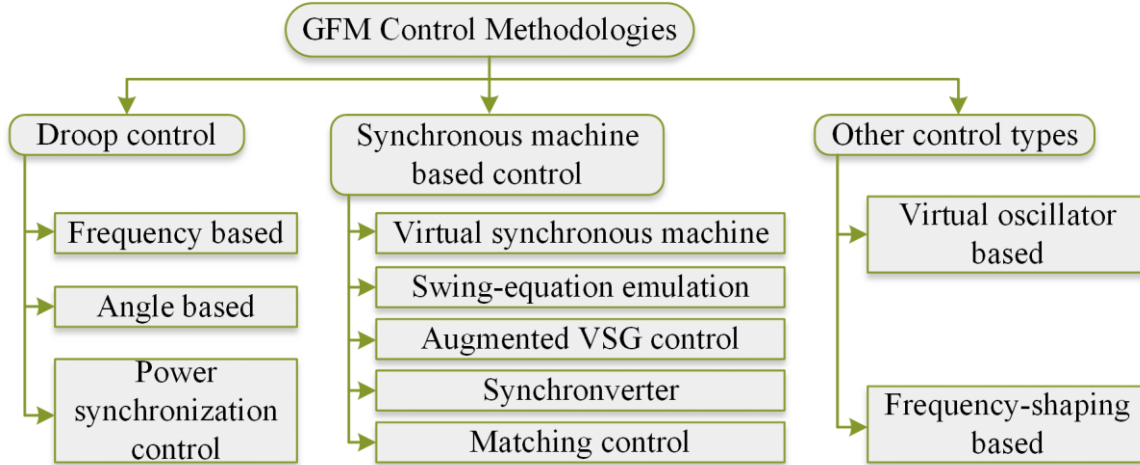


Figure 2.23: Classifications of GFM control schemes, Ref. [54]

The ‘VSG’ stands for virtual synchronous generator. The droop control offers an inverse relation between the real power injection and the reference frequency/angle. In frequency droop control, the frequency is inversely proportional to the real power mismatch. The proportional droop constant helps to change the reference real power linearly with the frequency mismatch between reference and measured frequencies. In angle-based droop control, the angle is directly calculated through real power mismatch [54].

The major drawback of the droop controls is the inertia less response. The controls based on the synchronous machine model offer virtual inertia. There are different techniques to emulate the response of the synchronous generator. Among them, the synchronverter is gaining more attention. There are also some other methods to control the GFM converter. Most of them are non-linear [54].

The general layout of the GFM scheme with the frequency and voltage droop is given in Figure 2.24.

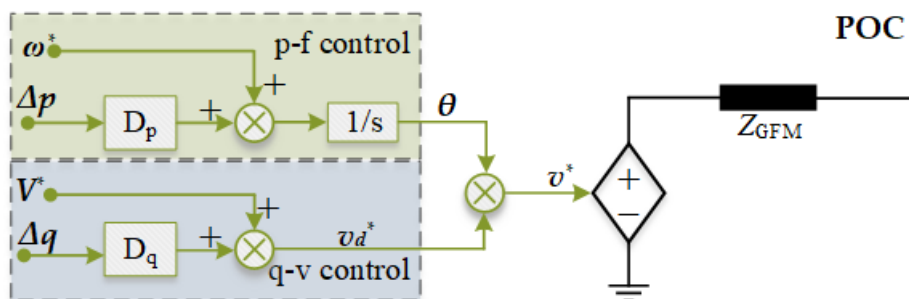


Figure 2.24: General layout of GFM based converter

Where ‘D’ is the droop constant, and the ‘ Δp ’ and ‘ Δq ’ stands for the difference between reference and measured active and reactive power respectively. The GFM scheme can also be designed in any

reference frame. It does not require a PLL as the reference angle is decided by the p-f loop. The amplitude of the reference voltage is decided by the q-v loop. It is robust and offers good performance in weak grids [89]. The droop controls have a strong effect on its stability. In faulty conditions, the slow response of droop controls enables the converter to behave like a conventional voltage source. However, due to the limited current handling capability, a fast response of the current limiting scheme is required when the converter's current limit is reached. Different current limitation schemes are proposed in the literature mainly involving virtual impedance/admittance, damping resistor and direct current limiting schemes, etc. Along with the current limit scheme, the other important challenge is to ensure the converter-driven stability, i.e., the synchronization of the converter particularly in fault and post fault scenarios. Normally, the synchronization can be ensured with the help of PLL or with power control. In GFM, the power control is preferred for the synchronization due to its slow dynamics [90].

In [91], the authors presented the idea of synchronverter which mimics the response of the conventional synchronous generator. It is easy to analyze the response of the synchronverter as the theory for SG is well established. The real and reactive power injections are adjusted with the help of frequency and voltage droop controls respectively. The basic layout of the control scheme for the synchronverter is discussed in [91]. The general control layout for the synchronverter is shown in Figure 2.25.

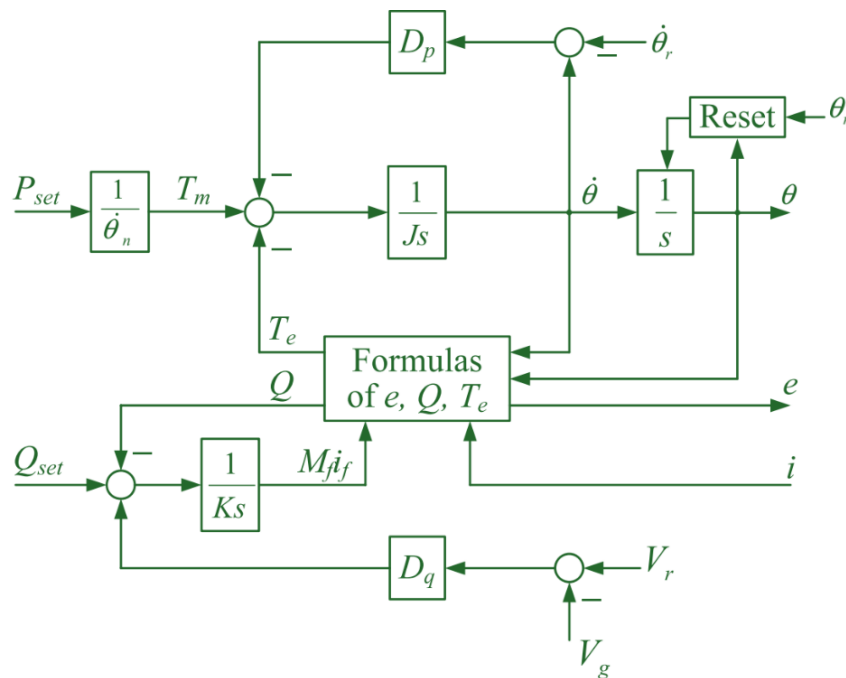


Figure 2.25: Control layout of Synchronverter, Ref. [91]

D_p and D_q are the droop constants for frequency and voltage respectively. Moreover, T_e , i , $\dot{\theta}$, e , Q , θ , J and K stand for electrical torque, three-phase line current, angular frequency, three-phase internal voltage, reactive power, voltage angle, emulated moment of inertia and virtual gain for reactive power control respectively. The ' $M_f i_f$ ' represents the emulated effect of field windings and field current in SG.

The real power loop decides the reference angle/frequency and the reference voltage amplitude is decided by the reactive power loop. The active power loop also combines the synchronous control inherently [90].

The synchronverter equations are discussed in [91] and given in equation (2.1).

$$\begin{aligned} T_e &= M_f i_f \langle i, \sin \theta \rangle \\ e &= \omega M_f i_f \sin \theta \\ Q &= -\omega M_f i_f \langle i, \cos \theta \rangle \end{aligned} \quad (2.1)$$

Where the operator $\langle \cdot, \cdot \rangle$ represents the conventional inner product in \mathfrak{R}^3 and ‘ ω ’ represents the angular frequency. The current limit scheme can be developed for ensuring the converter’s safety in faulty conditions. There are different current limitation schemes for the GFM which are discussed in [89]. A comparison of these schemes for the symmetrical faults is given in Table 2.9.

Table 2.9: Comparison of different current limiting schemes for GFM, Ref. [89]

Method	Current limitation performance	Fault current controllability	Fault recovery capability
Direct Current Limiter	Steady state response is good	Switch to PLL to decide the reference current	Q-V control windup may cause failure to recover
Virtual Impedance (VI)	Transient overcurrent	Depends on VI and grid’s strength	Better performance in post fault scenarios
Voltage Limiter	Steady state response is good	Depends on the voltage limiter and grid’s strength	Better performance in post fault scenarios

2.3.2.1 Review of GFM Control Schemes

In [90], the authors discussed the control of doubly fed induction generator (DFIG) based wind power plants. It discussed the physical limitations of the wind power plants against the synchronous control especially for the frequency support as it may be feasible at the expense of reduced service life of wind turbines or increased capital cost for the additional energy storage elements. They also discussed the physical phenomena for damping control and virtual inertia. However, the current limitation schemes and post fault behaviors are not discussed.

Different power control-based synchronization techniques are discussed in [86]. A comparison among different Q-V controls is also presented along with different schemes for inner current control. Some open problems are also identified e.g., synchronization stability under faulty conditions, smooth transition from grid connected to islanded mode and vice versa, and current limitation. However, the priority injection is not discussed. The response of the scheme under stiff grid connection is also not presented. In [92], the authors discussed the power sharing scheme for the PV based grid forming converter. The proportional resonant controller (PR) is used to achieve a stable output power in case of unbalanced conditions. However, they did not discuss its performance under different grid strengths.

Performance comparison of virtual impedance and direct current limiting scheme is presented in [93]. The authors also discussed the PR controller for inner current and outer voltage control loops. However, the smooth transition from one operation mode to the other is not discussed. The performance of the control scheme under varying grid strengths is also not presented.

In [94], the authors presented a consensus-based scheme for GFM converters. The proposed scheme helps to distribute the equal load change to each converter and enhances the stability. However, the authors did not discuss the current limiting strategy for GFM and its performance under different operating conditions. In [89], different current control schemes are presented for the GFM under symmetrical faults. The study confirms that the direct current limit scheme offers minimum over current transient, but the transient over-voltage may go up to 1.3 per-unit (p.u). The virtual impedance and voltage limiter schemes offer low transient over-voltage but the transient over current may reach up to 2 p.u. This study only considers the symmetrical faults. Instead of conventional p-f control, a cascaded angle, frequency, and power control is presented in [95]. It offers stable operation in many conditions. Moreover, a non-linear controller can enhance its large signal stability. However, the authors did not discuss the Q-V control and the synchronization scheme.

In [96], the authors discussed a circular current limiting scheme for the synchronverter in rotating reference frame. They also presented a filter compensation scheme under different modes of operation. However, the circular current limiting scheme is valid only for symmetrical faults and the asymmetrical fault behavior is not investigated. In [97], the authors proposed a self-synchronization scheme for the synchronverter which eliminates the PLL for synchronization. It ensures the smooth grid connection. However, the scope of the work did not include the other key factors e.g., current limitation, performance under asymmetrical faults, response in stiff grid connection, etc. In [98], the authors discussed the voltage support of the synchronverter under different operating conditions. However, they did not consider the asymmetrical faults and the limited current handling capability of the synchronverters.

A new synchronization scheme for the GFM is discussed in [99] which is based on the reactive power balance instead of active power. This scheme is useful for the integration of non-dispatchable DES. However, its performance under different faulty conditions needs to be evaluated. In [100], the authors discussed the requirements of British system operators (NGESO) for the GFM under symmetrical and asymmetrical faults. The p-f loop is frozen under faulty conditions. The voltage source behind the impedance nature of GFM enables it to support the voltage under such conditions. However, the authors did not investigate its performance under different modes of operation. Moreover, the performance of the above stated schemes is not investigated in case of dual faults (simultaneous frequency and voltage dips).

2.3.2.2 Identified Research Gaps in GFM Scheme

The above given review identifies some of the research gaps in the GFM control which can enhance its response and make the control more flexible. The potential points are given below.

- Ensure synchronization in different operating conditions including dual faults.
- Post fault recovery.
- Stable operation during normal and faulty conditions.
- Priority injections based flexible control.
- Smooth transition from grid-connected to islanded mode and vice versa.
- Current limitation schemes.
- Unified control for weak to stiff grid connections, and for standalone operations.

2.4 Potential Test Networks for Micro-grid

There are many benchmark networks available in literature which can be used as a test network for micro-grid studies. These networks cover high to low voltage systems with different topologies, generation structure and loads. In [101], the authors discussed different IEEE distribution test feeders. Some of the benchmark feeders involve the on-load tap changing transformers and some have the single-phase feeders. The total load and operating voltages are also different for each feeder. In [102], the European and north American benchmark networks are discussed. In [103], the authors presented different networks and discussed the application of these networks. From the MG's perspective, the total service area, total load, and the operating voltage are the key parameters to decide a network. Based on these limitations, the following benchmark networks are considered.

2.4.1 IEEE 34 Bus System

The IEEE 34 bus system contains unbalanced loads. It includes some single phase and two-phase laterals. Moreover, it also includes voltage regulators as the distributors are very long and lightly loaded. Most of the distributors operate at 24.9 kV, however, there is a short section of the feeder operating at 4.16 kV. Thus, a 24.9/4.16 kV transformer is also installed. The total load of this network is around 2 MVA [104]. As the name suggests, it has 34 nodes. The total effective length of this network is 92 km. This length is defined as the sum of the lengths of all the feeders. The common portion is considered only once in the calculation of the effective length. The layout of this network is discussed in [105] and presented in Figure 2.26. The possible locations for the connection of the three-phase DGs are nodes 832-890, 834-848 and 836-840 [105]. The below given layout is typical for North American LV systems.

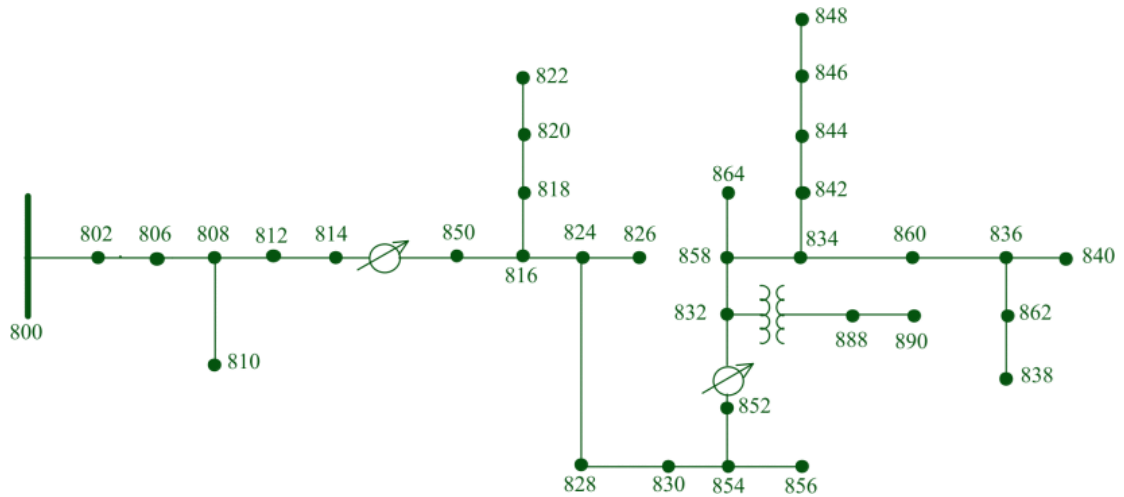


Figure 2.26: Layout of IEEE 34 bus system [105]

2.4.2 Generic European Network

A grid model, based on typical European distribution grid data is discussed in [103]. It has 92 nodes, and the effective length of the network is roughly 5.7 km. It has a total load of 0.5 MVA. The operation voltage for this network is 0.4 kV (line to line RMS). The load is not uniformly distributed. The layout of the generic European network is given below.

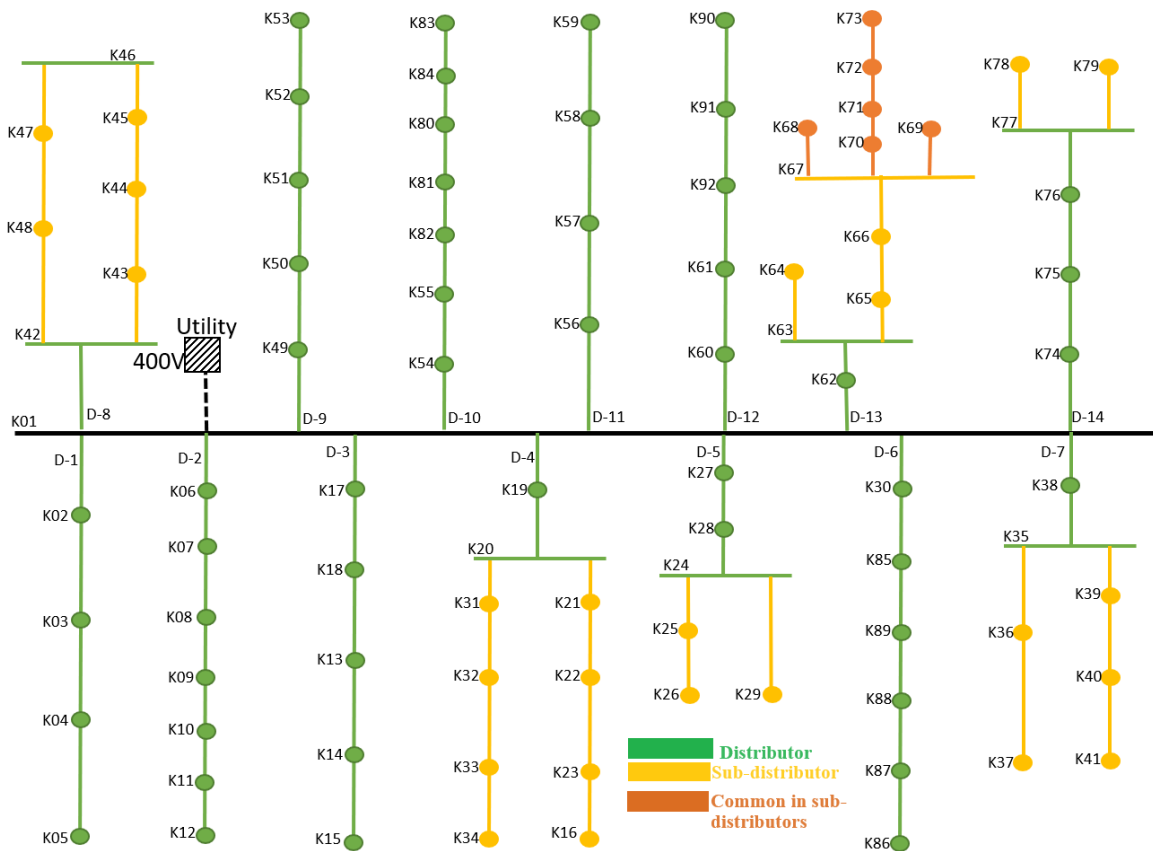


Figure 2.27: Layout of generic European network

The grid is connected at K01 node through a transformer having a power rating of 630 kVA. Each dot represents a node. However, large number of line impedances and loads slow down the simulation. The data of the generic European network is given in the appendix A.

2.4.3 European LV Distribution Network

In [102], the European LV distribution network is discussed which has 400 V L-L RMS voltage. It has three feeders i.e., residential, industrial, and commercial. Underground cables are used for the residential and industrial feeders whereas overhead lines are used for the commercial feeder. Combined load of three feeders is 746 kVA out of which the residential load is 404 kVA, industrial load is 100 kVA and commercial load is 242 kVA. The effective length of the network is roughly 1.34 km with 570 m each for residential and commercial feeders. The industrial feeder is 200 m long. The data of the European LV distribution network is given in appendix B. The layout of the European LV distribution network is given below.

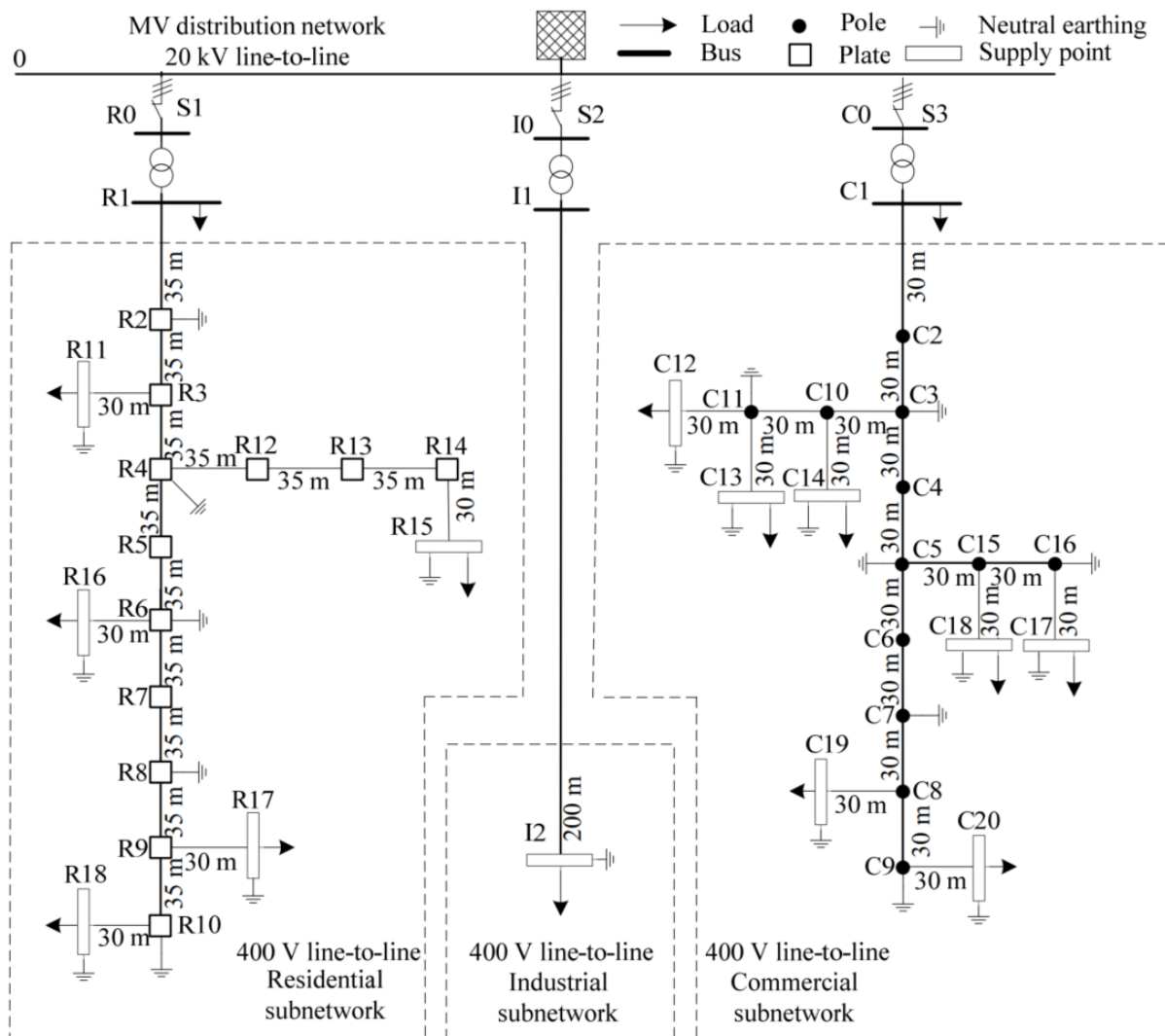


Figure 2.28: Layout of European LV distribution network, Ref. [102]

3. GRID FOLLOWING CONTROL SCHEME

The three-phase, three-leg converters are the most common type used for the integration of low power RES. The physical part contains the six semiconductor switches i.e., two switches per leg, filter, and breaker. In some cases, the coupling transformer (Tr) is also included. The six semiconductor switches are controlled with the help of pulses generated through pulse width modulation (PWM). The reference signal for the PWM is decided by the control scheme. The behavior of the converter-based generation is largely dependent on the control scheme. However, the physical arrangement can also have some impact on the converter's response i.e., the three-leg converter is unable to inject the zero-sequence current. Similarly, the type of semiconductor switches is also important to identify its reactive power control capability i.e., Insulated-gate bipolar transistor (IGBT) and gate turn-off (GTO) Thyristor have different characteristics. The simplified schematic diagram for the physical arrangement of the converter is given in Figure 3.1.

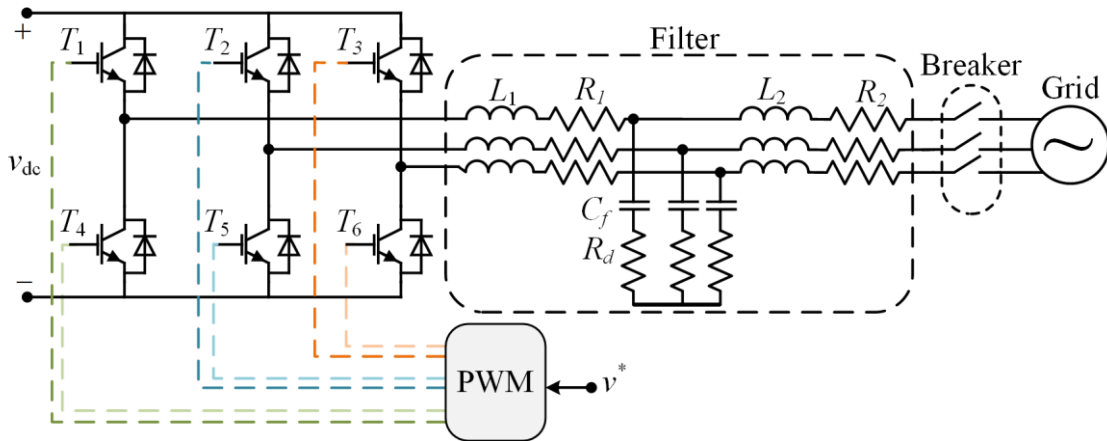


Figure 3.1: Schematic diagram of converter arrangement

Where the v_{dc} , L_1 , R_1 , C_f , R_d , L_2 , and R_2 represents dc side voltage, inductance of LCL filter on converter's side, resistance of LCL filter on converter's side, filter's capacitance, damping resistor, inductance of LCL filter on grid's side, and resistance of LCL filter on grid's side respectively. The control scheme requires the three-phase voltage and current measurements at POC. The simplified diagram for a converter-based generation is shown in Figure 3.2.

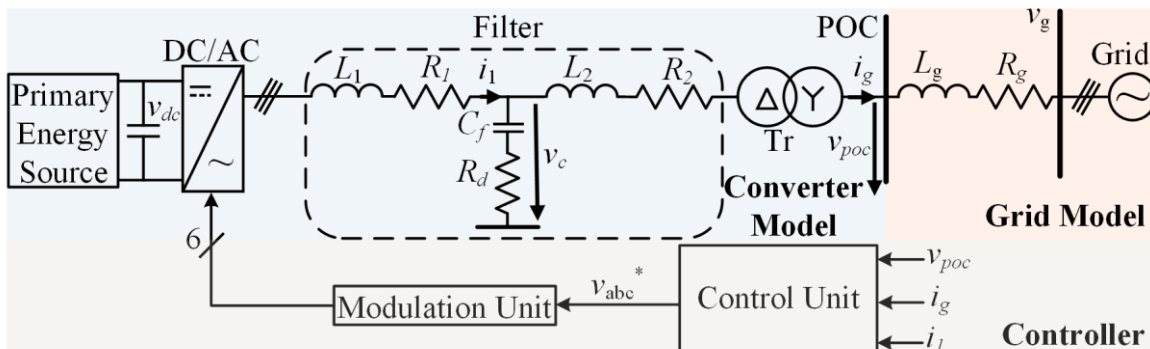


Figure 3.2: Layout of converter-based generation

Where the i_l , v_c , i_g , L_g , R_g and v_g represents converter's side current, voltage across shunt elements of LCL filter, measured current on converter's side of POC, grid's inductance, grid's resistance, and grid's voltage respectively. The subscript 'poc' stands for the measured parameters at POC. The grid impedance is inversely proportional to the grid's SCP at POC. The converter is a three-phase, three-leg converter. From the modeling perspective, the dc side is considered as a constant dc voltage source. The modeling of the filter needs to be done along with the modeling of the control schemes as it helps to improve the power quality by suppressing the harmonics. It also protects the loads from the transient over-voltages. Different arrangements for the filter are discussed in [106]. LCL filter design will be discussed here. Moreover, referring to above figure, even-though the converter is unable to inject the zero-sequence current due to its hardware limitations, but some ground faults on the Y-side of the coupling transformer are analyzed in this thesis. Therefore, the performance of the control schemes is also analyzed for the ground faults even-though the converter can't feed zero sequence. The faults are introduced at POC, measured positive and negative sequence voltage and current phasors are passed on to the control scheme.

3.1 LCL Filter Design

The design of LCL filter is discussed in [107]. The single line and block diagrams of the LCL are given in Figure 3.3.

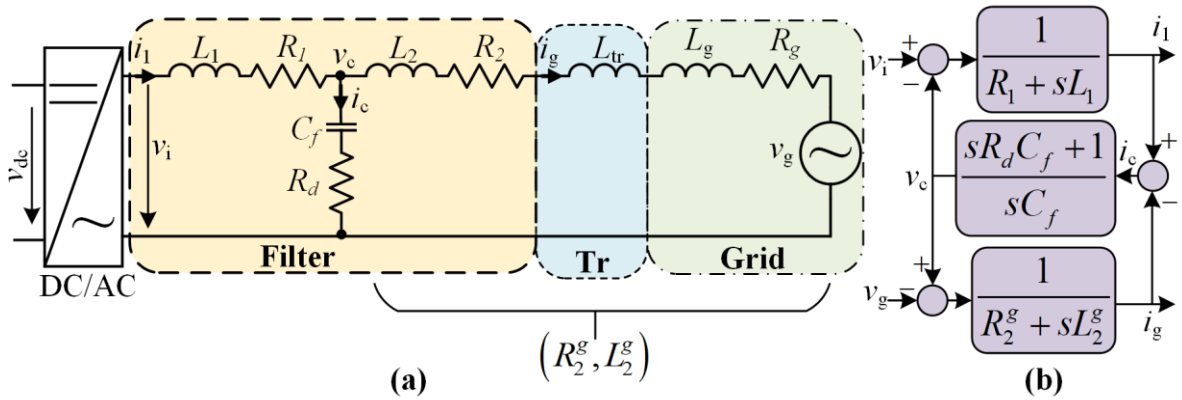


Figure 3.3: Diagrams for LCL filter; (a) single line diagram, (b) block diagram

Where the v_i , i_c , and L_{tr} represents converter's terminal voltage, current flowing through shunt elements of the filter, and inductance of coupling transformer respectively. Moreover, R_2^g and L_2^g represent the sum of grid's, transformer's, and filter's resistance and inductance on the grid side respectively. The related equations are given below.

$$Z_2^g = Z_2 + Z_{tr} + Z_g \rightarrow \begin{bmatrix} R_2^g \\ \omega L_2^g \end{bmatrix} = \begin{bmatrix} R_2 + R_g \\ \omega(L_2 + L_{tr} + L_g) \end{bmatrix} \quad (3.1)$$

$$i_1 = \frac{v_i - v_c}{R_1 + sL_1}; i_g = \frac{v_c - v_g}{R_2^g + sL_2^g}; v_c = \frac{sR_d C_f + 1}{sC_f} i_c \quad (3.2)$$

The transfer function of $i_g/v_i/v_{g=0}$ is given in equation (3.3). Its detailed derivation is discussed in appendix C.

$$H_{CL}(s) = \frac{i_g}{v_i} = \frac{sR_d C_f + 1}{y_1 s^3 + y_2 s^2 + y_1 s + y_4} \quad (3.3)$$

$$\begin{cases} y_1 = L_1 L_2^g C_f; y_2 = L_2^g C_f (R_1 + R_d) + L_1 C_f (R_2^g + R_d) \\ y_3 = R_d C_f (R_1 + R_2^g) + R_1 R_2^g C_f + L_1 + L_2^g; y_4 = R_1 + R_2^g \end{cases}$$

Where ‘H’ represents the transfer function and subscript ‘CL’ stands for closed loop. Considering the loss-less filter and grid, transfer function of $i_g/v_i/v_{g=0}$ is discussed in [107] and given in equation (3.4).

$$H_{CL}(s) = \frac{i_g}{v_i} = \frac{1}{C_f L_2^g L_1 s^3 + s(L_1 + L_2^g)} \quad (3.4)$$

The resonance frequency for the LCL filter can be derived from the above expression and is given in equation (3.5).

$$\omega_{res} = 2\pi f_{res} = \sqrt{\frac{L_2^g + L_1}{L_2^g L_1 C_f}} \xrightarrow{\because L_2^g = L_2 + L_{tr} + L_g} f_{res} = \frac{1}{2\pi} \sqrt{\frac{L_2 + L_{tr} + L_g + L_1}{(L_2 + L_{tr} + L_g) L_1 C_f}} \quad (3.5)$$

Where the subscript ‘res’ stands for resonance and ‘ ω ’ stands for angular frequency. Equation (3.5) calculates the impact of grid’s and coupling transformer’s inductance on the resonance frequency which have inverse effect on the resonance frequency. To avoid the resonance frequency in weak to strong grid connections, the resonance frequency should be at least 2 times smaller than the switching frequency and 10 times greater than the grid’s nominal frequency [107-109].

$$10f_g \leq f_{res} \leq \frac{f_{sw}}{2} \quad (3.6)$$

Where the ‘ f_g ’ and ‘ f_{sw} ’ stands for grid frequency and switching frequency respectively. In some publications [107, 108], the authors suggested that the total inductance of the filter should be equal to or lower than the 10 % of the base inductance. However, in this design, this limit is considered as 15 %. The expressions for the base impedance, base inductance, base capacitance and total filter’s inductance are given in equation (3.7).

$$Z_b = \frac{V_{L-L}^2}{S}; L_b = \frac{V_{L-L}^2}{2\pi f_g S}; C_b = \frac{S}{2\pi f_g V_{L-L}^2} \quad (3.7)$$

$$L_{f,tot} \leq 0.15 \frac{V_{L-L}^2}{2\pi f_g S}$$

Where the subscript ‘b’, ‘L-L’, and ‘f,tot’ stand for respective base parameter, respective line-to-line parameter, and respective filter parameter’s total value respectively. Moreover, ‘Z’, ‘V’, ‘S’, ‘C’, ‘L’, ‘f’ stands for impedance, voltage magnitude, apparent power, capacitance, inductance, and frequency respectively. The maximum ripple current is resulted on the converter side if the switching voltage varies from $-v_{dc}/3$ to $+v_{dc}/3$ [107]. Its expression is given in equation (3.8).

$$\Delta i_{\max} = \frac{v_{dc}}{6f_{sw}L_1} \quad (3.8)$$

Where the Δi_{\max} represents the maximum ripple current. The maximum ripple current on the converter side only depends on the switching frequency, dc link voltage and the inductance of the converter's side inductor of the LCL filter. Normally, the ripple in the converter's side current is limited to 10 % of the nominal current. The inductance of converter's side inductor can be computed with the help of the expressions given in equation (3.9).

$$L_1 = \frac{v_{dc}}{6f_{sw}\Delta i_{\max}} \quad \therefore \Delta i_{\max} = 0.1\sqrt{\frac{2}{3}} \frac{S}{V_{L-L}} \quad (3.9)$$

The grid side inductor is designed to limit the total harmonic distortion (THD) according to the standards i.e. IEEE 519-1992 [107]. The expression for grid side inductor is given in equation (3.10).

$$L_2 = aL_1 \quad \therefore 0 \leq a \leq \frac{L_{f,tot}}{L_1} - 1 \quad (3.10)$$

Most of the authors considered the factor 'a' ranges from 0.2-0.6 and the capacitance of the filter is generally selected as 5 % of the base capacitance [106-109].

$$C_f = 0.05 \frac{S}{2\pi f_g V_{L-L}^2} \quad (3.11)$$

Where the subscript 'f' stands for filter. Passive damping is suggested by some authors to avoid instability if some voltage/current harmonic component is near the resonance frequency [106, 109]. A series resistor with the C_f is introduced for passive damping. The expression for the series damping resistor is given in equation (3.12).

$$R_d = \frac{1}{3\omega_{res} C_f} \quad (3.12)$$

The design of the filter can be verified by validating the equation (3.6) with the calculated parameters. Moreover, the sum of converter's side and grid's side inductance of the LCL filter should be less than 15 % of the base inductance. The performance of the designed LCL filter is discussed in Appendix D.

3.2 Mathematical Expressions for Different Reference Frames

Before discussing the modeling of control schemes for GFL and GFM, the mathematical expressions for different reference frames are discussed as these will be extensively used in the modeling of control schemes. These reference frames are interchangeable. The phase voltage can be expressed mathematically in the form of sinusoidal waves with some amplitude. The general form is given in equation (3.13).

$$\begin{bmatrix} v_a(t) \\ v_b(t) \\ v_c(t) \end{bmatrix} = \begin{bmatrix} V_a \cos(\omega t + \theta_v) \\ V_b \cos(\omega t + \theta_v - \frac{2}{3}\pi) \\ V_c \cos(\omega t + \theta_v + \frac{2}{3}\pi) \end{bmatrix} \xrightarrow{\text{Balanced Conditions}} \begin{bmatrix} v_a(t) \\ v_b(t) \\ v_c(t) \end{bmatrix} = V \begin{bmatrix} \cos(\omega t + \theta_v) \\ \cos(\omega t + \theta_v - \frac{2}{3}\pi) \\ \cos(\omega t + \theta_v + \frac{2}{3}\pi) \end{bmatrix} \quad (3.13)$$

Where the small letter ‘v’ represents the instantaneous phase voltage, capital letter ‘V’ represents the amplitude of the phase voltage, and subscripts ‘a’, ‘b’, and ‘c’ represent the phase number. Moreover, ‘ ω ’ and ‘ θ_v ’ represent the angular frequency and initial voltage phasor angle respectively. The three-phase system can be fully defined with the help of its magnitude and frequency. It can be represented in a complex stationary reference frame system. The Clark transformation helps to convert ‘abc’ to ‘ $\alpha\beta 0$ ’ and vice versa. For symmetrical system, the representation of ‘abc’ and ‘ $\alpha\beta$ ’ is shown in Figure 3.4.

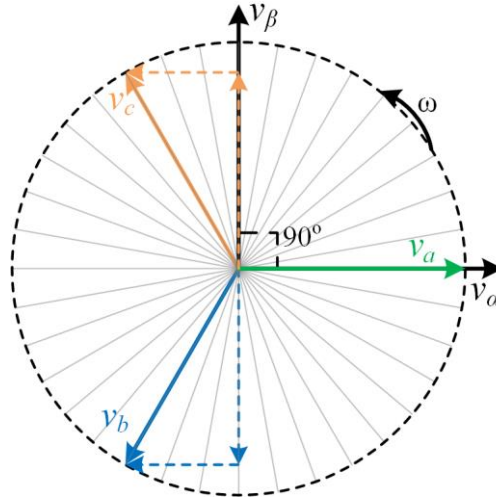


Figure 3.4: abc to $\alpha\beta$ representation

Where v_α , v_β represents the alpha-beta components of the voltage phasor respectively. In [110], the authors discussed the Clark transformation in detail. The expressions are given in equation (3.14) for the amplitude-invariant technique. For the rest of derivations, the amplitude-invariant technique will be used. This is discussed in detail in [110].

$$\begin{bmatrix} v_\alpha \\ v_\beta \\ v_0 \end{bmatrix} = \frac{1}{3} \underbrace{\begin{bmatrix} 2 & -1 & -1 \\ 0 & \sqrt{3} & -\sqrt{3} \\ 1 & 1 & 1 \end{bmatrix}}_{T_{abc/\alpha\beta 0}} \begin{bmatrix} v_a \\ v_b \\ v_c \end{bmatrix} \Rightarrow \begin{bmatrix} v_a \\ v_b \\ v_c \end{bmatrix} = \frac{1}{2} \underbrace{\begin{bmatrix} 2 & 0 & 2 \\ -1 & \sqrt{3} & 2 \\ -1 & -\sqrt{3} & 2 \end{bmatrix}}_{T_{\alpha\beta 0/abc}} \begin{bmatrix} v_\alpha \\ v_\beta \\ v_0 \end{bmatrix} \quad (3.14)$$

Thus, with the help of Clark transformation, the three-phase system can be fully represented with the help of stationary complex system. Assuming the zero sequence being zero, the expressions for the real and reactive power in the stationary reference frame are discussed in [111] and given in equation (3.15)

. It is equally applicable in case of unbalanced conditions. However, the coupling of current components is also proved from below given expressions.

$$\begin{bmatrix} p \\ q \end{bmatrix} = \frac{3}{2} \begin{bmatrix} v_\alpha & v_\beta \\ v_\beta & -v_\alpha \end{bmatrix} \begin{bmatrix} i_\alpha \\ i_\beta \end{bmatrix} \quad (3.15)$$

Where ‘ p ’ and ‘ q ’ stands for active and reactive power respectively.

In Park transformation, the reference frame rotates with the frequency of voltage phasor. With such arrangement, the resultant real and imaginary components are time invariant in case of balanced steady state conditions which helps to reduce the computation burden and to use a simple PI controller as inner current controller. The transformation from $\alpha\beta$ to dq frame is explained graphically in Figure 3.5.

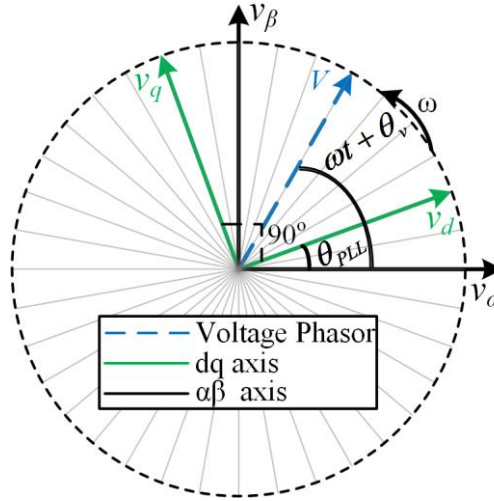


Figure 3.5: $\alpha\beta$ to dq representation

Where v_d, v_q represents the dq components of the voltage phasor respectively. Moreover, ‘ θ_{PLL} ’ is the angle assessed by the PLL and the ‘ V ’ is the voltage phasor. The mathematical expressions for the $\alpha\beta$ to dq transformation and vice versa are given in equation (3.16).

$$\begin{aligned} v_d + jv_q &= (v_\alpha + jv_\beta) e^{-j\theta_{PLL}} \\ \begin{bmatrix} v_d \\ v_q \end{bmatrix} &= \underbrace{\begin{bmatrix} \cos(\theta_{PLL}) & \sin(\theta_{PLL}) \\ -\sin(\theta_{PLL}) & \cos(\theta_{PLL}) \end{bmatrix}}_{T_{\alpha\beta/dq}} \begin{bmatrix} v_\alpha \\ v_\beta \end{bmatrix} \\ \Rightarrow & \\ \begin{bmatrix} v_\alpha \\ v_\beta \end{bmatrix} &= \underbrace{\begin{bmatrix} \cos(\theta_{PLL}) & -\sin(\theta_{PLL}) \\ \sin(\theta_{PLL}) & \cos(\theta_{PLL}) \end{bmatrix}}_{T_{dq/\alpha\beta}} \begin{bmatrix} v_d \\ v_q \end{bmatrix} \end{aligned} \quad (3.16)$$

The subscripts ‘ dq ’, and ‘ $\alpha\beta$ ’ represent the components in dq- and $\alpha\beta$ - frames respectively and ‘ j ’ represents the imaginary component. The zero-sequence component for both the reference frames is same. The expressions for the real and reactive power in the dq-frame are given in equation (3.17).

$$\begin{bmatrix} p \\ q \end{bmatrix} = \frac{3}{2} \begin{bmatrix} v_d & v_q \\ v_q & -v_d \end{bmatrix} \begin{bmatrix} i_d \\ i_q \end{bmatrix} \quad (3.17)$$

The direct expressions from abc to dq0 and vice versa can be derived with the help of expressions given in equations (3.14) and (3.16).

$$\begin{bmatrix} v_d \\ v_q \\ v_0 \end{bmatrix} = \frac{2}{3} \underbrace{\begin{bmatrix} \cos(\theta_{PLL}) & \cos\left(\theta_{PLL} - \frac{2}{3}\pi\right) & \cos\left(\theta_{PLL} + \frac{2}{3}\pi\right) \\ -\sin(\theta_{PLL}) & -\sin\left(\theta_{PLL} - \frac{2}{3}\pi\right) & -\sin\left(\theta_{PLL} + \frac{2}{3}\pi\right) \\ \frac{1}{2} & \frac{1}{2} & \frac{1}{2} \end{bmatrix}}_{T_{abc/dq0}} \begin{bmatrix} v_a \\ v_b \\ v_c \end{bmatrix} \quad (3.18)$$

$$\Rightarrow \begin{bmatrix} v_a \\ v_b \\ v_c \end{bmatrix} = \underbrace{\begin{bmatrix} \cos(\theta_{PLL}) & -\sin(\theta_{PLL}) & 1 \\ \cos\left(\theta_{PLL} - \frac{2}{3}\pi\right) & -\sin\left(\theta_{PLL} - \frac{2}{3}\pi\right) & 1 \\ \cos\left(\theta_{PLL} + \frac{2}{3}\pi\right) & -\sin\left(\theta_{PLL} + \frac{2}{3}\pi\right) & 1 \end{bmatrix}}_{T_{dq0/abc}} \begin{bmatrix} v_d \\ v_q \\ v_0 \end{bmatrix}$$

If the dq reference frame adjusts its speed to align measured voltage phasor with the d-axis, the imaginary axis component (v_q) can be eliminated, and the power expressions can be further simplified. The speed of the rotation of the dq-axis can be controlled with the help of PLL which tries to keep $v_q = 0$. Graphically, this condition is expressed in Figure 3.6.

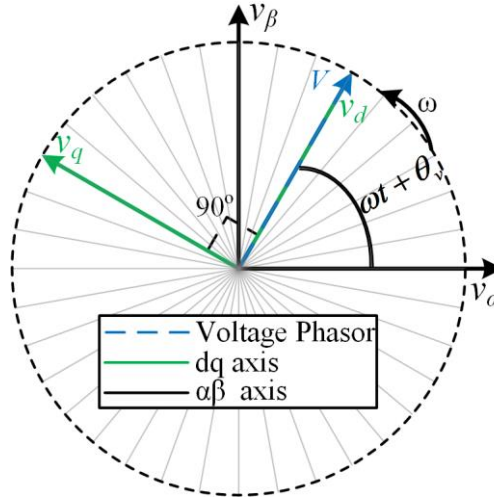


Figure 3.6: Graphical representation of automatically adjusted dq-frame

The expressions for the real and reactive power can be simplified with the above-mentioned alignment. The simplified expressions are given in equation (3.19).

$$\begin{bmatrix} p \\ q \end{bmatrix} = \frac{3}{2} v_d \begin{bmatrix} i_d \\ -i_q \end{bmatrix} \quad (3.19)$$

The equation (3.19) also confirms the decoupling of the current components in dq reference frame.

3.3 Modeling and Performance Analysis of Conventional GFL Scheme

The block diagram of a conventional GFL scheme is given in Figure 3.7. This scheme works fine for the normal operation and for symmetrical faults.

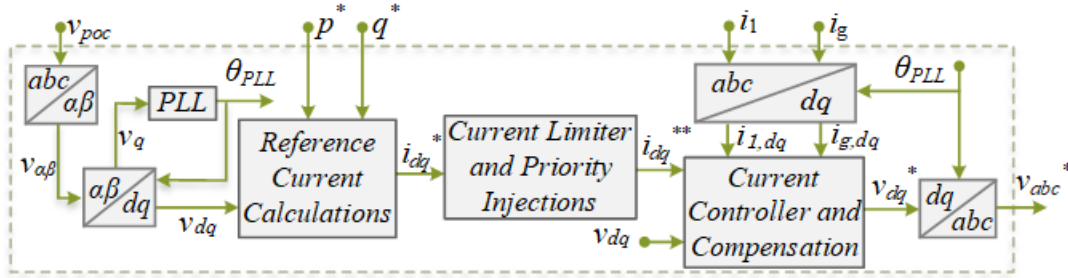


Figure 3.7: Conventional control scheme for GFL

The superscripts ‘*’ and ‘**’ represent the reference parameters and the parameters after applying its limits respectively. The key blocks of the above figure are explained explicitly here. The reference frame conversions are already explained in subsection 3.2.

3.3.1 Phase Locked Loop (PLL)

The synchronous reference frame phase locked loop (SRF-PLL) is commonly used for grid connected converters. The layout of the PLL is given in Figure 3.8.

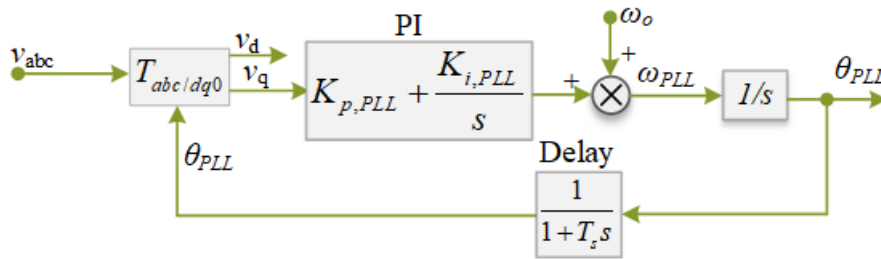


Figure 3.8: Block diagram of PLL

The K_p and K_i represent the proportional and integral gain respectively. The subscript ‘PLL’ and ‘o’ stands for the quantities related to PLL and initial value of the respective parameter respectively. ‘ T_s ’ stands for sampling time. The PLL estimates the actual frequency and initial phase angle with the help of a PI controller and a feedforward loop. It tracks the system’s frequency and adjusts its speed to keep the imaginary axis (v_q) of the measured voltage phasor to zero. The response time of the PLL has a huge impact on the stability of the system particularly in weak grid conditions. High gains for PI controller can be used in a strong grid and it helps to react quickly in case of faults, but it has negative impact on

the stability of the system in weak grid conditions. On the other hand, the slow PI controller ensures stable current injection under weak grid conditions, but it takes more time to achieve the desired power levels at POC. Mathematically, the PLL introduces a negative admittance in parallel to the network's admittance which has a negative impact on the converter-driven stability of the GFL in weak grid conditions [40]. To achieve a quick response under faulty conditions and to ensure the stability of PLL in weak grid connections, a compromise needs to be made. Normally, the time constant of PI controller is selected in accordance with the fundamental frequency of the grid.

For the balanced system, the expressions for the dq components are given in equation (3.20).

$$\begin{bmatrix} v_d \\ v_q \end{bmatrix} = V \begin{bmatrix} \cos(\theta_g - \theta_{PLL}) \\ \sin(\theta_g - \theta_{PLL}) \end{bmatrix} \quad \therefore V = \sqrt{v_d^2 + v_q^2}; \quad \theta_g = \omega t + \theta_v \quad (3.20)$$

From equation (3.20), it is clear that this is a non-linear system. However, in normal conditions, the angle difference between θ_g and θ_{PLL} is small. Thus, it can be linearized with the assumption of small angle difference.

$$\begin{bmatrix} \Delta v_d(s) \\ \Delta v_q(s) \end{bmatrix} = V \begin{bmatrix} 0 \\ \Delta \theta_g(s) - \Delta \theta_{PLL}(s) \end{bmatrix} \quad (3.21)$$

The above equation shows the change in dq-components whereas the actual v_d in such conditions is equal to the magnitude of the voltage phasor (V). The block diagram for the linearized PLL is given in Figure 3.9.

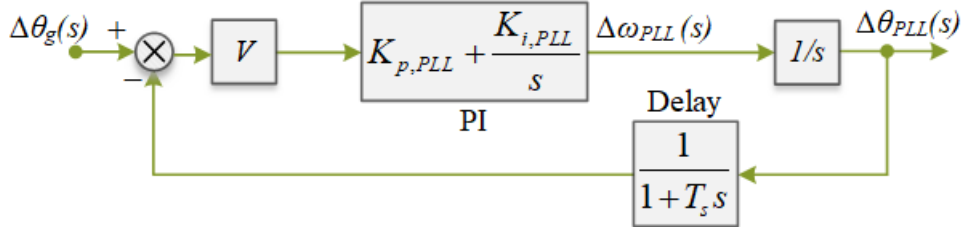


Figure 3.9: Linearized PLL

For the tuning of the PLL, linearized PLL is considered. The gains of the PI controller are tuned based on the open loop transfer function of the above system and comparing it with the general transfer function of type-II systems. The mathematical expressions for the linearized PLL are given in equation (3.22).

$$\begin{aligned} \Delta \theta_{PLL}(s) &= V \left(K_{p,PLL} \frac{1 + \tau_{PLL}s}{\tau_{PLL}s} \right) \frac{1}{s} \left(\frac{1}{1 + T_s s} \right) (\Delta \theta_g(s) - \Delta \theta_{PLL}(s)) \\ \therefore \begin{cases} \tau_{PLL} = \frac{K_{p,PLL}}{K_{i,PLL}}; K_{p,PLL} + \frac{K_{i,PLL}}{s} = K_{p,PLL} \frac{1 + \tau_{PLL}s}{\tau_{PLL}s} \end{cases} & \quad (3.22) \\ \Rightarrow H_{OL}(s) &= V \left(K_{p,PLL} \frac{1 + \tau_{PLL}s}{\tau_{PLL}s} \right) \frac{1}{s} \left(\frac{1}{1 + T_s s} \right) \end{aligned}$$

Where ‘ τ ’ represents the time constant for the PI controller and subscript ‘OL’ stands for open loop. The open loop transfer function (H_{OL}) of a typical type II system can be written as:

$$H_{OL}(s) = \frac{\omega_c^2 (as + \omega_c)}{s^2 (s + a\omega_c)} \quad (3.23)$$

Where the ω_c corresponds to the critical angular frequency. By comparing equation (3.22) and (3.23), mathematical expressions for the PLL control gains can be derived.

$$K_{p,PLL} = \frac{\omega_c}{V}; K_{i,PLL} = \frac{K_{p,PLL}}{\tau_{PLL}}; \tau_{PLL} = \frac{1}{T_s \omega_c^2} \quad (3.24)$$

This works fine in a balanced three-phase system. However, in case of unbalanced conditions, its performance degrades. Some authors suggested notch filter based PLL to improve its performance under unbalanced conditions [112].

For a typical 50 Hz power system, the settling time for PLL can be selected as the inverse of the grid’s frequency. The magnitude of the voltage phasor can be selected as ‘1’ in per-unit system. For a 10 kHz converter controller, the control gains of the PLL are given in Table 3.1.

Table 3.1: Parameters for PLL tuning

<i>Given Parameters</i>	$V_{L-L,RMS}$ (p.u)	f_c (Hz)	f_s (kHz)
	1	20	10
<i>Derived Parameters</i>	$K_{p,PLL}$	$K_{i,PLL}$	τ_{PLL} (s)
	125.66	198.44	0.633

3.3.2 Reference Current Calculations

The reference current calculations are performed both for the normal operation and for the LVRT conditions. According to the new grid codes, voltage support is demanded if the minimum of line-to-line RMS voltage drops below 90 % of its nominal value. In symmetrical faults, this condition can be detected with the help of magnitude of the voltage phasor as the voltage phasor has a circular trajectory in such cases. Equation (3.25) summarizes the condition for *fault_flag* activation which then forces to inject the currents accordingly.

$$fault_flag = \begin{cases} 1 & \text{if } \sqrt{v_d^2 + v_q^2} < 0.9 \\ 0 & \text{if } \sqrt{v_d^2 + v_q^2} \geq 0.9 \end{cases} \quad (3.25)$$

For the calculation of reference current, it can be generated through open loop or closed loop controls. The open loop control is simple and easy to implement but it may cause inaccuracy due to the control of converter’s side current (i_l) rather than grid’s side current (i_g) in the inner current controller. To confirm the desired power levels, the closed loop control can provide better results. It takes the difference between the reference and measured power and the error signal is then passed to a PI controller which decides the respective reference current components.

The current components can be decoupled if $v_q=0$. Thus, in normal conditions, the reference current in the d-axis (active current component) is proportional to the reference real power. The q-axis component of reference current (reactive current component) is proportional to the reference reactive power. In open loop control, the reference current calculations for the GFEL are given in equation (3.26).

$$i_d^* = \frac{2}{3} \frac{p^*}{v_d}; \quad i_q^* = \frac{-2}{3} \frac{q^*}{v_d} \quad (3.26)$$

For the GSL, the reference reactive current component is calculated based on the different modes of operation. Different modes of reactive power injection in GSL are explained in Table 2.8. In voltage control mode, the reference reactive power injection is dependent on the actual voltage at POC. The block diagram for the voltage control is given in Figure 3.10.

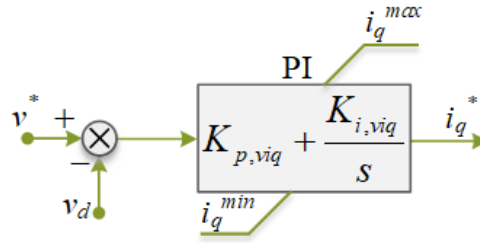


Figure 3.10: Voltage control of GSL

The superscripts ‘max’, and ‘min’ stand for the upper, and lower limit for the respective parameter respectively. The subscript ‘viq’ represents the gains for the controller that decides reactive current from voltage error. The gains of the voltage control PI controller also affect the closed loop control of the reactive power as it uses cascaded PI controllers to ensure voltage limits. The control diagram for the closed loop reactive power control is given in Figure 3.11.

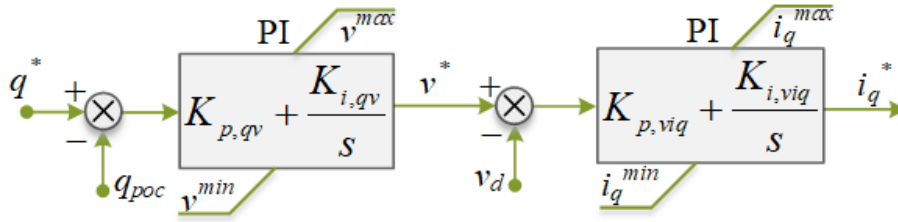


Figure 3.11: Closed loop reactive power control of GSL

The subscript ‘qv’ represents gains for the controller that decides reference voltage from reactive power error. The expression for the open loop reactive power control is given in equation (3.26). The control layout for the power factor control is same with the exception that the reference reactive power is calculated based on the desired power factor. However, in LVRT conditions, additional voltage support is demanded by the grid operators. The proportionality constant (k) for the additional demanded reactive current is discussed graphically in Figure 2.21. The expression for the active reference current component is the same as given in equation (3.26) but the reactive component, again, has three different

modes as discussed in Table 2.8. The mathematical expressions for the reactive reference current component are given in equation (3.27) for different injection modes.

$$i_q^* = \begin{cases} k\Delta v_d & \text{if } M_{qUVRT} = 0 \\ k\Delta v_d + i_{q,prefault}^* & \text{if } M_{qUVRT} = 1 \\ k\Delta v_d + i_{q,prefault}^* + i_{q,c} & \text{if } M_{qUVRT} = 2 \end{cases} \quad (3.27)$$

Where the $i_{q,prefault}^*$ and $i_{q,c}$ stand for the pre-fault reference reactive current and additional constant reactive current respectively. Moreover, Δv_d is the difference between the nominal and measured value of the voltage phasor's magnitude.

3.3.3 Current Limiter and Priority Current Injection

Due to the limited current handling capability of the converters, the current limit scheme is a vital part of the control scheme. It ensures the safety of the converter against over current in abnormal conditions. It also encompasses the priority scheme to prioritize the different current components in different conditions. As the active current component is proportional to the active power injection and in normal conditions, the prime target is to inject the active power, thus, this current component is prioritized in normal conditions. The remaining current capacity of the converter is used for the reactive power injection in normal conditions. Similarly, in faulty conditions, the prime target is to inject the reactive current component for the voltage support and the remaining current capacity is used for the real power injection. The expressions for the priority and current limitation in normal and abnormal condition are given in equation (3.28).

$$\begin{cases} i_d^{lim} = i_{max}; i_q^{lim} = \sqrt{(i_{max})^2 - (i_d^{**})^2} & \text{if } fault_flag = 0 \\ i_q^{lim} = i_{max}; i_d^{lim} = \sqrt{(i_{max})^2 - (i_q^{**})^2} & \text{if } fault_flag = 1 \end{cases} \quad (3.28)$$

Where the superscript '*lim*' stands for limit of the respective parameter and subscript '*max*' represents the maximum value of the respective parameter. The superscript '**' presents the reference parameters after applying their limits. The above expressions confirm that the magnitude of the reference current phasor never exceeds the current limit of the converter. Depending on the design, i_{max} in faulty and normal conditions can be different.

3.3.4 Current Controller and Compensation

The inner current controller confirms the current injection according to the reference current. However, due to the current and voltage coupling of different axes, the current controller's performance may degrade. These voltage and current coupling terms are introduced due to the filter. However, with proper compensation terms introduced in the input signal, the coupling between the d and q-axis controllers can be avoided which results in a simpler current controller.

In dq-frame, a PI controller is used as the inner current controller. The coupling terms, their respective compensations, and tuning of the controller are discussed in this section. For simplicity, the grid is assumed to be ideal, and the effect of R_d is also ignored. From Figure 3.3, the following set of equations can be written.

$$\begin{aligned}
 L_1 \frac{di_1(t)}{dt} + R_1 i_1(t) &= v_i(t) - v_c(t) \\
 C_f \frac{dv_c(t)}{dt} &= i_1(t) - i_g(t) \\
 L_2^g \frac{di_g(t)}{dt} + R_2^g i_g(t) &= v_c(t) - v_g(t) \xrightarrow[L_2^g = L_2 + L_{tr}]{R_2^g = R_2} (L_2 + L_{tr}) \frac{di_g(t)}{dt} + R_2 i_g(t) = v_c(t) - v_g(t)
 \end{aligned} \tag{3.29}$$

After linearization and Laplace transformation, the expressions for each component in dq-frame are given in equation (3.30). The details of linearization and Laplace transformation can be found in appendix E.

$$\begin{cases}
 \Delta i_{1d}(s) = \frac{1}{L_1 s + R_1} (L_1 \omega \Delta i_{1q}(s) + \Delta v_{id}(s) - \Delta v_{cd}(s)) \\
 \Delta i_{1q}(s) = \frac{1}{L_1 s + R_1} (-L_1 \omega \Delta i_{1d}(s) + \Delta v_{iq}(s) - \Delta v_{cq}(s)) \\
 \Delta v_{cd}(s) = \frac{1}{C_f s} (C_f \omega \Delta v_{cq}(s) + \Delta i_{1d}(s) - \Delta i_{gd}(s)) \\
 \Delta v_{cq}(s) = \frac{1}{C_f s} (-C_f \omega \Delta v_{cd}(s) + \Delta i_{1q}(s) - \Delta i_{gq}(s)) \\
 \Delta i_{gd}(s) = \frac{1}{L_2^g s + R_2} (L_2^g \omega \Delta i_{gq}(s) + \Delta v_{cd}(s) - \Delta v_{gd}(s)) \\
 \Delta i_{gq}(s) = \frac{1}{L_2^g s + R_2} (-L_2^g \omega \Delta i_{gd}(s) + \Delta v_{cq}(s) - \Delta v_{gq}(s))
 \end{cases} \tag{3.30}$$

The expressions for v_c can be derived in terms of i_g and v_g from the last set of equations in (3.30).

$$\begin{aligned}
 \Delta v_{cd}(s) &= \Delta v_{gd}(s) + (L_2^g s + R_2) \Delta i_{gd}(s) - L_2^g \omega \Delta i_{gq}(s) \\
 \Delta v_{cq}(s) &= \Delta v_{gq}(s) + (L_2^g s + R_2) \Delta i_{gq}(s) + L_2^g \omega \Delta i_{gd}(s)
 \end{aligned} \tag{3.31}$$

Putting the expressions given in (3.31) to the first set of equations in (3.30), the updated expressions for i_l are given in equation (3.32).

$$\begin{aligned}
 \Delta i_{1d}(s) &= \frac{1}{L_1 s + R_1} \left\{ \Delta v_{id}(s) - \Delta v_{gd}(s) + L_1 \omega \Delta i_{1q}(s) + L_2^g \omega \Delta i_{gq}(s) - (L_2^g s + R_2) \Delta i_{gd}(s) \right\} \\
 \Delta i_{1q}(s) &= \frac{1}{L_1 s + R_1} \left\{ \Delta v_{iq}(s) - \Delta v_{gq}(s) - L_1 \omega \Delta i_{1d}(s) - L_2^g \omega \Delta i_{gd}(s) - (L_2^g s + R_2) \Delta i_{gq}(s) \right\}
 \end{aligned} \tag{3.32}$$

The transfer function block diagram of the hardware part of converter's setup (Figure 3.2) is given in Figure 3.12.

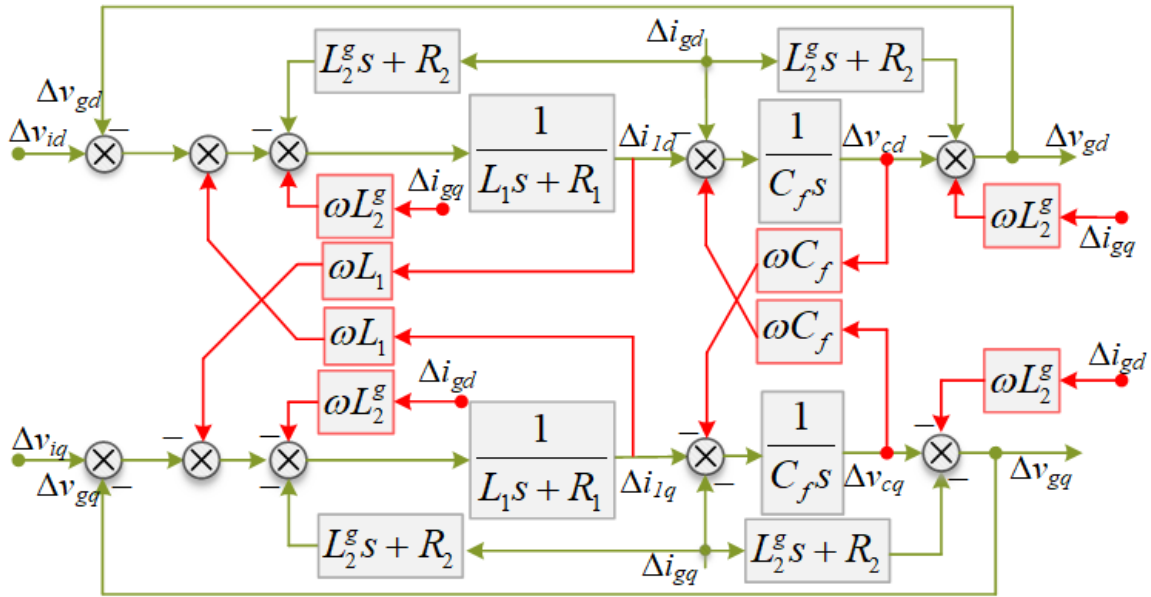


Figure 3.12: Transfer function diagram of the converter's setup

Where v_i is the voltage at the converter's terminal (before filter). The coupling of current component is evident from the above given figure. To decouple the current components, some compensation terms are introduced in the inner current controller. The block diagram of the control part is given in Figure 2.13.

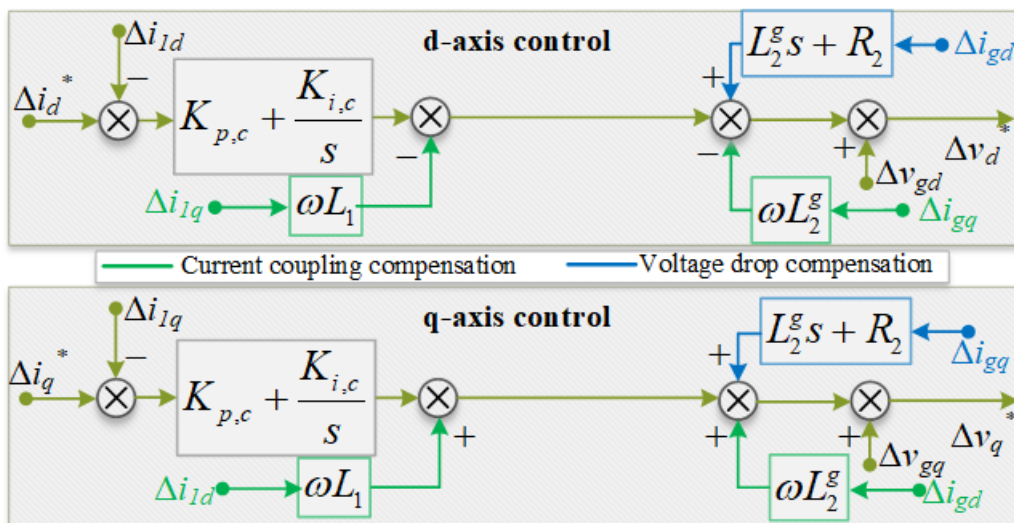


Figure 3.13: Block diagram of inner current controller

The subscript 'c' stands for current control. A delay term is introduced between the control and the hardware part of the converter. The complete diagram is shown in appendix P. With the help of compensation terms introduced in the control diagram, the current loops can be decoupled. The simplified diagram is shown in Figure 3.14.

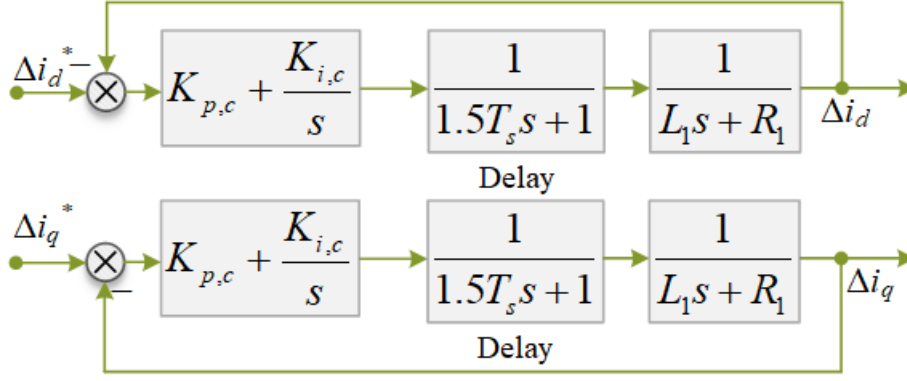


Figure 3.14: Current control diagram

Where the delay is approximated by the first order Padé approximation. Due to the PWM characteristics, the delay time is 1.5 times of the sampling time (T_s). The open loop transfer function of above control diagram can be written as:

$$H_{OL}(s) = \left(K_{p,c} + \frac{K_{i,c}}{s} \right) \left(\frac{1}{1.5T_s s + 1} \right) \left(\frac{1}{L_1 s + R_1} \right) \quad (3.33)$$

There are two methods for the parameter tuning of the PI controller. One is based on the cutoff frequency of the open loop transfer function and the other one is based on the natural oscillation frequency of the closed loop transfer function. Both the methods are briefly discussed below.

3.3.4.1 Cutoff Frequency Method

The amplitude of the open loop transfer function is unity if the frequency of the open loop transfer function matches its cutoff frequency. It is written mathematically in equation (3.34).

$$\left| H_{OL}(j\omega_{cut}) \right| = 1 \xrightarrow{\omega_{cut} = 2\pi f_{cut}} \left| H_{OL}(j2\pi f_{cut}) \right| = 1 \quad (3.34)$$

Where the ' ω_{cut} ' stands for cutoff angular frequency. To improve the performance of the system, the equation (3.33) can be re-arranged to cancel the pole and zero. The condition for the pole-zero cancellation is discussed in equation (3.35).

$$H_{OL}(s) = \frac{K_{p,c}}{s} \left(s + \frac{K_{i,c}}{K_{p,c}} \right) \left(\frac{1}{1.5T_s s + 1} \right) \frac{1}{L_1} \left(\frac{1}{s + R_1 / L_1} \right)$$

$$\text{if } \frac{K_{i,c}}{K_{p,c}} = \frac{R_1}{L_1}; \text{ pole and zero are cancelled} \quad (3.35)$$

$$H_{OL}(s) = \frac{K_{p,c}}{L_1 s} \left(\frac{1}{1.5T_s s + 1} \right)$$

Now introduce the condition given in equation (3.34) to the final expression of equation (3.35).

$$\begin{aligned}
 |H_{OL}(j2\pi f_{cut})| &= \left| \frac{K_{p,c}}{j2\pi f_{cut} L_1} \left(\frac{1}{j2\pi f_{cut} 1.5T_s + 1} \right) \right| = 1 \\
 K_{p,c} &= 2\pi f_{cut} L_1 \sqrt{1 + (3\pi f_{cut} T_s)^2} \\
 \therefore \frac{K_{i,c}}{K_{p,c}} &= \frac{R_1}{L_1} \\
 K_{i,c} &= 2\pi f_{cut} R_1 \sqrt{1 + (3\pi f_{cut} T_s)^2}
 \end{aligned} \tag{3.36}$$

To achieve the desired cutoff frequency, the PI parameter tuning can be done with the help of expressions given in equation (3.36). The settling time for the PI controller is defined as the ratio of proportional to integral gain.

$$\tau_c = \frac{K_{p,c}}{K_{i,c}} \tag{3.37}$$

Where ‘ τ_c ’ represents the time constant for the current controller.

3.3.4.2 Natural Oscillation Frequency

The expressions for the closed loop transfer function can be derived from the Figure 3.14. The final form is given in equation.

$$H_{CL}(s) = \frac{H_{OL}(s)}{H_{OL}(s) + 1} \xrightarrow{\frac{K_{i,c} = R_1}{K_{p,c} L_1}} \frac{\frac{K_{p,c}}{1.5T_s L_1}}{s^2 + \frac{1}{1.5T_s} s + \frac{K_{p,c}}{1.5T_s L_1}} \tag{3.38}$$

The closed loop transfer function of a second order system is given in equation (3.39).

$$H_{CL}(s) = \frac{\omega_n^2}{s^2 + 2\zeta\omega_n s + \omega_n^2} \tag{3.39}$$

Where the ω_n and ζ are the natural oscillation frequency and damping constant respectively.

By comparing the equation (3.38) and (3.39), the expressions for proportional and integral gain can be derived which are given in equation (3.40).

$$\begin{cases} K_{p,c} = 1.5\omega_n^2 L_1 T_s \\ K_{i,c} = 1.5\omega_n^2 R_1 T_s \end{cases} \tag{3.40}$$

As example, the tuned parameters for the PI controller, with the cutoff frequency method, are given in Table 3.2. The parameters refer to a converter with 100 kVA rating. For the tuning, the cutoff frequency is selected as 9 times of the grid frequency. The converter’s side inductance (L_1) is discussed in LCL filter, and the resistance is chosen as 5 % of the reactance on the converter’s side. The series resistance has no negative effect on the performance of the LCL filter.

Table 3.2: Parameter tuning for inner current controller

<i>Given Parameters</i>	$L_1(mH)$	$R_1(m\Omega)$	$f_g(Hz)$	$f_s(kHz)$
	0.226	3.55	50	10
<i>Derived Parameters</i>	$K_{p,c}$	$K_{i,c}$	$\tau_c(s)$	
	0.693	10.877	0.064	

f_s represents the sampling frequency. The performance of the designed PI controller for an RLC circuit is given below.

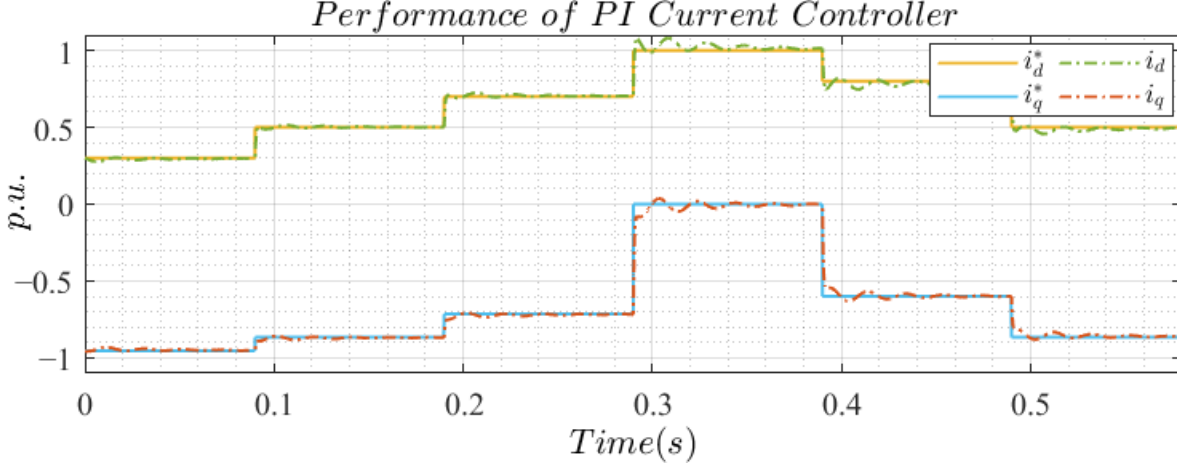


Figure 3.15: Performance of PI controller as inner current controller

The above figure shows that the designed PI controller results in acceptable performance with sudden reference current changes.

3.3.5 Exemplary Performance Analysis of Conventional GFL Scheme

The conventional GFL scheme is developed in Simulink and its response under different operating conditions is analyzed. The general layout of the setup is same as given in Figure 3.2. To avoid the sudden rise in power, the rate of change in reference active current component is limited to 1 p.u./sec. The key parameters for the setup are given in Table 3.3.

Table 3.3: Parameters for the test setup of conventional GFL converter

<i>Grid Parameters</i>					
<i>Voltage (L-L) (V)</i>	$f_g(Hz)$	<i>SCP (MVA)</i>		<i>X/R</i>	
400	50	5		5	
<i>Coupling Transformer</i>					
<i>Type</i>	<i>Voltage (V)</i>	<i>Rated Power (kVA)</i>	<i>Reactance (p.u.)</i>	<i>Resistance (p.u.)</i>	
Yd1	400/260	200	0.03	6×10^{-4}	
<i>LCL Filter</i>					
$L_1(mH)$	$R_1(m\Omega)$	$L_2(mH)$	$R_2(m\Omega)$	$C_f(mF)$	$R_d(m\Omega)$
0.225	3.54	0.0451	0	0.236	133.17
<i>Converter's Parameters</i>					
V_{dc}	<i>Rated Power</i>	$[p^*, q^*]$	i_{max}	K_{qv}	K_{qiv}
425	100 kVA	[0.95, 0.2] p.u.	1.2 (p.u)	[0.5, 5]	[3, 50]
k	K_c	$f_s(kHz)$	K_{PLL}		
2	[0.693, 10.877]	10	[62.84, 24.8]		

3.3.5.1 Performance in Normal Conditions

Different schemes for the reactive current injection are tested on the above setup. Open loop control is used for the real power injection. i_l is used as the measured current for the inner current controller. The load convention is used for the signs of real and reactive power. The reference voltage for the voltage control is set to 1.02 p.u. The steady state results are presented in Table 3.4.

Table 3.4: Performance of conventional GFL in normal conditions

M_{qG}	p_{poc} (p.u.)	q_{poc} (p.u.)	V_{poc} (p.u.)
0	1.19	0.22	1.01
1	1.18	0.20	1.01
2	0.92	-0.26	1.00
3	1.19	0.22	1.01
4	0.98	-0.15	1.00

The above table confirms the better performance of the closed loop systems as compared to the open loop for the reactive power injection. The reason for so much variation in the reactive power (in open loop system) is the angle difference between the i_g and i_l . The real power injection is also different than its reference due to the open loop control and the angular difference between the i_g and i_l . The reference currents are calculated for the desired powers at POC but the measured current in the inner current controller is the converter side current which has angular difference than the grid side current. A true current injection with such an arrangement is hard to achieve. The reason for using the converter's side current in inner current control is the limited current handling capability of the IGBTs which needs to be ensured in all conditions. Hence for such an arrangement, the closed loop control's performance is better than the open loop control. Thus, the point of improvement in the normal operation is to compensate the angular difference between converter's side current and grid's side current.

3.3.5.2 Performance in LVRT/ Faulty Conditions

For the low voltage response, a three phase to ground fault is introduced at POC. Different modes of reactive current injection (M_{qUVRT}) are tested against both the active current priority (p-priority) and reactive current priority (q-priority) injections. For the pre-fault reactive current, the voltage control scheme ($M_{qG} = 0$) is used. Table 3.5 summarizes the fault response of the conventional control scheme.

Table 3.5: Performance of conventional GFL in faulty conditions

Priority	M_{qUVRT}	p_{poc} (p.u.)	q_{poc} (p.u.)	V_{poc} (p.u.)	Voltage Improvement (%)	$I_{l,max}$
	0					
p-priority	1	0.82	-0.41	0.77	0.91	1.2
	2					
q-priority	0	0.93	-0.12	0.78	1.68	
	1	0.47	0.85	0.79		1.2
	2	0.47	0.85	0.79	2.78	

The above table shows that there is not much difference between the different modes of reactive current injection in faulty situations if the p-priority is selected. The reason is the limited current capacity available for the reactive current injection due to prioritizing the active current component and all the

modes of M_{qUVRT} result in higher reference reactive current than its limit. However, in q-priority injection the response is different based on the M_{qUVRT} mode. The maximum voltage improvement results in the case of maximum reactive current injection which verifies the dependence of voltage magnitude on the reactive power support. The voltage improvement is quite evident in weaker grids. Moreover, the current limitation scheme works well for both the schemes.

The stability of the conventional GFL is highly dependent on the grid's strength at POC. This is because the PLL introduces a negative admittance in parallel to the network's admittance which has a negative effect on the converter-driven stability of the GFL. A slow PLL and inner current control may help to improve the converter-driven stability (which is related to the stability of the PLL) of the GFL in weaker grids, but slower PLL and inner current controller cause the delayed response in the faulty conditions. The severity of fault also affects the response of the PLL and can cause instability particularly in post-fault scenarios.

The impact of priority injection on the post fault stability is discussed in Figure 3.16. The same conditions are simulated for 'p' and 'q' priority and it is clear that for the low impedance faults, the 'p' priority may cause the post-fault instability. For the following figure, the cutoff frequency for the PLL is 20 Hz, $M_{qUVRT} = 0$ and fault is balanced three-phase to ground. The fault is introduced at 0.2 seconds and its duration is 0.3 seconds.

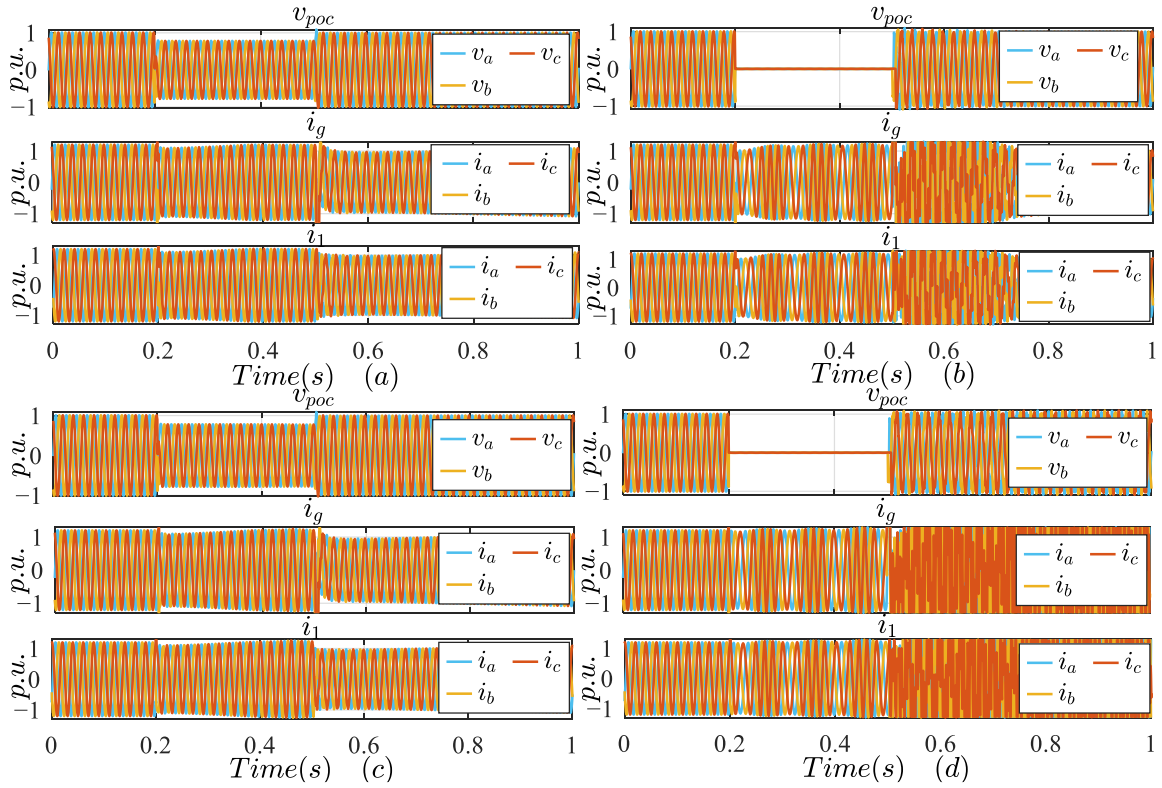


Figure 3.16: Impact of priority injection on post fault stability of GFL; (a) Q-priority in high impedance fault, (b) Q-priority in low impedance fault, (c) P-priority in high impedance fault, (d) P-priority in low impedance fault

Where i_g is the measured current on converter’s side of POC. By comparing subplots (a) with (b) and (c) with (d), it is clear that the low impedance faults have a negative impact on the post fault stability of the GFL. Similarly, by comparing subplot (b) and (d), it is clear that the p-priority injection has low post-fault stability and it is more evident in low impedance faults. One of the reasons is the $\Delta Q-\theta$ relation due to the PLL which shows the higher dependency of the reference angle on the reactive power. Similarly, by comparing the i_l and i_g for these tests, it is clear that both are in close agreement with each other as far as peak phase currents are concerned.

The other important factor is the speed of the PLL which has a huge impact on the stability of GFL. For the Q-priority injection, the cutoff frequency of the PLL varies from 10 to 20 Hz. All the other conditions are same as for Figure 3.16 (b). The response is plotted in Figure 3.17.

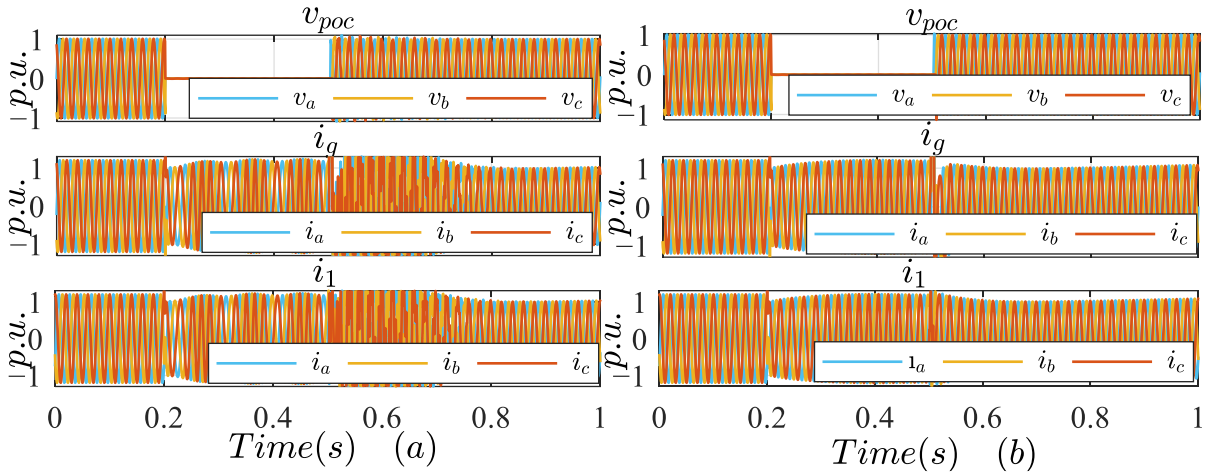


Figure 3.17: Impact of speed of PLL on post fault stability of GFL; (a) cutoff frequency for PLL is 20 Hz, (b) cutoff frequency for PLL is 10 Hz

The subplot (a) of the above figure corresponds to a relatively faster PLL which shows that the post fault stability is not good for the initial fraction of seconds. Its frequency response during fault is also not stable but it offers relatively fast response to the fault. On the other hand, subplot (b) corresponds to a relatively slower PLL which offers stable response in the post fault scenario and its frequency variations during fault are also not abrupt. However, it is relatively slower in response to a fault.

The stability of PLL is also largely affected by the short circuit power of the grid at POC. For relatively stronger grids, the conventional control scheme offers stable response even with relatively faster PLL but in case of weaker grids, the stability can’t be ensured for the same PLL. The SCP of the grid at POC is changed from 5 MVA to 1 MVA keeping all the other parameters same. The response of conventional GFL scheme is plotted in Figure 3.18.

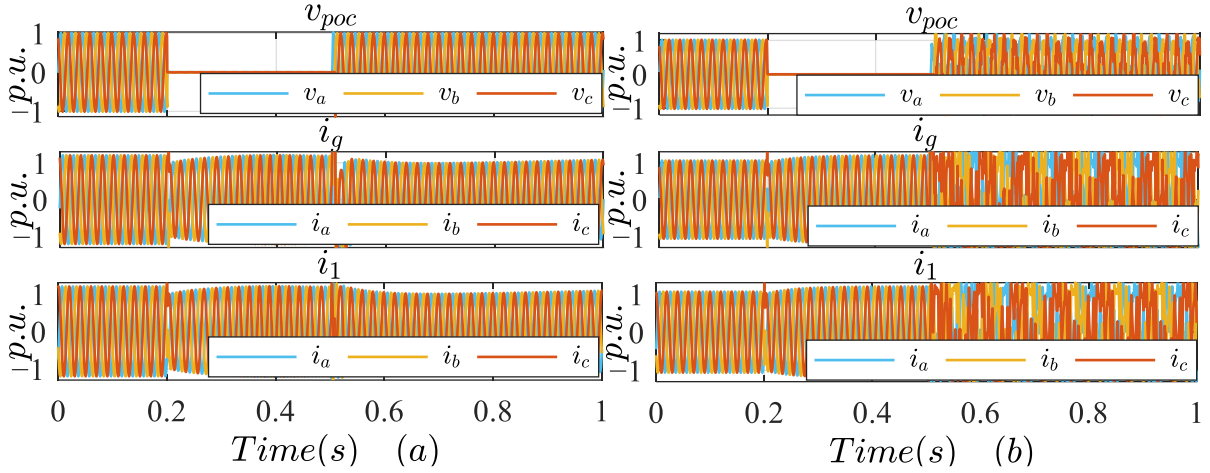


Figure 3.18: Impact of speed of grid's strength on post fault stability of GFL; (a) grid's SCP at POC is 5 MVA, (b) grid's SCP at POC is 1 MVA

From Figure 3.18, it is clear that the response of the control scheme is better for relatively stronger grid as compared to a weaker grid. From the above comparisons, it can be concluded that a slower PLL with the Q-priority injection in a stronger grid connection ensures the stability of the conventional GFL converter. Moreover, by comparing the peak phase currents for i_g and i_l , it can be concluded that there is not a much difference between the two. Due to the presence of filter's capacitor, the transient peak current at POC may be higher than the converter's side current which is fine as far as the current limit of the converter is concerned because this current does not pass through the IGBTs of the converter which have limited current handling capability. The comparison of using i_g or i_l as measured current for the inner current controller is given in Table 3.6 for both the normal and faulty conditions.

Table 3.6: Comparison of i_g and i_l as measured current for current controller

Current	Operating Conditions	Comments
i_g	Normal	Helps to achieve the reference power levels at POC.
	Faulty	Helps to ensure the grid's code injection at POC in faulty conditions. However, can't ensure the exact current limit of the converter (i_l) in faulty situations.
i_l	Normal	Can't ensure the reference power levels at POC. However, it can be partially improved with the help of angle compensation for measured i_l .
	Faulty	Ensures the exact current limit of the converter (i_l) in faulty situations.

As the conventional control scheme does not include the voltage sequence extraction, this scheme is not able to provide a stable response in case of unbalanced faults. To test the performance of the conventional GFL scheme in case of unbalanced faults, a line-to-line fault is introduced between phase 'b' and 'c' at 0.2 seconds for a duration of 0.3 seconds. The response of the conventional GFL for such type of faults is plotted in Figure 3.19.

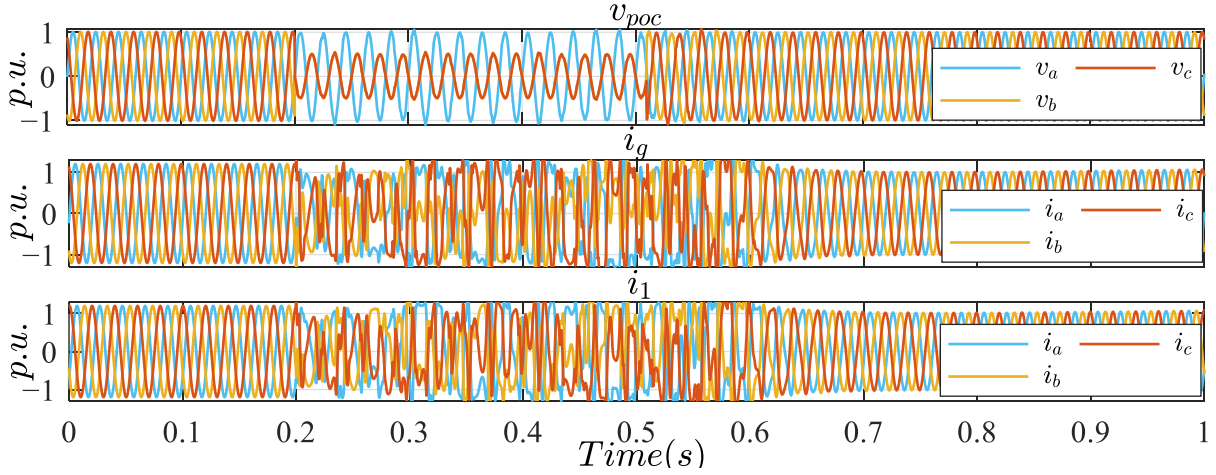


Figure 3.19: Response of conventional GFL control scheme for line to line (bc) fault

The above figure shows that the conventional GFL scheme based on dq-frame is unable to provide a stable response in case of unbalanced faults. The fault detection in such conditions is also not very accurate as it detects the fault with the help of v_d at POC which is not constant in such conditions.

3.3.6 Possible Improvements in Conventional GFL Scheme

The above discussion confirms that some improvements are possible in the conventional GFL scheme. Some of the improvements are already discussed in the available literature and each option among those improvements has its own consequences. Thus, some new improvements are suggested in this thesis and some of these suggestions have already been published by the scholar in different international journals and conferences [113-116]. The possible improvements are discussed in Table 3.7. In the right most column, the (A) stands for the already available schemes in literature and (N) stands for the novel schemes.

Table 3.7: Possible improvements in conventional scheme of GFL

Mode	Limitations	Possible Improvements	Available / Novel
Normal	Achieving reference powers at POC	(a) Use of closed loop control for real and reactive powers	(A)
		(b) Use of i_g as measured current for current controller	(A)
		(c) Angle correction for the measured converter's side current (i_i)	(N)
Unbalanced Fault	Sequence Extraction	(a) First order generalized integrator (FOGI)	(A)
		(b) Second order generalized integrator (SOGI)	(A)
		(c) Delay sampling method (DSM) in $\alpha\beta$ -frame	(N)
	Fault Detection	(a) Magnitude of positive sequence voltage phasor	(A)
		(b) Simple sequence-based scheme without phasors' angle	(N)
		(c) SOGI based fault detection scheme	(N)
		(d) Accurate sequence-based scheme with sequence voltage phasors' angle	(N)
Reference current calculation	(a) Using $\alpha\beta$ -frame with the power control mode	(A)	
	(b) Using dedicated PLLs for positive and negative sequences	(A)	
	(c) Using a hybrid scheme	(N)	
	(d) Using $\alpha\beta$ -frame with the current control mode	(N)	

Current limitation and priority	(a) Numeric addition of sequence current phasors' magnitudes	(A)
	(b) Numeric addition of respective sequence current phasors' components	(N)
	(c) Vector addition of sequence current phasors without considering angle between sequence voltage phasors	(N)
	(d) Vector addition of sequence current phasors with considering angle between sequence voltage phasors	(N)
Inner Current Controller	(a) Dedicated PI controllers for the positive and negative sequence currents.	(A)
	(b) Unified proportional resonant (PR) or quasi proportional resonant (QPR) controller in $\alpha\beta$ -frame.	(A)
Further Improvements	(a) Study the impact of active component of current in the negative sequence on the VUF and assess the optimal distribution of the negative sequence current components to achieve minimum VUF.	(N)
	(b) New reference current calculation scheme offering minimum real power fluctuations and minimum VUF during unbalanced faults.	(N)

3.4 Design of a Novel Control Scheme for GFL

Based on the improvements, discussed in Table 3.7, a novel control scheme for the GFL is designed. Before discussing the control diagram for the new control scheme, the possible improvements against each limitation are discussed.

3.4.1 Achieving Reference Powers at POC in Normal Conditions

From Table 3.4, it is clear that the reference real power is not observed at the POC for any control mode. This is mainly due to the mismatch of angular difference between the reference current phasor and the measured current phasor at the converter's side. This problem can be addressed with three possible solutions given in Table 3.7. Each of the solutions is briefly discussed below.

In [117], the authors proposed closed loop control for the real and reactive power injections. The closed loop control can offer better performance as compared to the open loop control if the i_l is used as measured current for the current controller. In this case, real power is controlled with the help of a PI controller and reactive power can have voltage closed loop or reactive power closed loop. The outputs of the PI controllers are saturated with the help of the current limiter.

The other solution is to use the line current at POC (i_g) as the measured signal to inner current controller. The time domain simulations of the conventional control scheme confirm that the current at grid's side is always higher than the converter's side current. The reason for such behavior is the presence of the filter's capacitor which can deliver the reactive current in case of low voltage at POC. Thus, if the line currents on the converter's side of POC are limited to the converter's current limit, then the current on the converter's side will be somewhat less than this and will ensure the safe operation of the converter.

The other solution is to correct the angular difference on the high voltage (HV) and low voltage (LV) side of the coupling transformer. Due to the angular difference between the grid's side current and converter's side current, the dq transformation of the converter's side current needs to take the angular difference into account. The type of coupling transformer is the major reason for this angular difference. The Δ -Y transformation introduces an angle difference of $\pm \pi/6$ between the high and low voltage sides. The POC is at HV side of the coupling transformer whereas the converter's side current is at LV side of the coupling transformer. Similarly, the voltage and coupling compensation for the i_g current also needs to incorporate this angular difference as the grid side inductance is also connected to the LV side of the coupling transformer. This coupling correction can be performed in the reference current.

The dq axis relation for the HV and LV side of the coupling transformer is given Figure 3.20.

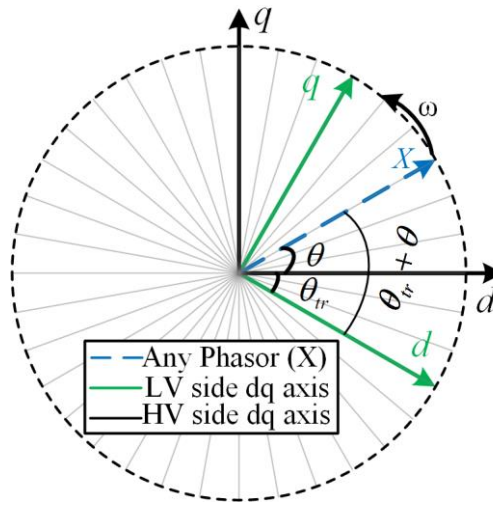


Figure 3.20: Relation of dq-axis on HV and LV side of coupling transformer

Where ' θ_r ' is the angle difference between the HV and LV side of the transformer. The mathematical relation is given in equation (3.41).

$$\begin{aligned} i_{d,LV} &= i_{d,HV} \cos(\theta_r) - i_{q,HV} \sin(\theta_r) \\ i_{q,LV} &= i_{d,HV} \sin(\theta_r) + i_{q,HV} \cos(\theta_r) \end{aligned} \tag{3.41}$$

The subscripts 'LV' and 'HV' represent the respective parameter on the LV and HV side of the transformer respectively. The performances of these schemes are presented in Table 3.8. The reference real power is 0.95 p.u. and the reference reactive power is 0.2 p.u.

Table 3.8: Performance comparison of different methods in normal conditions for GFL

Method	P_{poc} (p.u.)	Q_{poc} (p.u.)	V_{poc} (p.u.)
Open loop real and reactive power control with i_l as measured current.	0.92	-0.26	1.00
Open loop real power and closed loop reactive power control with i_l as measured current.	1.19	0.20	1.01
Open loop real and reactive power control with i_g as measured current.	0.95	0.20	1.01
Angular correction in open loop real and reactive power control with i_l as measured current.	0.95	0.25	1.01

The above table confirms the better performance of the angular correction technique. It still allows to control the converter’s side current and ensures the current limitation on the converter’s terminal. The rest of the modifications are particularly important for the low voltage response of the converter, especially in case of unbalanced faults.

3.4.2 Sequence Extraction

In unbalanced conditions, the alpha and beta components of the measured voltage phasor are no longer orthogonal to each other, and they also have different amplitudes. It can be derived from equation (3.14) . The derived equations are discussed in appendix F. The unbalanced three-phase system can be fully represented with the help of balanced three-phase systems named positive, negative and a zero-sequence system. As the three-phase, three-leg converters are unable to inject the zero-sequence component, thus, it will not be discussed here. Both the positive and negative sequence systems rotate with the same frequency but in opposite directions. The scholar discussed vector representation summation of sequence components in [116] which is given in Figure 3.21.

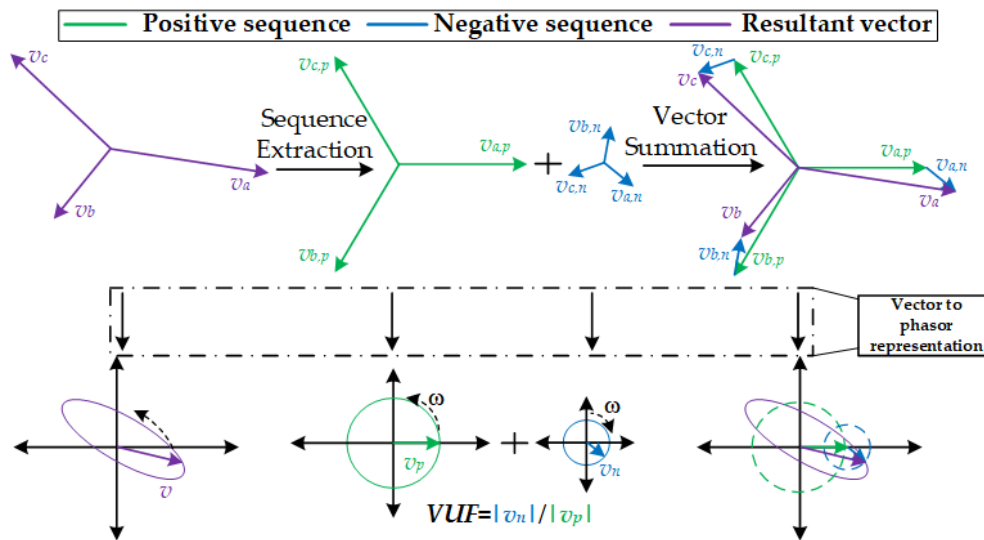


Figure 3.21: Vector and phasor representations of three-phase system into its positive and negative sequence systems

The above figure shows that the resultant phasor has an elliptical trajectory while the balanced systems have circular trajectories. Such trajectories suggest the opposite rotation of the negative sequence system as compared to the positive sequence system. The advantage of the circular trajectory is the easy control of its magnitude and priority injections while this is challenging with the elliptical trajectory as it needs time dependent adjustments which are hard to implement. This will be further discussed while designing the current limit schemes for the improved GFL scheme.

The mathematical expressions for the resultant three-phase system in terms of its positive and negative sequence systems are given in equation (3.42).

$$\begin{aligned}
 \begin{bmatrix} v_a(t) \\ v_b(t) \\ v_c(t) \end{bmatrix} &= \begin{bmatrix} v_{ap}(t) \\ v_{bp}(t) \\ v_{cp}(t) \end{bmatrix} + \begin{bmatrix} v_{an}(t) \\ v_{bn}(t) \\ v_{cn}(t) \end{bmatrix} \quad \therefore \begin{bmatrix} \delta_p \\ \delta_n \end{bmatrix} = \begin{bmatrix} \omega t + \theta_{vp} \\ -\omega t - \theta_{vn} \end{bmatrix} \\
 \begin{bmatrix} v_{ap}(t) \\ v_{bp}(t) \\ v_{cp}(t) \end{bmatrix} &= |v_p| \begin{bmatrix} \cos \delta_p \\ \cos \left(\delta_p - \frac{2}{3}\pi \right) \\ \cos \left(\delta_p + \frac{2}{3}\pi \right) \end{bmatrix}; \quad \begin{bmatrix} v_{an}(t) \\ v_{bn}(t) \\ v_{cn}(t) \end{bmatrix} = |v_n| \begin{bmatrix} \cos \delta_n \\ \cos \left(\delta_n - \frac{2}{3}\pi \right) \\ \cos \left(\delta_n + \frac{2}{3}\pi \right) \end{bmatrix}
 \end{aligned} \tag{3.42}$$

Where, the subscript ‘ p ’ and ‘ n ’ stands for the positive and negative sequence systems respectively and ‘ θ_i ’ is the initial angle of the respective voltage phasor. Equation (3.42) can be represented in stationary reference frame as:

$$\begin{aligned}
 \begin{bmatrix} v_\alpha(t) \\ v_\beta(t) \end{bmatrix} &= \begin{bmatrix} v_{\alpha p}(t) \\ v_{\beta p}(t) \end{bmatrix} + \begin{bmatrix} v_{\alpha n}(t) \\ v_{\beta n}(t) \end{bmatrix} \\
 \begin{bmatrix} v_{\alpha p}(t) \\ v_{\beta p}(t) \end{bmatrix} &= |v_p| \begin{bmatrix} \cos(\omega t + \theta_{vp}) \\ \sin(\omega t + \theta_{vp}) \end{bmatrix}; \quad \begin{bmatrix} v_{\alpha n}(t) \\ v_{\beta n}(t) \end{bmatrix} = |v_n| \begin{bmatrix} \cos(-\omega t - \theta_{vn}) \\ \sin(-\omega t - \theta_{vn}) \end{bmatrix} \\
 \therefore |v_p| &= \sqrt{v_{\alpha p}(t)^2 + v_{\beta p}(t)^2}; \quad |v_n| = \sqrt{v_{\alpha n}(t)^2 + v_{\beta n}(t)^2}
 \end{aligned} \tag{3.43}$$

The stationary components for the positive and negative sequences can be derived from the measured voltage at POC presented in stationary reference frame. The detailed derivation is discussed in the appendix G. The final expressions are given in equation (3.44).

$$\begin{bmatrix} v_{\alpha p}(t) \\ v_{\alpha n}(t) \\ v_{\beta p}(t) \\ v_{\beta n}(t) \end{bmatrix} = \frac{1}{2} \begin{bmatrix} v_\alpha(t) + v_\beta^T(t) \\ v_\alpha(t) - v_\beta^T(t) \\ v_\beta(t) - v_\alpha^T(t) \\ v_\beta(t) + v_\alpha^T(t) \end{bmatrix} \tag{3.44}$$

Where the superscript ‘ T ’ represents the orthogonal of the respective signal. To achieve the real time sequence extraction, the real time orthogonal signals of the measured voltage phasor’s components are essential. There are several schemes discussed in literature to assess the real time orthogonal signal for stationary reference frame components. Some of these methods are discussed in this section and their qualitative comparison will be presented.

3.4.2.1 First Order Generalized Integrator (FOGI)

First order generalized integrator (FOGI) helps to assess the orthogonal component with the help of a single integrator. Its layout is presented in Figure 3.22.

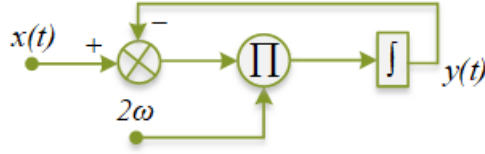


Figure 3.22: Control layout of FOGI

Where ‘x’ and ‘y’ represent the input and output signals respectively. ‘ ω ’ is the fundamental rotational frequency of the input signal. The transfer function of the FOGI (in Laplace domain) and time domain expressions for the output are given in equation (3.45).

$$H_{FOGI}(s) = \frac{2\omega}{s + 2\omega} \xrightarrow{s=j\omega} H_{FOGI}(j\omega) = \frac{4}{5} - \frac{2}{5}j \quad (3.45)$$

$$y(t) = \frac{4}{5}x(t) - \frac{2}{5}x^T(t)$$

The above equation confirms the presence of orthogonal component of the input signal in the output of the FOGI. Equation (3.44) needs to be modified for the FOGI as the input signal is also present in the output. Due to the direct mathematical addition and subtraction of the instantaneous signals, the FOGI may not result in true sequence estimation in case of transients. Moreover, the share of orthogonal signal in the output is relatively smaller. The share of orthogonal signal in the output can be enhanced with the help of introducing a gain in the feedback path. The updated layout is presented in Figure 3.23.

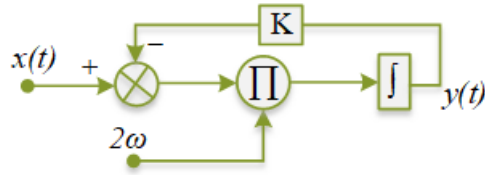


Figure 3.23: Layout of improved FOGI scheme

Where ‘K’ is the gain. The transfer function of the improved FOGI (in Laplace domain) and time domain expressions for the output are given in equation (3.46).

$$H_{FOGI}(s) = \frac{2\omega}{s + 2K\omega} \xrightarrow{s=j\omega} H_{FOGI}(j\omega) = \frac{4K}{4K^2 + 1} - \frac{2}{4K^2 + 1}j \quad (3.46)$$

$$\Rightarrow \angle H_{FOGI}(j\omega) = -\tan^{-1}\left(\frac{1}{2K}\right)$$

$$y(t) = \frac{4K}{4K^2 + 1}x(t) - \frac{2}{4K^2 + 1}x^T(t)$$

With the help of gain ‘K’, the angle of the transfer function can be increased which is the indication of the increase in orthogonal part in the output. It also enhances the overall magnitude of the signal. ‘K’ should be a positive value less than or equal to unity. If ‘K’ is chosen as 0.1, the angle for the transfer function and the output equation in time domain is given below.

$$\angle H_{FOGI}(j\omega) = -\tan^{-1}(5) = -78.7^\circ$$

$$y(t) = \frac{5}{13}x(t) - \frac{25}{13}x^T(t) \quad (3.47)$$

The FOGI can also act as a low pass filter (LPF) but due to the subtraction/addition from the input, the effect of filter is not dominant. Thus, it needs LPF for measuring signals. By using equation (3.44) and (3.46), the updated equations for the sequence extraction in case of FOGI are given in equation (3.48).

$$\begin{bmatrix} v_{\alpha p}(t) \\ v_{\alpha n}(t) \\ v_{\beta p}(t) \\ v_{\beta n}(t) \end{bmatrix} = \frac{1}{2} \begin{bmatrix} v_\alpha(t) + v_\beta^T(t) \\ v_\alpha(t) - v_\beta^T(t) \\ v_\beta(t) - v_\alpha^T(t) \\ v_\beta(t) + v_\alpha^T(t) \end{bmatrix} = \frac{1}{2} \begin{bmatrix} v_\alpha(t) + 2Kv_\beta(t) - \frac{4K^2+1}{2}y_\beta(t) \\ v_\alpha(t) - 2Kv_\beta(t) + \frac{4K^2+1}{2}y_\beta(t) \\ v_\beta(t) - 2Kv_\alpha(t) + \frac{4K^2+1}{2}y_\alpha(t) \\ v_\beta(t) + 2Kv_\alpha(t) - \frac{4K^2+1}{2}y_\alpha(t) \end{bmatrix} \quad (3.48)$$

Where ‘K’ is the gain defined in Figure 3.23 and ‘ $y_{\alpha\beta}$ ’ is the output for the respective input signal. The performance of FOGI is analyzed in different operating conditions. Till 0.15 seconds, balanced input is generated in stationary reference frame. A negative sequence of 0.5 p.u. amplitude is added in the input of FOGI at 0.15 seconds for period of 0.3 seconds. The response of the FOGI with different gains is given in Figure 3.24.

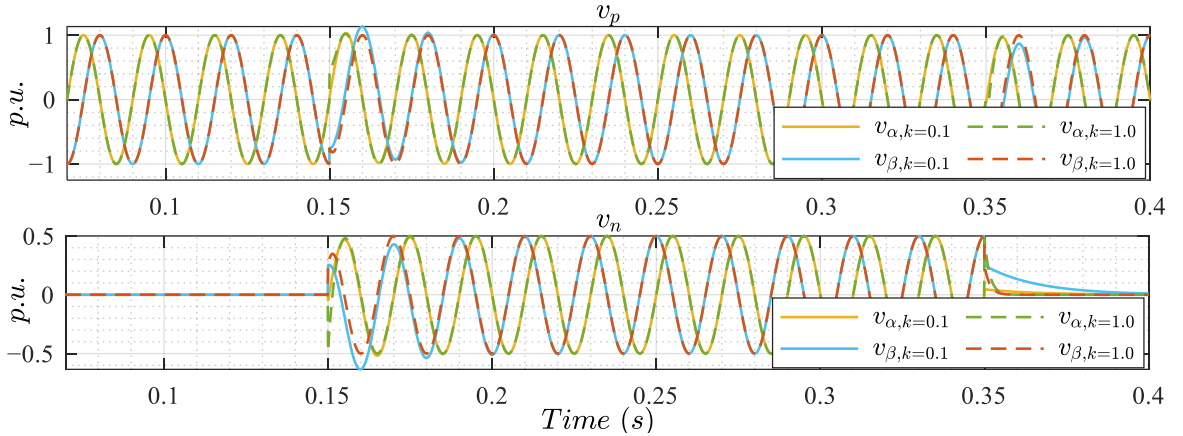


Figure 3.24: Response of FOGI in unbalanced conditions

By comparing the response of the FOGI with different gains, Figure 3.24 shows that the response of FOGI with feedback gain of 0.1 is slower than the unity feedback gain. It almost takes two cycles to reach the steady state response. However, it results in smooth extraction for the positive sequence. This comparison is also performed in case of some distorted input signal. 3rd harmonic is introduced with (33 %) amplitude in the input signal and the response of the FOGI is analyzed which is given in Figure 3.25.

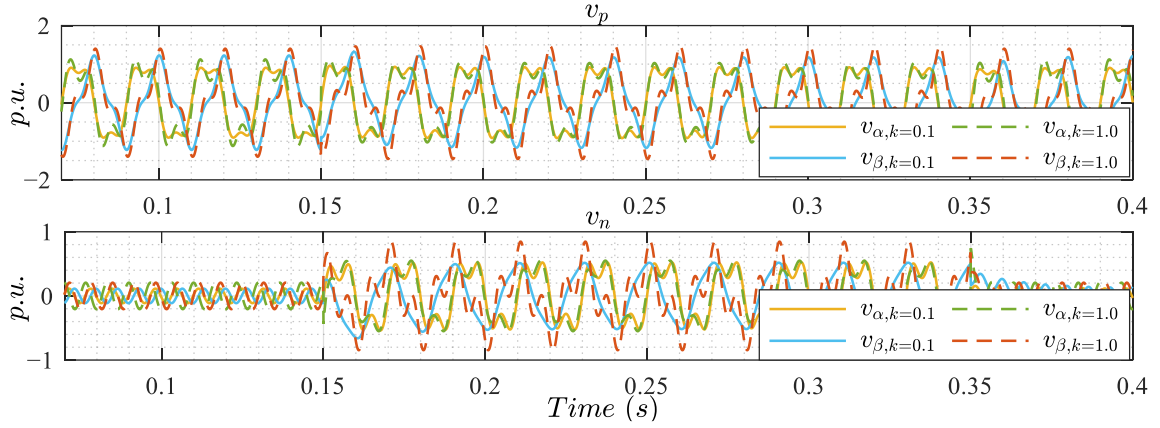


Figure 3.25: Response of FOGI in case of unbalanced distorted signal

It shows that the FOGI wrongly assesses some negative sequence components in case of distorted signal from 0 to 0.15 seconds. However, lower feedback gain results in smaller error as compared to unity feedback gain. Similarly, in presence of negative sequence component, the FOGI with lower feedback gain again results in smaller error as far as the amplitude of the positive and negative sequences is concerned. It is important to mention here that the vector sum of extracted positive and negative sequences results in the input signal with both the feedback gains. Hence, it can be concluded that the FOGI with lower feedback gain results in better assessment in case of harmonics and it also offers smooth extraction for the positive sequence. However, for the negative sequence it may take 2-3 cycles to reach the steady state. Moreover, FOGI can act as an adaptive LPF by controlling the input rotational frequency which can be assessed by PLL from the extracted positive sequence voltage.

3.4.2.2 Second Order Generalized Integrator (SOGI)

The second order generalized integrator (SOGI) uses two integrators and results in two outputs i.e., an active band-pass filtered input and low pass filtered orthogonal signal. Thus, it does not require extra filtering for the measured signal. The layout for the SOGI is given in Figure 3.26.

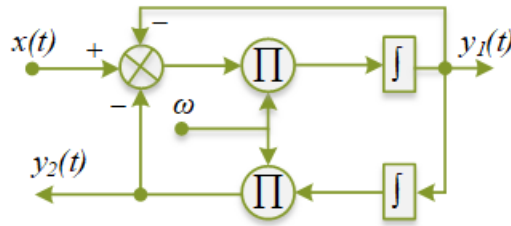


Figure 3.26: Layout of SOGI

The expressions for transfer function and outputs for SOGI are given in equation (3.49).

$$\begin{aligned}
 H_1(s) &= \frac{Y_1(s)}{X(s)} = \frac{\omega s}{s^2 + \omega s + \omega^2} \rightarrow H_1(j\omega) = 1 \\
 H_2(s) &= \frac{Y_2(s)}{X(s)} = \frac{\omega^2}{s^2 + \omega s + \omega^2} \rightarrow H_2(j\omega) = -j \\
 y_1(t) &= x(t); y_2(t) = -x^T(t)
 \end{aligned} \tag{3.49}$$

By using the expressions given in equation (3.44) and (3.49), the expressions for the sequence extraction in case of SOGI are given in equation (3.50).

$$\begin{bmatrix} v_{\alpha p}(t) \\ v_{\alpha n}(t) \\ v_{\beta p}(t) \\ v_{\beta n}(t) \end{bmatrix} = \frac{1}{2} \begin{bmatrix} y_{1,\alpha}(t) - y_{2,\beta}(t) \\ y_{1,\alpha}(t) + y_{2,\beta}(t) \\ y_{1,\beta}(t) + y_{2,\alpha}(t) \\ y_{1,\beta}(t) - y_{2,\alpha}(t) \end{bmatrix} \quad (3.50)$$

The response of the SOGI under different conditions is given in Figure 3.27.

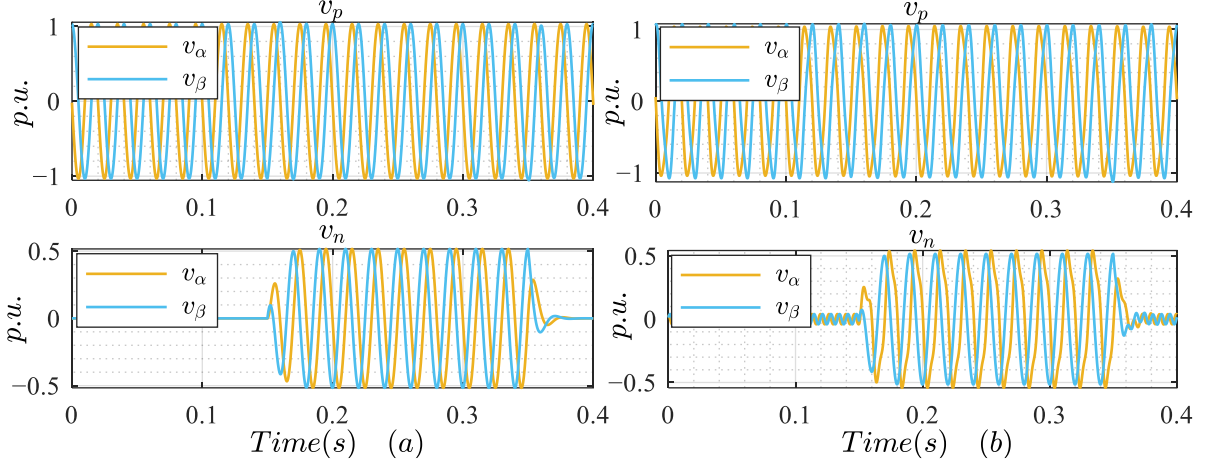


Figure 3.27: Response of SOGI in unbalanced conditions; (a) fundamental frequency input signal, (b) harmonic injected signal

Due to the adaptive filtering feature of the SOGI for both the outputs, its response is better than FOGI in both fundamental frequency signal and harmonic injected signals. However, in case of harmonic injected input signal, it wrongly assesses some negative sequence signal, and the amplitude of the assessed negative sequence phasor has some error.

3.4.2.3 Delay Sample Method (DSM)

The other method is the delay sample method (DSM) for sequence extraction, this method is discussed in literature for the assessment of positive sequence in dq reference frame [69]. The scholar developed the delay sample method for the sequence extraction in stationary reference frame and discussed it in [115]. In this method, a unit step delay is introduced in the measured signals and the sequence components are assessed with the help of these delayed signals. The expressions for the unit step delayed signals are given in equation (3.51). The detailed derivation is discussed in the appendix H.

$$\begin{bmatrix} v_{\alpha}(t+T_s) \\ v_{\alpha}(t-T_s) \end{bmatrix} = \begin{bmatrix} \cos(\omega T_s) & -\sin(\omega T_s) & \sin(\omega T_s) \\ \cos(\omega T_s) & \sin(\omega T_s) & -\sin(\omega T_s) \end{bmatrix} \begin{bmatrix} v_{\alpha}(t) \\ v_{\beta p}(t) \\ v_{\beta n}(t) \end{bmatrix} \quad (3.51)$$

$$\begin{bmatrix} v_{\beta}(t+T_s) \\ v_{\beta}(t-T_s) \end{bmatrix} = \begin{bmatrix} \cos(\omega T_s) & \sin(\omega T_s) & -\sin(\omega T_s) \\ \cos(\omega T_s) & -\sin(\omega T_s) & \sin(\omega T_s) \end{bmatrix} \begin{bmatrix} v_{\beta}(t) \\ v_{\alpha p}(t) \\ v_{\alpha n}(t) \end{bmatrix}$$

After rearranging the equation (3.51), the expressions for the sequence components can be derived in term of measured and delayed signals. The expressions for the positive and negative sequence components are given in equation (3.52).

$$\begin{aligned} \begin{bmatrix} v_{\alpha p}(t) \\ v_{\beta p}(t) \end{bmatrix} &= \frac{1}{4} \begin{bmatrix} v_{\alpha}(t+T_s) + v_{\alpha}(t-T_s) & v_{\beta}(t+T_s) - v_{\beta}(t-T_s) \\ v_{\beta}(t+T_s) + v_{\beta}(t-T_s) & v_{\alpha}(t-T_s) - v_{\alpha}(t+T_s) \end{bmatrix} \begin{bmatrix} \sec(\omega T_s) \\ \csc(\omega T_s) \end{bmatrix} \\ \begin{bmatrix} v_{\alpha n}(t) \\ v_{\beta n}(t) \end{bmatrix} &= \frac{1}{4} \begin{bmatrix} v_{\alpha}(t+T_s) + v_{\alpha}(t-T_s) & v_{\beta}(t-T_s) - v_{\beta}(t+T_s) \\ v_{\beta}(t+T_s) + v_{\beta}(t-T_s) & v_{\alpha}(t+T_s) - v_{\alpha}(t-T_s) \end{bmatrix} \begin{bmatrix} \sec(\omega T_s) \\ \csc(\omega T_s) \end{bmatrix} \end{aligned} \quad (3.52)$$

Where ‘sec’ and ‘csc’ represent the secant and cosecant operators respectively. The above expressions can be implemented in discrete domain with the help of double delay function. The updated expressions in discrete domain are given in equation (3.53).

$$\begin{aligned} \begin{bmatrix} v_{\alpha p}(z) \\ v_{\beta p}(z) \end{bmatrix} &= \frac{1}{4} \begin{bmatrix} v_{\alpha}(z) + v_{\alpha}(z-2) & v_{\beta}(z) - v_{\beta}(z-2) \\ v_{\beta}(z) + v_{\beta}(z-2) & v_{\alpha}(z-2) - v_{\alpha}(z) \end{bmatrix} \begin{bmatrix} \sec(\omega T_s) \\ \csc(\omega T_s) \end{bmatrix} \\ \begin{bmatrix} v_{\alpha n}(z) \\ v_{\beta n}(z) \end{bmatrix} &= \frac{1}{4} \begin{bmatrix} v_{\alpha}(z) + v_{\alpha}(z-2) & v_{\beta}(z-2) - v_{\beta}(z) \\ v_{\beta}(z) + v_{\beta}(z-2) & v_{\alpha}(z) - v_{\alpha}(z-2) \end{bmatrix} \begin{bmatrix} \sec(\omega T_s) \\ \csc(\omega T_s) \end{bmatrix} \end{aligned} \quad (3.53)$$

Where ‘z’ represents the discrete domain. The response of the DSM under different conditions is given in Figure 3.28.

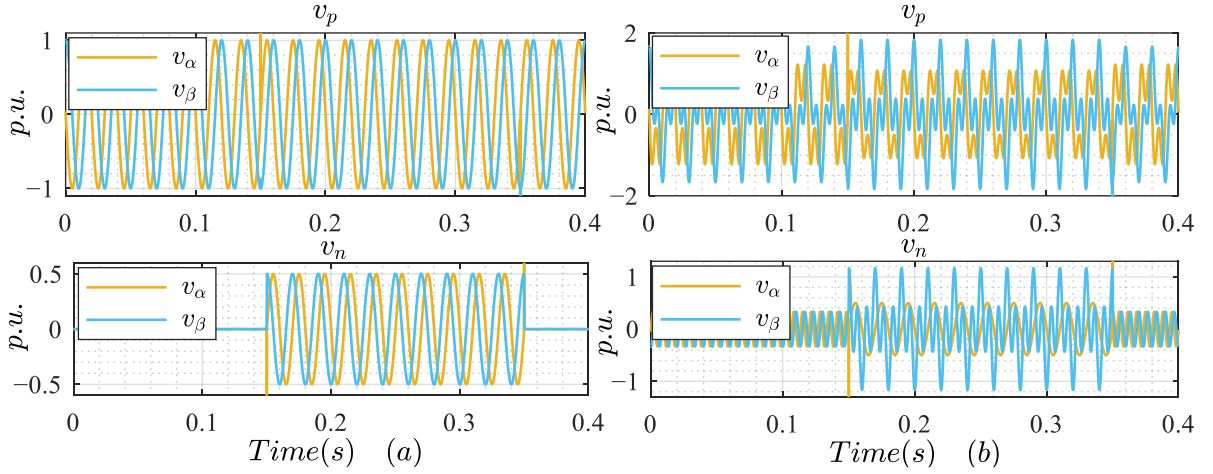


Figure 3.28: Response of DSM in unbalanced conditions; (a) fundamental frequency input signal, (b) harmonic injected signal

The above figure confirms that the DSM results in fast sequence separation as compared to the rest of the techniques, but its performance is worst among the other schemes for the input containing harmonics. One of the reasons for this drawback is the absence of filter as this scheme can’t act as a filter and needs adaptive filtering for the accurate sequence separation in case of distorted input signals.

To improve the response of the DSM for distorted signals, an active filter is used for filtering of the extracted signals. The response of the improved delay sample method (IDSMS) is given in Figure 3.29.

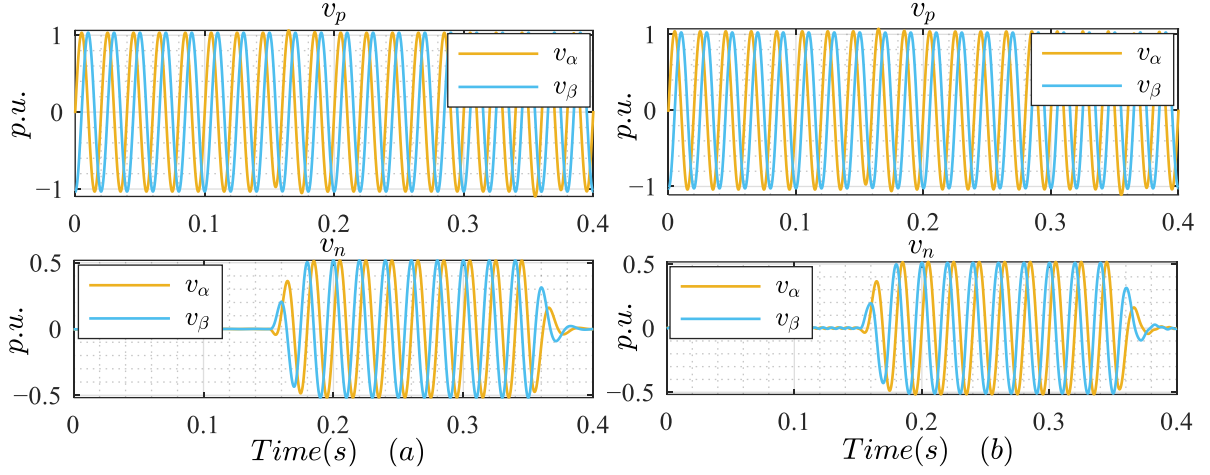


Figure 3.29: Response of IDSM in unbalanced conditions; (a) fundamental frequency input signal, (b) harmonic injected signal

The above graph shows that the IDSM offers stable and fast response as compared to the other schemes in case of distorted input signals. However, it introduces a phase difference between the input signals and the vector sum of the sequence components.

3.4.3 Fault Detection

According to the grid codes, voltage support is demanded if any of the line-to-line (L-L) voltage drops below 90 % of its nominal value. In balanced faults, this condition can be confirmed from the magnitude of the voltage phasor in stationary or rotating reference frame. However, in case of unbalanced faults, the resultant phasor in stationary reference frame follows an elliptical trajectory. Thus, it changes its amplitude along its trajectory. It can be visualized from Figure 3.21. It is important to estimate the minimum line to line RMS voltage in terms of positive and negative sequence phasors' magnitude and the initial angle difference between them. Mostly in literature, the positive sequence voltage is considered for the fault detection which is not correct in case of high impedance unbalanced faults. The expression for fault detection based on only positive sequence is given below.

$$fault_flag = \begin{cases} 1 & \text{if } |v_p| \leq 90\% \\ 0 & \text{if } |v_p| > 90\% \end{cases} \quad (3.54)$$

The above scheme is termed as conventional fault detection scheme in this thesis.

The scholar developed a fault detection scheme based on the magnitude of the positive and negative sequence voltage phasors and presented it in [114]. The phase difference between the phase voltages was considered to be 120° . The worst-case scenario was considered by keeping one phase healthy and the magnitude of other two phases is varied to achieve the 90 % of the nominal L-L voltage. The following equation is used as the primary equation for fault detection which is the expression for L-L voltage between two phases which are 120° apart.

$$\sqrt{|v_x|^2 + |v_y|^2 + |v_x||v_y|} = 0.9\sqrt{3} \quad (3.55)$$

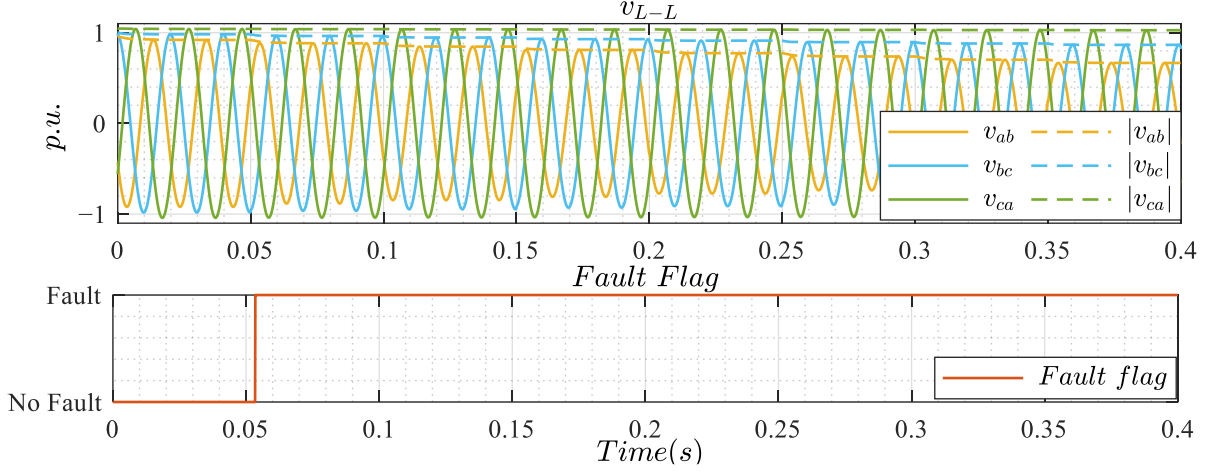


Figure 3.31: Performance of SOGI based scheme for amplitude and fault detection

This scheme detects the correct amplitude for each line-to-line voltage. However, it requires extra computation efforts as it needs a dedicated SOGI for each amplitude detection.

To overcome the drawback of SOGI based fault detection scheme, the scholar developed a new fault detection scheme based on the magnitude of the positive and negative sequence voltage phasors and the angle between them. Thus, it is termed as sequence-based scheme (SBS) in this thesis. The normalized expressions for line-to-line voltages in the form of $\alpha\beta$ -components are given below.

$$\begin{bmatrix} v_{ab}(t) \\ v_{bc}(t) \\ v_{ca}(t) \end{bmatrix} = \frac{1}{2} \begin{bmatrix} \sqrt{3} & -1 \\ 0 & 2 \\ -\sqrt{3} & -1 \end{bmatrix} \begin{bmatrix} v_{\alpha}(t) \\ v_{\beta}(t) \end{bmatrix} \quad (3.58)$$

The voltage phasor in $\alpha\beta$ is replaced with the phasors sum of positive and negative sequence voltage phasors. The final expression for the amplitude of each line-to-line voltage in terms of the magnitude of sequence phasors is given in equation (3.59). The detailed derivation can be found in appendix J.

$$\begin{aligned} \therefore \theta_{vpn} &= \theta_{vp} - \theta_{vn} \\ |v_{ab}| &= \sqrt{|v_p|^2 + |v_n|^2 + |v_p||v_n|\{\cos(\theta_{vpn}) - \sqrt{3}\sin(\theta_{vpn})\}} \\ |v_{bc}| &= \sqrt{|v_p|^2 + |v_n|^2 - 2|v_p||v_n|\cos(\theta_{vpn})} \\ |v_{ca}| &= \sqrt{|v_p|^2 + |v_n|^2 + |v_p||v_n|\{\cos(\theta_{vpn}) + \sqrt{3}\sin(\theta_{vpn})\}} \\ \cos(\theta_{vpn}) &= \frac{v_{\alpha p}v_{\alpha n} - v_{\beta p}v_{\beta n}}{|v_p||v_n|}; \sin(\theta_{vpn}) = \frac{v_{\alpha p}v_{\beta n} + v_{\beta p}v_{\alpha n}}{|v_p||v_n|} \end{aligned} \quad (3.59)$$

' θ_{vpn} ' is the angle between positive and negative sequence voltage phasors. The above equation results in amplitudes of line-to-line voltages and then the expressions given in equation (3.57) are used for the fault detection. The performance of this scheme is given in Figure 3.32.

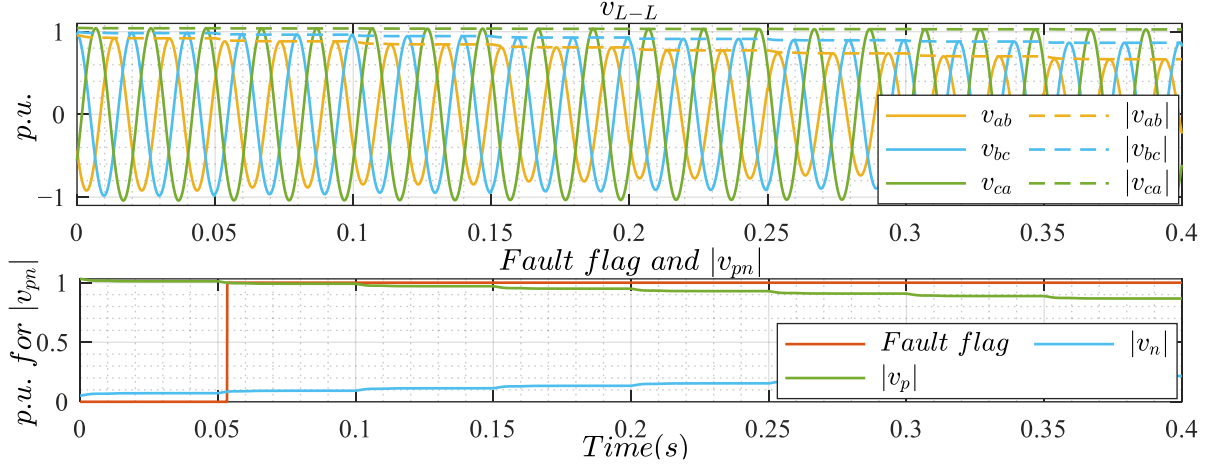


Figure 3.32: Performance of SBS for amplitude and fault detection

The results confirm the true detection of the fault with this scheme. It is fast as compared to other schemes and does not involve extra assessments for the fault detection. The other advantage of the SBS is that the minimum or maximum amplitudes among the three line-line voltages can be estimated based on the angle between positive and negative sequence phasors. Hence, there is no need to calculate the individual three amplitudes to decide the minimum of them. The conditions for minimum amplitudes are given in equation (3.60).

$$\text{Min_Amplitude} = \begin{cases} |v_{bc}| & \text{if } |(\theta_{vp} - \theta_{vn})| \leq \frac{\pi}{3} \\ |v_{ab}| & \text{if } \frac{\pi}{3} < (\theta_{vp} - \theta_{vn}) \leq \pi \\ |v_{ca}| & \text{if } -\pi \leq (\theta_{vp} - \theta_{vn}) < -\frac{\pi}{3} \end{cases} \quad (3.60)$$

Four different methods for fault detection are discussed in this section. The first method is termed as conventional method which only considers the magnitude of the positive sequence voltage phasor, the other method, having the governing equation (3.56), is termed as simple sequence based (SSB) method, the 3rd is the SOGI based, and the last one is the SBS. The performance comparison of these schemes for fault detection in case of unbalanced conditions is given in Figure 3.33.

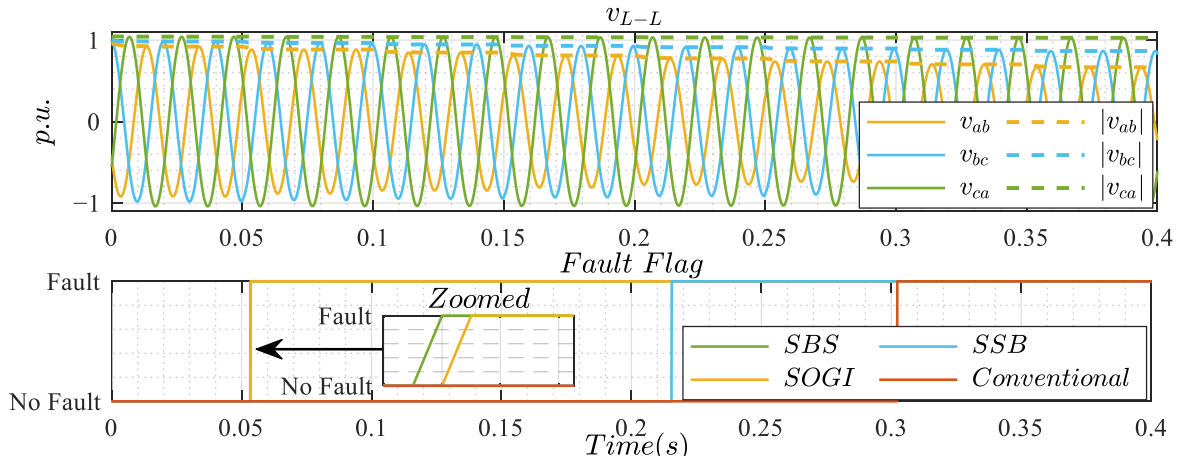


Figure 3.33: Performance comparison of different fault detection schemes

The above figure shows that the SBS and SOGI based fault detection schemes are fast and accurate. Moreover, the SSB scheme results in better accuracy as compared to the conventional scheme.

3.4.4 Reference Current Calculation

The reference current calculation in case of unbalanced conditions is a challenging task due to the presence of negative sequence voltage. Injecting only the positive sequence current is a conventional approach where no negative sequence current is injected. It has several drawbacks such as higher VUF, oscillations in real and reactive power, and dc link voltage oscillations. Thus, the negative sequence current can be used to minimize the above discussed drawbacks. In literature, there are several schemes for the reference current calculation. It can be broadly divided into two main categories i.e., reference power-based scheme and direct current calculation scheme.

Equation (3.15) can be used to establish a relation between the current and power in stationary reference frame. The expressions for real and reactive power in term of positive and negative sequence components are given in equation (3.61).

$$\begin{bmatrix} p \\ q \end{bmatrix} = \begin{bmatrix} v_{\alpha p}(t) + v_{\alpha n}(t) & v_{\beta p}(t) + v_{\beta n}(t) \\ v_{\beta p}(t) + v_{\beta n}(t) & -(v_{\alpha p}(t) + v_{\alpha n}(t)) \end{bmatrix} \begin{bmatrix} i_{\alpha p}(t) + i_{\alpha n}(t) \\ i_{\beta p}(t) + i_{\beta n}(t) \end{bmatrix} \quad (3.61)$$

Due to the negative sequence phasor, both real and reactive power contain frequency dependent components oscillating with double of the fundamental frequency. The expressions for these components are given in equation (3.62). Its derivation is discussed in the appendix K.

$$\begin{aligned} p &= p_o + \tilde{p} \\ q &= q_o + \tilde{q} \\ \begin{bmatrix} p_o \\ \tilde{p} \\ q_o \\ \tilde{q} \end{bmatrix} &= \begin{bmatrix} v_{\alpha p}(t) & v_{\beta p}(t) & v_{\alpha n}(t) & v_{\beta n}(t) \\ v_{\alpha n}(t) & v_{\beta n}(t) & v_{\alpha p}(t) & v_{\beta p}(t) \\ v_{\beta p}(t) & -v_{\alpha p}(t) & v_{\beta n}(t) & -v_{\alpha n}(t) \\ v_{\beta n}(t) & -v_{\alpha n}(t) & v_{\beta p}(t) & -v_{\alpha p}(t) \end{bmatrix} \begin{bmatrix} i_{\alpha p}(t) \\ i_{\beta p}(t) \\ i_{\alpha n}(t) \\ i_{\beta n}(t) \end{bmatrix} \\ p_o &= |v_p| |i_p| \cos(\theta_{vp} - \theta_{ip}) + |v_n| |i_n| \cos(\theta_{vn} - \theta_{in}) \\ \tilde{p} &= |v_n| |i_p| \cos(2\omega t + \theta_{vn} + \theta_{ip}) + |v_p| |i_n| \cos(2\omega t + \theta_{vp} + \theta_{in}) \\ q_o &= |v_p| |i_p| \sin(\theta_{vp} - \theta_{ip}) + |v_n| |i_n| \sin(\theta_{vn} - \theta_{in}) \\ \tilde{q} &= |v_p| |i_n| \sin(2\omega t + \theta_{vp} + \theta_{in}) - |v_n| |i_p| \sin(2\omega t + \theta_{vn} + \theta_{ip}) \end{aligned} \quad (3.62)$$

Where ‘ p_o ’ and ‘ q_o ’ represent the mean active and reactive power in case of unbalanced conditions respectively. Moreover, \tilde{p} and \tilde{q} represent the fluctuating component of the active and reactive power respectively. It is clear from the above equation that, in unbalanced conditions, the real and reactive power have oscillating components which oscillate with the double of the fundamental frequency. With the power control scheme, the reference real and reactive powers are changed in unbalanced conditions introducing an oscillating component into it which is responsible for the negative sequence current

injection. The injection of such oscillating component into reference real and reactive power is a complex process as it needs to consider the angle difference between the sequence voltage phasors.

Due to the complexity of power control mode in unbalanced conditions, most of the reference current calculation schemes use the direct current calculation method. The simplest of the scheme is to inject only the positive sequence current based on the reference power or based on the positive sequence voltage drop. It calculates the reference currents like the conventional GFL does. The only difference is that it uses the positive sequence voltage for the calculation of the reference currents. This scheme does not inject the negative sequence current.

To fulfill the requirement of recent grid codes, the injection of negative sequence current is important in case of unbalanced conditions. The injected negative sequence current should be reactive, and its magnitude should be proportional to the magnitude of the negative sequence voltage phasor. The proportionality constant may vary from 2-6. These requirements are illustrated in Figure 2.21. The reference negative sequence current can be calculated in dq-frame by using a dedicated PLL for the negative sequence. For a scheme having dedicated PLL for positive and negative sequence, the expressions for the sequence reference current components are given in equation (3.63).

$$\begin{bmatrix} i_{dp}^* \\ i_{qp}^* \\ i_{dn}^* \\ i_{qn}^* \end{bmatrix} = \begin{cases} \begin{bmatrix} f(p^*, |v_p|) \\ f(q^*, v^*, |v_p|, M_{qG}) \\ 0 \\ 0 \end{bmatrix} & \text{if } fault_flag = 0 \\ \begin{bmatrix} f(p^*, |v_p|) \\ k\Delta |v_p| + f(M_{qUVRT}) \\ 0 \\ k\Delta |v_n| \end{bmatrix} & \text{if } fault_flag = 1 \end{cases} \quad (3.63)$$

Where the dq subscripts are for the horizontal and vertical projections of the phasor in a rotating reference frame and ' $f(\cdot)$ ' represents the function. The functions used in the above equation are discussed in conventional GFL design. Although, this scheme allows the negative sequence current injection but the stability of PLL for the negative sequence is poor which is discussed in [59].

To overcome the stability issue of the negative sequence PLL, the scholar introduced a hybrid reference current generation scheme in [115]. This scheme allows to calculate the magnitude of the negative sequence current phasor just like the expression given in equation (3.63). To inject a capacitive reactive current of amplitude i_{qn}^* , the following expression is derived in stationary reference frame.

$$\begin{bmatrix} i_{\alpha n}^*(t) \\ i_{\beta n}^*(t) \end{bmatrix} = \frac{i_{qn}^*}{|v_n|} \begin{bmatrix} -v_{\beta n}(t) \\ v_{\alpha n}(t) \end{bmatrix} \quad (3.64)$$

The above expression enables to calculate the reference reactive current in a virtual dq frame considering the v_{dn} equal to the magnitude of the negative sequence voltage phasor. It helps to limit the reference current's magnitude which is a bit challenging in $\alpha\beta$ -frame. Thus, it offers both the advantages of dq- and $\alpha\beta$ -frame. As the reference reactive current in the negative sequence is also proportional to the magnitude of the negative sequence voltage phasor, thus the expression given in (3.64) can be further simplified.

$$\begin{bmatrix} i_{\alpha n}^*(t) \\ i_{\beta n}^*(t) \end{bmatrix} = \frac{i_{qn}^*}{|v_n|} \begin{bmatrix} -v_{\beta n}(t) \\ v_{\alpha n}(t) \end{bmatrix} \xrightarrow{i_{qn}^* = k(0-|v_n|)} \begin{bmatrix} i_{\alpha n}^*(t) \\ i_{\beta n}^*(t) \end{bmatrix} = k \begin{bmatrix} v_{\beta n}(t) \\ -v_{\alpha n}(t) \end{bmatrix} \quad (3.65)$$

The above expressions result in only the reactive power injection as the real power injection in the negative sequence is not demanded by the grid codes. However, the real power injection in the negative sequence can enhance the VUF and helps in minimizing the real power oscillations. Thus, the expression for the negative sequence reference current calculation needs to be modified to inject the real power. If the magnitude of the reference negative sequence current phasor is the same, then the following expression can be used to decide its active and reactive components. The scholar discussed these expressions in [114] and the final expression is given below.

$$\begin{bmatrix} i_{\alpha n}^*(t) \\ i_{\beta n}^*(t) \end{bmatrix} = k \begin{bmatrix} \cos(\theta) & \sin(\theta) \\ -\sin(\theta) & \cos(\theta) \end{bmatrix} \begin{bmatrix} v_{\alpha n}(t) \\ v_{\beta n}(t) \end{bmatrix} \quad (3.66)$$

Where ‘ θ ’ is the angle between negative sequence voltage and current phasors. The above expression results in the same expression for the magnitude of the negative sequence current phasor as given in equation (3.63) and it also offers a flexibility to decide its active and reactive components based on the angle involved in equation (3.66).

It is important to mention here that the expressions given in equation (3.66) are not effective for the positive sequence current injection as the real and reactive current components are explicitly calculated in the positive sequence and the reactive current in normal conditions involves different modes. Moreover, the separate current limits for the positive sequence current components also restrict the use of these expressions for the positive sequence. However, by following the same procedure, the PLL for the positive sequence can also be eliminated. The real and reactive current components for the positive sequence can be calculated considering an ideal PLL with v_{dp} equal to the magnitude of the positive sequence voltage phasor. The current components can then be transformed to the stationary reference frame with the help of the voltage components in the stationary reference frame. The expressions are given below.

$$\begin{bmatrix} i_{\alpha p}^*(t) \\ i_{\beta p}^*(t) \end{bmatrix} = \frac{1}{|v_p|} \begin{bmatrix} i_{dp}^* & -i_{qp}^* \\ i_{qp}^* & i_{dp}^* \end{bmatrix} \begin{bmatrix} v_{\alpha p}(t) \\ v_{\beta p}(t) \end{bmatrix} \quad (3.67)$$

Although the expressions for the positive sequence can be calculated in $\alpha\beta$ - frame to eliminate the PLL but the scholar advocates the use of hybrid scheme rather than complete dq or $\alpha\beta$ - based scheme. The reason for using the PLL for the positive sequence is its ability to act like an active filter and restricts unwanted harmonic current injections. It also estimates the frequency which is important for sequence extraction. However, in weak grids, a slow PLL works fine for the stability of the system but the speed of PLL may cause some inaccuracy especially in post fault scenarios. To address this problem, the

reference currents can be adjusted based on the actual v_{dq} components of the positive sequence. The expressions for this adjustment are given in equation (3.68).

$$\begin{bmatrix} i_{dp,adj}^* \\ i_{qp,adj}^* \end{bmatrix} = \frac{1}{|v_p|} \begin{bmatrix} i_{dp}^* & -i_{qp}^* \\ i_{qp}^* & i_{dp}^* \end{bmatrix} \begin{bmatrix} v_{dp} \\ v_{qp} \end{bmatrix} \quad (3.68)$$

Where the subscript ‘adj’ represents the adjusted parameters. The current components are adjusted to consider the PLL error while deciding the reference currents. A hybrid reference current calculation scheme works well for the GFL, and scholar discussed its performance in [114-116].

3.4.5 Current Limitation and Priority

Due to the limited current handling capability of the converter, it is important to limit the line currents especially in case of faults which may result in very high currents. The negative sequence current injection makes the current limitation difficult due to the elliptical trajectory of the resultant current phasor. The resultant current phasor along with positive and negative sequence components is shown in Figure 3.34.

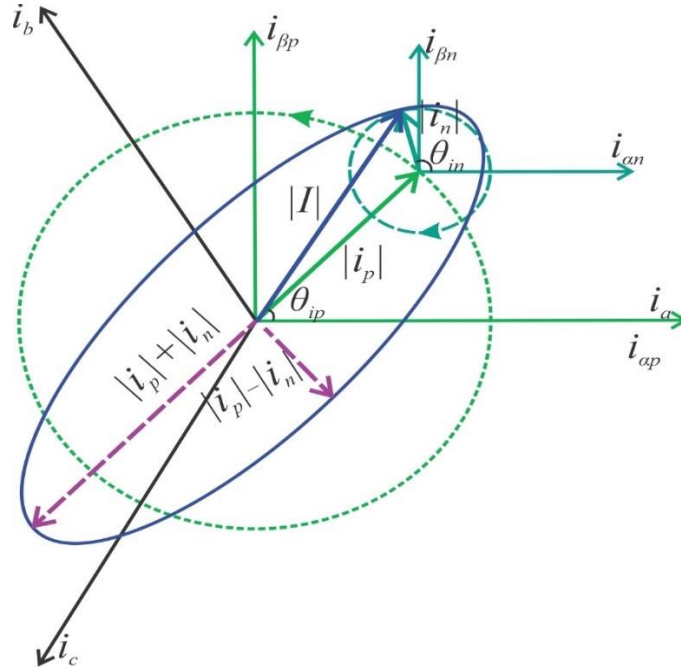


Figure 3.34: Current phasors in unbalanced conditions

3.4.5.1 Priority Schemes

In normal operating conditions, the active current component should be prioritized as the prime target of these converter-based sources is to inject the active power into the power system. In faulty conditions, the reference currents are very high and due to the limited current handling capability of the converters, the reference current components need to be prioritized to ensure the desired response from the converter while ensuring its current limit. These priority injection schemes are essential in case of unbalanced conditions as the four reference current components (two for each sequence) need to be

decided. In faulty situations, the selective voltage support is demanded by the grid operators so the positive and negative sequence reactive current injections should be prioritized over the active current component injections.

For the faulty conditions, the scholar discussed three priority injection schemes in [115] named NQP, QNP and balanced current injection with i_q -priority (BCI). The NQP priority scheme prioritizes the negative sequence reactive current component then the positive sequence reactive current component and the least priority is associated with the positive sequence active current component. Similarly, QNP scheme prioritizes the reactive current component in positive sequence followed by reactive current in the negative sequence and then the active current component in the positive sequence. The BCI scheme provides the uniform voltage support to each phase irrespective of the fault type and prioritizes the reactive current in positive sequence followed by the active current component in the positive sequence. These priority schemes don't consider the active current in the negative sequence as it is not demanded by the grid codes. The performance comparison of these schemes under different faulty conditions is discussed in [115].

It is important to mention here that these priority injection schemes change the current distributions in both the sequences to ensure the current limit of the converter. The other schemes can also be developed which only reduce the magnitude of the current phasor without changing its distribution. However, due to the presence of the positive and negative sequence current components, the priority needs to be decided. Two more priority schemes are discussed at the end of this section in which one scheme prioritizes the positive sequence current phasor's magnitude and represented by $|i_p|$ whereas the other scheme prioritizes the negative sequence current phasor's magnitude and represented by $|i_n|$. The last two scheme only limits the magnitude of the sequence current phasors, but their distribution is not changed.

3.4.5.2 Current Limitation Schemes

In this section, the general expressions for each current limiting scheme will be discussed for different priority schemes. The active current component in the negative sequence is ignored as the grid codes do not demand to inject the active current component in the negative sequence. The expression for the BCI scheme can be derived from the general governing expression for the current limiting scheme. The expressions for the $|i_p|$ and $|i_n|$ schemes will only be discussed for the conventional current limiting scheme and for the detailed sequence vector summation (DSVS) based current limiting scheme.

Conventional Current Limiting Scheme

The conventional current limitation scheme is based on the numeric addition of the positive and negative sequence current phasors. It ensures that the extreme points of elliptical trajectory should not exceed

the maximum current limit of the converter. The mathematical expression for the conventional current limiting scheme is given below.

$$i_{\max} = |i_p| + |i_n| = \sqrt{i_{dp}^2 + i_{qp}^2} + \sqrt{i_{dn}^2 + i_{qn}^2} \quad (3.69)$$

By using equation (3.69), the priority to individual current components can be assigned. For NQP priority, the equation (3.69) is solved for i_{qn} considering the other current components to be zero. This results in the limit for the i_{qn} . To find the limit for i_{qp} , the equation (3.69) is solved for i_{qp} having all other current components to be zero except the i_{qn} which is its referenced value after applying its limit. Similarly, the limit for i_{dp} is estimated by the same equation but this time, the i_{qn} and i_{qp} are the actual referenced values after passing through their respective limits. The expressions for the NQP priority scheme on the conventional current limiting scheme are given below.

$$\begin{aligned} \therefore i_x^{**} &= \text{sign}(i_x^*) \min(|i_x^*|, i_x^{\text{lim}}) \\ \begin{cases} i_{qn}^{\text{lim}} &= i_{\max} \\ i_{qp}^{\text{lim}} &= i_{\max} - |i_{qn}^{**}| \\ i_{dp}^{\text{lim}} &= \sqrt{(i_{\max} - |i_{qn}^{**}|)^2 - (i_{qp}^{**})^2} \end{cases} \end{aligned} \quad (3.70)$$

The same procedure can be repeated to calculate current limits for QNP priority. The derived expressions for the QNP for the conventional current limiting scheme are given below.

$$\begin{aligned} \therefore i_x^{**} &= \text{sign}(i_x^*) \min(|i_x^*|, i_x^{\text{lim}}) \\ \begin{cases} i_{qp}^{\text{lim}} &= i_{\max} \\ i_{qn}^{\text{lim}} &= i_{\max} - |i_{qp}^{**}| \\ i_{dp}^{\text{lim}} &= \sqrt{(i_{\max} - |i_{qn}^{**}|)^2 - (i_{qp}^{**})^2} \end{cases} \end{aligned} \quad (3.71)$$

For the $|i_p|$ priority scheme, the full converter's current capacity is assigned to the positive sequence current magnitude. After applying the limit on the reference positive sequence current's magnitude and subtracted it from the maximum current capacity of the converter, the remaining capacity is assigned to the limit for $|i_n|$. For the conventional current limiting scheme, the expressions for the $|i_p|$ priority scheme are given below.

$$\begin{aligned} \therefore i_x^{**} &= \text{sign}(i_x^*) \min(|i_x^*|, i_x^{\text{lim}}) \\ \begin{cases} |i_p|^{\text{lim}} &= i_{\max} \\ |i_n|^{\text{lim}} &= i_{\max} - |i_p|^{\text{lim}} \end{cases} \end{aligned} \quad (3.72)$$

Similarly, the expressions for the $|i_n|$ priority with the conventional current limiting scheme are given below.

$$\begin{aligned} \therefore i_x^{**} &= \text{sign}(i_x^*) \min(|i_x^*|, i_x^{\text{lim}}) \\ \begin{cases} |i_n|^{\text{lim}} = i_{\text{max}} \\ |i_p|^{\text{lim}} = i_{\text{max}} - |i_n|^{**} \end{cases} \end{aligned} \quad (3.73)$$

Component-wise Sequence Numeric Summation Scheme

The scholar presented an alternative current limiting scheme in [113]. This scheme considers respective active and reactive current components of the positive and negative sequences in-phase with each other. This technique is termed as component-wise sequence numeric summation (CSNS) in this thesis. The governing equation for this scheme along with the individual limits for NQP priority are given in equation (3.74).

$$\begin{aligned} i_{\text{max}} &= \sqrt{(i_{dp}^* + i_{dn}^*)^2 + (i_{qp}^* + i_{qn}^*)^2} \\ \therefore i_x^{**} &= \text{sign}(i_x^*) \min(|i_x^*|, i_x^{\text{lim}}) \\ \begin{cases} i_{qn}^{\text{lim}} = i_{\text{max}} \\ i_{qp}^{\text{lim}} = i_{\text{max}} - |i_{qn}^{**}| \\ i_{dp}^{\text{lim}} = \sqrt{(i_{\text{max}})^2 - (i_{qp}^{**} + i_{qn}^{**})^2} \end{cases} \end{aligned} \quad (3.74)$$

Following the same procedure, the expressions for the QNP priority scheme for the CSNS current limiting scheme are given below.

$$\begin{aligned} i_{\text{max}} &= \sqrt{(i_{dp}^* + i_{dn}^*)^2 + (i_{qp}^* + i_{qn}^*)^2} \\ \therefore i_x^{**} &= \text{sign}(i_x^*) \min(|i_x^*|, i_x^{\text{lim}}) \\ \begin{cases} i_{qp}^{\text{lim}} = i_{\text{max}} \\ i_{qn}^{\text{lim}} = i_{\text{max}} - |i_{qp}^{**}| \\ i_{dp}^{\text{lim}} = \sqrt{(i_{\text{max}})^2 - (i_{qp}^{**} + i_{qn}^{**})^2} \end{cases} \end{aligned} \quad (3.75)$$

Both the conventional and CSNS techniques are simplified techniques and do not consider the angle between the positive and negative sequence current phasors. These techniques ensure that none of the line currents exceed the current limit, but they do not ensure the maximum utilization of the converter as none of the line current approaches the current limit.

Simplified Sequence Vector Summation Scheme

To enhance the utilization of the current capacity of the converter in faulty situations, the scholar presented another scheme in [115] which offers better utilization of the converter's current limit. This scheme is termed as simplified sequence vector summation (SSVS) in this thesis. The final expression for this technique is given in equation (3.76). The derivation of this expression can be found in appendix L.

$$\begin{aligned} |i|^2 &= |i_p|^2 + |i_n|^2 + 2(i_{dp}i_{dn} + i_{qp}i_{qn})\cos(\delta(t)) + 2(i_{dp}i_{qn} - i_{qp}i_{dn})\sin(\delta(t)) \\ \therefore \delta(t) &= 2\omega t + \theta_{vp} + \theta_{vn} \end{aligned} \quad (3.76)$$

As there is no grid code requirement for the active current component injection in the negative sequence, hence, the above expression can be simplified by putting i_{dn} equal to zero. The simplified expression is given in equation (3.77).

$$\begin{aligned} |i|^2 &= |i_p|^2 + |i_n|^2 + 2i_{qn} \{i_{qp} \cos(\delta(t)) + i_{dp} \sin(\delta(t))\} \\ \therefore \delta(t) &= 2\omega t + \theta_{vp} + \theta_{vn} \end{aligned} \quad (3.77)$$

The above equation shows that the magnitude of the resultant current phasor is the function of time, and it also depends on the angle between the positive and negative sequence voltage phasors. The cosine term in the above expression is taken as unity (maximum) for computing the limit for i_{qp} . Similarly, for computing the limit for i_{dp} , the sine term is maximized. The cosine term is critical for computing i_{dp} . If it is taken as zero then the maximum line current may go above the current limit but if it is taken as unity, then it results in conventional current limiting scheme. To improve the utilization of the current capacity of the converter, the cosine term is taken as $\frac{1}{4}$. The current components' limits for different current components for NQP priority injection with SSVS current limiting scheme are given in equation (3.78).

$$\begin{aligned} \therefore i_x^{**} &= \text{sign}(i_x^*) \min(|i_x^*|, i_x^{\text{lim}}) \\ i_{qn}^{\text{lim}} &= i_{\text{max}} \\ i_{qp}^{\text{lim}} &= i_{\text{max}} - |i_{qn}^{**}| \\ i_{dp}^{\text{lim}} &= \sqrt{(i_{\text{max}})^2 - (i_{qp}^{**})^2 - \frac{|i_{qp}^{**}||i_{qn}^{**}|}{2}} - |i_{qn}^{**}| \end{aligned} \quad (3.78)$$

The expressions for the QNP priority are given below.

$$\begin{aligned} \therefore i_x^{**} &= \text{sign}(i_x^*) \min(|i_x^*|, i_x^{\text{lim}}) \\ i_{qp}^{\text{lim}} &= i_{\text{max}} \\ i_{qn}^{\text{lim}} &= i_{\text{max}} - |i_{qp}^{**}| \\ i_{dp}^{\text{lim}} &= \sqrt{(i_{\text{max}})^2 - (i_{qp}^{**})^2 - \frac{|i_{qp}^{**}||i_{qn}^{**}|}{2}} - |i_{qn}^{**}| \end{aligned} \quad (3.79)$$

As the SSVS scheme does not use the information of true angle between the positive and negative sequence current phasors, it can't guarantee the full utilization of the current capacity of the converter.

Detailed Sequence Vector Summation Scheme

The last proposed scheme is based on the limitation of the per phase peak current. This scheme is termed as detailed sequence vector summation (DSVS). The expression for the per-phase peak current is developed in terms of magnitude of the positive and negative sequence current phasors and the angle between the positive and negative sequence voltage phasors. The graphical explanation of this scheme is given in Figure 3.35.

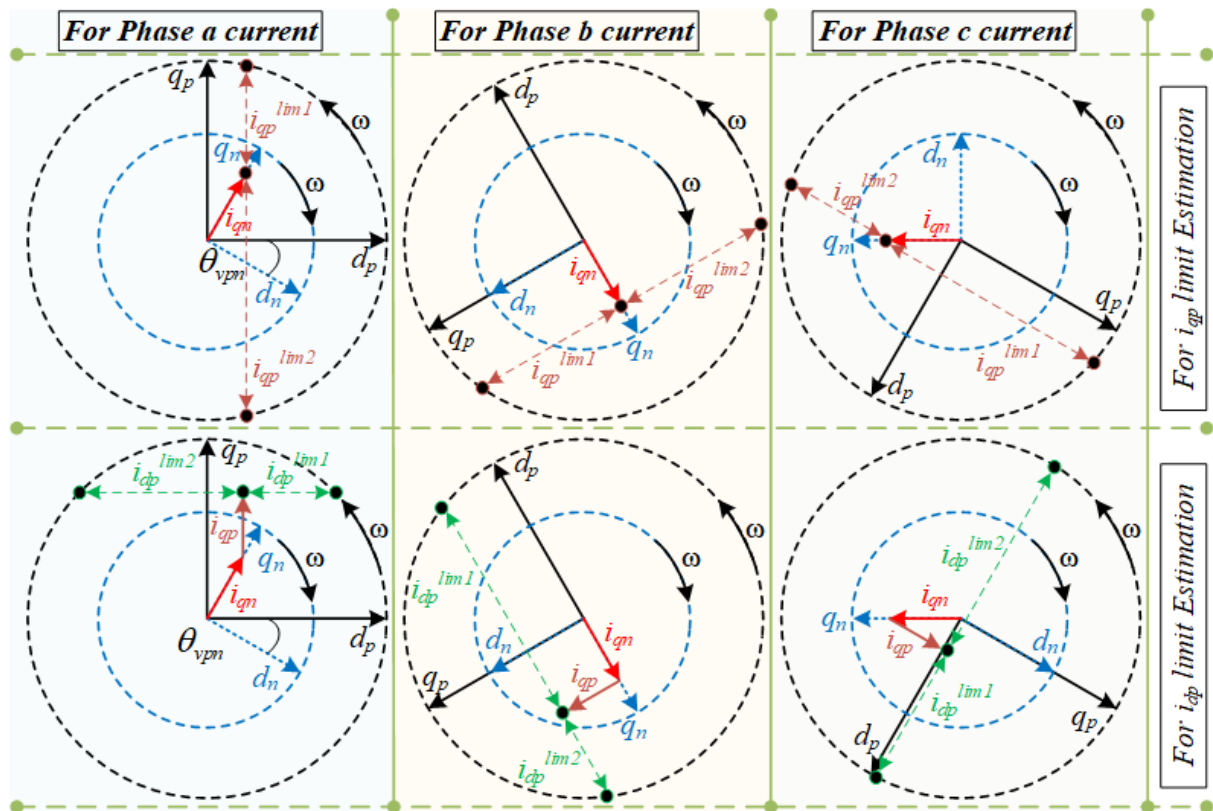


Figure 3.35: Graphical explanation of different current limits for DSVS scheme

Figure 3.35 shows that all the phase currents result in different current limits for the i_{qp} and to ensure that no phase current should exceed the current limit, the minimum of all the possible values should be used. In such cases, the resultant current phasor remains within the current limit. The same is also true while deciding the limit for the i_{dp} .

To derive the mathematical expressions for the DSVS scheme, the resultant current in $\alpha\beta$ frame can be written as the vector sum of the positive and negative sequence current phasors.

$$\begin{aligned}
 i_{\alpha\beta} &= |i_p| e^{j(\omega t + \theta_{vp} + \theta_p)} + |i_n| e^{-j(\omega t + \theta_{vn} - \theta_n)} \\
 \therefore \begin{cases} i_{dq,p} = |i_p| e^{j\theta_p} \\ i_{dq,n} = |i_n| e^{j\theta_n} \end{cases} & \quad (3.80) \\
 i_{\alpha\beta} &= i_{dq,p} e^{j(\omega t + \theta_{vp})} + i_{dq,n} e^{-j(\omega t + \theta_{vn})}
 \end{aligned}$$

By using the equation (3.14) and (3.80), the expression for the phase current can be derived. The derivation for phase current expressions is discussed in appendix M. The expressions for each phase current are given in (3.81).

$$\begin{aligned}
 i_{abc}(t) &= \frac{A}{2} \cos(\omega t) + \frac{B}{2} \sin(\omega t) \\
 A &= \begin{bmatrix} 2i_{dp} & -2i_{qp} & 2i_{dn} & 2i_{qn} \\ (\sqrt{3}i_{qp} - i_{dp}) & (\sqrt{3}i_{dp} + i_{qp}) & (\sqrt{3}i_{qn} - i_{dn}) & -(\sqrt{3}i_{dn} + i_{qn}) \\ -(\sqrt{3}i_{qp} + i_{dp}) & -(\sqrt{3}i_{dp} - i_{qp}) & -(\sqrt{3}i_{qn} + i_{dn}) & (\sqrt{3}i_{dn} - i_{qn}) \end{bmatrix} \begin{bmatrix} \cos \theta_{vp} \\ \sin \theta_{vp} \\ \cos \theta_{vn} \\ \sin \theta_{vn} \end{bmatrix} \\
 B &= \begin{bmatrix} -2i_{qp} & -2i_{dp} & 2i_{qn} & -2i_{dn} \\ (\sqrt{3}i_{dp} + i_{qp}) & -(\sqrt{3}i_{qp} - i_{dp}) & -(\sqrt{3}i_{dn} + i_{qn}) & -(\sqrt{3}i_{qn} - i_{dn}) \\ -(\sqrt{3}i_{dp} - i_{qp}) & (\sqrt{3}i_{qp} + i_{dp}) & (\sqrt{3}i_{dn} - i_{qn}) & (\sqrt{3}i_{qn} + i_{dn}) \end{bmatrix} \begin{bmatrix} \cos \theta_{vp} \\ \sin \theta_{vp} \\ \cos \theta_{vn} \\ \sin \theta_{vn} \end{bmatrix}
 \end{aligned} \quad (3.81)$$

The mathematical expression for the amplitude of each phase current can be derived from equation (3.81).

$$\begin{aligned}
 \begin{bmatrix} |i_a(t)| \\ |i_b(t)| \\ |i_c(t)| \end{bmatrix} &= \sqrt{(i_{dp}^2 + i_{qp}^2) + (i_{dn}^2 + i_{qn}^2) + x(i_{dp}i_{dn} - i_{qp}i_{qn}) + y(i_{dp}i_{qn} + i_{qp}i_{dn})} \\
 \therefore \theta_{vpn} &= \theta_{vp} - \theta_{vn} \\
 x &= \begin{bmatrix} 2 & 0 \\ -1 & -\sqrt{3} \\ -1 & \sqrt{3} \end{bmatrix} \begin{bmatrix} \cos(\theta_{vpn}) \\ \sin(\theta_{vpn}) \end{bmatrix}; y = \begin{bmatrix} 0 & -2 \\ -\sqrt{3} & 1 \\ \sqrt{3} & 1 \end{bmatrix} \begin{bmatrix} \cos(\theta_{vpn}) \\ \sin(\theta_{vpn}) \end{bmatrix}
 \end{aligned} \quad (3.82)$$

In NQP priority scheme, the maximum current limit is assigned to i_{qn} . Equation (3.82) is solved separately for each phase to compute the limit for the i_{qp} (ignoring the i_{dp}). Due to quadratic equation for i_{qp} , each phase solution results in two values for the i_{qp} and solving three equations results in total six possible values for i_{qp} . The minimum of these calculated values is assigned as limit for the i_{qp} . The expression for the limit of i_{qp} is given in equation (3.83).

$$\begin{aligned}
 \begin{bmatrix} i_{qp,a}^{\lim} \\ i_{qp,b}^{\lim} \\ i_{qp,c}^{\lim} \end{bmatrix} &= \frac{1}{2} \left\{ x i_{qn} \pm \sqrt{4 i_{\max}^2 - i_{qn}^2 (4 - x^2)} \right\} \\
 x &= \begin{bmatrix} 2 & 0 \\ -1 & -\sqrt{3} \\ -1 & \sqrt{3} \end{bmatrix} \begin{bmatrix} \cos(\theta_{vpn}) \\ \sin(\theta_{vpn}) \end{bmatrix}; y = \begin{bmatrix} 0 & -2 \\ -\sqrt{3} & 1 \\ \sqrt{3} & 1 \end{bmatrix} \begin{bmatrix} \cos(\theta_{vpn}) \\ \sin(\theta_{vpn}) \end{bmatrix} \\
 i_{qp}^{\lim} &= \min(|i_{qp,a}^{\lim}|, |i_{qp,b}^{\lim}|, |i_{qp,c}^{\lim}|)
 \end{aligned} \tag{3.83}$$

Finally, the same set of equations are solved for the i_{dp} , and the minimum of the calculated values is assigned as the limit for the i_{dp} . In this way, the maximum utilization of the converter's current capacity is ensured without exceeding the current in any phase beyond its capacity. The expression for the limit of i_{qp} is given below.

$$\begin{aligned}
 \begin{bmatrix} i_{dp,a}^{\lim} \\ i_{dp,b}^{\lim} \\ i_{dp,c}^{\lim} \end{bmatrix} &= \frac{1}{2} \left\{ -y i_{qn} \pm \sqrt{4 (i_{\max}^2 - i_{qp}^2 + i_{qp} i_{qn} x) - i_{qn}^2 (4 - y^2)} \right\} \\
 x &= \begin{bmatrix} 2 & 0 \\ -1 & -\sqrt{3} \\ -1 & \sqrt{3} \end{bmatrix} \begin{bmatrix} \cos(\theta_{vpn}) \\ \sin(\theta_{vpn}) \end{bmatrix}; y = \begin{bmatrix} 0 & -2 \\ -\sqrt{3} & 1 \\ \sqrt{3} & 1 \end{bmatrix} \begin{bmatrix} \cos(\theta_{vpn}) \\ \sin(\theta_{vpn}) \end{bmatrix} \\
 i_{dp}^{\lim} &= \min(|i_{dp,a}^{\lim}|, |i_{dp,b}^{\lim}|, |i_{dp,c}^{\lim}|)
 \end{aligned} \tag{3.84}$$

By using the same procedure, the expressions for the QNP priority can be derived for the DSVS current limit scheme. These expressions are given below.

$$\begin{aligned}
 i_{qp} &= i_{\max} \\
 \begin{bmatrix} i_{qn,a}^{\lim} \\ i_{qn,b}^{\lim} \\ i_{qn,c}^{\lim} \end{bmatrix} &= \frac{1}{2} \left\{ x i_{qp} \pm \sqrt{4 i_{\max}^2 - i_{qp}^2 (4 - x^2)} \right\} \\
 i_{qn}^{\lim} &= \min(|i_{qn,a}^{\lim}|, |i_{qn,b}^{\lim}|, |i_{qn,c}^{\lim}|) \\
 \begin{bmatrix} i_{dp,a}^{\lim} \\ i_{dp,b}^{\lim} \\ i_{dp,c}^{\lim} \end{bmatrix} &= \frac{1}{2} \left\{ -y i_{qn} \pm \sqrt{4 (i_{\max}^2 - i_{qp}^2 + i_{qp} i_{qn} x) - i_{qn}^2 (4 - y^2)} \right\} \\
 i_{dp}^{\lim} &= \min(|i_{dp,a}^{\lim}|, |i_{dp,b}^{\lim}|, |i_{dp,c}^{\lim}|) \\
 x &= \begin{bmatrix} 2 & 0 \\ -1 & -\sqrt{3} \\ -1 & \sqrt{3} \end{bmatrix} \begin{bmatrix} \cos(\theta_{vpn}) \\ \sin(\theta_{vpn}) \end{bmatrix}; y = \begin{bmatrix} 0 & -2 \\ -\sqrt{3} & 1 \\ \sqrt{3} & 1 \end{bmatrix} \begin{bmatrix} \cos(\theta_{vpn}) \\ \sin(\theta_{vpn}) \end{bmatrix}
 \end{aligned} \tag{3.85}$$

By prioritizing the individual current components, the angle of the current phasor is changed. In some scenarios, the current angle needs to be preserved and only the magnitude of the current phasors is

limited. For such scenarios, the conventional current limitation scheme is easy to implement. The rest of the schemes can be modified to prioritize the current phasors instead of their individual components. The governing expression for the DSVS scheme is given in equation (3.86) for phasor priority.

$$\begin{aligned} \begin{bmatrix} |i_a(t)| \\ |i_b(t)| \\ |i_c(t)| \end{bmatrix} &= \sqrt{|i_p|^2 + |i_n|^2 + |i_p||i_n|\{x \cos(\theta_{ip} + \theta_{in}) + y \sin(\theta_{ip} + \theta_{in})\}} \\ x &= \begin{bmatrix} 2 & 0 \\ -1 & -\sqrt{3} \\ -1 & \sqrt{3} \end{bmatrix} \begin{bmatrix} \cos(\theta_{vpn}) \\ \sin(\theta_{vpn}) \end{bmatrix}; y = \begin{bmatrix} 0 & -2 \\ -\sqrt{3} & 1 \\ \sqrt{3} & 1 \end{bmatrix} \begin{bmatrix} \cos(\theta_{vpn}) \\ \sin(\theta_{vpn}) \end{bmatrix} \end{aligned} \quad (3.86)$$

Where ' θ_i ' is the initial angle for the respective current phasor. If negative sequence phasor is prioritized, then the expressions for the phasor limits are given in equation (3.87).

$$\begin{aligned} |i_n|^{\lim} &= i_{\max} \\ \begin{bmatrix} i_{p,a}^{\lim} \\ i_{p,b}^{\lim} \\ i_{p,c}^{\lim} \end{bmatrix} &= \frac{1}{2} \left\{ -A|i_n| \pm \sqrt{4i_{\max}^2 - |i_n|^2(4 - A^2)} \right\} \\ \therefore A &= x \cos(\theta_{ip} + \theta_{in}) + y \sin(\theta_{ip} + \theta_{in}) \\ x &= \begin{bmatrix} 2 & 0 \\ -1 & -\sqrt{3} \\ -1 & \sqrt{3} \end{bmatrix} \begin{bmatrix} \cos(\theta_{vpn}) \\ \sin(\theta_{vpn}) \end{bmatrix}; y = \begin{bmatrix} 0 & -2 \\ -\sqrt{3} & 1 \\ \sqrt{3} & 1 \end{bmatrix} \begin{bmatrix} \cos(\theta_{vpn}) \\ \sin(\theta_{vpn}) \end{bmatrix} \\ |i_p|^{\lim} &= \min(|i_{p,a}^{\lim}|, |i_{p,b}^{\lim}|, |i_{p,c}^{\lim}|) \end{aligned} \quad (3.87)$$

3.4.5.3 Performance Comparison of Current Limitation Schemes

The performance comparison of these current limiting schemes for NQP priority is discussed in Table 3.9. The maximum phase current is assumed to be 1.2 p.u. The limits for different current components are computed with each discussed scheme. For simplicity, i_{dn} is assumed to be zero. The right most column states the maximum phase current achieved with each of the current limiting schemes. The angle between positive and negative sequence voltage phasors is changed from 0° to 90° with the step of 30° . For other angles, only the maximum current is shifted from one phase to the other phase. The reference current components without current limitation are given below.

$$i_{dp}^* = 1.58; i_{qp}^* = -0.8; i_{qn}^* = -0.6 \quad (3.88)$$

Table 3.9: Performance comparison of different current limiting schemes for NQP

$\theta_{vp}-\theta_{vn}$ Deg.	DSVS $[i_{dp}^{\lim}, i_{qp}^{\lim}, i_{qn}^{\lim}]$	SSVS	CSNS	Conventional	I_{\max} Phase [DSVS, SSVS, CSNS, Conv.]
0	$[\approx 0, 0.782, 1.2]$	$i_{dp}^{\lim} = 0.35$	$i_{dp}^{\lim} = 0.0$	$i_{dp}^{\lim} = 0.0$	$[1.2, 1.25, 1.04, 1.04]$
30	$[\approx 0, 0.640, 1.2]$	$i_{qp}^{\lim} = 0.60$	$i_{qp}^{\lim} = 0.6$	$i_{qp}^{\lim} = 0.6$	$[1.2, 1.29, 1.15, 1.15]$
60	$[\approx 0, 0.600, 1.2]$	$i_{qn}^{\lim} = 1.20$	$i_{qn}^{\lim} = 1.2$	$i_{qn}^{\lim} = 1.2$	$[1.2, 1.25, 1.20, 1.20]$

90	$[\approx 0, 0.640, 1.2]$	$[1.2, 1.12, 1.15, 1.15]$
-----------	---------------------------	---------------------------

Table 3.9 shows that DSVS scheme offers the maximum utilization of the converter’s current rating while the rest of the schemes underutilize the converter. As the SSVS scheme does not use the true angle difference between positive and negative sequence voltage phasors, thus it can’t ensure the exact current limit of the converter and based on the actual angle, this scheme may result in 10 % over current. Moreover, the DSVS provides a higher limit for the reactive current, but the other schemes result in a lower limit for i_{qp} .

The DSVS and the conventional current limiting schemes are also compared for the $|i_n|$ priority. The other conditions are the same as for the NQP scheme comparison. The results are presented in Table 3.10.

Table 3.10: Performance comparison of conventional and DSVS current limiting schemes for phasor priority

$\theta_{vp}-\theta_{vn}$ Deg.	DSVS $[i_p^{lim}, i_n^{lim}]$	Conventional $[i_p^{lim}, i_n^{lim}]$	I_{max} Phase [DSVS, Conv.]
0	$[\approx 0.60, 1.2]$		$[1.2, 1.19]$
30	$[\approx 0.65, 1.2]$		$[1.2, 1.15]$
60	$[\approx 0.76, 1.2]$	$[0.6, 1.2]$	$[1.2, 1.05]$
90	$[\approx 0.64, 1.2]$		$[1.2, 1.16]$

Table 3.10 shows that the DSVS provides better results as compared to the conventional scheme for the phasor priority schemes. The performance difference between two schemes is highly dependent on the angle between the positive and negative sequence voltage phasors which is influenced by the type of fault, fault impedance and the short circuit power of the grid at POC. Moreover, the sequence extraction scheme may cause some inaccuracy in the assessment of the angle between the sequence voltage phasors. Hence, it is easy to use the conventional scheme, but it can’t guarantee the maximum utilization of the converter’s current capacity.

3.4.6 Inner Current Controller

The selection of the inner current controller depends on the reference frame for the measured and reference currents. In dq-frame, a PI controller can be used as inner current controller, and its detailed tuning is discussed in section 3.3.4. The PI controller introduces a static error for the sinusoidal input and is not recommended for $\alpha\beta$ -frame. In such cases, a proportional resonant (PR) controller can be used to control the currents. The block diagram on a PR controller is given in Figure 3.36.

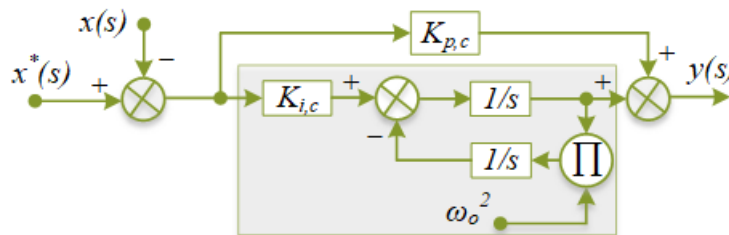


Figure 3.36: Layout for PR controller

The shaded area represents the resonant part which integrates the amplitude of input signal at resonant frequency (ω_0). Transfer function for the PR controller in Laplace domain is given in equation (3.89).

$$H_{PR}(s) = K_{p,c} + \frac{K_{i,c}s}{s^2 + \omega_0^2} \tag{3.89}$$

$$|H_{PR}(j\omega)| = \frac{1}{\omega_0^2 - \omega^2} \sqrt{K_{p,c}^2 (\omega_0^2 - \omega^2)^2 + (\omega K_{i,c})^2}$$

The above expression confirms a very huge gain near the resonant frequency. The resonant frequency is normally the same as the grid frequency which can be assessed with the help of PLL for the positive sequence voltage phasor. The advanced form of PR controller is the quasi-proportional resonant controller (QPR) which considers the offset in the frequency assessment. The block diagram for QPR is given in Figure 3.37.

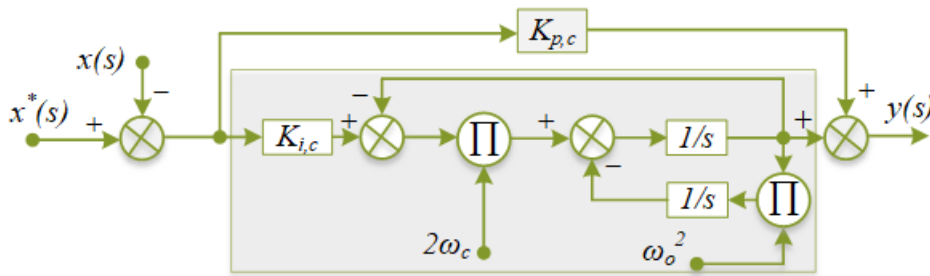


Figure 3.37: Block diagram for QPR

ω_c is the bandwidth frequency. It offers maximum gain at ω_0 . The transfer function for the PR controller in Laplace domain is given in equation (3.90).

$$H_{QPR}(s) = K_{p,c} + \frac{2\omega_c K_{i,c}s}{s^2 + 2\omega_c s + \omega_0^2} \tag{3.90}$$

The bode plots for both the PR and QPR are given in Figure 3.38 and Figure 3.39 respectively. The bandwidth for QPR is selected as 10 Hz. The proportional and integral gains are selected as unity for the following figures.

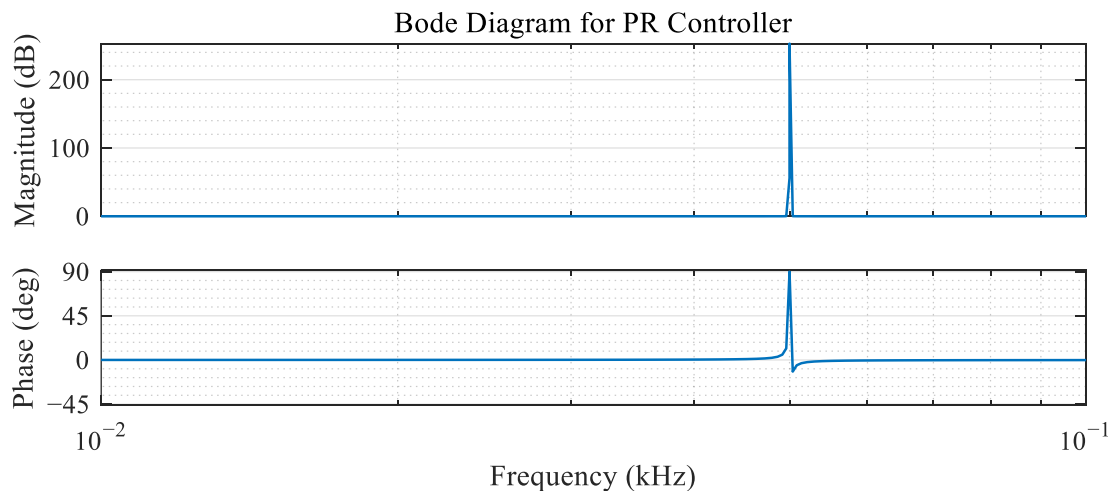


Figure 3.38: Bode-diagram for PR controller

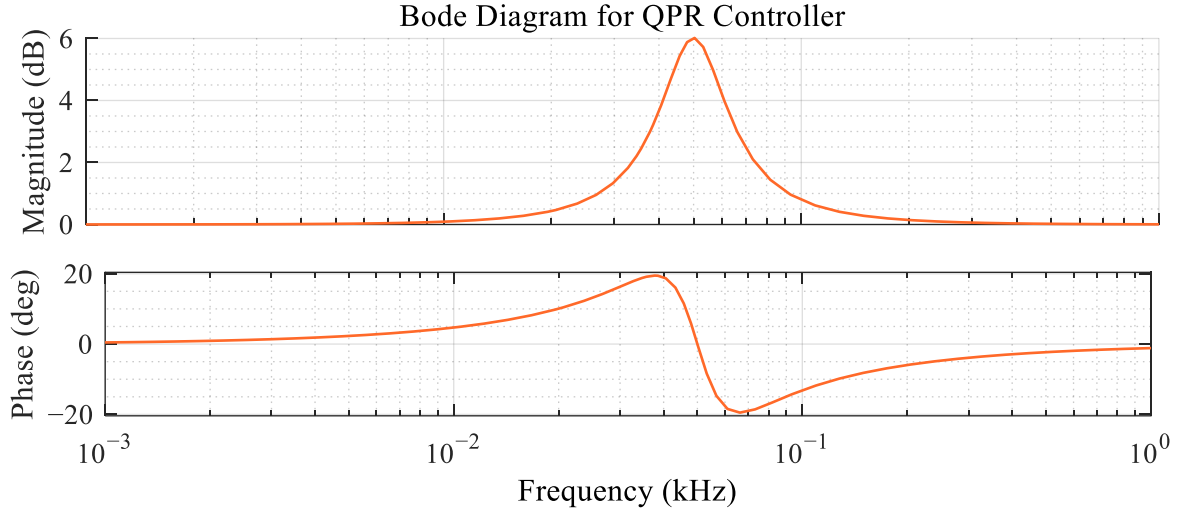


Figure 3.39: Bode-diagram for QPR controller

The above figures confirm that the resonant peak for the QPR is less as compared to PR controller, but it is widened which makes it suitable to address the frequency offset. In [93], the authors discussed the tuning of the QPR controller as inner current and outer voltage controller. The expressions for the proportional and integral gains are expressed in terms of the filter parameter and the desired cutoff frequency of the controller. The expressions for the QPR gains are given in equation (3.91).

$$\begin{aligned}
 K_{p,c} &= \sqrt{(\omega_i L_1)^2 + R_1^2} \\
 K_{i,c} &= \frac{\sqrt{(\omega_0 L_1)^2 + R_1^2}}{2Q} (H_{OL}^{cc} |j\omega_0| - 1)
 \end{aligned} \tag{3.91}$$

Where Q denotes the quality factor and ω_i represents the bandwidth for the inner current controller. Moreover, superscript 'cc' and subscript 'c' stand for current controller. The tuning parameters for the QPR controller with the cutoff frequency of 10 Hz, are given in Table 3.11. For the tuning, the bandwidth frequency is selected as 9 times of the grid frequency. The inductance is discussed in LCL filter, and the resistance is chosen as 5 % of the reactance on the converter's side. The series resistance has no negative effect on the performance of the LCL filter.

Table 3.11: Parameter tuning for QPR inner current controller

<i>Given</i>	$\omega_0 L_1$ (p.u)	R_1 (p.u)	Q	f_g (Hz)	ω_c (rad/sec)	ω_i (rad/sec)
<i>Parameters</i>	0.105	0.005	$2\pi \times 50$	50	$2\pi \times 10$	$2\pi \times 450$
<i>Derived</i>	$K_{p,c}$		$K_{i,c}$			
<i>Parameters</i>	0.945		0.167			

The performance of the above designed QPR current controller is given in Figure 3.40.

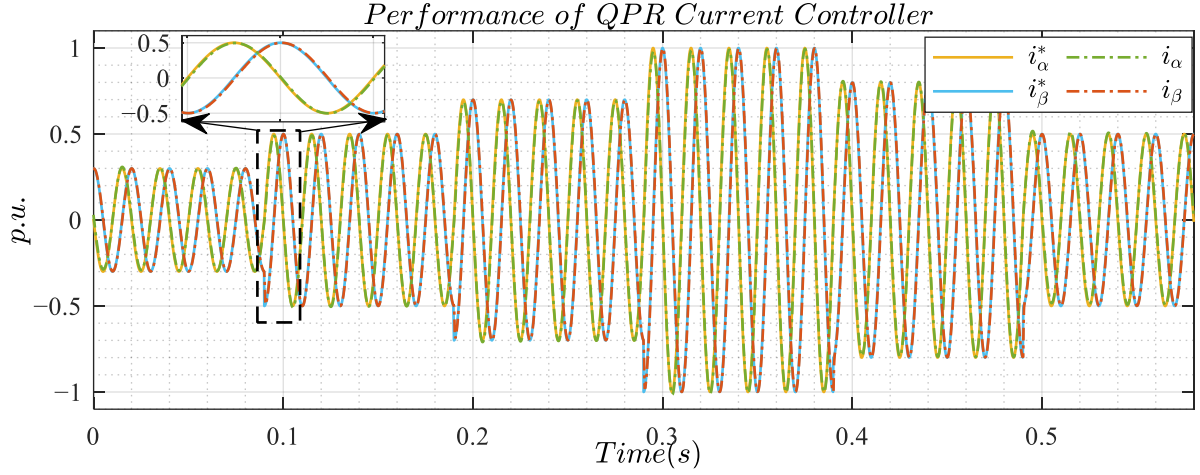


Figure 3.40: Performance of QPR current controller

The above figure shows the performance of QPR as a current controller in $\alpha\beta$ -frame. The controller is able to achieve the reference current and the error between measured and reference current is quite negligible. The other method for the QPR parameter tuning is the equivalent PI controller in the dq reference frame. The proportional and integral gains are the same if both the controllers work fine in their respective frames. By using equation (3.38) and (3.39), the expressions for the proportional and integral gains can be presented in the form of damping. The expressions for the parameter tuning are given below.

$$K_{p,c} = \frac{L_1}{6T_s\zeta^2}; K_{i,c} = \frac{R_1}{L_1}K_{p,c} \quad (3.92)$$

Where ζ represents the damping constant. The tuning parameters for the QPR controller with the damping method, are given in Table 3.12.

Table 3.12: Parameter tuning for QPR inner current controller with damping method

<i>Given Parameters</i>	ζ	L_1 (p.u)	R_1 (p.u)	T_s (s)
	0.707	0.0655	0.0033	1×10^{-4}
<i>Derived Parameters</i>	$K_{p,c}$		$K_{i,c}$	
	0.695		10.92	

3.5 Performance Analysis of Improved GFL Control Scheme

The improved control scheme is developed in Simulink and its response under different operating conditions is observed. The general layout of the setup is same as given in Figure 3.2. The block diagram of the improved control scheme is given in Figure 3.41.

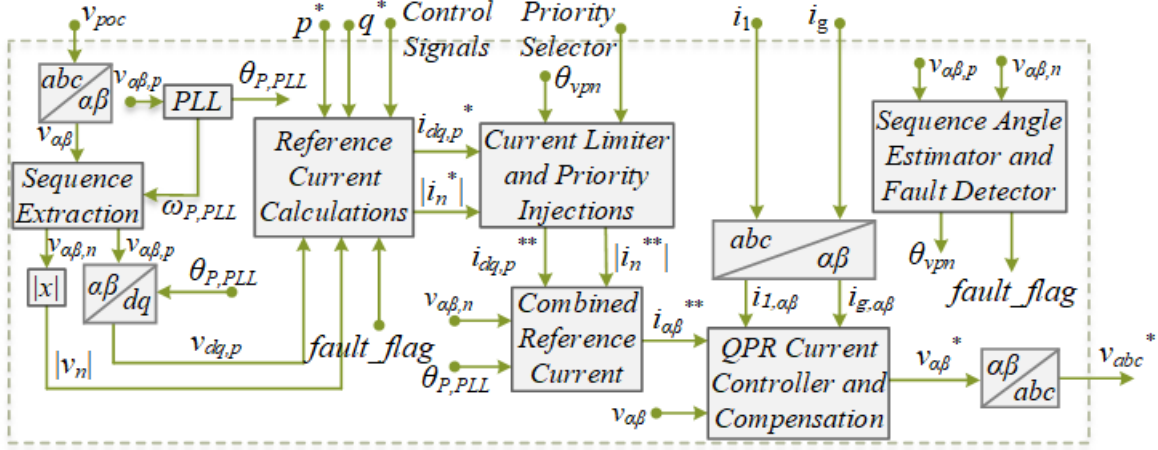


Figure 3.41: General layout of the improved GFL control scheme

To enhance the stability of the control scheme, the rate of change in reference active current component is limited to 1 p.u./sec. The key parameters for the setup are given in Table 3.13.

Table 3.13: Parameters for the test setup of Improved GFL converter

Grid Parameters					
Voltage (L-L) (V)	f_g (Hz)	SCP (kVA)	X/R		
400	50	800	5		
Coupling Transformer					
Type	Voltage (V)	Rated Power (kVA)	Reactance (p.u.)	Resistance (p.u.)	
Y- Δ	400/260	200	0.03	6×10^{-4}	
LCL Filter					
L_1 (mH)	R_1 (m Ω)	L_2 (mH)	R_2 (m Ω)	C_f (mF)	R_d (Ω)
0.141	2.2	0.0282	0	0.236	0.105
Converter's Parameters					
V_{dc} (V)	Rated Power	$[p^*, q^*]$	I_{max}	K_{qv}	K_{qiv}
425	100 kVA	[1.0,0] p.u.	1.2 (p.u.)	[0.5, 5]	[3, 50]
k	K_c	f_s (kHz)	K_{PLL}		
2	[0.695, 10.92]	10	[6.28, 0.025]		

3.5.1 Performance in Normal Conditions

Different reactive current injection schemes are tested with the angular correction in open loop power control with i_l as the measured current. The load convention is used for the signs of real and reactive power. The steady state results are presented in Table 3.14.

Table 3.14: Performance of conventional GFL in normal conditions

M_{qG}	p_{poc} (p.u.)	q_{poc} (p.u.)	V_{poc} (p.u.)
0	1.02	-0.25	1.02
1	1.03	0	1.05
2	1.03	0.02	1.06
3	1.04	0.34	1.09
4	1.04	0.38	1.10

The above table shows that the performance of the improved GFL control under different modes of reactive current injection. The reference power is closely matched to the measured power at POC with the angle correction for the i_l measured current. The $M_{qG} = 0$ mode relates to the closed loop voltage

control at POC, and the reference voltage is 1 p.u. due to which the scheme results in inductive reactive power to keep the voltage close to its reference value. The next two modes are related to the closed and open loop control of the reference reactive power at POC respectively, and the results confirm that both the reference and measured quantities are closely matched. The last two modes are related to the power factor (pf) closed and open loop control respectively. The reference pf is 0.95 p.u. leading. The results show that the reactive power is calculated to achieve the desired pf.

If the performance of the improved and conventional control schemes is compared, it clearly shows that the improved scheme results in quite accurate real and reactive power at POC as compared to the conventional scheme which was able to provide better results only if the i_g is used as measured current for inner current controller. Thus, by using the improved GFL control scheme allows to achieve the desired power levels at POC.

3.5.2 Performance in LVRT Conditions

3.5.2.1 Performance Comparison of Reference Current Adjustment Scheme

It is important to slow the speed of the PLL for the stability of the system especially in weaker grids, but this slow PLL causes some oscillations in measured powers due to the non-zero q-axis value and the v_d is also not stable during this period. To observe the impact of a slow PLL on the performance of the system, especially in post fault scenarios, at 1 second, a L-L fault is introduced at POC for a duration of 0.5 seconds. The conventional current limiting scheme is activated with QNP priority injection. The results are given below for the slow PLL with and without reference current adjustments.

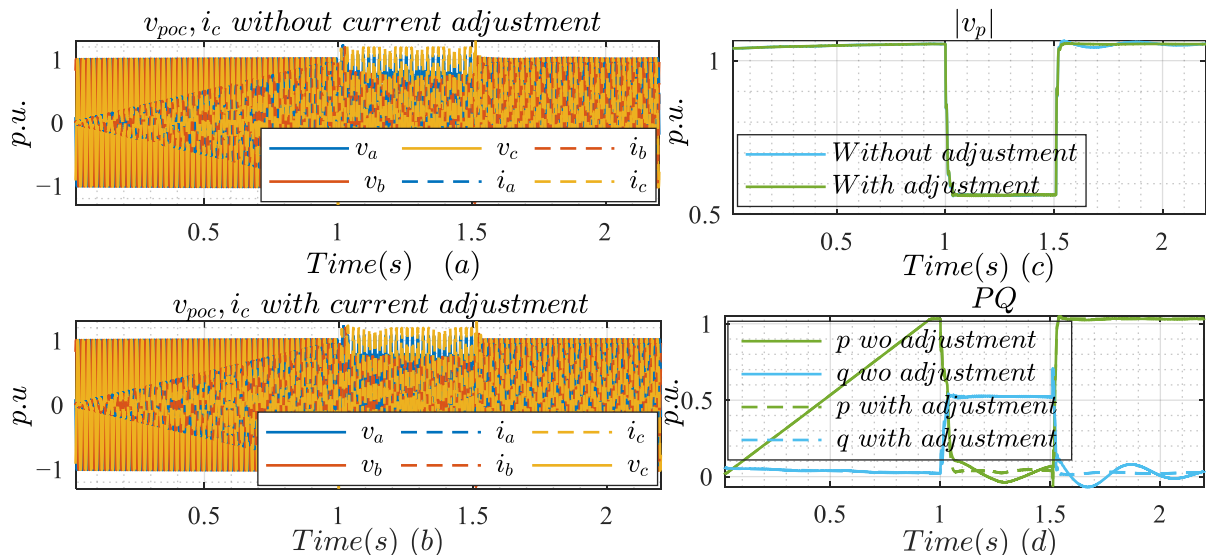


Figure 3.42: Performance of improved GFL with slower PLL in weak grid; (a) real time measured voltage at POC and converter's side current without reference current adjustments, (b) real time measured voltage and converter's side current with reference current adjustments, (c) magnitude of positive sequence voltage with and without reference current adjustments, (d) measured active and reactive power at POC with and without reference current adjustments

From the above figure, it is clear that both the schemes provide stable post fault response. From subplots (a) and (b), it is clear that the current limiting and priority injection schemes are working fine both with and without adjusting in the reference current. However, with correct adjustments in the reference currents, the oscillations in the voltage can be suppressed in the post fault period which are dominant in slower PLL with weaker grids (subplot (b)). From subplot (b), it is clear that these oscillations can be eliminated with proper adjustment in the reference currents. The expressions for these reference current adjustments are given in equation (3.68). The same conclusion can be drawn by the subplot (d) comparison for with and without adjustments which shows the oscillations in the reactive power due to the oscillations in the positive sequence voltage.

From subplot (d), the real power oscillations are observed in fault duration and reactive power oscillations are observed in post fault duration without any reference current adjustment. The reason for such response is the priority of reactive and active current in the respective durations. For example, in post fault duration, the active current injection is prioritized over the reactive current and the change in voltage is being compensated by the respective change in reference current to keep the constant real power at POC. This is the reason that no oscillations in the real power are observed in post fault duration even without making any adjustments in the reference current. On the other hand, the reactive power has those oscillations in the post fault scenario without current adjustment and it is due to the limited current capacity of the converter which can't compensate these oscillations to keep the reactive power constant.

Thus, it can be concluded from this comparison that a slower PLL may cause some voltage and power oscillations in case of fault or post fault scenario, but the response can be improved by introducing proper adjustment in the reference currents.

3.5.2.2 Performance Comparison of the Priority Injection Schemes

The priority injection schemes have a huge impact on the resultant VUF and phase over voltage (OV). Different priority injection schemes are compared for different types of faults. For simplicity, the conventional current limiting scheme is used with these priority injection schemes. A repeated fault is introduced at POC with an interval of 0.25 seconds. The proportionality constant (k) for the reactive current calculation in LVRT conditions is chosen as 3 for this study. The BCI, QNP, NQP, $|i_n|$ and $|i_p|$ priority injection schemes are applied consecutively.

The response of these schemes for the single line to ground (SLG) fault is given in Figure 3.43. A single phase to ground fault is introduced on phase 'b'.

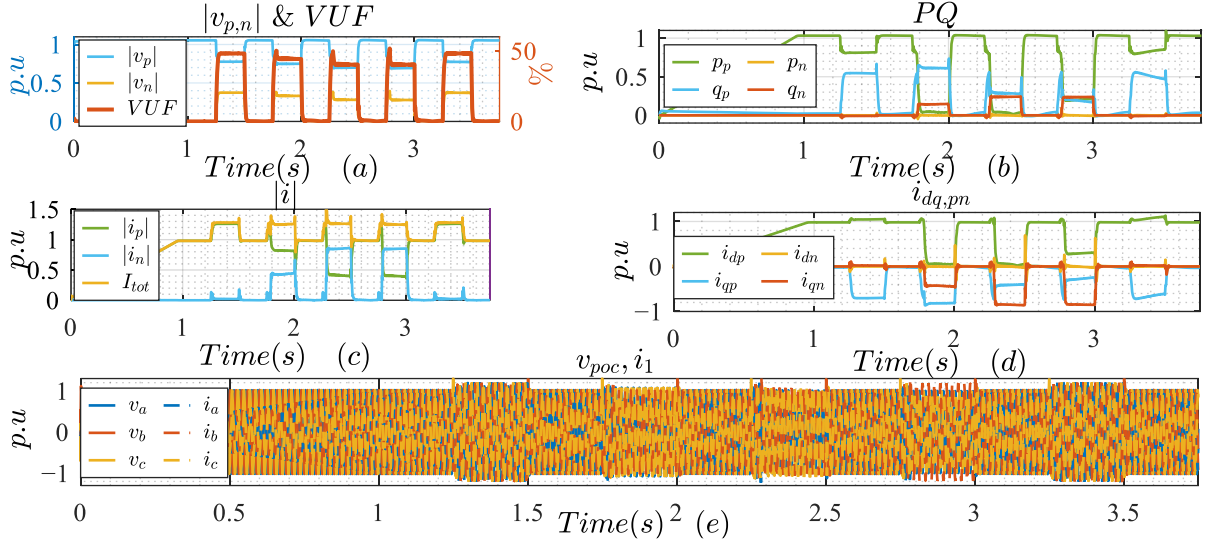


Figure 3.43: Response of different priority schemes for single line to ground fault; (a) magnitude of positive and negative sequence voltage phasors at POC and % VUF, (b) measured real and reactive power in positive and negative sequence, (c) magnitude of positive and negative sequence current phasors of i_g and their numeric sum, (d) individual current components for the positive and negative sequences of i_g , (e) measured three phase voltage at POC and measured three phase converter's side current

I_{tot} in subplot (c) represents the numeric addition of the positive and negative sequence current phasors. Subplot (a) shows that the priority injection scheme has an impact on the resultant VUF. The first voltage dip corresponds to the BCI scheme followed by QNP, NQP, $|i_n|$ and $|i_p|$ respectively. The minimum VUF results with the NQP and with $|i_n|$ priority which is the indication of the less voltage imbalance between different phases.

Subplot (b) shows the injected real and reactive power in both positive and negative sequence. It helps to confirm the priority current injection as each current component is associated with specific real or reactive power in dq reference frame with SRF-PLL. With BCI scheme, the reactive current component in positive sequence is prioritized over its active current component but still the real injected power is greater than the reactive power. The reason for such behavior is the proportionality constant (k) which decides the reference reactive current. As the remaining positive sequence voltage magnitude is relatively high, thus the reference reactive current in this case is much lower than the current capacity of the converter so the active current component is larger than its reactive component. Hence, the real power injection is more as compared to the reactive power injection with the BCI scheme. This can also be confirmed from subplot (d) which shows the individual measured current components for each sequence. In BCI scheme, the i_{dp} is larger than i_{qp} . From subplot (c), it is clear that for BCI scheme, the magnitude of the resultant current phasor is in good agreement to the magnitude of the positive sequence current phasor. The subplot (e) shows that the injected three phase currents have the same magnitude.

Similarly, in the next fault event, the QNP priority scheme is activated, and it is clear from subplot (a) that this scheme results in lower VUF as compared to the BCI scheme. The reason is the negative sequence reactive current injection which helps to improve the VUF as it is prioritized over the positive

sequence active current injection. Subplot (b), (c) and (d) shows that the reactive current and power in positive sequence is larger than the reactive current/power in negative sequence followed by the active current in the positive sequence which is in accordance with the selected priority scheme. Subplot (e) shows that the selective voltage support is provided with this scheme.

In the third fault event, the NQP priority injection scheme is activated, and the subplot (a) shows that this scheme results in the lowest VUF among all priority injection schemes. Hence, for better voltage balance among the phases, the NQP priority scheme should be preferred. The subplots (c) shows that the magnitude of the negative sequence current phasor is more than the magnitude of the positive sequence current phasor. The subplot (d) shows that the i_{qn} is larger than i_{qp} followed by i_{dp} . However, the subplot (b) shows that during NQP priority injection, the reactive power in positive sequence is still larger than the reactive power in the negative sequence and the reason is the higher magnitude of the positive sequence voltage phasor as compared to the magnitude of the negative sequence voltage phasor. The subplot (e) shows the better selective voltage support with the NQP priority.

In the next fault event, the $|i_n|$ is prioritized over the $|i_p|$. Only the magnitude of the current phasor is limited but its distribution into active and reactive components is not changed. For the negative sequence current calculation, the initial current angle is selected as 90° to fulfill the grid code recommendations (GCR). This is the reason that this scheme and NQP are identical as far as the negative sequence current is concerned. For the positive sequence current limitation, the current angle is not changed due to which the active current component is slightly higher than the reactive current component which is clear from subplots (b) and (d). Subplot (e) shows the impact of the higher active current component on the line currents.

In the last fault event, $|i_p|$ is prioritized over $|i_n|$ and the plots show that the response is similar to the BCI scheme and the fundamental reason for this is the higher magnitude of the positive sequence current phasor than the current limit of the converter which left nothing for the negative sequence current injection. However, the individual reference values for the active and reactive current components in positive sequence are slightly different than the BCI scheme and the reason is the preservation of the current angle with this scheme.

To analyze the response of these priority schemes in case of L-L fault, a fault is introduced between phase 'b' and 'c'. The response of these schemes for L-L fault is given in Figure 3.44.

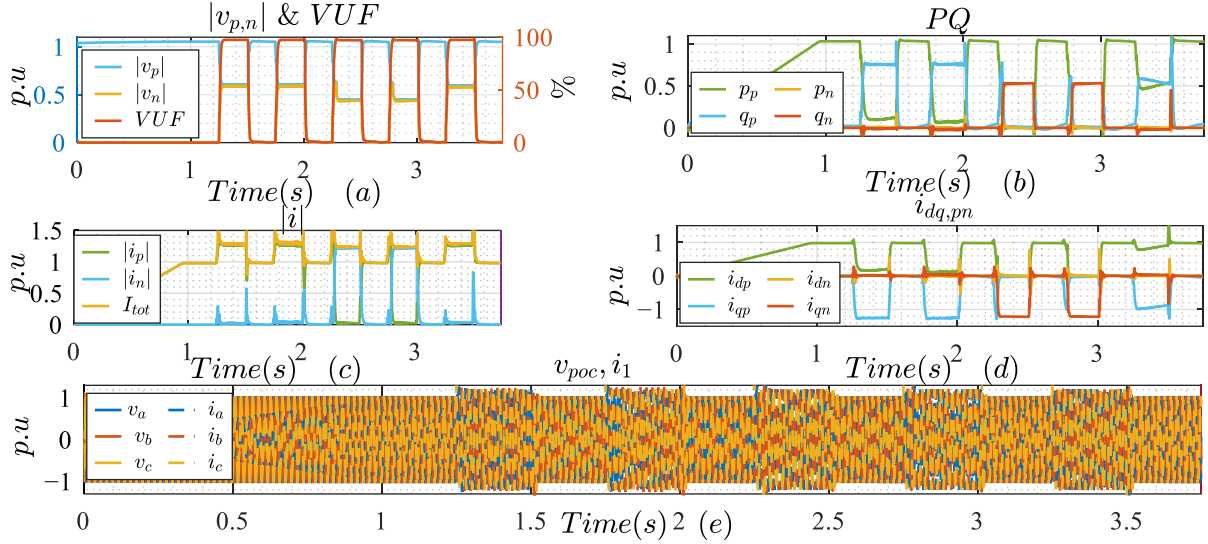


Figure 3.44: Response of different priority schemes for line to line fault; (a) magnitude of positive and negative sequence voltage phasors at POC and % VUF, (b) measured real and reactive power in positive and negative sequence, (c) magnitude of positive and negative sequence current phasors of i_g and their numeric sum, (d) individual current components for the positive and negative sequences of i_g , (e) measured three phase voltage at POC and measured three phase converter's side current

The NQP scheme results in lowest VUF for the L-L fault as well but due to the severity of the fault and relatively stronger grid, the impact of the NQP scheme on VUF is limited. The response of BCI and QNP is same. The reason for this is the higher reference i_{qp} which leaves very low limit for the i_{dp} and for i_{qn} in case of BCI and QNP priority schemes respectively. The same is true for the NQP which assigns all the converter's current limit to the i_{qn} and the limit for i_{qp} and i_{dp} is almost zero.

The response of these schemes for double line to ground (DLG) fault is given in Figure 3.45. A ground fault is introduced on phase 'a' and 'c'.

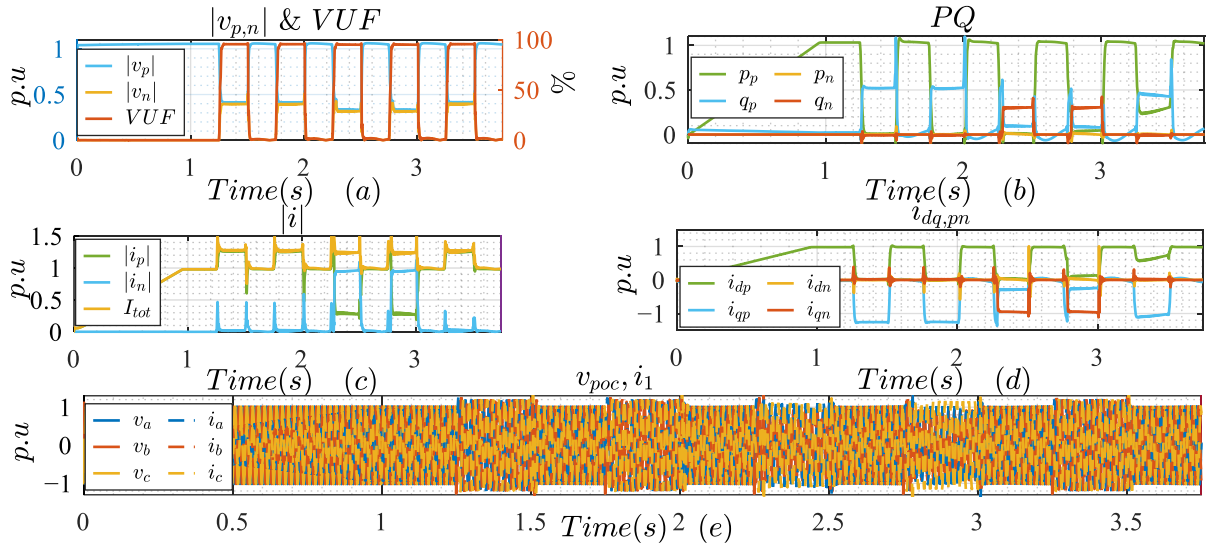


Figure 3.45: Response of different priority schemes for DLG fault; (a) magnitude of positive and negative sequence voltage phasors at POC and % VUF, (b) measured real and reactive power in positive and negative sequence, (c) magnitude of positive and negative sequence current phasors of i_g and their numeric sum, (d) individual current components for the positive and negative sequences of i_g , (e) measured three phase voltage at POC and measured three phase converter's side current

The above figure shows that the response of NQP is still better as compared to the other priority injection schemes as far as VUF is concerned. The response of the BCI and QNP scheme is the same in this case. It is due to the higher reference reactive current in the positive sequence due to the lower remaining positive sequence voltage magnitude. Thus, in QNP scheme, all the converter's current capacity belongs to the i_{qp} , and nothing is left for the i_{qn} which can be confirmed from subplot (d).

A quantitative comparison between different priority injection schemes for different types of faults is given in Table 3.15.

Table 3.15: Quantitative comparison of different priority injection schemes

Fault Type	Parameter	BCI ≈	$ i_p $ ≈	QNP ≈	NQP ≈	$ i_n $ ≈	% Reduction w.r.t. BCI respectively
SLG	Phase OV (p.u)	1.11	1.1	1.07	1	0.99	[0.9,3.6,9.9,10.8]
	VUF (%)	48.2	48.2	44.3	40.2	40.2	[0,8.1,16.6,16.6]
	Grid's side i_p	1.05-j0.7	1.1-j0.63	0.05-j0.82	0.04-j0.4	0.3-j0.27	
SLG	Grid's side i_n	0-j0.02	0-j0.02	0-j0.44	0-j0.85	0-j0.85	
	i_l^{max}	1.2	1.2	1.08	1.1	1.18	
	Phase OV (p.u)	1.12	1.12	1.12	0.85	0.85	[0,0,24.1,24.1]
L-L	VUF (%)	97.5	97.5	97.5	97.1	97.1	[0,0,0.41,0.41]
	Grid's side i_p	0.19-j1.25	0.87-j0.92	0.1-j1.26	0	0	
	Grid's side i_n	0	0-j0.03	0-j0.02	0-j1.2	0-j1.2	
L-L	i_l^{max}	1.22	1.2	1.24	1.2	1.2	
	Phase OV (p.u)	1.14	1.14	1.14	0.92	0.92	[0,0,19.3,19.3]
	VUF (%)	95.5	95.5	95.5	95.12	95.22	[0,0,0.4,0.3]
DLG	Grid's side i_p	0.01-j1.26	0.69-j1.01	0.01-j1.26	0.04-j0.29	0.13-j0.3	
	Grid's side i_n	0	0	0	0-j0.96	0-j0.96	
	i_l^{max}	1.2	1.2	1.2	1.1	1.16	
Compliance with recent grid codes		✗	✗	✓	✓✓✓	✓✓	

Different colors are used to rank the performances of different priority schemes against different evaluation parameters. Green color relates to the best performance followed by the orange and red colors. The above table shows that the phase over voltage is increased for BCI scheme as the type of the fault is changed. The VUF shows that the line-to-line fault is the most severe fault, as far as voltage balancing among different phases is concerned, followed by DLG and SLG respectively. It is clear from the above table that NQP and $|i_n|$ priority schemes offer better voltage balancing and lower VUF in all types of faults but due to the severity of fault and limited current handling capability of the converter, the percentage reduction in VUF may vary. The BCI, $|i_p|$ and QNP offer different responses for the SLG and their response for the rest of the fault types is same and the reason for this is the lower remaining voltage with sever faults which demands more positive sequence reactive current injection. The reference positive sequence reactive current in such cases is even more than the total current handling capacity of the converter. Hence with these three schemes, there is no capacity left for any other current component which results in the same performance of these three schemes for L-L and DLG faults.

Moreover, from the above table, it can be noticed that in case of L-L and DLG faults, the measured current components on the grid side have a higher amplitude than the total current capacity of the converter. The reason for this is the shunt capacitor of LCL filter as the peak phase currents on the converter's side are still lower than the current handling capability of the converter. The sequence extraction scheme also causes some inaccuracy in the measured sequence current components. In case of unbalanced faults, the shunt capacitor may also cause some negative sequence current at POC even with the BCI scheme as the GFL control scheme is responsible to control the converter's side current and the share from the shunt capacitor is uncontrolled and has no negative effect on the stability and safety of the system.

Hence, it can be concluded from the comparison of different priority schemes that the NQP priority scheme offers better results than the others as far as grid code compliance is concerned as the other priority schemes may result in zero negative sequence current injection due to the severity of the fault. Moreover, it also offers lower VUF. The $|i_n|$ priority scheme also offers almost identical results as that of NQP and the reason for this is the zero active current component in the negative sequence but if the negative sequence active current component is non-zero than the response of both the scheme varies from each other. The scholar presented such comparisons in [113].

3.5.2.3 Performance Comparison of Current Limiting Schemes

From Table 3.15, it is clear that in some cases, the maximum phase current on the converter's side is less than the current handling capacity of the converter. The reason for this is the use of the conventional current limiting scheme. The other schemes offer better use of the current handling capacity of the converter. The next comparative study involves the performance comparison of different current limiting schemes. For this comparison, the NQP priority injection is considered. The proportionality constant (k) is selected as 2 for this comparison. The rest of the conditions are the same as those for the priority scheme comparison.

In the first fault event, the conventional current limiting scheme is activated followed by CSNS, SSVS, DSVS respectively for next fault events. To analyze the performance of these schemes for SLG fault, a repeated ground fault is introduced at POC on phase 'b'. The performance of different current limiting scheme can be compared with the help of the maximum line current on the converter's side. For the sake of better utilization of the current capacity of the converter, the individual current components in positive and negative sequence should be measured along with the measured positive and negative sequence current phasors' magnitudes.

The results of these schemes for SLG fault are given in Figure 3.46.

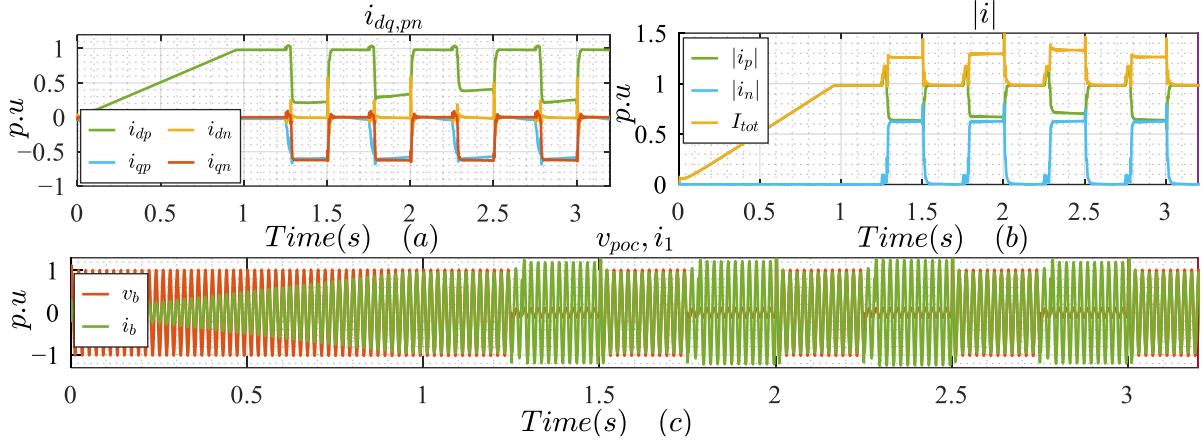


Figure 3.46: Performance comparison of different current limiting schemes for SLG fault; (a) individual current components for the positive and negative sequences of i_g , (b) magnitude of positive and negative sequence current phasors of i_g and their numeric sum, (c) real time voltage at POC and converter's side current for the faulted phase(s)

For the sake of visibility, only the faulted phase' voltage and current are shown in subplot (c). For the first fault event, the conventional current limiting scheme is activated which is based on the numeric addition of the positive and negative sequence current phasors. The subplot (b) shows that the conventional scheme offers minimum resultant current as compared to the other schemes. The maximum line current on the converter's side is also lower than the current capacity of the converter. In the next fault event, the CSNS scheme is activated which is based on the linear summation of the respective current components of positive and negative sequences. Subplots (a) and (b) show that this scheme offers more active current in the positive sequence to better utilize the current capacity of the converter. However, the subplot (c) shows a marginal increase of the maximum phase current than the current limit of the converter.

The SSVS current limiting scheme is activated for the third fault event. This scheme does not require the information of the true angle between the voltage sequences. From subplots (a) and (b), it is clear that this scheme offers even more active current in the positive sequence to better utilize the current capacity of the converter as compared to conventional and CSNS scheme. However, the subplot (c) shows a marginal increase of the maximum phase current than the current limit of the converter. For the last fault event, the DSVS scheme is activated which is the most accurate current limiting scheme as it requires the true angle between the positive and negative sequence voltage phasors and it limits the amplitude of each phase current which results in three limits for each current component and then the minimum of them is chosen to ensure that no phase current is higher than the current capacity of the converter. From subplots (a) and (b), it is clear that this scheme results the current phasors' magnitude between conventional and CSNS scheme but from subplot (c), it is clear that it limits the maximum phase current accurately than the other schemes.

The performance comparison of these schemes for L-L fault is given in Figure 3.47. The fault is introduced between phase b and c.

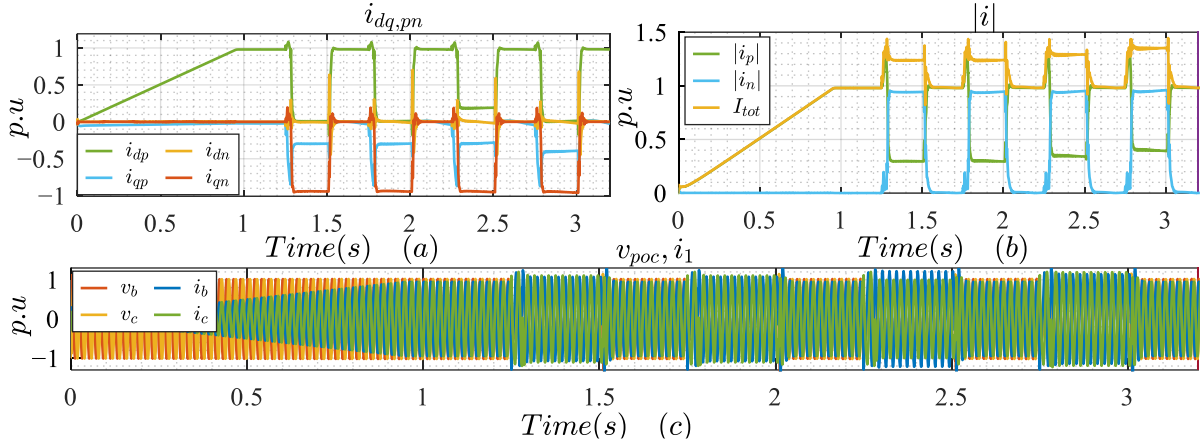


Figure 3.47: Performance comparison of different current limiting schemes for L-L fault; (a) individual current components for the positive and negative sequences of i_g , (b) magnitude of positive and negative sequence current phasors of i_g and their numeric sum, (c) real time voltage at POC and converter's side current for the faulted phase(s)

The subplots (a) and (b) of the above figure show that the conventional and CSNS schemes do not ensure maximum utilization of the converter's current handling capacity as the maximum current in the faulty phase(s) is less than the current capacity of the converter. It is due to the large angle variation between the sequence voltage phasors due to L-L fault. SSVS shows better performance than the previous two schemes, but it also results in lower total current (numeric summation of sequence current phasors) than the DSVS. Moreover, SSVS results in lower reactive current component and higher active current limit in positive sequence (compared to DSVS). For voltage support, the reactive current should be maximized, which the DSVS scheme provides (Subplot (a)). Moreover, subplot (c) shows that the selective voltage support for the faulty phases is not the same for the SSVS scheme. For the DSVS scheme, the line currents in the faulty phases are comparatively equal. Hence, in such faults, DSVS results in better performance than the rest of the schemes.

To compare the performance of these current limiting schemes in case of double line to ground fault, a simultaneous ground fault is introduced on phase 'a' and 'c'. The response of these schemes for DLG fault is given in Figure 3.48. The results show that the response of the current limiting schemes is same as that for the L-L fault. The magnitude of the negative sequence current is almost same for each scheme, but the magnitude of the positive sequence current varies largely based on the current limiting scheme and it also decides the better utilization of the converter's current capacity. As far as maximum phase current is concerned, DSVS scheme offers the best performance followed by SSVS and CSNS scheme. The performance of conventional and CSNS scheme is identical in this case.

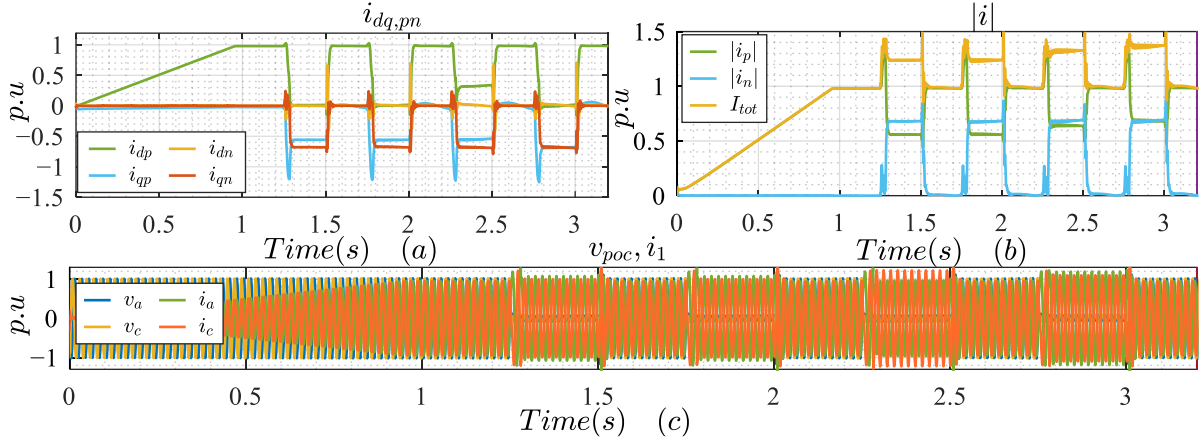


Figure 3.48: Performance comparison of different current limiting schemes for DLG fault; (a) individual current components for the positive and negative sequences of i_g , (b) magnitude of positive and negative sequence current phasors of i_g and their numeric sum, (c) real time voltage at POC and converter's side current for the faulted phase(s)

A quantitative comparison between different priority injection schemes for different types of faults is given in Table 3.16.

Table 3.16: Quantitative comparison of different current limitation schemes

Fault Type	Parameter	Conv.	CSNS	SSVS	DSVS
		\approx	\approx	\approx	\approx
SLG	Converter's side peak current	1.19	1.22	1.24	1.2
	Grid's side i_p	0.2-j0.6	0.33-j0.58	0.4-j0.58	0.25-j0.59
	Grid's side i_n	0-j0.62	0-j0.63	0-j0.63	0-j0.63
	Numeric sum of i_p and i_n	1.26	1.3	1.33	1.27
L-L	Converter's side peak current	[1.06, 1.11]	[1.07, 1.11]	[1.22, 1.0]	[1.14, 1.19]
	Grid's side i_p	0-j0.3	0-j0.3	0.19-j0.29	0.01-j0.4
	Grid's side i_n	0-j0.94	0-j0.94	0-j0.95	0-j0.95
	Numeric sum of i_p and i_n	1.24	1.24	1.29	1.35
DLG	Converter's side peak current	[1.08, 1.0]	[1.08, 1.0]	[0.96, 1.22]	[1.19, 1.1]
	Grid's side i_p	0-j0.56	0-j0.56	0.33-j0.55	0.01-j0.69
	Grid's side i_n	0-j0.68	0-j0.68	0-j0.69	0-j0.69
	Numeric sum of i_p and i_n	1.24	1.24	1.33	1.37
Peak current limitation and better utilization of converter's current limit		✓	✓	✓✓	✓✓✓

Two important functions of a current limiting scheme are to ensure that no phase current exceeds the current capacity of the converter, and it should also ensure the maximum utilization of the current capacity of the converter. The maximum phase current can be measured and compared but for the maximum utilization of the converter, the positive and negative sequence currents can be summed up numerically and the scheme which offers maximum resultant current (while keeping the maximum phase current in limit) better utilizes the current capacity of the converter as compared to the other

schemes. Based on these two points, the above table shows that the conventional scheme and DSVS scheme provides better results as compared to the other two schemes for SLG fault. The CSNS and SSVS schemes offer the better utilization of the converter's current, but they exceed the maximum phase current 1.7 and 3.3 % respectively.

It is important to mention here that the conventional and CSNS schemes confirm the maximum utilization of the current capacity if the positive and negative sequence current phasors are in-phase which is dependent on the type of the fault. This is the reason that the conventional scheme is unable to maximize the use of converter's current capacity in case of L-L faults. For L-L fault, the DSVS scheme offers better results followed by SSVS, CSNS and conventional scheme respectively. The same trend is observed for the DLG fault as well.

Thus, the current limiting scheme is mainly responsible for the safe operation of the converter, and it is also responsible for maximizing the utilization of the converter's current limit under faulty conditions. It is important to mention here that the performance of these current limiting scheme is also dependent on the actual faulty phase(s) as it changes the voltage angle between positive and negative sequence voltage phasors which impacts the better utilization of the converter's current limit. The DSVS scheme offers good results for all types of faults. The scholar presented the comparison of conventional and SSVS scheme in [115].

3.6 Further Improvements

Some further improvements in the GFL control are proposed in this section. The GCR demands the reactive current in the negative sequence, but it may not result in minimum VUF. A minimum VUF is desired in the sense of stabilising the voltage during a fault as close to normal conditions as possible. Thus, a proper investigation needs to be done to confirm the optimal negative sequence current distribution to achieve the minimum VUF while keeping the negative sequence current phasor's magnitude proportional to the change in negative sequence voltage. The other important task is to minimize the real power oscillations in case of unbalanced faults as it increases the cost and complexity of the dc-link protection. These two improvements are discussed in this section.

3.6.1 Optimal Angle for the Negative Sequence Current Phasor to Achieve Minimum VUF

The grid code recommendations (GCR) demand the reactive current injection in the positive and negative sequences in case of unbalanced faults. It does not specify any recommendations for the active current injection in the negative sequence. The prime purpose of the reactive current injection is to get the voltage support from the converter-based sources in case of voltage dips and the negative sequence current helps in improving the voltage uniformity. It is also used for fault detection and helps in selective voltage support to the faulty phases. However, due to the opposite rotation of the negative sequence phasor as compared to the positive sequence, the only reactive current injection in negative sequence

may not result in minimizing the VUF. Based on this, the scholar investigated the impact of active current component injection in the negative sequence on the VUF. For the sake of comparison, the magnitude of the negative sequence current phasor is not changed, and it is proportional to the magnitude of the negative sequence voltage phasor. The proportionality constant is assumed to be 2.

The outcomes of this investigation were presented in [114]. Equation (3.66) is used for the calculation of the reference current for the negative sequence. The current angle varies from 0° to 360° and its impact on the VUF is analyzed. All the other parameters are kept constant. The advantage of using equation (3.66) is that it allows to limit the magnitude of the current phasor without changing its angle. The mathematical expression for VUF can be found in equation (3.93).

$$\%VUF = 100 \times \frac{|v_n|}{|v_p|} \quad (3.93)$$

The X/R ratio of the grid and fault varies from purely resistive to highly inductive at POC. The angle of the negative sequence current varies with a step of 5° . The VUF is plotted against the angle of the negative sequence current phasor. Figure 3.49 presents the impact of the different current distributions for the negative sequence current phasor on the VUF. The $|I_n|$ priority injection scheme with the conventional current limiting scheme is used for this investigation.

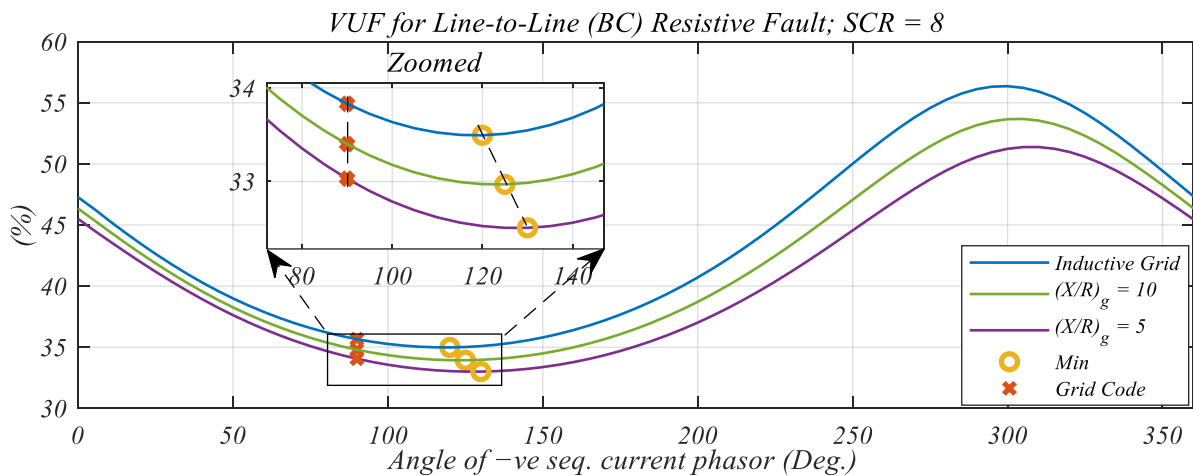


Figure 3.49: Impact of negative sequence current distribution on the VUF for resistive fault

The above figure shows that the GCR does not result in minimum VUF for a resistive L-L fault. The X/R ratio of the grid varies at POC. The pure inductive grid is closer to the GCR conditions (only reactive current injection in the negative sequence). The highly inductive grid is possible for high voltage grids and normally the converter-based sources are connected to the medium voltage system where the resistive component of the grid is relatively comparable. Its impact on the VUF dominates in the weaker grids.

The same process is repeated to study the impact of different current distributions for the negative sequence on the VUF for different X/R ratio of the grid and of the fault and its outcomes are presented in Figure 3.50.

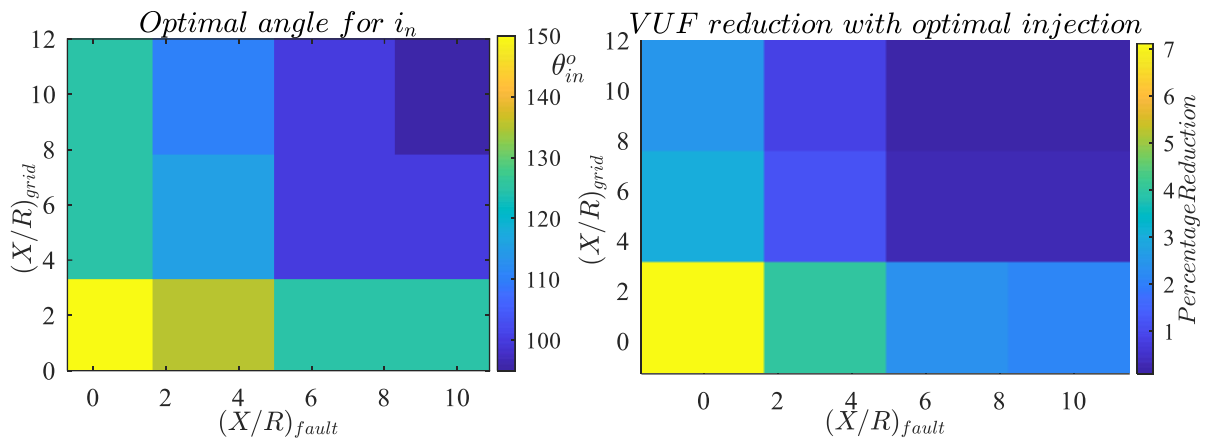


Figure 3.50: Impact of X/R ratio of fault and grid on the negative sequence current distribution and minimum VUF for line-to-line fault

The above figure shows that the GCR results in minimum VUF only in case of highly inductive grid with inductive faults. The negative sequence current distribution corresponding to the minimum VUF varies largely from GCR if the X/R ratio of the grid or the fault is comparatively resistive. The same procedure can be repeated for other types of faults. The results for different types of faults against a particular X/R ratio of the grid and fault are given in Figure 3.51.

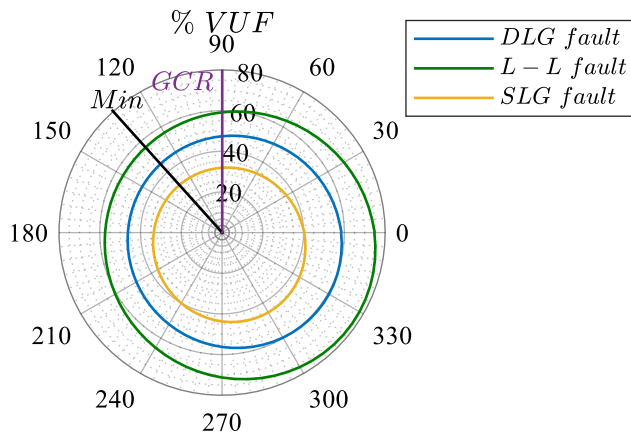


Figure 3.51: Impact of negative sequence current distribution on the VUF for different types of faults

The angle involved in the above figure represents the active and reactive current distribution for the negative sequence current phasor. The ‘min’ line corresponds to the angle resulting in minimum VUF. The above figure shows that the optimal current distribution is different than the GCR for each type of fault. The scholar presented such a study in [114].

The above study shows that the negative sequence current angle corresponding to the minimum VUF is dependent on the X/R ratio of the fault and of the grid at POC. It also depends on the type of the fault. Hence it is a challenging task to decide the optimum current angle as these are the unknown factors which vary largely and can’t be generalized. However, the impact of these factors can be estimated through the measured three-phase voltage at POC. The scholar investigated the change in angle between

the positive and negative sequence voltage phasors against the initial angle of the negative sequence current phasor. A L-L fault is introduced at POC. The results are presented in Figure 3.52.

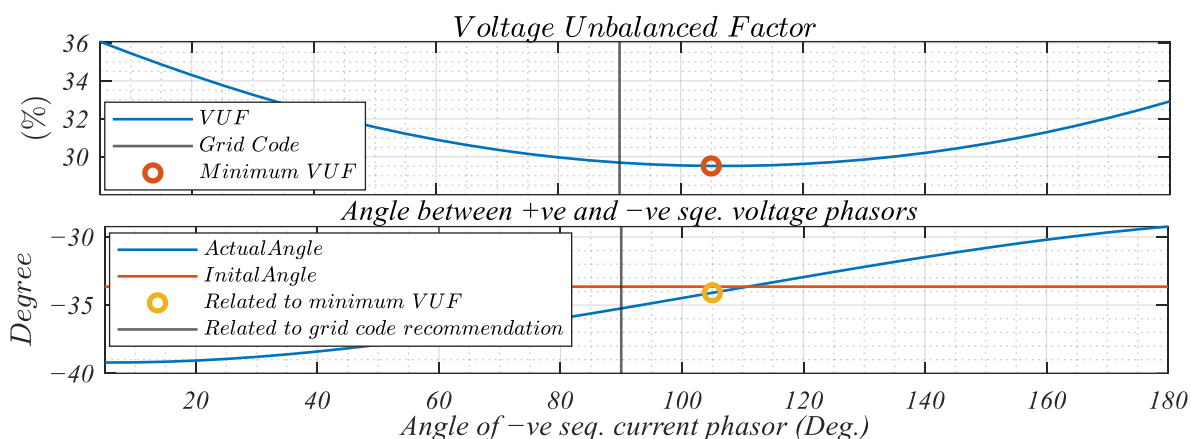


Figure 3.52: Impact of negative sequence current distribution on the angle between positive and negative sequence voltage phasors

The above figure shows that the minimum VUF is achieved if the angle between the positive and negative sequence voltage phasors is restored to its initial value. This initial value corresponds to the situation when an unbalanced fault occurs, and no negative sequence current is yet injected. Hence this angle can be used to assess the optimal distribution of negative sequence current phasor into its components. The same procedure is repeated to confirm this relation for all types of unbalanced faults and for different faulty phases, the outcome of this study is given in Table 3.17.

Table 3.17: Relation between negative sequence current distribution and θ_{vpn}

Fault Type	$(X/R)_r$	$(\theta_{vpn})_{pre}$	VUF_{min}	θ_n	$(\theta_{vpn})_{min}$	$(X/R)_r$	$(\theta_{vpn})_{pre}$	VUF_{min}	θ_n	$(\theta_{vpn})_{min}$	
		(Deg)	(%)	(Deg)	(Deg)		(Deg)	(%)	(Deg)	(Deg)	
ABG	0 (pure resistive)	AB	78.1		76.8	1	98.3			99	
		BC	-41.3	60.3	135		-43.2	-19	49.2	115	-21
		CA	-161.5				-163.2	-141.3			-141
		ABG	70				66.71	95.5			94.9
		BCG	-50.7	48.6	135		-53.3	-22.4	39.8	115	-25.1
		CAG	-176.3				-173.3	-145.4			-145.1
		AG	143.6				144	159.6			161.5
		BG	22.53	33.6	110		24	39.6	26.8	100	41.5
		CG	-96.4				-96	-79.8			-78.5
ABG	5 (pure inductive)	AB	113.7		115.1		119.2			120.8	
		BC	-6.6	46.7	95		-4.9	-1.5	46.8	90	0.8
		CA	-126.3				-124.9	-120.9			-119.2
		ABG	113.8				114.6	120.1			121.4
		BCG	-7.4	37.8	95		-5.4	-1.1	37.9	90	1.4
		CAG	-127				-125.4	-120.8			-118.6
		AG	173.4				175.7	178			180
		BG	53.6	25.3	95		55.7	58.4	25.4	90	60
		CG	-66.5				-64.3	-62			-60

The subscript ‘pre’ and ‘min’ and ‘f’ stands for ‘pre-fault’, ‘corresponding to minimum value’ and ‘fault’ respectively. θ_n is the angle of the negative sequence current phasor associated to the minimum VUF. The ‘A’, ‘B’, and ‘C’ represent the three phases respectively. From the above table, the following statements can be proved.

- For the same fault type, the negative sequence current angle corresponding to the minimum VUF is same but the angle between the sequence voltage phasors is different and depends on the faulty phase(s).
- Even for the same test conditions, the type of fault changes the optimum distribution of negative sequence current into its components.
- As the inductance of the fault increases, the difference of VUF for GCR and optimal injection starts to decrease.
- For all test conditions, the voltage sequence angle corresponding to the minimum VUF is in good agreement to its initial value (column 3 and 6).

Hence the above table validates the findings of Figure 3.52. The voltage sequence angle correction can be used to optimally distribute the negative sequence current into its components for achieving minimum VUF. Moreover, from the above study it is also clear that this angle can be between 90° to 180° . Thus, a PI controller can be used to find the optimal current angle for the negative sequence current. Equation (3.59) can be used to assess the θ_{vpn} . The pre-fault θ_{vpn} can be captured with the help of sample and hold function. The input to the PI controller is the error between the pre-fault and actual value of θ_{vpn} . The layout of the scheme for estimation of the optimal negative sequence current angle is given in Figure 3.53.

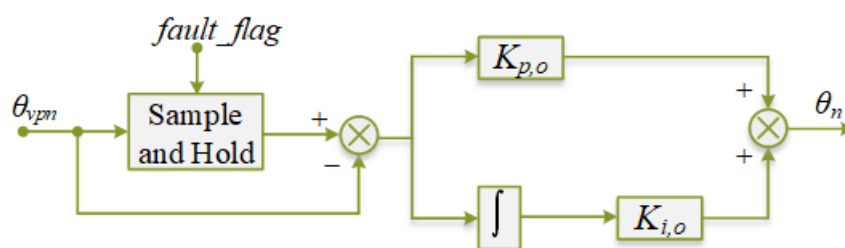


Figure 3.53: Control layout for estimation of optimum angle of negative sequence current

$K_{p,o}$ and $K_{i,o}$ stand for proportional and integral gain (respectively) for the negative sequence current angle estimator. Moreover, θ_n is the negative sequence current phasor's angle associated to the minimum VUF. The performance of this scheme will be discussed later in this section. This scheme is termed as optimum angle injection (OAI) scheme in this thesis.

3.6.2 Minimization of Real Power Oscillations

The next important task is to minimize the power oscillations in case of unbalanced faults. As the real and reactive power oscillations can't be eliminated simultaneously in case of unbalanced conditions,

the real power oscillations are eliminated with the help of a new scheme. The real power oscillations also cause the oscillations in the dc link voltage and can cause a power reversal which increases the cost and complexity of the dc side protection. This is the reason that real power oscillations are important to be minimized. By using equation (3.62), the time dependent component of the real power can be equated to zero. The new expressions are given in equation (3.94).

$$\begin{aligned} \tilde{p} = 0 \rightarrow (v_{\alpha p} i_{\alpha n}^{**} + v_{\beta p} i_{\beta n}^{**}) &= -(v_{\alpha n} i_{\alpha p}^{**} + v_{\beta n} i_{\beta p}^{**}) \\ |v_p| |i_n^{**}| \cos(2\omega t + \theta_{vp} + \theta_{in}) &= -|v_n| |i_p^{**}| \cos(2\omega t + \theta_{vn} + \theta_{ip}) \end{aligned} \quad (3.94)$$

The initial angles for current and voltage are with respect to the ωt . The angle of the current, decided by the control scheme, is actually the difference between the actual voltage and current angles due to the use of PLL or equation (3.66). Hence, the above equation can be modified to express it in terms of the current angle, which the control scheme can control, the new expression is given in (3.95).

$$\begin{aligned} |v_p| |i_n^{**}| \cos(2\omega t + \theta_{vp} + \theta_{in}) &= -|v_n| |i_p^{**}| \cos(2\omega t + \theta_{vn} + \theta_{ip}) \\ \therefore \begin{cases} \theta_{ip} = \theta_{vp} + \theta_p \\ \theta_{in} = \theta_{vn} + \theta_n \end{cases} & \\ |v_p| |i_n^{**}| \cos(2\omega t + \theta_{vp} + \theta_{vn} + \theta_n) &= -|v_n| |i_p^{**}| \cos(2\omega t + \theta_{vn} + \theta_{vp} + \theta_p) \end{aligned} \quad (3.95)$$

Where the $\theta_{p,n}$ is the angle of current with respect to the voltage in the respective sequence.

The above expression can be simplified if the cosine terms on both sides are equal which states that the positive and negative sequence current phasors are in-phase to each other. This results in simpler expressions for the magnitudes of positive and negative sequence current phasors.

$$|v_p| |i_n^{**}| = -|v_n| |i_p^{**}| \rightarrow |i_n^{**}| = \frac{-|v_n| |i_p^{**}|}{|v_p|} \quad (3.96)$$

The same process can be repeated to minimize the reactive power oscillations. The simpler expression for minimized reactive power oscillations is given in (3.97).

$$|v_p| |i_n^{**}| = |v_n| |i_p^{**}| \rightarrow |i_n^{**}| = \frac{|v_n| |i_p^{**}|}{|v_p|} \quad (3.97)$$

It can be verified from the above two equations that the active and reactive power oscillations can't be eliminated simultaneously. Hence to achieve the minimum real power oscillations, the updated expressions are given in equation (3.98).

$$\begin{aligned} i_{qp}^* &= k_p \Delta |v_p| + i_{qp,pre\text{fault}}^*; i_{dp}^* = \left| \frac{i_{qp}^*}{\tan(\theta)} \right| \\ |i_n^*| &= k_n \Delta |v_n| \\ i_{dn}^* &= |i_n^*| \cos(\theta); i_{qn}^* = |i_n^*| \sin(\theta) \end{aligned} \quad (3.98)$$

Where k_p and k_n represent the proportional gain constant for reactive current injection in positive and negative sequence respectively. The active current component in the positive sequence is computed with the help of its reactive component and the current angle of the negative sequence. This helps to minimize the real power fluctuations along with the minimization of VUF. In this case, the angle for the sequence current phasors is assessed by the control layout given in Figure 3.53. If the θ is 90° in the above equation, then it follows the grid code recommendations along with the minimization of real power fluctuations and this scheme is termed as minimum real power fluctuation (MRPF) in this thesis. If the angle is assessed with the help of OAI scheme, then the scheme is denoted as OAI&MRPF scheme. It is important to mention here that in MRPF or OAI&MRPF scheme, the $|I_p|$ or $|I_n|$ priority injection scheme should be selected so that the current angle is not changed due to the limited current handling capability of the converter.

The magnitude of the negative sequence current phasor is proportional to the negative sequence voltage drop. Thus, the condition, given in equation (3.96) can be used to define the proportionality constant for the negative sequence current.

$$k_n \Delta |v_n| = \frac{-|v_n| |i_p^{**}|}{|v_p|} \xrightarrow{\therefore \Delta |v_n| = -|v_n|} k_n = \frac{|i_p^{**}|}{|v_p|} \quad (3.99)$$

In such cases, the circular current limitation is used which ensures to keep the same current angle and only changes the magnitude of the current phasor so the above expression can be further simplified. The simplified expressions are given in equation (3.100) for $|I_n|$ priority.

$$k_n = \frac{|i_p^{**}|}{|v_p|} \xrightarrow{\begin{array}{l} \therefore |i_p^{**}| = x |i_p^*| \\ \therefore x = \frac{i_{\max} - |i_n^{**}|}{|i_p^*|} \end{array}} k_n = \frac{i_{\max} - |i_n^{**}|}{|v_p|} \quad (3.100)$$

$$k_n = \frac{i_{\max} - |i_n^{**}|}{|v_p|} \xrightarrow{\therefore |i_n^{**}| = k_n \Delta |v_n|} k_n = \frac{i_{\max}}{|v_p| + \Delta |v_n|}$$

The scholar discussed its performance in [116]. The performance comparison of GCR, OAI, MRPF and OAI&MRPF is also discussed here for different types of faults. A fault is repeated at POC, and different schemes are activated for each fault duration. The fault duration is varied to assess the steady response of the schemes. The proportional and integral gains for PI controller in Figure 3.53 are 0.2 and 100 respectively. The proportionality constant for the reactive current injection in positive sequence is selected as 2 and the k^- is 2 for GCR and OAI but for rest of two scheme, it is assessed with the help of equation (3.100).

A ground fault is applied on phase 'b' at POC. The performance of the four schemes for SLG is given in Figure 3.54 where the 'NC' stands for the normal condition operation.

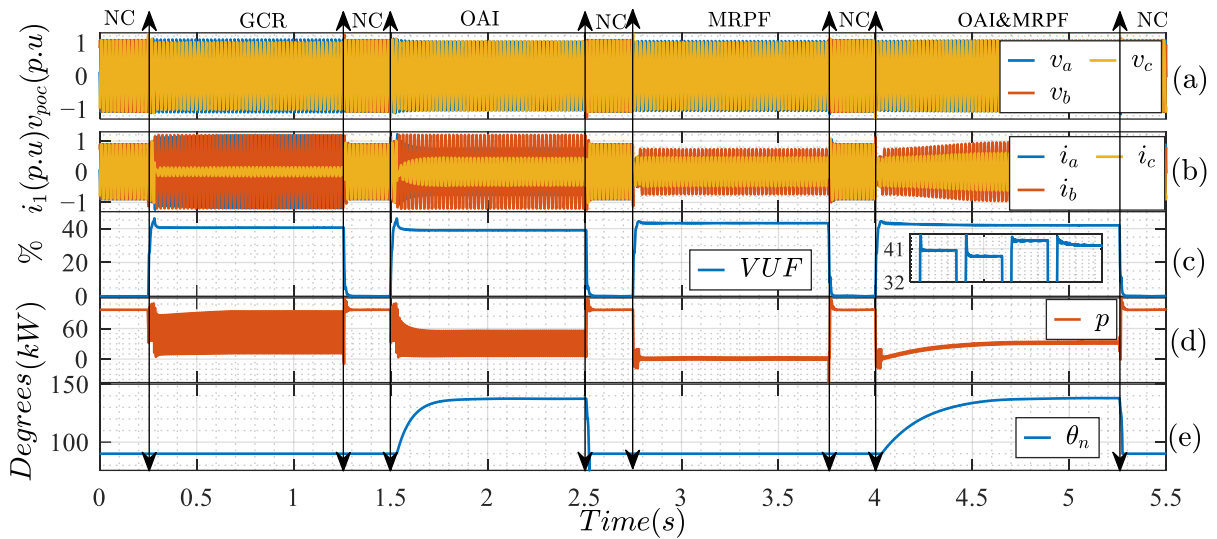


Figure 3.54: Response of different control schemes for SLG fault; (a) real time voltage at POC, (b) converter's side line currents, (c) % VUF, (d) active power at POC, (e) optimal negative sequence current angle corresponding to minimum VUF

All the quantities given in the above figure are in per unit except the active power at POC, VUF and negative sequence current angle which are in kW, % and degrees respectively. From subplot (a), it can be noticed that the voltage in healthy phases is a bit higher for MRPF and OAI&MRPF than the rest of the schemes and the reason for this is the lower k_n for these schemes. The subplot (b) confirms that none of the line currents exceeds its limit for any of the schemes. The maximum line current in the case of MRPF is the lowest which means that the converter's current limit is not being utilized optimally. The reason for this is the lower k_p value which caused lower positive sequence reactive current and as the active current is derived with the help of reactive current and the assessed angle which is 90° in case of MRPF. Thus, only the reactive current is supplied, and its calculated value is less than the converter's current limit. This is the reason that the line currents are less than the maximum current limit in case of MRPF. Moreover, from subplot (b) it is also clear that the maximum current is fed to the faulty phase which confirms the requirement of selective voltage support in case of unbalanced faults. This is true for all the schemes.

The subplot (c) presents the %VUF. The VUF is lowest for OAI scheme which optimally distributed the negative sequence current into its components to achieve minimum VUF. The VUF for OAI&MRPF scheme is a bit higher than GCR due to the lower k_n for the OAI&MRPF scheme as it also minimizes the active power oscillations. Thus, a fair comparison for VUF is between GCR and OAI, or between MRPF and OAI&MRPF so that the impact of only optimal distribution can be analyzed. Hence, it confirms that the optimal distribution of the negative sequence current results in minimum VUF.

The subplot (d) presents the active power at POC. It confirms high oscillations in the active power in case of unbalanced faults if the negative sequence current is not adjusted to damp these oscillations. Hence the active power oscillations for the GCR and OAI schemes are very high but for the next two

schemes, these oscillations are damped out to a great extent. The subplot (e) shows the angle for the negative sequence current which distributes it into active and reactive components. It shows that it is 90° for GCR and MRPF but for the rest of two schemes, the PI controller assesses this angle.

To compare the performance of these scheme in case of line-to-line fault, a L-L fault is introduced at POC between phase ‘b’ and ‘c’. The response of the four schemes is plotted in Figure 3.55.

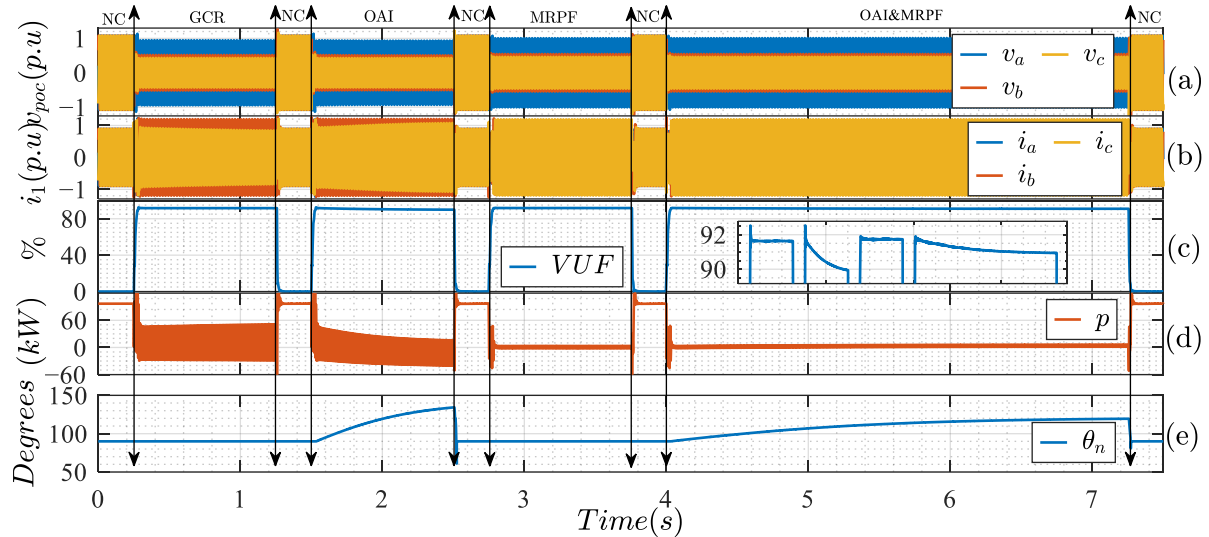


Figure 3.55: Response of different control schemes for L-L fault; (a) real time voltage at POC, (b) converter's side line currents, (c) % VUF, (d) active power at POC, (e) optimal negative sequence current angle corresponding to minimum VUF

The response of the four schemes is the same as for SLG but due to high severity of the fault, the levels of the measured quantities are different than SLG. Unlike SLG fault, in L-L fault, the line currents are not low and are limited to the maximum allowed level. Moreover, the response of the OAI&MRPF scheme (which will also be called as combined scheme afterwards) is slower as compared to the other schemes. For the MRPF and combined scheme, the real power oscillations are minimum, but some oscillations are evident at the start of the fault. It is due to the delay in the activation of the negative sequence current injection which is important to assess the initial angle between the positive and negative sequence voltage phasors (θ_{vpn}). The VUF is high due to the nature of the fault which causes more asymmetry among the phase voltages. However, the minimum VUF is achieved with the help of optimal distribution of the negative sequence current and the corresponding optimal angle is shown in subplot (e).

Similarly, to analyze the performance of these scheme in a double line to ground fault, a ground fault is applied on phase ‘a’ and ‘b’. The response is given in Figure 3.56.

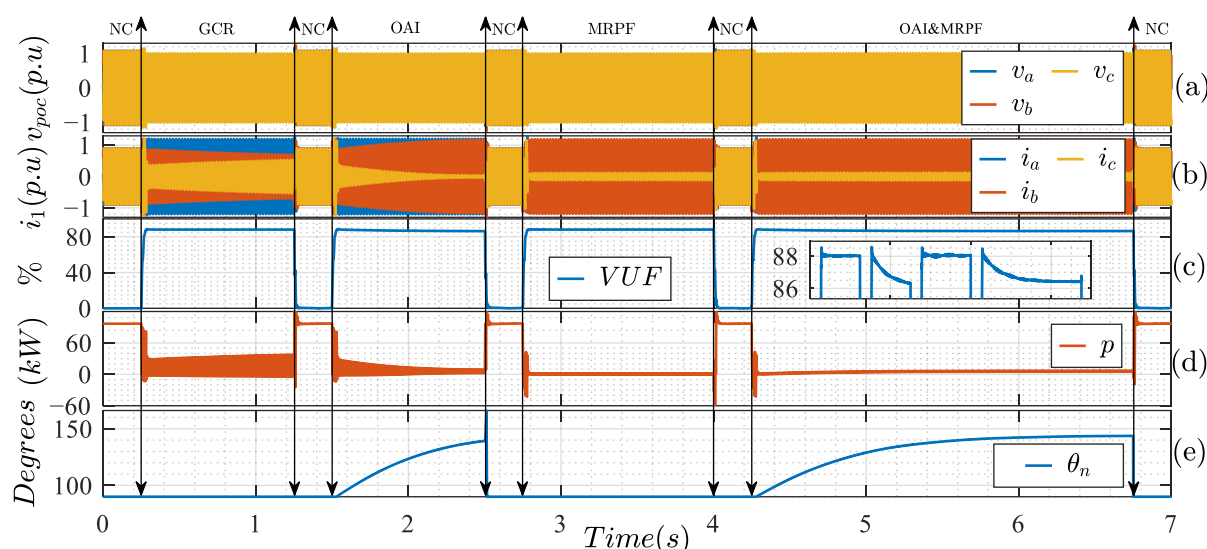


Figure 3.56: Response of different control schemes for DLG fault; (a) real time voltage at POC, (b) converter's side line currents, (c) % VUF, (d) active power at POC, (e) optimal negative sequence current angle corresponding to minimum VUF

It shows the same kind of response as for SLG and L-L faults. For quantitative analysis, Table 3.18 comprises the key indicators for each scheme against each fault type. Different colors are used for the ranking of the schemes. The green color represents the best performance followed by light green, orange and red color respectively.

Table 3.18: Quantitative comparison of GCR, OAI, MRPF and combined schemes

Fault Type	Parameters	GCR	MRPF	OAI	OAI&MRPF
		≈	≈	≈	≈
SLG	VUF (%)	40.6	43.3	39	41.9
	Active power fluctuation amplitude (kW)	82.5	4.9	49.8	4.4
	Mean active power (kW)	52.5	1	30.6	32.4
L-L	VUF (%)	91.6	91.7	90	90.1
	Active power fluctuation amplitude (kW)	80	5.5	56.7	4.9
	Mean active power (kW)	11.1	0.7	-12	3.82
DLG	VUF (%)	88	88	86.3	86.4
	Active power fluctuation amplitude (kW)	42.1	2.8	7.2	2
	Mean active power (kW)	16.4	0.6	5.7	6

Table 3.18 shows that the OAI scheme results in lowest VUF followed by GCR, combined scheme and MRPF scheme respectively. The main reason for higher VUF for the combined scheme than the GCR is the lower k_n value which results in lower negative sequence current injection. For fair comparison, combined scheme should be compared to MRPF scheme for VUF as there is only one parameter change between the two schemes and it shows that the combined scheme results in lower VUF than the MRPF scheme. Although the GCR scheme results in maximum mean active power injection, it also results in very high fluctuations in the active power which makes this scheme unfavorable. This causes higher dc link voltage fluctuations. Based on these two parameters (lower fluctuations and higher mean power), the combined scheme results in better performance followed by MRPF, OAI and GCR respectively.

For L-L fault, the MRPF results in worst performance as far as VUF is concerned followed by GCR, OAI&MRPF and OAI respectively. Due to the severity of the fault, the difference between the performance of these schemes is less as compared to their comparison for SLG fault but the schemes involving optimal negative sequence distribution results in lower VUF for this fault as well. As far as real power oscillations are concerned, the combined scheme offers better performance than the rest of the schemes and their ranking is clear in the above figure. Similarly, the ranking of the schemes for DLG fault against VUF and minimum real power fluctuations is also same as that in case of SLG fault.

Moreover, the Table 3.18 also shows that the performance of the OAI scheme is better than the other schemes as far as VUF is concerned for all types of faults. It also validates the findings of previous section that the minimum VUF is achieved with different distribution of negative sequence current phasor than the one recommended in grid codes. The percentage reduction in the VUF is however different for each fault type. Its impact is dominant in a low voltage system where the X/R ratio is comparatively smaller. The percentage reductions in real power fluctuations with MRPF and combined scheme are almost the same against each fault type. Hence, the fault type has no impact on the performance of the MRPF and combined scheme as far as reduction in real power fluctuations is concerned. Thus, by comparing all the four schemes for each fault type based on two factors i.e., minimum VUF and minimum real power fluctuations, it can be concluded that the OAI&MRPF scheme results in better performance than the rest of the schemes.

3.7 Take Aways from Modeling and Analysis of GFL

The important conclusions from the above analysis are given below.

- The grid's strength at point of connection, the speed of PLL and the active or reactive current priority in the faulty conditions have a huge impact on the post fault stability of the GFL. The slower PLL with the reactive current priority results in more stable post fault operation.
- Comparing the sequence extraction schemes based on the speed and accuracy, the improved delay sample method based, and second order generalized integrator-based schemes offer better results than the others.
- To detect the LVRT conditions, some new and accurate techniques are discussed as fault detection is particularly challenging for high impedance unbalanced faults. The sequence-based scheme offers accurate and quicker fault detection than the other schemes followed by the second order generalized integrator-based amplitude detection scheme.
- A slower PLL may cause some voltage and power oscillations in case of fault and post fault scenarios, but the response can be improved by introducing proper adjustments in the reference currents.

- The NQP and $|i_n|$ priority injection schemes result in lower phase over voltages and minimum VUF in case of unbalanced faults as compared to the other priority injection schemes.
- In unbalanced conditions, the detailed sequence vector summation (DSVS) current limiting scheme ensures the maximum utilization of the converter's current handling capacity as compared to the other schemes.
- The VUF can be further reduced by changing the angle of the reference negative sequence current phasor. The true angle for the negative sequence current phasor should be the one which results in restoration of the angle between the positive and negative sequence voltage phasors at POC.
- With the reduction in X/R values for the grid and for the fault, the optimum angle for the reference negative sequence current phasor (associated to the minimum VUF) deviates more from the grid's code recommendation.
- In the case of unbalanced conditions, the real power fluctuations can be minimized by properly selecting the reference currents for both the sequences. However, both the real and reactive power oscillations cannot be minimized simultaneously.
- The combined OAI&MRPF scheme results in optimum VUF while resulting minimum real power oscillations in unbalanced conditions.

4. GRID FORMING CONTROL SCHEME

Due to the several advantages of GFM over GFL (mentioned in Table 2.6), the new grid codes demand a voltage source behavior of the converters [118]. The voltage source converter (VSC) has several advantages i.e., standalone operation, natural response against the faults, stable operation in weak and stiff grid connections, and inherent power synchronization capability, etc. There are several GFM schemes but in this chapter, the focus will be on the modeling of synchronverter which mimics the response of the synchronous generator. Its fundamental equations are discussed in section 2.3.2. The hardware layout of the converter is the same as that of GFL converter. Only the control scheme will be discussed here.

For the synchronverter, the ideal round-rotor SG is considered and the equations for the synchronverter are derived in [91]. The synchronverter equations are given in equation (4.1).

$$\begin{aligned}
 T_e &= M_f i_f \langle i, \sin \theta \rangle; e = \omega M_f i_f \sin \theta; \\
 q &= -\omega M_f i_f \langle i, \cos \theta \rangle \\
 \sin \theta &= \left[\sin(\theta) \quad \sin\left(\theta - \frac{2}{3}\pi\right) \quad \sin\left(\theta + \frac{2}{3}\pi\right) \right]^T \\
 \langle i, \sin \theta \rangle &= [i_a(t) \quad i_b(t) \quad i_c(t)] \begin{bmatrix} \sin(\theta) \\ \sin\left(\theta - \frac{2}{3}\pi\right) \\ \sin\left(\theta + \frac{2}{3}\pi\right) \end{bmatrix}
 \end{aligned} \tag{4.1}$$

In the above equation, the superscript ‘ T ’ denotes the transpose of the matrix, the ‘ M_{jf} ’ is the term representing the flux linkage part of SG. ‘ e ’ is the internal voltage that is the reference voltage for PWM generator. Similarly, ‘ T_e ’ is the electrical torque, ‘ q ’ is the reactive power, ‘ i ’ is the line current, ‘ ω ’ is the angular frequency and ‘ θ ’ is the voltage angle. The subscripts ‘ a ’, ‘ b ’, and ‘ c ’ represent each phase.

4.1 Conventional Synchronverter Control Scheme

The layout of the synchronverter control is given in Figure 4.1.

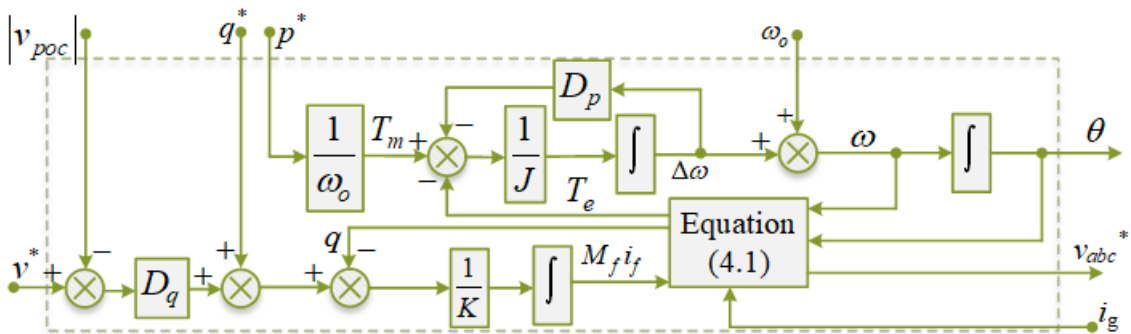


Figure 4.1: Control layout for conventional Synchronverter

D_p and D_q are the droop gains for active and reactive power controls respectively. The above-mentioned control layout can be broadly divided into two main parts i.e., active power-frequency (p-f) loop and reactive power-voltage loop. The real power of the conventional synchronous generator is changed with the change in its frequency. If the frequency of the system increases, it means the delivered active power is more than its consumption. Thus, a negative frequency droop is introduced. It helps to achieve the target frequency, and it also distributes the change in load demand among the connected converters according to their droop coefficient (D_p). In [118], the active power droop is defined as the ratio of relative change in frequency to the relative change in active power and its range is defined as 2 to 12 %. However, in the control scheme, D_p is defined as the ratio of relative change in active power to the relative change in frequency, thus, the range of D_p is calculated to be 16.7 to 100 %. The active power control has nested loops as the inner loop is the p-f droop loop and the more complex active power feedback control is through the measured current i_g which decides the electrical torque. The transfer function for the p-f loop is given in (4.2).

$$\begin{aligned}\Delta\omega &= \left(\frac{T_m - T_e - D_p \Delta\omega}{J} \right) \frac{1}{s} \\ (Js + D_p) \Delta\omega &= T_m - T_e \\ H_{p-f}(s) &= \frac{\Delta\omega}{T_m - T_e} = \frac{1/D_p}{\frac{J}{D_p}s + 1}\end{aligned}\quad (4.2)$$

The transfer function of the p-f loop is a low pass filter having gain of $1/D_p$ and time constant of J/D_p where ' J ' presents the virtual inertia.

The reactive power-voltage loop is responsible for maintaining the voltage magnitude. It provides the feedback loop for the voltage and ensures to achieve the reference reactive power provided the terminal voltage is within permissible limits. Both the voltage and reactive power have feedback loop in Q-V loop. The magnitude of the voltage phasor can be assessed with the help of the following equation.

$$|v| = \sqrt{\frac{-4}{3} (v_a v_b + v_b v_c + v_c v_a)} \quad (4.3)$$

However, the above equation helps to calculate the magnitude of the voltage phasor for balanced three-phase system. It requires a low pass filter (LPF) to filter out the component with twice of the frequency in case of unbalanced conditions. Moreover, the current limitation scheme is also missing in the conventional GFM control.

4.1.1 Performance Analysis of Conventional GFM Scheme

The conventional control scheme is developed in Simulink and its response is observed under different operating conditions. The key parameters for the setup are given in Table 4.1.

Table 4.1: Parameters for the test setup of conventional GFM converter

Grid Parameters							
Voltage (L-L) (V)	f_g (Hz)	SCP (MVA)	X/R				
400	50	[1–800]	5				
Coupling Transformer							
Type	Voltage (V)	Rated Power (kVA)	Reactance (p.u.)	Resistance (p.u.)			
Y-Y	400/260	200	0.03	6×10^{-4}			
LCL Filter							
L_1 (mH)	R_1 (m Ω)	L_2 (mH)	R_2 (m Ω)	C_f (mF)	R_d (m Ω)		
0.225	3.54	0.0451	0	0.236	133.17		
Converter's Parameters							
V_{dc}	Rated Power	$[p^*, q^*]$	D_p	f_s (kHz)	J	D_q	K
425	100 kVA	Variable	260	10	0.026	11.8	1.18

' f_s ' stands for sampling frequency.

4.1.1.1 Performance in Islanded Mode

One of the advantages of GFM is its ability to work in islanded mode. It does not need a grid connection for its operation and can supply isolated loads. To verify its operation in islanded conditions, the active and inductive loads are changed in a periodic interval. The active load is changed from 5 to 85 kW with a step of 20 kW. Similarly, the inductive load is changed from 5 to 45 kVAR with a step of 10 kVAR. The time period for each change is 0.1 seconds. The reference active and reactive powers are set to zero, thus, the active and reactive powers solely depend on the droop controls for frequency and voltage respectively. The performance of the GFM scheme for such condition is given in Figure 4.2.

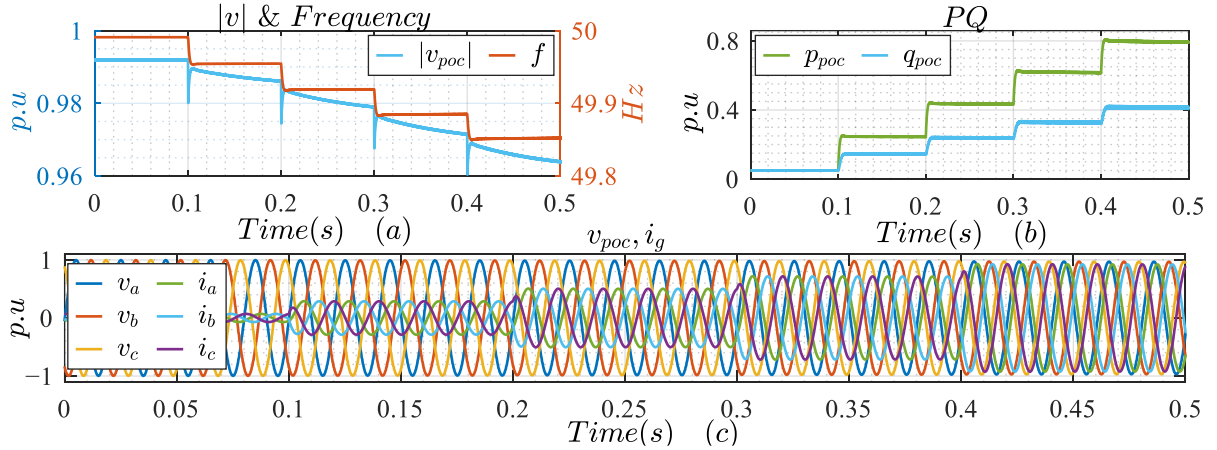


Figure 4.2: Performance of conventional Synchronverter in islanded mode; (a) frequency and terminal voltage, (b) active and reactive powers at POC, (c) three-phase measured voltage at POC and line currents on converter's side of POC

The above figure shows that the frequency drops as the load is increased. It is clear from subplot (a) that the frequency drops with the increase in active power demand. The frequency drops below the reference frequency because the reference real power is set to zero in this case. The subplot (b) shows that the injected active power is increased with the frequency drop. This increase in injected power is due to the negative frequency droop which limits the change in frequency. The subplot (c) shows the measured three phase voltages and currents, and it shows a smooth operation with the step power change

of 20 kW. Similarly, the performance of the converter for change in reactive power can be explained which contains a voltage droop. As the inductive load is increased, the capacitive reactive power of the converter is increased. It has a closed loop for the reactive power and voltage simultaneously and in this case, as the reference reactive power is zero, thus, the main driving factor is the voltage difference between the measured and reference value. In this case, the reference voltage is set to 1.0 p.u. Moreover, the voltage profile shows that the voltage does not achieve a steady state value in 0.1 seconds time-period but the change in voltage is small.

4.1.1.2 Performance in Grid-connected Mode

The performance of the conventional synchronverter scheme is tested for weak and stiff grid connections. The term ‘stiff grid’ is used here for the grids having very high short circuit power at POC. For weak grid, the SCP at POC is selected equal to the converter’s power rating and for stiff grid, it is selected as high as 800 times than the converter’s power rating. The grid frequency is set to 49.9 Hz for each grid connection and the response of the converter is observed. The reference active and reactive powers are periodically increased. The reference active power is increased from 5 to 85 kW with the step change of 20 kW in time interval of 0.1 seconds. Similarly, the reference reactive power is increased from 5 to 45 kVAR with the step change of 10 kVAR in the time interval of 0.1 seconds. The performance of the converter in stiff grid connected mode is given in Figure 4.3.

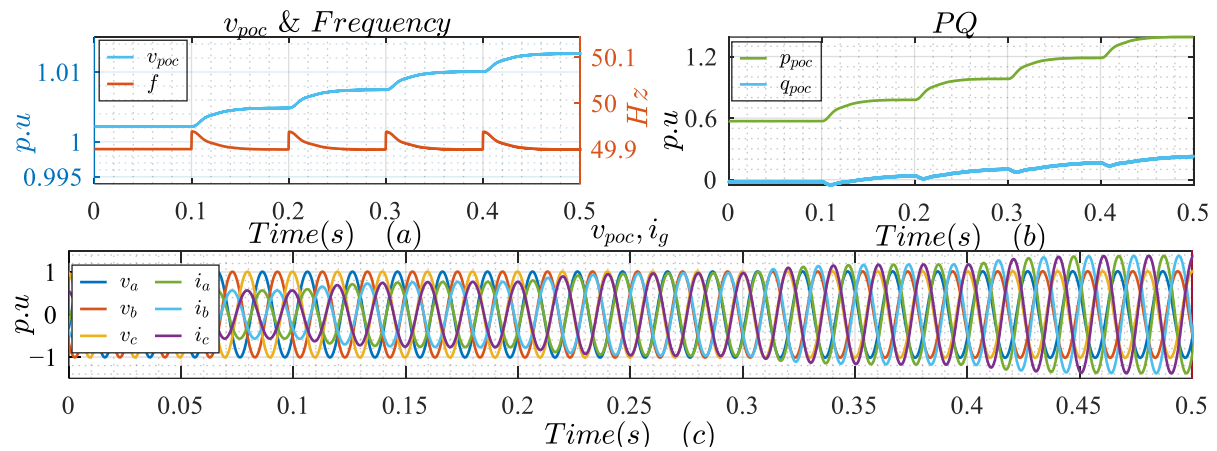


Figure 4.3: Performance of conventional Synchronverter in stiff grid-connection mode; (a) converter’s frequency and terminal voltage, (b) active and reactive powers at POC, (c) three-phase measured voltage at POC and line currents on converter’s side of POC

In the above figure, the frequency is the output of the p-f loop. The above figure shows that the active power injection of the converter is increased periodically. The measured real power is greater than its reference, this difference is due to the negative frequency droop which injects some additional active power support to raise the frequency to its nominal value (50 Hz). As the grid is stiff so its frequency does not change significantly due to the converter’s active power injection. Thus, a constant additional active power is injected in case of stiff grid with frequency below its rated frequency. The mismatch between reference and injected reactive power is noticeable and the reason for this is the terminal

voltage which is higher than the reference voltage (1 p.u. in this case). Thus, an inductive reactive power is introduced due to voltage control which minimizes the overall reference reactive power.

Moreover, the step change in converter’s frequency (output of p-f loop) is observed when a step change in reference active power is introduced. The frequency then settles down to the grid’s frequency. This change in frequency and its speed to return to its steady state level depends on the inertia of the p.f loop and droop constant (D_p). The measured three-phase voltage and current are plotted which shows that the peak phase current is increased to almost 1.5 p.u. This is due to the additional active power injection relative to frequency mismatch and due to the absence of current limiter scheme in the conventional control scheme.

The same procedure is repeated to study the performance of the synchronverter in a weak grid connection. The grid’s SCP at POC is equal to the converter’s power rating. The performance of the GFM for weak grid is given in Figure 4.4.

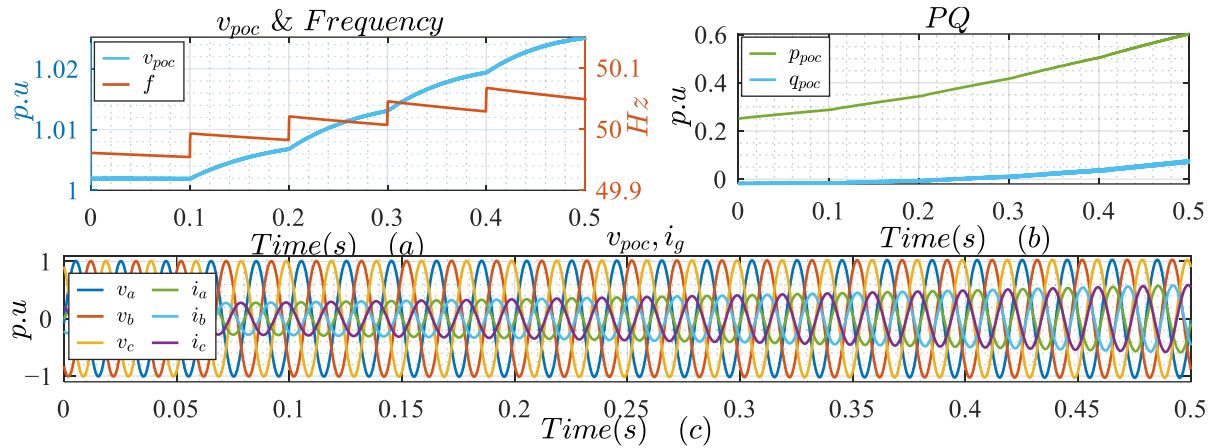


Figure 4.4: Performance of conventional Synchronverter in weak grid-connected mode; (a) converter’s frequency and terminal voltage, (b) active and reactive powers at POC, (c) three-phase measured voltage at POC and line currents on converter’s side of POC

Unlike stiff grid connection, the impact of active power injection on the frequency is more in this case. The actual injected real power is less than the reference active power and the reason for such behavior is the frequency change due to the active power injection by the converter. Overall, the impact of converter’s power injection is more in weak grids as compared to stiff grids. Moreover, the settling time in weak grids is high due to the external power loop. The grid is modeled with a three-phase voltage source behind an impedance; thus, the frequency is restored to its nominal value by the grid, but the settling time is highly influenced by the control of GFM.

In the above figure, it is clear that the frequency did not achieve its steady state value in the defined period of 0.1 seconds with the selected gains. However, it achieved a steady state in case of stiff grid with the same gains. This refers to the long-term stability against small disturbances. Hence the selection of droop gains and inertia constant is vital for the steady response of the converter. The D_p needs to be halved to achieve the steady state value in case of weak grid with the settling time of 3 seconds. Thus,

the gain values may be different for achieving a steady response in stiff and weak grids and a common solution can be a challenging task. The faster response can cause oscillations in frequency whereas the slower response may cause converter-driven stability issues related to the synchronization of GFM especially in post fault scenarios.

4.1.1.3 Limitations of Conventional GFM Scheme

From Figure 4.1, it is clear that this scheme can't ensure the current limitation of the converter. Moreover, it also does not offer synchronization scheme, but the synchronization scheme is vital especially in the initial grid-connection phase and in the post fault scenario to keep the converter synchronized with the grid. Moreover, it works fine only for balanced systems and in case of unbalanced conditions, it needs to eliminate the fluctuations in measured powers. It is also unable to follow the grid codes and priority injections are also not discussed. The coupling of real and reactive power loop (From equation (4.1)) can also cause stability issues in weak grids with lower X/R ratios. The ideal behavior of the GFM considered in this thesis is given below.

- i. It should maintain its voltage source behavior in all conditions.
- ii. It should offer a stable response in all conditions.
- iii. It should ensure the current limitation in all conditions.
- iv. In case of LVRT conditions with rated frequency, it should be able to support the grid's voltage.
- v. In the case of LVRT with frequency dip, it should inject the maximum real power to the system while ensuring the synchronization with the grid to enhance the converter-driven stability.
- vi. It should stay connected to the grid and offer stable response in case of high to low impedance faults.
- vii. It should be able to provide selective voltage support in case of unbalanced faults.
- viii. It should offer smooth transition from grid connected to islanded mode and vice versa.
- ix. It should offer unified control for weak to stiff grid connections.
- x. It should also ensure the small and large signal stability in islanded, and grid connected mode.

4.1.2 Possible Improvements in Conventional GFM Scheme

Considering the points discussed in the previous section, the improvements are possible in the normal/fault operation of the conventional control scheme. Some of the improvements are already discussed in the available literature and each of the improvements has its own pros and cons. Some new improvements are also suggested in this thesis which are given in Table 4.2.

Table 4.2: Possible improvements in conventional scheme of GFM

Sub-blocks	Possible Improvements
Synchronization	(a) Conventional dedicated synchronization unit (b) Self-synchronization
P-f loop	(a) Ramp reference power for smooth transitions (b) Maximum real power limit in case of LVRT conditions (c) Ensuring maximum real power injection in case of frequency dips while ensuring the converter-driven stability

	(d) Post fault recovery and synchronization
Q-V loop	(a) Positive and negative sequence Q-V loops (b) Ensuring grid code recommendations in case of faults
Priority injection scheme	(a) Development of six different priority injection schemes considering the conventional current limiting scheme
Current limitation and current control	(a) Cascaded voltage and current controllers (b) Damping Resistor (c) Limitation of maximum peak phase current (equivalent to DSVS)

4.2 Design of an Enhanced GFM Scheme

Based on the improvements, discussed in Table 4.2, an enhanced GFM scheme, with novel sub-blocks, is proposed which addresses the points mentioned in section 4.1.1.3. The key sub-blocks of the proposed scheme are discussed in this section.

4.2.1 Synchronization

The conventional synchronverter scheme does not include a dedicated synchronization unit. For GFL, the PLL works as synchronization unit but in GFM, a synchronization unit is required which could ensure a smooth connection with the public grid. It can also disconnect the converter in case of severe faults on the grid’s side. The conventional synchronization unit works on the same principles on which an SG is connected with the grid. It ensures that the phase sequence, frequency, and phase voltage on both sides of the coupling circuit breaker are the same and then it triggers the circuit breaker (CB) to connect both the systems. Based on the conventional synchronization method, the synchronization scheme is given in Figure 4.5.

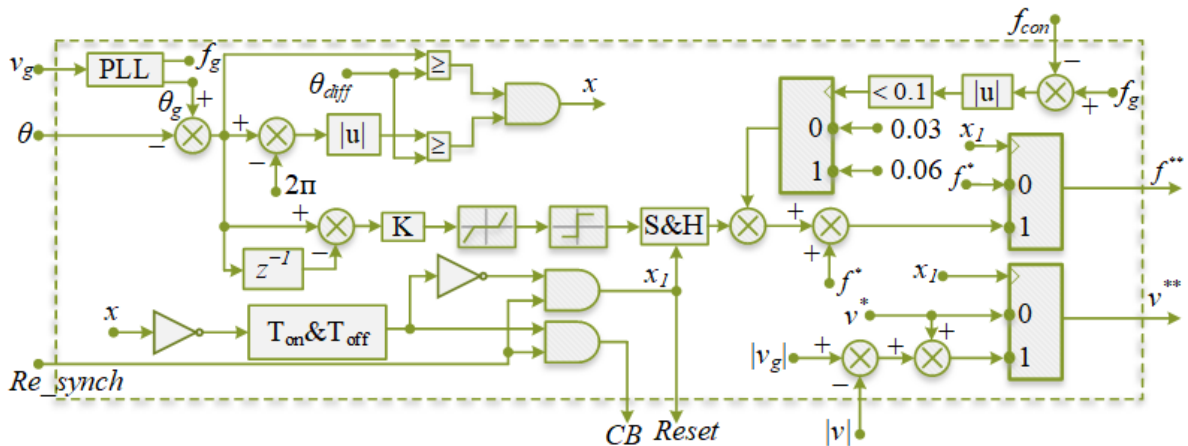


Figure 4.5: Conventional synchronization scheme

f_{con} in the above figure is the converter’s frequency assessed by p-f loop in hertz (Hz), θ is the voltage angle on converter’s side and θ_{diff} is the allowed voltage angle difference between grid and converter. ‘CB’ represents circuit breaker, and ‘S&H’ stands for sample and hold. T_{on} , T_{off} stand for on- and off-time delays. The above figure shows that the dedicated synchronization unit requires a PLL to assess the grid side frequency and phase angle. If the phase angle difference between the grid side and

converter side is below a predefined limit, then the CB is closed. If it is greater than the predefined limit, the reference frequency for p-f loop is perturbed and the perturbation sign is dependent on the sign of the angle difference between grid side and converter side. The frequency is perturbed up to 0.06 Hz depending upon the frequency difference between grid side and converter side systems. This perturbation is activated only during the synchronization process. Once the synchronization is completed, the reference frequency is set to its original reference value. As the reference frequency is perturbed to achieve the synchronization, the $\Delta\omega$ in p-f loop is reset during this process. Like the perturbation in reference frequency, a perturbation in the reference voltage is also introduced based on the voltage difference on both sides of the CB.

On- and off- time delays are introduced to avoid the temporary change upon the closure of the CB. If the resynchronization signal is false or the angle difference on both side of the CB is more than the predefined limit, then the CB is open. The resynchronization process starts as soon as the resynchronization signal is activated (true). The performance of this scheme for synchronization with the different frequency system is discussed below.

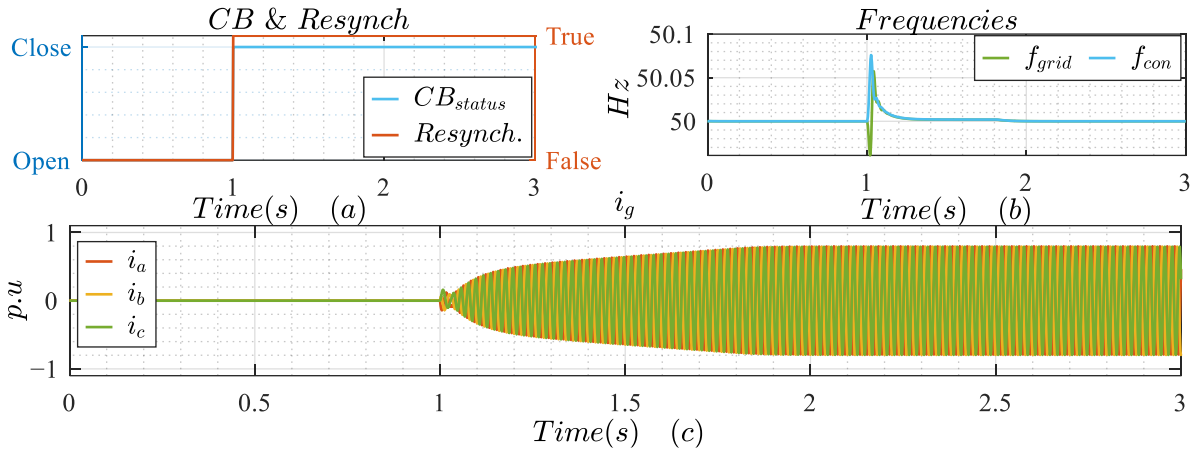


Figure 4.6: Performance of conventional synchronization unit for 50 Hz system; (a) resynchronization signal and CB status, (b) frequencies of grid and converter, (c) measured line currents on converter's side of POC

f_{con} stands for the converter's frequency which is assessed by the p-f loop of the GFM. The above figure shows the performance of the conventional dedicated synchronization unit to synchronize the GFM with a 50 Hz grid. Synchronization signal is activated at 1 second and the synchronization conditions are achieved instantaneously as both the grid and converter are operating at the same frequency. The subplot (b) shows the frequencies of both the grid and converter which are fairly in agreement even before the synchronization process. There is no load connected to the GFM. Thus, it supplies no current in islanded operation and after synchronization, the reference power is ramped up to 0.7 p.u. and the line currents corresponding to reference power are also ramped up after synchronization.

The same procedure is repeated to synchronize the GFM converter with a 49.9 Hz grid. The performance of the dedicated synchronization unit is presented in Figure 4.7.

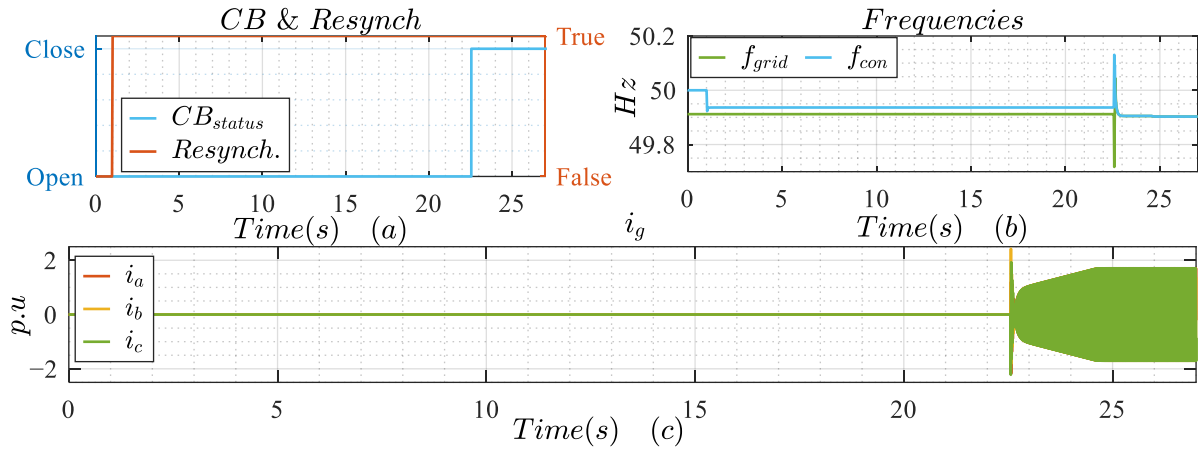


Figure 4.7: Performance of conventional synchronization unit for 49.9 Hz system; (a) resynchronization signal and CB status, (b) frequencies of grid and converter, (c) measured line currents on converter's side of POC

The above figure shows that the synchronization process takes more time to synchronize a 50 Hz islanded GFM with a 49.9 Hz grid. The synchronization time is also dependent on the perturbation frequency which is limited to 0.06 Hz in this dedicated unit. Moreover, it also causes a temporary high current due to the activation of p-f loop and changing the reference frequency after the synchronization. Subplot (b) shows that the converter's frequency is perturbed and made closer to the grid's frequency as the synchronization process is started at 1 second. The subplot (c) shows higher line currents as compared to the 50 Hz grid connection. This is due to the additional active power injection by the negative frequency droop as the reference frequency for the converter is 50 Hz.

The performance of this synchronization unit is also discussed to synchronize the 50 Hz GFM with a 50.1 Hz grid. Its results are given in Figure 4.8.

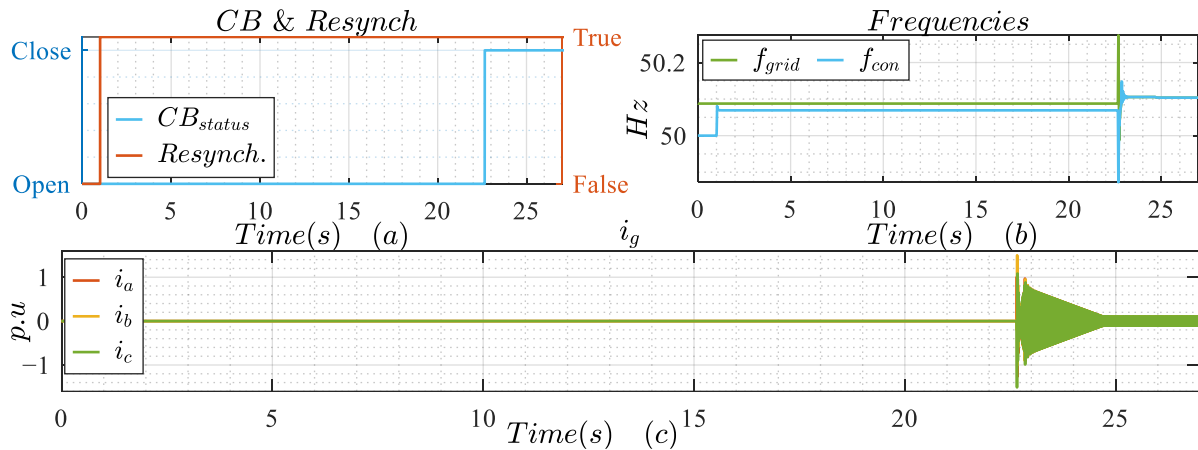


Figure 4.8: Performance of conventional synchronization unit for 50.1 Hz system; (a) resynchronization signal and CB status, (b) frequencies of grid and converter, (c) measured line currents on converter's side of POC

The above figure shows that it successfully synchronized a 50 Hz islanded GFM converter with a 50.1 Hz grid. The subplot (b) shows that the converter's frequency is positively perturbed as soon as the synchronization process is initiated. The initial current peaks are due to the activation of the p-f loop and change in reference frequency after the synchronization. The steady state current is less than the

initial current after the synchronization and the reason for this is the higher grid frequency which caused a negative power due to the frequency droop.

In conclusion, it can be stated that the dedicated synchronization unit can ensure the synchronization of the GFM converter with the grid. However, it needs a dedicated PLL for estimating of the frequency and phase angle of the grid. It also causes some initial over currents after synchronization. Synchronization time varies and depends on several factors i.e., actual grid frequency, limit for frequency perturbation, and minimum allowed angle difference for synchronization.

In [97], the authors proposed a new synchronization technique which does not require a dedicated PLL to assess the frequency and phase angle on the grid side. This technique is termed a self-synchronization capability as no dedicated unit is required for synchronization process. Figure 4.9 shows the coupling of a SG with the grid through a reactance.

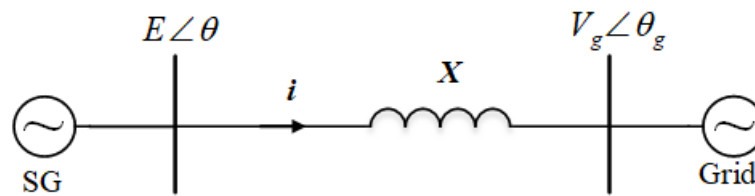


Figure 4.9: Coupling of SG with grid

Where ‘E’ represents the voltage phasor at SG terminal and ‘X’ represents the line reactance. For the above figure, the mathematical expressions for the active and reactive power flow are given in equation (4.4).

$$P = \frac{3V_g E}{2X} \sin(\theta - \theta_g) \quad (4.4)$$

$$Q = \frac{3V_g}{2X} \{E \cos(\theta - \theta_g) - V_g\}$$

For synchronization, the voltage angle and magnitude of both the sources should be identical which leads to zero active and reactive power. Thus, if the active and reactive power are simultaneously zero then it can be connected to the grid seamlessly, but the challenge is to achieve the zero active and reactive power relative to the grid side voltage without having the physical connection with the grid. The authors proposed the following scheme to address this challenge.

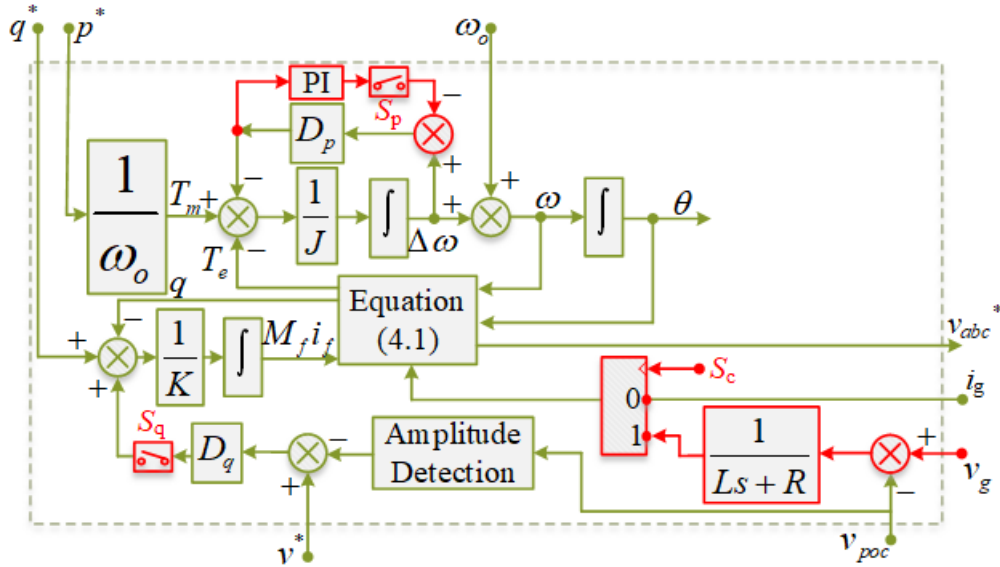


Figure 4.10: Control scheme of self-synchronized synchronverter

In the above figure, red color shows the additional connections to achieve the self-synchronization capability for the synchronverter. ‘L’ and ‘R’ represent virtual inductance and resistance respectively. For synchronization, the reference active and reactive powers are set to zero. The external voltage control loop is deactivated by opening the switch S_q . The impact of frequency droop is cancelled with the help of a PI controller (by closing the switch S_p). Finally, a virtual current is fed for the calculation of active and reactive powers which is derived from the difference of grid side voltage and GFM voltage (S_c set to 1). A low pass filter (LPF) is used to assess the virtual current from the voltage difference on both sides of CB. It is important to mention here that this is not the physical current as the CB is still open. The gain and time constant for LPF can be calculated based on the filter’s parameters. Thus, if there is difference in angle or voltage on both sides of CB, a virtual current flows which results in non-zero active and reactive power. The p-f and Q-V loops adjust the phase angle and voltage magnitude respectively to match it with the grid side and once both the sides are matched, the virtual current drops to zero and results in zero active and reactive powers. Hence, the trigger signal for CB can also be derived from the real time voltage difference (ΔV_{gc}) on both sides of the CB and if the magnitude of the ΔV_{gc} is less than the predefined level then the CB can be closed. The control layout for the CB triggering is given in Figure 4.11.

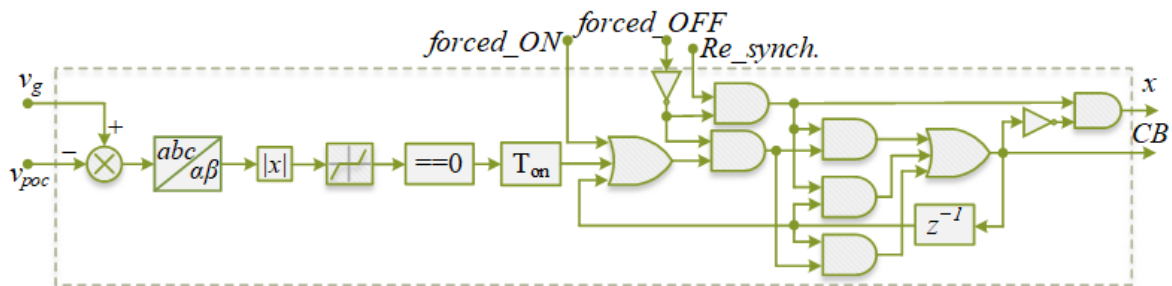


Figure 4.11: CB triggering scheme for self-synchronization technique

In the above figure, the synchronization conditions are assessed with the help of real time voltage difference on both sides of CB. This difference is minimized if the frequency and voltage magnitudes are same on both sides of CB. To eliminate the false triggering, an on-time delay is introduced as the voltage difference may go to zero for a very short time due to frequency mismatch. Once the synchronization conditions are achieved, the CB latches its state unless it is switched off manually with “forced_OFF” input. Similarly, it can also be manually closed with the help of “forced_ON” input. The ‘x’ signal in the above figure initiates the synchronization process by closing S_p , opening S_q and setting S_c equal to 1.

The performance of self-synchronization technique is verified for 50 Hz, 49.9 Hz and 50.1 Hz grid connections. A synchronization signal is activated at 1.2 seconds. The reference active power is set to 0.5 p.u for this analysis which forces a line current after synchronization. Moreover, in islanded condition, there is no load connected to the converter. Thus, the line current before synchronization is zero. The response of the self-synchronization technique to synchronize with 50 Hz grid is given in Figure 4.12.

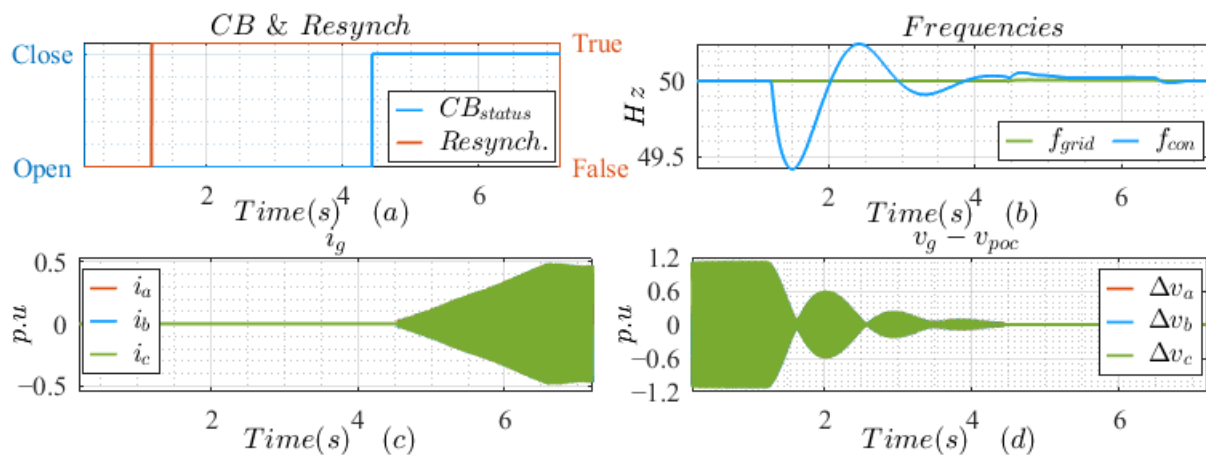


Figure 4.12: Performance of self-synchronization technique for 50 Hz system; (a) resynchronization signal and CB status, (b) frequencies of grid and converter, (c) measured line currents on converter’s side of POC, (d) voltage difference between grid and GFM converter

The above figure shows that the self-synchronization scheme successfully synchronizes the GFM with the grid. A higher frequency perturbation is observed with self-synchronous technique as compared to the conventional synchronization unit. The frequency perturbation depends on the tuning of the PI controller to cancel out the impact of frequency droop. Subplot (c) shows that the synchronization is performed smoothly, and no current peaks are observed. Subplot (d) presents the real time voltage difference on both sides of the CB. It shows that the difference of voltage is decreased as the synchronization process starts and upon its completion, voltages on both sides of the CB are identical. The performance of this technique for 49.9 Hz grid synchronization is given in Figure 4.13.

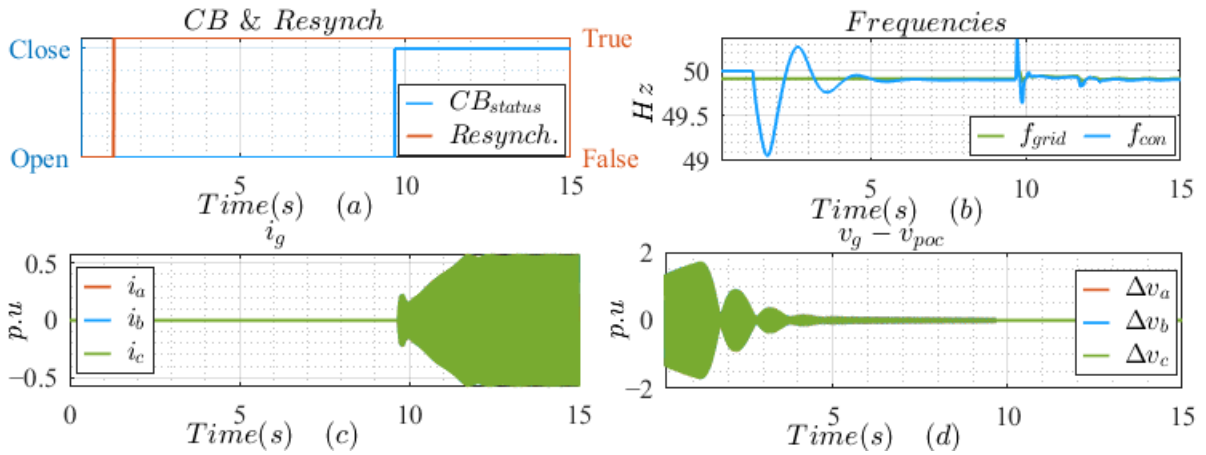


Figure 4.13: Performance of self-synchronization technique for 49.9 Hz system; (a) resynchronization signal and CB status, (b) frequencies of grid and converter, (c) measured line currents on converter's side of POC, (d) voltage difference between grid and GFM converter

The above figure shows that this scheme successfully synchronizes the 50 Hz islanded GFM converter with 49.9 Hz grid. Unlike conventional dedicated unit, this scheme ensures the smooth connection, and no current peaks are observed after synchronization. However, the time for synchronization and the frequency fluctuations are more as compared to the first scenario in which the grid frequency was 50 Hz. Moreover, the higher line currents after synchronization are due to the frequency droop which forced the converter to inject more active power for frequency support.

The performance of this technique to synchronize a 50 Hz islanded converter with a 50.1 Hz grid is given in Figure 4.14.

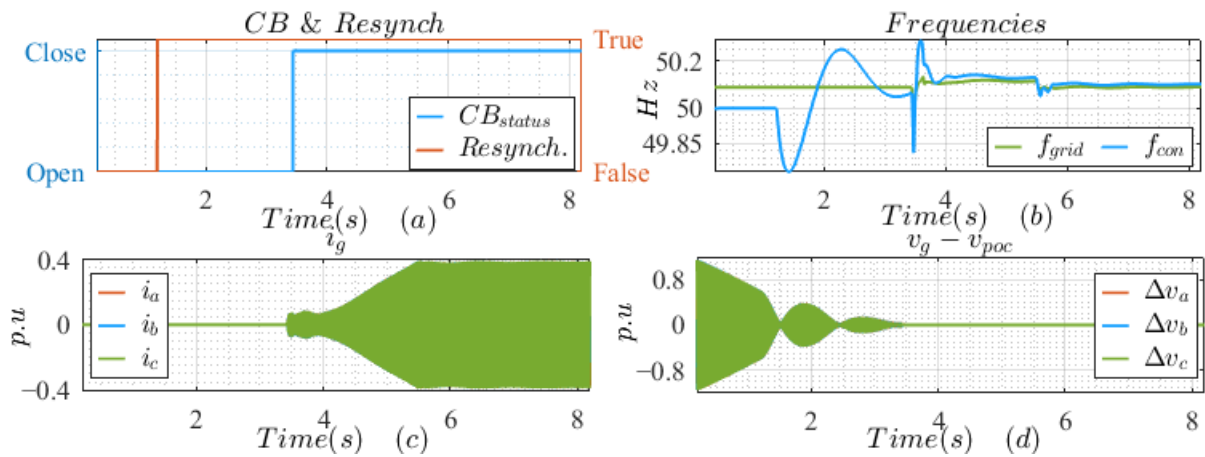


Figure 4.14: Performance of self-synchronization technique for 50.1 Hz system; (a) resynchronization signal and CB status, (b) frequencies of grid and converter, (c) measured line currents on converter's side of POC, (d) voltage difference between grid and GFM converter

From the above figure, it is clear that this scheme is able to synchronize the 50 Hz converter with a 50.1 Hz grid smoothly. The time for synchronization is also small as compared to the first two scenarios. It is due to the negative frequency droop which helps the p-f loop to quickly achieve the synchronization conditions. The comparison of both the techniques for different grid frequencies is given in Table 4.3.

Table 4.3: Performance comparison of dedicated synchronization technique and self-synchronization

<i>Method</i>	<i>Parameters</i>	<i>49.9 Hz Grid</i>	<i>50 Hz Grid</i>	<i>50.1 Hz Grid</i>
Dedicated synchronization unit	Time taken for synchronization (s)	22.5	0.0005	22.5
	Peak frequency fluctuation during synchronization (Hz)	0.23	0.08	0.27
	Smooth connection	✗	✓	✗
Self- synchronization technique	Time taken for synchronization (s)	8.5	3.2	2.2
	Peak frequency fluctuation during synchronization (Hz)	1.2	0.82	0.52
	Smooth connection	✓	✓	✓

The above table shows that the frequency fluctuations during the synchronization are less with the dedicated synchronization unit, but it takes more time for synchronization if the grid frequency is different than the converter's frequency. Moreover, it takes the same time if the grid frequency is perturbed negatively or positively. The reason for such behavior is the deactivation of the complete p-f loop during synchronization process in case of dedicated synchronization unit. Moreover, it is also unable to ensure a smooth connection for different grid frequencies. On the other hand, the self-synchronization technique offers fast and smooth synchronization. However, its drawback is the higher initial frequency oscillations when the synchronization process is initiated.

Moreover, in self-synchronization technique, the time for synchronization and frequency oscillations are higher for grid frequencies less than the rated frequency and are less for the higher grid frequencies. The reason for such behavior is the p-f loop in which the negative frequency droop helps the PI controller if the grid frequency is greater than the converter's rated frequency. The lower frequency has the opposite effect and opposes the PI controller due to which it takes more time to achieve the grid frequency. The other advantage of the self-synchronization technique is that it does not need a dedicated PLL for the frequency and phase angle assessment on the grid side. Thus, it can be concluded that the self-synchronization technique is robust provided the LPF and PI controller are properly tuned.

4.2.2 Enhanced Real Power-Frequency Control

The performance of the real power-frequency (p-f) control is vital for stable operation of the GFM in different operating conditions. Due to the voltage source behavior of GFM, it is very important to ensure that the angular difference between the GFM and grid does not exceed from a predefined limit. Moreover, two coupled ac systems with different frequencies may have a drastic effect, thus, it is important to ensure that the frequencies of GFM and grid are in good agreement. It becomes challenging in faulty situations due to the limited current handling capability of the converters. Thus, in case of frequency dips, the GFM can support the grid up to a certain power level due to its limited current handling capability. Beyond this level, it is important that the GFM should still supply the maximum possible real power to the grid and should ensure the synchronization with the grid. Some hybrid schemes suggest shifting to GFL mode under such conditions or simply disconnecting the GFM to save

the system from negative effect due to frequency mismatch. Thus, it is a challenging task to keep the voltage source behavior of GFM in case of frequency dips and operating it at maximum possible real power without causing frequency mismatch.

The other important factor is the limited active power supply capability of ac voltage source under LVRT conditions. It is important for the p-f loop to assess the maximum possible real power which can be transferred based on the terminal voltages of grid and converter. It should ensure that the sum of reference real power and frequency droop share does not exceed this level. The other important function of p-f loop is to ensure the synchronization in case of fault and post fault scenarios. In case of fault/post fault, the phase angle jump on the grid side may cause power oscillations and may lead to converter-driven instability. Thus, the p-f control should be robust to respond quickly to such phase angle jumps on the grid's side. The control layout of the p-f loop for the improved GFM is given in Figure 4.15.

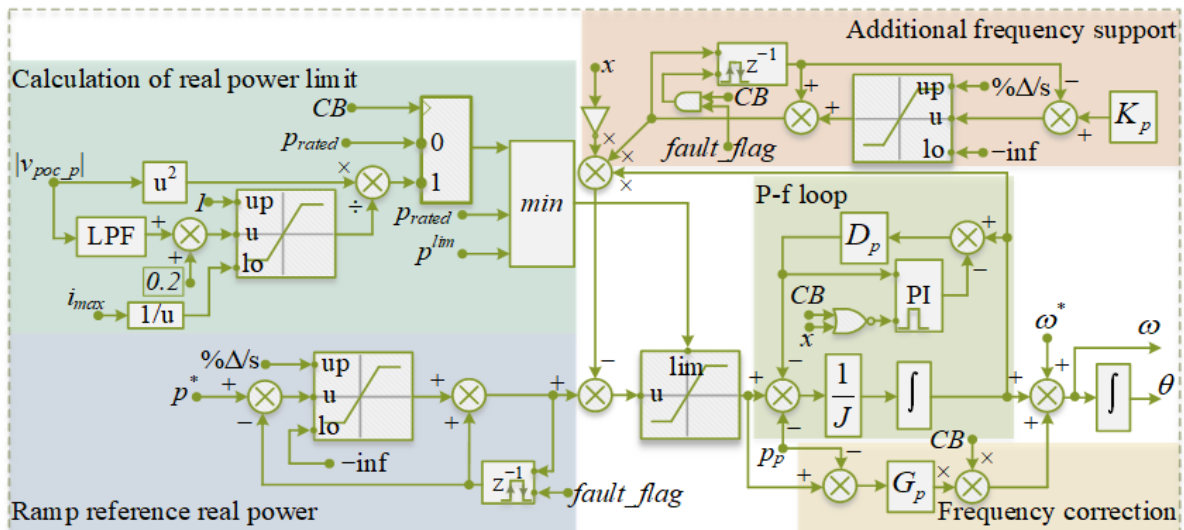


Figure 4.15: Control layout of real power-frequency control for improved GFM

p_{rated} stands for the rated real power of the converter (1 p.u.), p^{lim} represents the limit for the real power that is decided by the priority injection scheme, K_p is the proportional constant for additional frequency support, G_p is the proportional gain for frequency correction and $\% \Delta/s$ represents the percentage rate of change. The above diagram is comprised of different sub-blocks which ensure different design objectives. These sub-blocks are briefly explained here.

To ensure the smooth post fault operation, the reference real power should be ramped up. The ramp reference real power block in the above figure ensures that the reference power is ramped up at the start of voltage dip and in post fault conditions. The rate of change for the reference real power can be adjusted externally. It helps to ensure synchronization and smooth operation, particularly in post fault scenarios. In case of voltage dips, the maximum real power which can be transmitted between two ac voltage sources is dependent on the voltage level and the coupling impedance. Due to the limited current handling capability, the virtual coupling impedance is changed based on the terminal voltage. The

minimum virtual impedance corresponds to the maximum converter's current with solid ground fault at POC. The maximum possible real power transfer may be less than the real power limit calculated by the priority injection block. It is important to mention here that such power limitation is the result of two coupled ac voltage sources. Thus, in the case of islanded operation, it is not considered to calculate the real power limit.

The conventional p-f frequency droop is bypassed for synchronization, and it is also used to follow the grid virtually in case of grid connected mode. An additional frequency support loop is introduced in grid connected mode to support the frequency. This loop is also deactivated at the time of synchronization. The gain of this loop is changed when a fault is sensed. This ensures the stability of the p-f loop in case of sudden dual faults (voltage and frequency dips). Finally, a proportional frequency correction is performed for sudden voltage angle change in case of post faults. It is important to mention here that the positive sequence real power is used as measured power to avoid the power oscillations in case of unbalanced conditions. The resulted frequency of p-f loop is used for voltage and current sequence extraction on the converter's side.

To test the designed p-f loop, ramp and step frequency changes are introduced in the grid after the synchronization of the converter and the response of the converter is observed in such conditions. The input parameters for such tests are given in Table 4.4.

Table 4.4: Parameters for performance testing of p-f control of improved GFM

<i>Given Parameters</i>					
p^* (p.u)	% dp^*/dt (% p.u/s)	i_{max} (p.u)	P_{rated} (p.u)	p^{lim} (p.u)	G_p
0.5	25	1.2	1.0	1.2	0.346
K_p	% dK_p/dt (%/s)	D_p	PI	J	ω^* (p.u)
50	25	48.75	[0.0432 19.2]	1	1

The power rating of the converter is 100 kVA and the grid's SCP at POC is 800 kVA for these tests. The response of the p-f control for ramp frequency change is given in Figure 4.16.

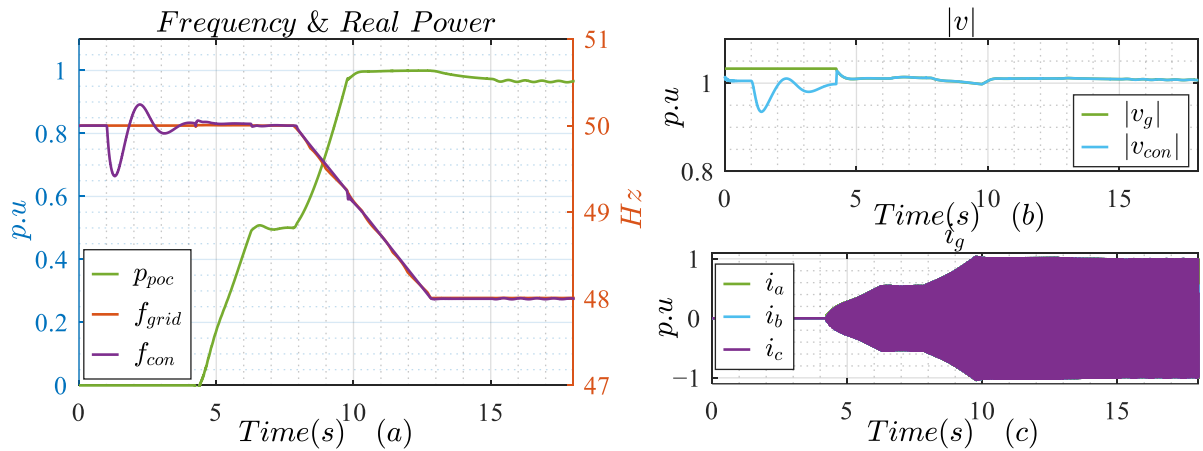


Figure 4.16: Performance of p-f control for ramp change in grid's frequency; (a) frequencies of grid and converter, and injected real power, (b) magnitude of grid and converter's voltage phasors, (c) measured line currents on converter's side of POC

v_{con} in the above figure represents the voltage on the converter's terminal. For the above ramp test, a synchronization signal is initiated at 1 second, the converter is synchronized with the grid around 4.5 seconds. A frequency ramp is introduced with the slope of -0.4 Hz/s at 8 seconds. The duration for this frequency ramp is 5 seconds and grid achieved a frequency of 48 Hz at 13 seconds.

The subplot (a) shows that the converter injects more real power to support the grid in case of frequency dips. It keeps on injecting more real power as the frequency keeps on dropping. At 49 Hz, the converter's maximum power level is reached which is in accordance with the parameter given in Table 4.4. Once the maximum power rating of the converter is reached then its real power injection is stabilized at that point even though the frequency is still dropping. This is important to ensure synchronization and keep on supporting the grid in case of frequency dip. Moreover, the converter is also able to ensure the synchronization after achieving its maximum real power. The subplot (b) shows that the voltage magnitude on both sides of the CB is the same in case of frequency dip. The subplots (a) and (b) confirm the synchronization between two sources in such conditions. The subplot (c) shows the measured line currents at POC which are associated to the real power injection. Hence, this test confirms that the above discussed p-f control is able to ramp up the real power to ensure the smooth transition. Moreover, it also ensures synchronization in case of large frequency dips.

The response of the designed p-f control is also investigated against a step change in grid's frequency. Normally the step change in grid's frequency is unlikely but a fast ramp change in frequency may be experienced in a weak grid. The grid's frequency steps down to 49 Hz at 8 seconds, and it is restored at 13 seconds. With this test, the performance of the converter in post fault can also be investigated. The results are given in Figure 4.17.

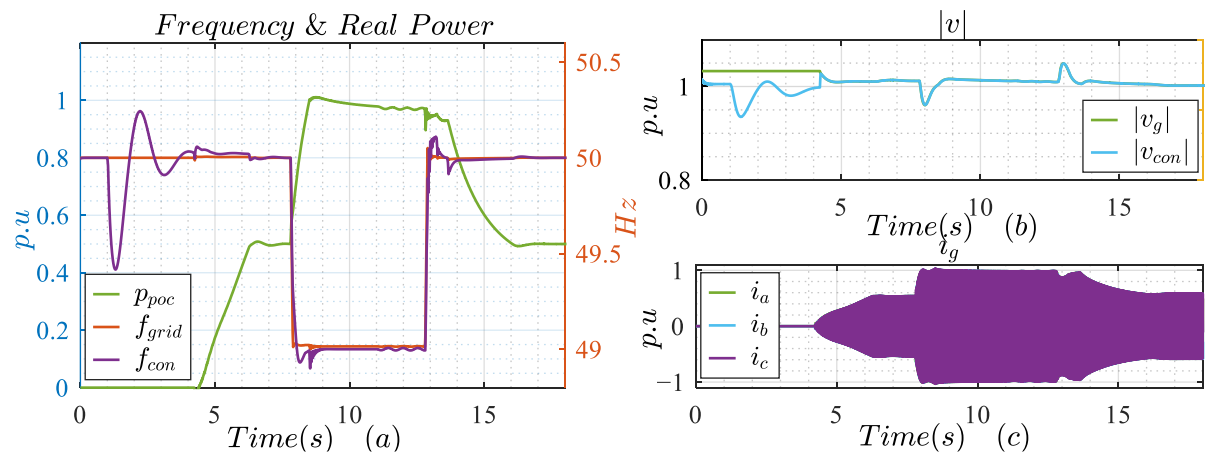


Figure 4.17: Performance of p-f control for step change in grid's frequency; (a) frequencies of grid and converter, and injected real power, (b) magnitude of grid and converter's voltage phasors, (c) measured line currents on converter's side of POC

The subplot (a) in above figure shows that the frequency of the grid and the computed frequency by p-f control of GFM are in good agreement when a step change in grid's frequency is introduced. Moreover, the converter's real power increases to its maximum level as the frequency dips down. The

real power then settles to a lower steady state level. The reason for lower steady state power is the droop gain and PI controller. The PI controller is responsible for cancelling the effect of droop but due to its gains, it takes a definite time to completely cancel out the effect of droop control. Thus, in the start, the injected real power is higher than its steady value. Moreover, when the frequency is restored, the real power is smoothly changed to its initial level. The subplot (b) shows that both voltages are in good agreement although a voltage change is recorded against the step change in frequency which is due to the coupling of real power and voltage as the X/R ratio of the grid is 5 for these tests. Subplots (a) and (b) confirm that the synchronization between grid and converter is ensured in all operational phases of this test.

Thus, from the above discussed results, the performance of the real power control is confirmed against following points.

- Ramp power changes for smooth transition.
- Ensure maximum real power injection in case of frequency dips while ensuring converter-driven stability.
- Post fault recovery and ensure the synchronization in different operational phases.

4.2.3 Enhanced Reactive Power-Voltage Control

The performance of the reactive power-voltage control is vital for the stable operation of GFM in all operating conditions. To address the unbalanced conditions, the Q-V control of the improved GFM includes the positive and negative sequence voltage controls. It can be designed to follow the GCR i.e., injection of reactive current in case of voltage dips while maintaining its voltage source behavior. The natural response of the voltage source against a faulty condition is also proposed in new GFMs. Unlike GFL converter, the slow Q-V loop reacts quickly against any change due to the voltage source behavior (behind an impedance) of the GFM. Thus, the slow Q-V control actually reacts quickly against faulty conditions. On the other hand, due to large voltage change in post fault conditions, the quick response of Q-V loop can ensure the post fault stability of the GFM. Moreover, it also controls the reactive power injection and closed loop voltage control in normal conditions. The negative sequence Q-V control is only activated when a predefined negative sequence voltage level is observed at POC. The control layout of the Q-V control for the improved GFM is given in Figure 4.18 where T_{on} is the on-time delay whereas K_{qp} and K_{qn} represent the proportional gains for positive and negative sequence Q-V controls respectively. The superscript 'lim' stands for the limits for the respective parameters that is decided by the priority control scheme whereas ' v_{n_der} ' represents the minimum negative sequence voltage to activate the negative sequence Q-V control.

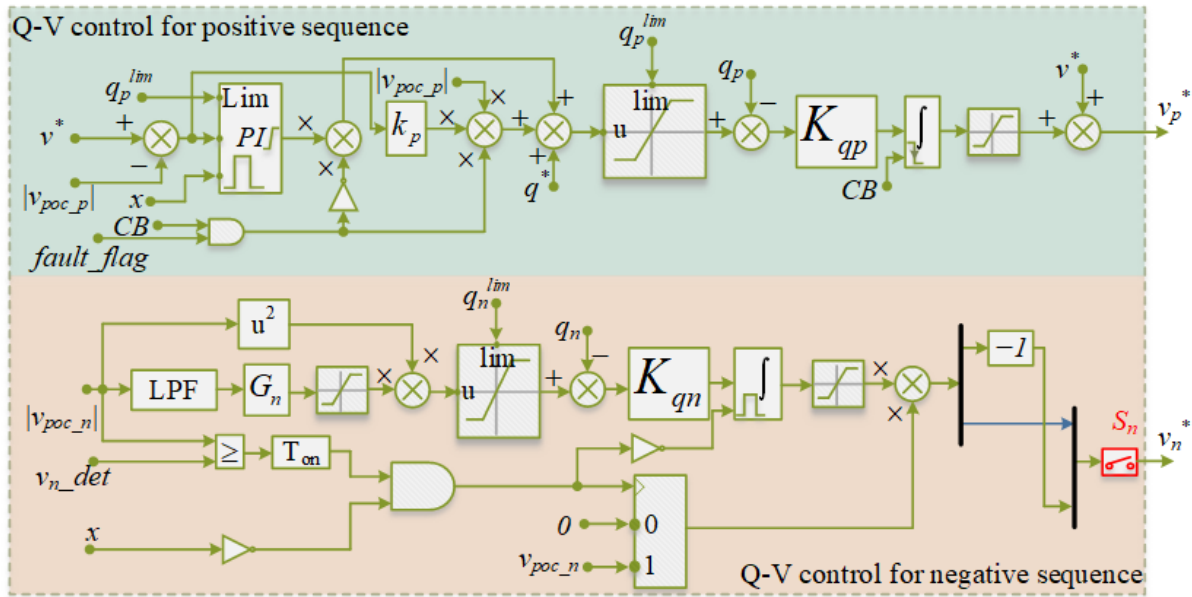


Figure 4.18: Control layout of reactive power-voltage control for improved GFM

The above figure presents the positive and negative sequence Q-V controls. The positive sequence Q-V control is responsible for voltage control in normal conditions. It is also responsible to inject the reference reactive power in addition to the reactive power required for maintaining the terminal voltage in specified limits. In normal conditions, a PI controller or a fast p-controller can be used to ensure the terminal voltage in specified limits. In faulty situations, the p-controller is used instead of the PI controller. The PI controller results in very high reactive power demand and due to the limited current handling capability of the converter, no capacity is left for the p-f control in such conditions, and it also poses problems in post fault conditions. To follow GCR, the reactive power demand can be proportional to the voltage dip and the proportional gain. The limit for the positive sequence reactive power is decided by the priority control which will be discussed later. It is important to mention here that the first response of the GFM against any change in the operating conditions is according to the natural response of a voltage source and the specific power injection is prioritized as soon as the respective controls starts to react against that change. The reactive power mismatch is integrated to decide the magnitude of the reference voltage. To ensure the smooth transition, the integrator is reset when the converter shifts from grid connected to islanded mode.

Due to the voltage source behavior of GFM, it is able to naturally respond to the unbalanced conditions and cascaded voltage and current controllers try to achieve the voltage uniformity if no negative sequence is introduced in the internal reference voltage signal (before the voltage and current controllers). It results in minimum VUF. However, the negative sequence injection in such scenarios is uncontrolled and depends on the terminal conditions. It also results in large real power fluctuations. To control the large fluctuations and to control the negative sequence injection, the reference negative sequence voltage magnitude is decided by the above given control scheme. The angle for the reference negative sequence voltage is assessed from the measured negative sequence voltage at POC. Thus, if

S_n is closed in the above figure, then the negative sequence injection is controlled, and the real power oscillations are less as compared to the case in which S_n is open and negative sequence injection is uncontrolled.

The input parameters of Q-V control for performance tests are given in Table 4.5. The SCP of grid at POC is 1 MVA and the rated power of the converter is 100 kVA.

q^* (p.u.)	% dq^*/dt (% p.u./s)	v^* (p.u.)	K_{qp}
0, 0.2, 0.5, 0.7	70	1.0	1.06
k_p	G_n	K_{qn}	PI
2	8	2.12	[2 0]

To test the performance of the Q-V control in normal conditions, the reference reactive power is changed from 0 to 0.2 to 0.5 and then to 0.7 capacitive reactive power with a time step of 5 seconds. The reference real power is 0.5 p.u. The performance of the Q-V loop is presented in Figure 4.19.

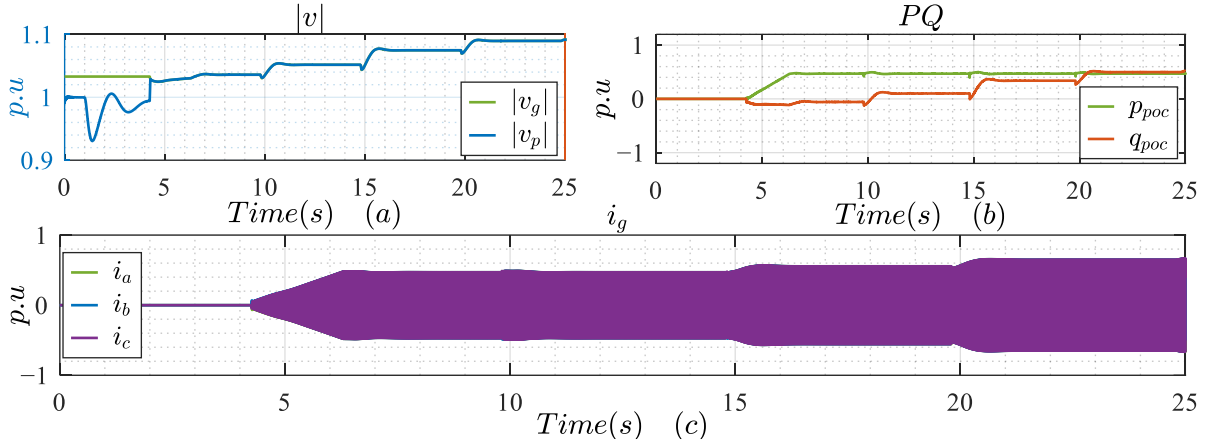


Figure 4.19: Performance of Q-V control in normal conditions; (a) voltage on both sides of coupling CB, (b) real and reactive powers at POC, (c) measured line currents on converter's side of POC

The above figure shows that the grid connection is established at 4.2 seconds. Subplot (b) shows a ramp change in real and reactive power once the grid connection is established. The rate of change for the reference reactive power is much higher than the one for the reference active power. Zero reference reactive power is set till 10 seconds and the results show that the injected reactive power is inductive during this period. The reason for this is the voltage control which injects some inductive reactive power as the terminal voltage is higher than its reference (1 p.u.). From 10 to 15 seconds, the reference reactive power is set to 0.2 p.u. The measured reactive power at POC is 0.1 p.u., in this duration due to the voltage rise which injects more inductive reactive power in reference resulting in a lower reference reactive power. The same is true for other reference power levels. The subplot (c) shows the measured line currents at grid's side and a change in current level evident due to change in reference reactive power. The performance results of Q-V control for normal operation are given in Table 4.6.

q^* (p.u.)	V_{poc} (p.u.)	q_{poc} (p.u.)
0	1.04	-0.06

0.2 (capacitive reactive power)	1.05	0.10
0.5 (capacitive reactive power)	1.08	0.34
0.7 (capacitive reactive power)	1.09	0.50

To test the performance of Q-V control in unbalanced faulty conditions, a L-L fault is introduced between phase ‘b’ and ‘c’ at POC. The fault is introduced at 9.8 seconds and the duration of the fault is 5 seconds. A damping resistor technique is used to ensure the current limit of the converter which will be discussed later in this chapter. The performance of the Q-V control for uncontrolled negative sequence injection is given in Figure 4.20.

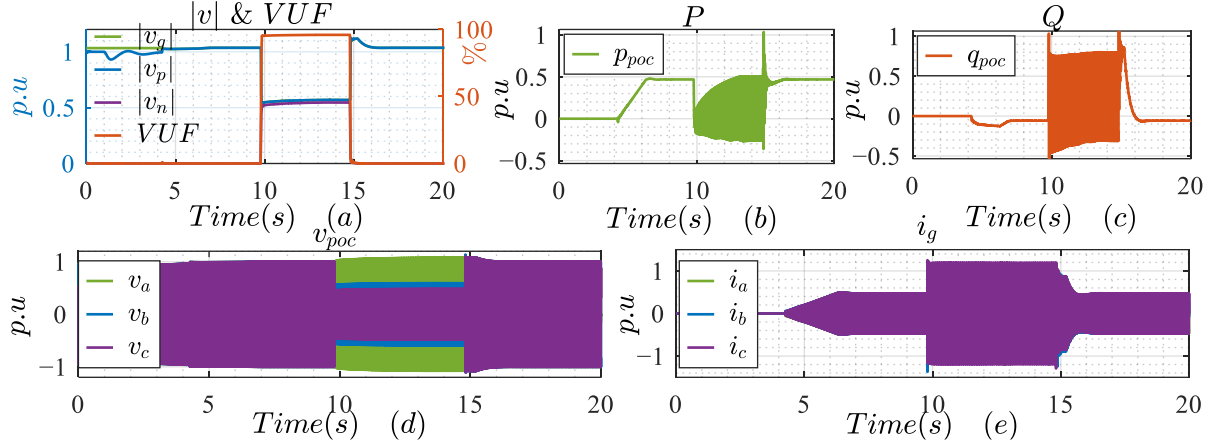


Figure 4.20: Performance of Q-V control in unbalanced faulty conditions with uncontrolled negative sequence injection; (a) sequence voltages and VUF at POC, (b) real power at POC, (c) reactive power at POC, (d) measured phase voltages at POC, and (e) measured line currents on converter’s side of POC

The above figure shows that the GFM is able to provide selective voltage support to the faulty phases due to its voltage source behavior. No negative sequence voltage is introduced in the reference voltage. The voltage controller results in different reference line currents to achieve uniformity among phase voltages. The maximum line reference current is limited to the maximum current capacity of the converter. It results in minimum VUF as it can change the negative sequence injection to minimize the voltage difference among different phases. However, the negative sequence current injection is not controllable in this technique as it is fed depending on the actual terminal conditions. In case of L-L fault, it results in non-zero active and reactive power in the negative sequence. The real and reactive power oscillations are also shown in the above figure. Without controlling the negative sequence injection, these oscillations are also not being controlled. The subplots (d) and (e) show the measured phase voltages and line currents on converter’s side of POC respectively. It confirms unbalanced conditions at POC along with the different current injection in each phase. The current limit is also confirmed from subplot (e).

The same fault is repeated to analyze the performance of the Q-V control with controlled negative sequence injection. The S_n in Figure 4.18 is closed in this case. The results are given in Figure 4.21.

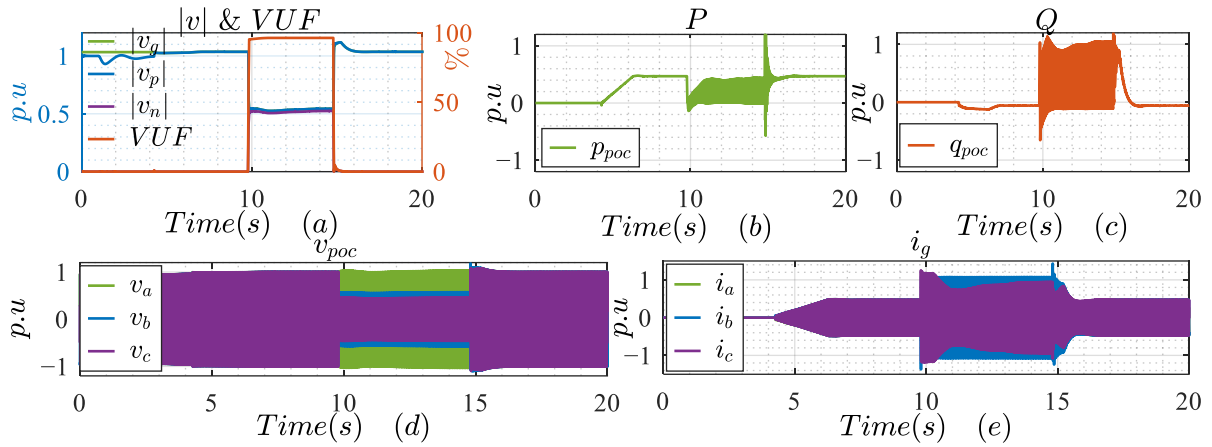


Figure 4.21: Performance of Q-V control in unbalanced faulty conditions with controlled negative sequence injection; (a) sequence voltages and VUF at POC, (b) real power at POC, (c) reactive power at POC, (d) measured phase voltages at POC, and (e) measured line currents on converter's side of POC

The above figure shows that the VUF is slightly higher with controlled negative sequence injection. However, it results in smaller oscillations in the real power due to controlled negative sequence injection. The current in the faulty phase is higher than the healthy phase and the current limit is also ensured. A momentary high phase current is observed in the post fault scenario with this scheme. The reason for this is the negative sequence voltage in the reference voltage for a couple of cycles after the fault removal which is due to the delay in resetting the integrator of Q-V control for negative sequence. Moreover, Q-V control with uncontrolled negative sequence injection is the initial response of the GFM against an unbalanced fault because this is the natural response of a three-phase voltage source behind an impedance. However, after some time (depending upon the negative sequence voltage controller), the negative sequence injection can be controlled by introducing appropriate reference negative sequence voltage phasor.

Both the schemes (controlled and uncontrolled negative sequence injection) can be compared for VUF and oscillations in the real power. The comparison results are presented in Figure 4.22.

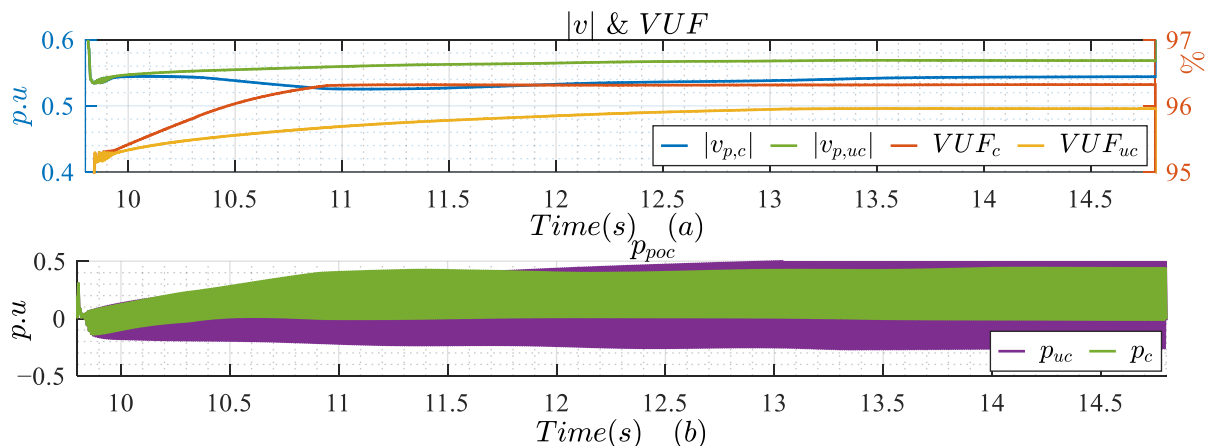


Figure 4.22: Performance comparison of controlled and uncontrolled negative sequence injection; (a) magnitude of sequence voltage phasors and VUF at POC, (b) real power at POC

In the above figure, the subscript ‘c’ is used for controlled scheme and ‘uc’ used for uncontrolled scheme. The subplot (a) shows that uncontrolled negative sequence injection scheme results in minimum VUF as compared to the controlled scheme. The positive sequence voltage is also better with uncontrolled scheme. However, it results in more real power oscillations as compared to the controlled scheme. Thus, to achieve less real power oscillations, controlled negative sequence injection scheme is preferred and to achieve minimum VUF, the uncontrolled negative sequence scheme is selected.

4.2.4 Priority Injection Schemes

Due to the limited current handling capability, priority injection schemes can be designed for GFM control. The active current component in the negative sequence is uncontrolled. Thus, its actual value is considered while deciding the limits for other sequence powers. Depending upon the remaining three quantities, six different priority control schemes can be designed. These schemes are designed based on the conventional current limiting scheme which considers both sequence phasors in-phase. The basic equation for the conventional current limiting scheme is given in equation (3.69). While designing the priority schemes, it is considered that the GFM is synchronized with the power grid. In such condition, the q-axis of the voltage phasor can be ignored in dq-frame. Thus, the q-axis voltage component is not considered in the design of these schemes.

4.2.4.1 PQN Priority Scheme

PQN scheme prioritizes the real power in positive sequence. The active component in negative sequence is considered while calculating the limit for the real power in positive sequence. The other current components are considered zero as priority is given to the active power in positive sequence. The expressions for the active power limit in case of PQN priority scheme are given in equation (4.5).

$$\begin{aligned} i_{dp} &= i_{\max} - |i_{dn}| \\ p_p^{\text{lim}} &= v_{dp} i_{dp} = v_{dp} \left(i_{\max} - \left| \frac{p_n}{v_{dn}} \right| \right) \end{aligned} \quad (4.5)$$

To calculate the limit for the reactive power in the positive sequence, the actual active powers in the positive and negative sequences are considered and the reactive power in the negative sequence is considered as zero. Considering the conventional current limiting scheme, the mathematical expression for the positive sequence reactive power limit is given in equation (4.6).

$$\begin{aligned} i_{qp} &= \sqrt{(i_{\max} - |i_{dn}|)^2 - i_{dp}^2} \\ q_p^{\text{lim}} &= v_{dp} i_{qp} = \sqrt{\left\{ \left(i_{\max} - \left| \frac{p_n}{v_{dn}} \right| \right) v_{dp} \right\}^2 - p_p^2} \end{aligned} \quad (4.6)$$

The limit for the reactive power in the negative sequence is least prioritized in this scheme. The measured real power in positive and negative sequence is considered along with the measured positive

sequence reactive power in the calculation of limit for the negative sequence reactive power. The expressions for the negative sequence reactive power are given in equation (4.7).

$$\begin{aligned}
 i_{qn} &= \sqrt{\left(i_{\max} - \sqrt{i_{dp}^2 + i_{qp}^2}\right)^2 - i_{dn}^2} \\
 q_n^{\lim} &= v_{dn} i_{qn} = \sqrt{\left\{\left(i_{\max} - \frac{\sqrt{p_p^2 + q_p^2}}{v_{dp}}\right) v_{dn}\right\}^2 - p_n^2}
 \end{aligned} \tag{4.7}$$

4.2.4.2 PNQ Priority Scheme

By using the same procedure, the expressions for the limits of positive sequence active power, negative sequence reactive power and positive sequence reactive power can be derived from the conventional current limiting scheme. The expressions for PNQ limit are given in equation (4.8).

$$\begin{aligned}
 p_p^{\lim} &= v_{dp} i_{dp} = v_{dp} \left(i_{\max} - \left|\frac{p_n}{v_{dn}}\right|\right) \\
 q_n^{\lim} &= v_{dn} i_{qn} = \sqrt{\left\{\left(i_{\max} - \left|\frac{p_p}{v_{dp}}\right|\right) v_{dn}\right\}^2 - p_n^2} \\
 q_p^{\lim} &= v_{dp} i_{qp} = \sqrt{\left\{\left(i_{\max} - \frac{\sqrt{p_n^2 + q_n^2}}{v_{dn}}\right) v_{dp}\right\}^2 - p_p^2}
 \end{aligned} \tag{4.8}$$

4.2.4.3 QPN Priority Scheme

The expressions for QPN priority for the conventional current limiting scheme are given below.

$$\begin{aligned}
 q_p^{\lim} &= v_{dp} i_{qp} = v_{dp} \left(i_{\max} - \left|\frac{p_n}{v_{dn}}\right|\right) \\
 p_p^{\lim} &= v_{dp} i_{dp} = \sqrt{\left\{\left(i_{\max} - \left|\frac{p_n}{v_{dn}}\right|\right) v_{dp}\right\}^2 - q_p^2} \\
 q_n^{\lim} &= v_{dn} i_{qn} = \sqrt{\left\{\left(i_{\max} - \frac{\sqrt{p_p^2 + q_p^2}}{v_{dp}}\right) v_{dn}\right\}^2 - p_n^2}
 \end{aligned} \tag{4.9}$$

4.2.4.4 QNP Priority Scheme

The expressions for QNP priority for the conventional current limiting scheme are given below.

$$\begin{aligned}
 q_p^{\text{lim}} &= v_{dp} i_{qp} = v_{dp} \left(i_{\text{max}} - \left| \frac{p_n}{v_{dn}} \right| \right) \\
 q_n^{\text{lim}} &= v_{dn} i_{qn} = \sqrt{\left\{ \left(i_{\text{max}} - \left| \frac{q_p}{v_{dp}} \right| \right) v_{dn} \right\}^2 - p_n^2} \\
 p_p^{\text{lim}} &= v_{dp} i_{dp} = \sqrt{\left\{ \left(i_{\text{max}} - \frac{\sqrt{p_n^2 + q_n^2}}{v_{dn}} \right) v_{dp} \right\}^2 - q_p^2}
 \end{aligned} \tag{4.10}$$

4.2.4.5 NQP Priority Scheme

The expressions for NQP priority for the conventional current limiting scheme are given below.

$$\begin{aligned}
 q_n^{\text{lim}} &= v_{dn} i_{qn} = v_{dn} \sqrt{i_{\text{max}}^2 - \left(\frac{p_n}{v_{dn}} \right)^2} \\
 q_p^{\text{lim}} &= v_{dp} i_{qp} = \left(i_{\text{max}} - \frac{\sqrt{p_n^2 + q_n^2}}{v_{dn}} \right) v_{dp} \\
 p_p^{\text{lim}} &= v_{dp} i_{dp} = \sqrt{\left\{ \left(i_{\text{max}} - \frac{\sqrt{p_n^2 + q_n^2}}{v_{dn}} \right) v_{dp} \right\}^2 - q_p^2}
 \end{aligned} \tag{4.11}$$

4.2.4.6 NPQ Priority Scheme

The expressions for NPQ priority for the conventional current limiting scheme are given below.

$$\begin{aligned}
 q_n^{\text{lim}} &= v_{dn} i_{qn} = v_{dn} \sqrt{i_{\text{max}}^2 - \left(\frac{p_n}{v_{dn}} \right)^2} \\
 p_p^{\text{lim}} &= v_{dp} i_{dp} = \left(i_{\text{max}} - \frac{\sqrt{p_n^2 + q_n^2}}{v_{dn}} \right) v_{dp} \\
 q_p^{\text{lim}} &= v_{dp} i_{qp} = \sqrt{\left\{ \left(i_{\text{max}} - \frac{\sqrt{p_n^2 + q_n^2}}{v_{dn}} \right) v_{dp} \right\}^2 - p_p^2}
 \end{aligned} \tag{4.12}$$

In case of low voltage conditions, due to the voltage source behavior of GFM, the maximum transferable real power can be less than the power limit calculated by the priority schemes discussed above. This is due to the coupling of two ac sources and the maximum transferable power corresponds to the

- i. rotor angle stability in case of conventional power source.
- ii. converter-driven stability to ensure the synchronization of the converter with the power grid.

4.2.4.7 Performance of Priority Injection Schemes

The performance of these priority schemes is discussed in Table 4.7 for normal and faulty conditions. The controlled Q-V loop for negative sequence is considered in this analysis. Moreover, the reference positive sequence real and reactive powers are 1.0 and 0.7 (capacitive) p.u respectively. For faulty conditions, a L-L fault is introduced at POC. The SCP of the grid at POC is selected to be 10 MVA. The values mentioned in the table are in p.u. except the VUF which is in percentage. In normal conditions, the positive sequence voltage magnitude, at POC, is 1.04 p.u. whereas negative sequence voltage is zero. In case of unbalanced fault, without converter support, the positive and negative sequence voltages drop to 0.71 and 0.4 p.u. respectively.

Table 4.7: Performance of different priority injection schemes in grid connected mode

Priority Scheme	Normal Conditions		Faulty Conditions			
	PQ Limits	[p q] (p.u)	[p* q _p * q _n *] (p.u)	PQN Limits (p.u)	[p q _p q _n] (p.u)	VUF (%)
PQN	[1.25, 0.75]			[0.86, 0.72, 0.12]	[0.46, 0.45, 0.12]	56.1
PNQ				[0.86, 0.16, 0.23]	[0.46, 0.16, 0.21]	56.0
QPN	[1.04, 1.25]	[1.0, 0.7]	[1.0, 1.28, 0.51]	[0.73, 0.86, 0.12]	[0.46, 0.45, 0.12]	56.1
QNP				[0.24, 0.86, 0.17]	[0.24, 0.55, 0.14]	56.1
NQP	[1.04, 1.25]			[0.24, 0.60, 0.48]	[0.24, 0.55, 0.14]	56.1
NPQ	[1.25, 0.75]			[0.48, 0.16, 0.48]	[0.46, 0.16, 0.21]	56.0

The above table shows that the performance of different priority schemes in normal conditions is the same. Due to the absence of negative sequence voltage in normal conditions, the priority is only limited to positive sequence components. In normal conditions, the reference powers are already less than or equal to its limit value. Thus, there is no difference between the schemes as far as normal conditions are concerned. However, the positive sequence power limits are different for different priority schemes in normal conditions which is clear from the above table.

In case of voltage dips, the reference reactive powers in the respective sequences are changed by the Q-V loops to inject more reactive power for the voltage support. The reference real power is not changed as the frequency experienced no change. Moreover, the injected real power is further limited by the maximum possible real power transfer between two voltages (in case of low voltages) whose expression is given in equation (4.13).

$$P_{\max} = \frac{EV}{X} \quad (4.13)$$

This is the maximum possible real power transfer between two nodes having voltages ‘E’ and ‘V’ and the reactance between these nodes is ‘X’. In GFM, as the control scheme can see a virtual impedance which is responsible to limit the current to its maximum value, so the ‘X’ is not the physical reactance value but the virtual reactance responsible to limit the current. Thus, the real power measured at POC is less than its limit and this can be seen in the above table.

Furthermore, in faulty conditions, the response of the priority schemes is different. The calculated limits for the real and reactive powers correspond to the respective priority scheme. In PQN scheme, the injected real power is less than its limit and this is due to the maximum possible real power transfer between two ac sources as the GFM is in synchronism with the power grid. Moreover, the measured reactive power in positive sequence is less than its limit even though its reference value is greater than its limit. The reason for not achieving the reference value (after applying the limit) is the saturation of the integrator in Q-V control which is limited to keep ΔV less than or equal to 1 p.u. This is the reason that the measured positive sequence reactive power is less than the minimum of its reference and limit value. Due to the positive sequence reactive power mismatch, the limit for the reactive power in negative sequence is non-zero and its measured value is matched with its reference (after applying its limit).

Similarly, the response of the other priority schemes can also be explained. It can be concluded that due to the Q-V integrator saturation, the reference reactive power may not be achieved for some of the priority schemes but still these schemes offer the flexibility in prioritizing any current component to some extent. It is important to mention here that the initial response of the GFM is like a three-phase voltage source due to slow Q-V controls. This is the reason that the reference reactive powers are achieved after a definite delay. Moreover, PNQ and NPQ schemes were able to result in maximum negative sequence reactive power injection, due to which the minimum VUF is achieved with these schemes.

4.2.5 Current Limitation and Current Control

Due to the voltage source behavior of the GFM, its current limitation is a challenging task. There are different schemes stated in the literature to ensure the current limit of the converter in different operating conditions. In this design, the virtual damping resistor scheme is implemented to change the reference voltage with the change in measured current at POC. The direct phase current amplitude limitation scheme is also used to ensure that no phase current exceeds the current limit of the converter. The overall current limitation and current controller is shown in Figure 4.23.

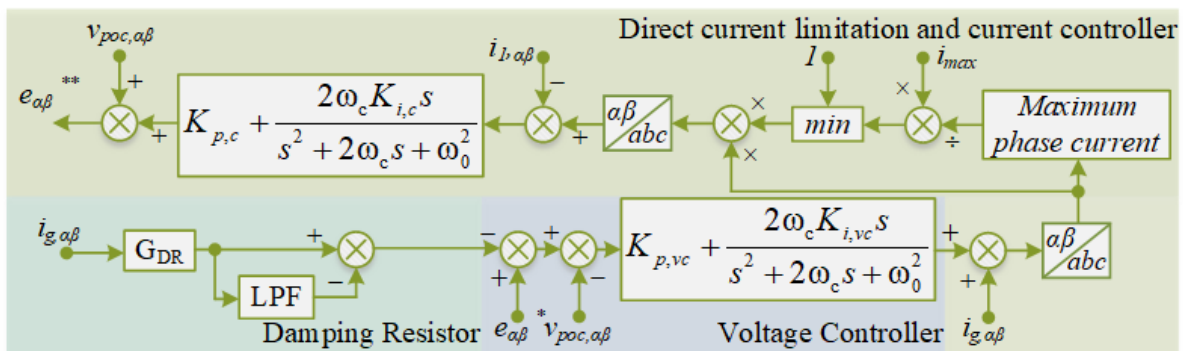


Figure 4.23: Current limitation and current controller for GFM

Where ‘K’ represents the controller gains, the subscripts ‘c’ and ‘vc’ stand for current and voltage controller respectively whereas the subscripts ‘p’ and ‘i’ stand for proportional and integral gains respectively. G_{DR} represents the virtual damping resistor. Moreover, ω_o is the nominal angular frequency and ω_c is the critical angular frequency. i_l is the line current measured on the converter’s side of the LCL filter. Due to the priority injection scheme and its power limit calculations with respect to the current limit of the converter, the priority injection scheme is also able to limit the phase currents. However, due to the slow response of the p-f and Q-V controls, the current exceeds its limit initially and then stable to somewhat lower value. The damping resistor (DR) technique can also be used to limit the phase currents in case of low voltage. Its arrangement is discussed in the above figure. It decreases the reference voltage if a sudden change in the current at POC is observed. Its impact is decayed out with time and the rate of change depends on the time constant of the LPF. The damping resistor technique needs to be separately implemented for positive and negative sequence current components. The other method for current limitation is the direct current control (DCC) which enables to change the amplitude of the phase currents without changing its shape. It assesses the amplitude of each phase current with the help of SOGI (Figure 3.30). The maximum phase current is limited to the current limit of the converter and current in other phases is also limited accordingly. The layout of the DCC scheme is given in the above figure. However, DCC scheme can be used if the reference currents are known and in GFM, normally the reference voltage is computed with the help of p-f and Q-V controls.

In [93], the authors proposed cascaded voltage and current controller for GFM. The QPR controllers are used as voltage and current controllers. The voltage controller results in reference current. The basic arrangement is the same as that of GFL inner current controller. As the voltage controller provides the reference current, thus, the DCC method can be used to limit the converter’s current. For QPR controller, 1 Hz cutoff frequency and 50 Hz mean frequency is selected. The other important task is the tuning of these controllers which requires the filter’s parameters. The current controller tuning is the same as discussed for GFL. The tuning of these controllers is discussed in [93]. For the voltage control, the expressions for the gains are given below.

$$K_{p,vc} = \frac{\omega_v C_f}{K_{p,c}} \sqrt{(\omega_i L_1)^2 + (R_1 + K_{p,c})^2}$$

$$K_{i,vc} = \frac{\omega_0 C_f (H_{ol}^{vc} |j\omega_0|) \sqrt{(\omega_0 L_1)^2 + (R_1 + K_{p,c})^2} - K_{p,c} K_{p,vc}}{2K_{p,c} Q}$$
(4.14)

Where ω_v represents the bandwidth of inner voltage controller and ω_i represents the bandwidth of the inner current controller. Q represents the quality factor and C_f is the filter’s capacitance. The tuning parameters for the current and voltage QPR controllers are given in Table 4.8. For the tuning, the bandwidth frequency for current controller is selected as 9 times of the grid frequency and for voltage controller, it is four times smaller than the bandwidth frequency of the current controller. It ensures that

the current controller is faster than the voltage controller, which is useful for the stability of the control scheme under different operating conditions. The open loop gains for both the controllers at nominal frequency are selected as 1000 and the quality factor (Q) for both the controllers is the same. The inductance is discussed in LCL filter, and the resistance is chosen as 5 % of the reactance on the converter's side (L_l). The series resistance has no negative effect on the performance of the LCL filter.

Table 4.8: Parameter tuning for current and voltage controllers for GFM

GFM Current Controller							
Given Parameters	$\omega_0 L_l$ (p.u)	R_l (p.u)	C_f (mF)	Q	f_g (Hz)	ω_c (rad/sec)	ω_i (rad/sec)
	0.105	0.005	0.236	$2\pi \times 50$	50	$2\pi \times 1$	$2\pi \times 450$
Derived Parameters	$K_{p,c}$			$K_{i,c}$			
	0.943			0.167			
GFM Voltage Controller							
Given Parameters	$\omega_0 C_f$ (p.u)				ω_v (rad/sec)		
	0.05				225π		
Derived Parameters	$K_{p,vc}$				$K_{i,vc}$		
	0.16				0.08		

The performance of the above designed cascaded QPR controllers is given in Figure 4.24.

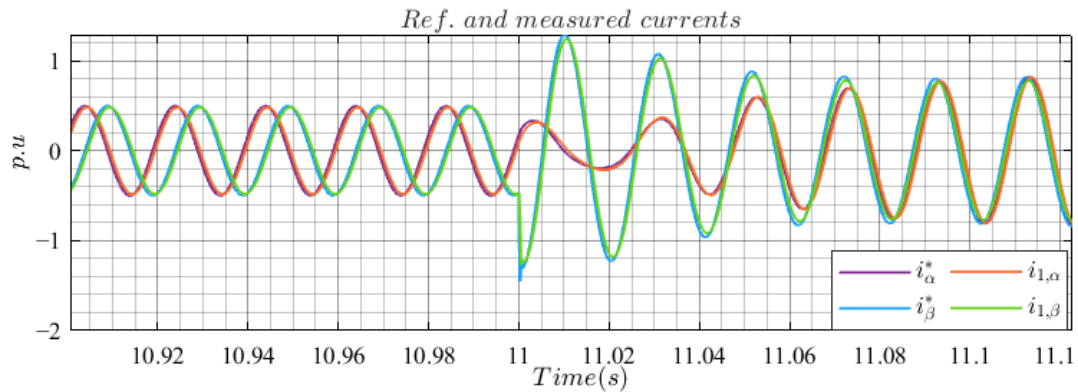


Figure 4.24: Measured and reference currents for GFM on the converter's side

The above figure shows that the reference and measured converter's side currents (i_l) are in close agreement with each other both in normal and faulty conditions. The reference current for GFM is assessed with the help of voltage controller. As far as the performance of different current limitation schemes is concerned, a L-L fault is introduced at POC at 10.8 seconds and the response of different current limitation methods, discussed in the start of this section, is analyzed. The peak measured line current on the converter's side of the LCL filter is plotted for each current limitation scheme in Figure 4.25.

Subplot (a) in the below figure shows that the priority injection control is also able to limit the maximum converter's current, but its performance is poor as it is unable to keep the current below its rating. However, it does not allow the phase current to keep on increasing indefinitely and stabilizes it at some level. The DR method reduces the reference voltage as the change in current at POC is detected. However, it only suppresses the current injection for initial cycles depending upon the tuning of LPF.

This is the reason that the DR scheme also stabilizes the current at the same level as that of priority control. The DCC is comparatively faster than the other methods and it is also able to ensure the current limitation in all conditions. With this method, the maximum measured current is limited below the converter’s current rating in case of faults. The performance of combined DR and DCC scheme is very close to the DCC’s performance. However, a difference can be noticed in the initial few cycles where the combined scheme results in lower measured current.

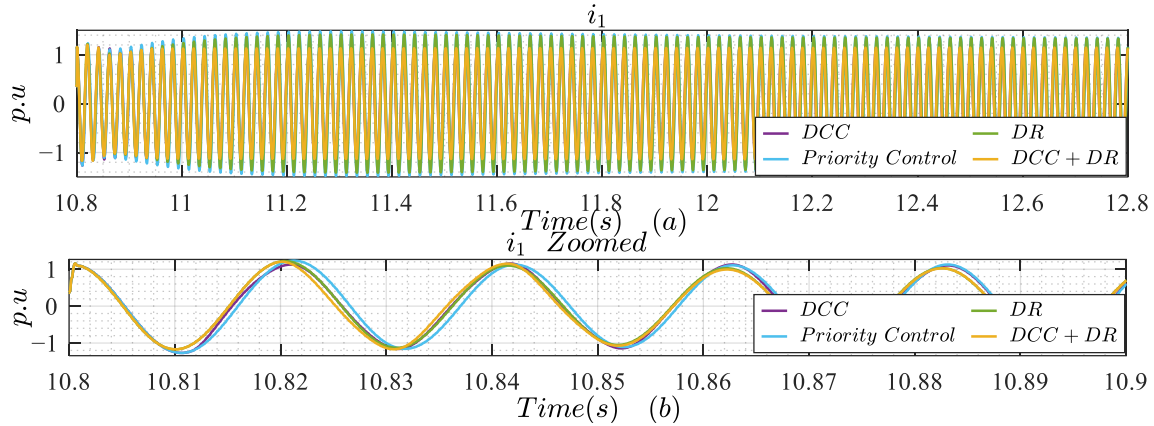


Figure 4.25: Comparison of different current limitations for GFM

The overall converter’s setup along with the GFM control scheme is given in Figure 4.26.

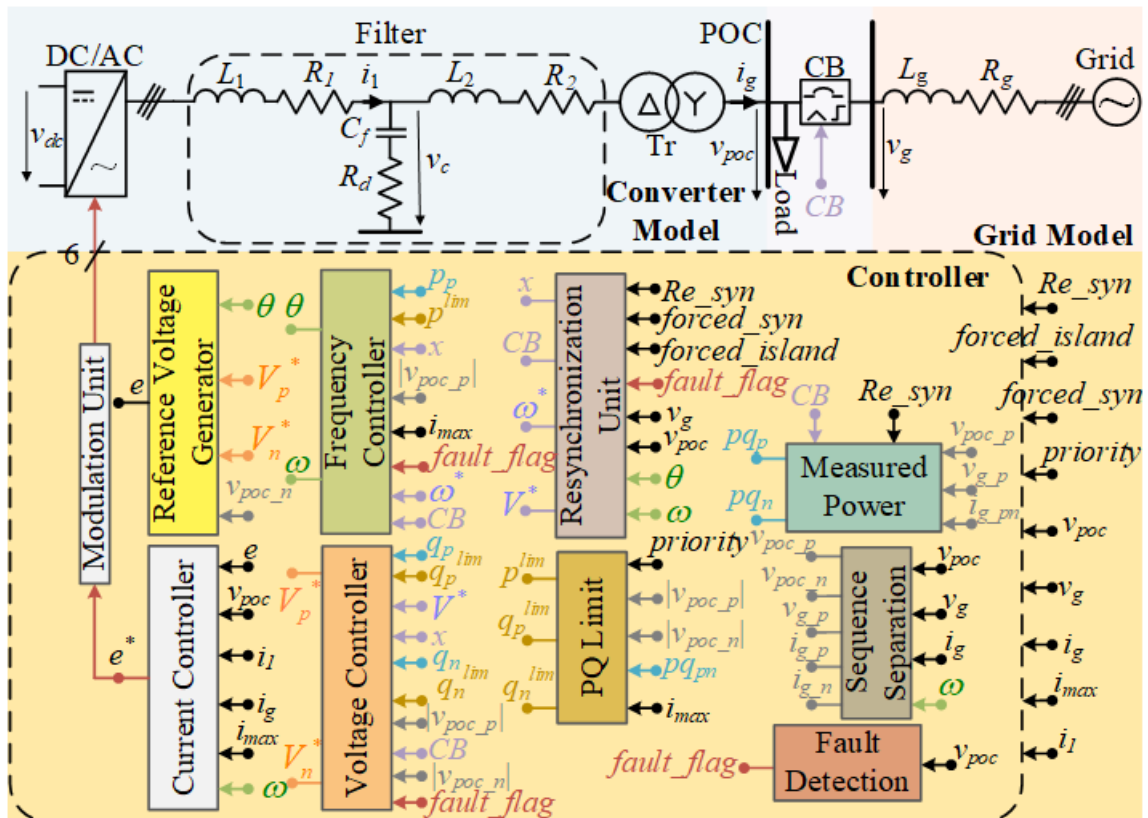


Figure 4.26: Overall setup of grid forming converter

For the detection of LVRT conditions, the SBS based fault detection method is used. Due to the varying grid strength conditions for GFM, the LVRT conditions are activated if the minimum L-L voltage drops

below 0.8 p.u. and it is latched until the voltage is restored and goes beyond 0.9 p.u. This is to ensure stability with weak grid connections where the converter's power injections have a significant impact on the voltage.

4.3 Performance Analysis of Improved GFM Control Scheme

The improved control scheme is developed in Simulink and its response under different operating conditions is observed. Short circuit ratio (SCR) of the grid is defined as the ratio between the SCP of the grid at POC to the nominal power of the converter. It helps in defining the grid's strength. The key parameters for the setup are given in Table 3.13.

Table 4.9: Parameters for the test setup of Improved GFM converter

		Grid's Parameters				
		Voltage (L-L) (V)	f_g (Hz)	SCR	X/R	
Hardware parameters		400	50	1.5–1000	5	
		Load				
		Active power (kW)	Reactive power (kVAR)	Voltage (L-L) (V)	f (Hz)	
		10	5	400	50	
		Coupling Transformer				
		Type	Voltage (V)	Rated Power (kVA)	Reactance (p.u.)	Resistance (p.u.)
		Y-Y	400/260	200	0.03	6×10^{-4}
		LCL Filter				
		L_1 (mH)	R_1 (mΩ)	L_2 (mH)	R_2 (mΩ)	C_f (mF)
		0.226	3.54	0.045	0	0.236
				R_d (mΩ)		
				133.2		
Converter Control Parameters		General Parameters				
		V_{dc} (V)	Rated Power	I_{max}	f_s (kHz)	LVRT limits
		425	100 kVA	1.2 (p.u)	10	[0.8, 0.9]
		p-f Control				
		p^* (p.u)	$(\% \Delta / s)_{p^*}$	p_{rated} (p.u)	J	D_p
		0.5	25	1	1	48.75
		PI Gains	K_p	$(\% \Delta / s)_{K_p}$	G_p	ω^* (p.u)
		[0.043, 19.2]	50	12.5	0.0865	1
		Q-V Control				
		q_p^* (p.u)	$(\% \Delta / s)_{q_p^*}$	v^* (p.u)	PI Gains	k_p
		0.1	72	1	[20, 5]	2
		$(Q-V)_p$ limits	LPF [k, T]	G_n	k_n limits	K_{qn}
		[-1, 1]	[1, 0.06]	8	[0, 6]	2.121
		Synchronization				
		LPF [k, T]	Dead band		On-time delay (s)	
[3, 0.08]	[-0.05, 0.05]		0.2			
Current Control						
$[K_{p,vc}, K_{i,vc}]$	$[K_{p,c}, K_{i,c}]$	G_{DR}	LPF [k, T]			
[0.16, 0.08]	[0.943, 0.167]	0.8	[1, 0.18]			

In islanded conditions, the PQN priority scheme is activated both for normal and faulty conditions. However, in grid connected mode, the PQN priority scheme is activated in normal conditions. It is also activated if the grid's frequency drops in case of short circuit faults. PQN is prioritized to support the

frequency if the resultant frequency is below its rated value. The PQN priority scheme may also work in case of faulty situations as the active power is further limited based on the terminal voltage which provides flexibility to inject more reactive power. The QNP priority scheme is activated in case of LVRT conditions in grid connected mode.

4.3.1 Small Signal Stability

The performance of the proposed GFM scheme is analyzed for different operating conditions in islanded and grid connected modes. In islanded mode, the reference active and reactive powers are set to zero. Thus, the injected real and reactive powers are the result of frequency and voltage droop controls respectively. The load power is changed, and the response of the control scheme is analyzed against these changes in load. The results are presented in Table 4.10.

Table 4.10: Performance of proposed GFM scheme in normal conditions in islanded mode

P_L (p.u.)	Q_L (p.u.)	p_{poc} (p.u.)	q_{poc} (p.u.)	f (Hz)	V_{poc} (p.u.)
0.0	0.0	0.00	0.00	50.0	1.01
0.5	0.3	0.48	0.28	49.6	1.01
0.8	0.5	0.76	0.47	49.3	1.01
1.0	0.7	0.90	0.62	49.2	0.98
1.2	0.9	0.72	0.53	49.4	0.81

Where P_L and Q_L stand for the real and reactive power of the load. The above table shows that the steady state response of the GFM control scheme is good for different load conditions. For the last two loading conditions, the converter's power rating is reached. Thus, the active and reactive powers are limited by the PQN priority scheme with prioritizing the active power injection for the frequency support. As per the control parameters, the scheme injects its rated active power if frequency drops to 49.2 Hz and the above table confirms this.

For the small signal stability, the response of the scheme is analyzed for these sudden load changes. At the start of the simulation, no load is connected to the converter. At 5 seconds, a load of 0.5 p.u active and 0.3 p.u. reactive power is connected to the converter. This is a large load variation from converter's perspective as it is a step change of 58 % of the converter's capacity which means that from no load to sudden 58 % loading conditions are simulated. At 10 seconds, an additional 0.3 p.u active and 0.2 p.u reactive power load is connected with the 58 % loaded converter. This results in 36 % step load change to the converter and the effective loading of the converter reaches 94 %. Similarly, the extra 28 % loading is introduced to already loaded system on 15 and 20 seconds respectively which results the converter to be loaded to 122 % load from 15 to 20 seconds and 150 % loaded onwards. Different parameters are observed during these sudden load changes while paying special attention to the frequency and voltage stability. Different parameters are plotted in Figure 4.27.

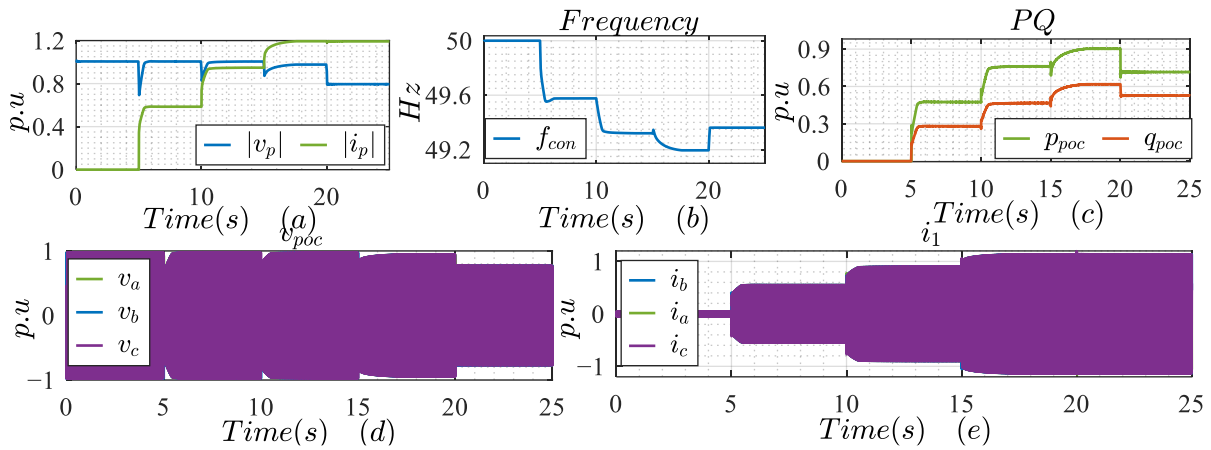


Figure 4.27: Small signal stability of GFM in islanded conditions; (a) magnitude of voltage and current phasors at POC, (b) frequency of GFM, (c) measured active and reactive powers at POC, (d) measured phase voltages at POC, (e) measured phase currents on converter's side

The above figure shows that a large voltage dip is recorded for the first load change of 58 % of converter's power rating. However, the voltage is quickly recovered to its steady state value. This is a large load change from perspective of the small signal stability. Normally, $\pm 10\%$ load change is recommended. However, for this load change, the frequency smoothly changes and achieves a new equilibrium point while the voltage experiences a voltage dip of 0.3 p.u. and restores to its normal value in less than half a second. For other load change events, the frequency shows smooth transition and achieves a new stable value while the voltage experiences a voltage dip which is proportional to the load change. For 36 % step load change, the voltage dip is 0.18 p.u. and, for load step of 28 %, it is 0.12 p.u. In all these load changes, the terminal voltage restores and achieves some new steady state value. Even with 150 % loading, the terminal voltage is stable at 0.8 p.u. These results confirm small signal stability of the proposed GFM scheme in islanded conditions.

The next analysis is performed for the weak grid connection of the GFM. Normally the small signal stability is decided by the grid in grid connected mode. However, the converter may have an impact on the small signal stability in case of very weak grids and with different operating frequencies. The reference active and reactive powers are changed in this case with a defined ramp function. The rate of change for reference active power is set to 25 %/s and for reactive power, it is 72 %/s. The reference powers are changed as the load was changed in the islanded mode. The analysis is performed for different grid frequencies to ensure the small signal stability in varying grid conditions. The SCR of the grid at POC is selected as unity to model a very weak grid. The synchronization is achieved at the start of the simulation. The reference active and reactive powers are repeatedly changed with a duration of 5 seconds. The performance of the proposed scheme under weak grid conditions is given in Figure 4.28.

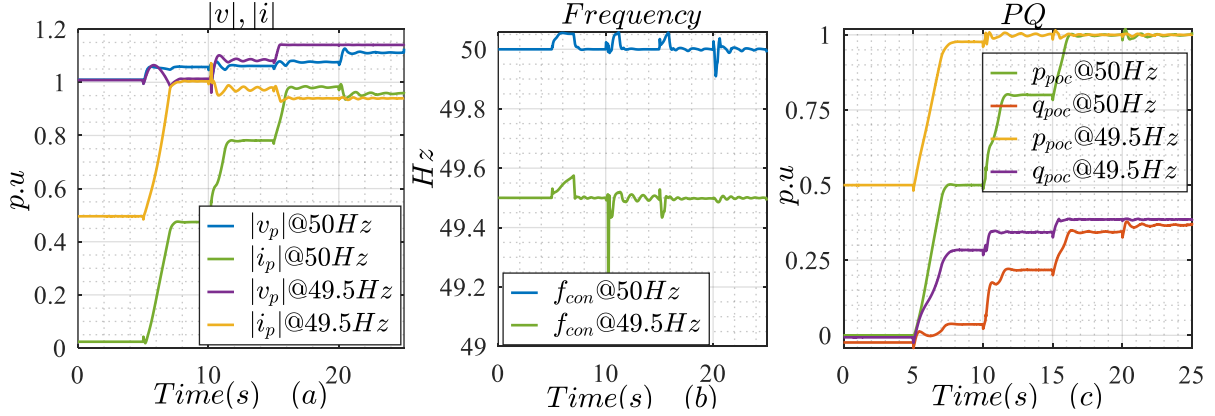


Figure 4.28: Small signal stability of GFM in weak grid conditions; (a) magnitude of voltage phasor at POC and magnitude of current phasor measured on converter's side of POC, (b) frequency of GFM, (c) measured active and reactive powers at POC

The above figure shows that measured real power is in good agreement to the reference real power for 50 Hz grid frequency. It is due to the fact that the frequency droop control does not contribute to the reference real power due to low variations in frequency. However, the measured active power is limited to 1 p.u., even if the reference active power exceeds from 1 p.u. It can be explained with the help of the real power limit whose upper limit is set at 1 p.u. The change in reference power changes the system frequency and terminal voltage for weak grids. However, the frequency is settled again to its initial value by the grid. The terminal voltage achieves a new stable value. Due to the weak grid, the increased reference reactive power increases the terminal voltage and voltage control in Q-V control opposes this change by introducing some inductive power in the reference reactive power. This is the reason that the measured reactive power is less than the reference reactive power.

For a 49.5 Hz grid, the converter is already supporting the grid frequency by injecting 0.5 p.u. active power when the reference powers are zero. With this situation, the converter needs to ensure the synchronization at 10 seconds as its active power limit is reached. Thus, no further active power is injected to the system, but the converter is able to ensure the synchronization in these scenarios. The current phasor magnitude for 49.5 Hz grid drops at 15 seconds. The reason for this is the increase in the terminal voltage which forced the current to drop from its previous steady state value. The change in terminal voltage at 15 seconds is due to the additional reactive power injection.

Hence, it can be concluded that the proposed scheme offers a stable response for different reference power changes in a weak grid with different grid frequencies. The same procedure is repeated for a grid having its SCP 1000 times greater than the power rating of the GFM converter. The response of the converter for different grid frequencies is given in Figure 4.29.

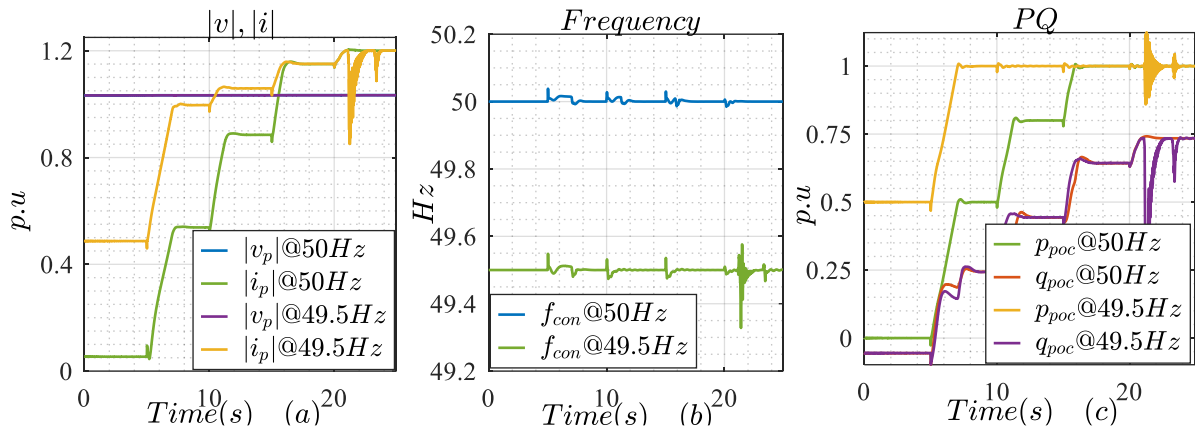


Figure 4.29: Small signal stability of GFM in stiff grid conditions; (a) magnitude of voltage phasor at POC and magnitude of current phasor measured on converter's side of POC, (b) frequency of GFM, (c) measured active and reactive powers at POC

The above figure shows that the converter is able to smoothly operate for different reference power changes with 50 Hz stiff grid. The measured active power follows its reference value for 50 Hz grid connection as no additional reference power is introduced due to the frequency droop. Moreover, the frequency oscillations are also suppressed at the start of load change as compared to the weak grid response. The terminal voltage is stable for all different power levels. Due to the stiff grid, the terminal voltage and system frequency are hardly affected by the change in injected power. This is the reason that the reactive power is also in good agreement to its reference value. However, it does not achieve the exact reference value due to the voltage control and saturation of the Q-V control. The full current rating of the converter is utilized in this case. The response of the GFM for a 49.5 Hz stiff grid is also same as the response for a 50 Hz stiff grid with an exception in the reference power change when the converter is already operating at its maximum real power. The change in reference power introduces oscillations in measured powers and converter's frequency but the synchronization is ensured, and it achieves a stable value in less than two seconds. Thus, it can be concluded that in a stiff grid, the small signal stability is largely decided by the grid, but some oscillations may be observed if the converter is operating at its full capacity and a change in reference power is introduced.

4.3.2 Large Signal Stability

Large signal stability of GFM is very critical as the response of the converter is dependent on the true operating conditions, maximum rate of change of voltage/frequency and the grid's SCP at POC, etc. To study the large signal stability, different types of faults are introduced at POC in case of nominal and low frequency conditions. The converter should offer a stable output both in fault and post fault conditions. The post fault performance is equally important as the sudden restoration of voltage level at POC may cause the instability of the converter. Even with limited current handling capability, the GFM should ensure synchronism with the grid in all these conditions to ensure the converter-driven stability.

At first step, the large signal stability of GFM is investigated in islanded condition by introducing balanced and unbalanced faults at POC. The converter is operated in no load conditions from 0 to 1 second. At 1 second, the loading is changed, and the converter is 50 % loaded before a balanced three phase fault is introduced at POC at 5 seconds for a duration of 5 seconds. At 10 seconds, the fault is cleared, and the converter regains its pre fault state. At 15 seconds, a L-L fault is introduced between phase ‘b’ and ‘c’ with the duration of 5 seconds. Finally at 20 seconds, the fault is cleared to analyze the post fault response for unbalanced faults. PQN priority scheme is activated in islanded mode. The response of the converter is given in Figure 4.30.

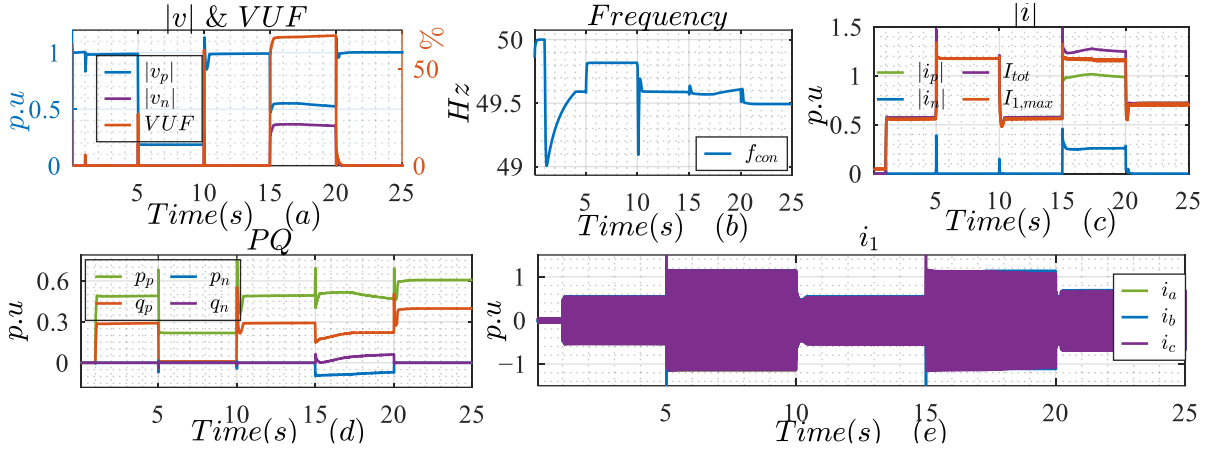


Figure 4.30: Large signal stability of GFM in islanded conditions; (a) magnitude of sequence voltage phasors and VUF at POC, (b) frequency of GFM, (c) magnitude of sequence current phasors, their numeric sum and converter's side maximum phase current, (d) measured sequence real and reactive powers at POC, (e) measured phase currents on converter's side

I_{tot} represents the numeric addition of the sequence currents and $I_{I,max}$ stands for the maximum phase current on the converter's side. i_l is the three-phase line current on the converter's side. The subplot (a) of the above figure shows a small dip in voltage at the time when the converter loading is changed from 0 to 50 %. From 10 to 15 seconds, a large voltage dip is measured at POC which contains only the positive sequence component which means a balanced fault is introduced. As the fault is cleared, the terminal voltage experiences an instantaneous over voltage due to the slower Q-V control and voltage source behavior of the GFM. The voltage at POC soon settles to its pre fault level. Similarly, in L-L fault duration, a VUF is calculated at POC with the help of non-zero positive and negative sequence voltage phasors. The post fault behavior is the same as that of balanced fault. Hence in both these cases, the voltage is restored to its pre-fault level smoothly after the fault clearance.

The subplot (b) shows that the dip in frequency is observed as the converter loading is changed to 50 % and then it achieves a new steady state level. This dip is introduced due to the reset of additional frequency support control gain in the p-f loop which is reset on the start of the fault and post fault scenario to ensure the synchronism in such conditions. However, this reset is not necessary for the islanded operation. As the fault is introduced, the frequency gets closer to nominal frequency due to the fact that the load is of constant impedance type whose active power consumption is dependent on the

terminal voltage. As the fault is cleared, a mismatch in supply and demand for the active power causes a frequency dip at 10 seconds. However, the frequency regains its pre-fault value. The same type of response is also recorded for the unbalanced fault but with different operating values. It is because of relatively higher terminal voltage in case of unbalanced fault as compared to three phase balanced fault which results in higher active power for the constant impedance load. The frequency achieves a new steady state value as the second fault is removed. It is due to the higher terminal voltage which causes more real power consumption and results in a bit lower frequency. From subplot (b), it is clear that the converter is not only stable under these faults, but it also achieves a steady state after the fault removals.

The subplot (c) shows the magnitude of the measured sequence currents, its numeric sum, and the maximum line current on the converter's side. It confirms that the measured maximum phase current is less than the current limit of the converter. Moreover, it also shows that the converter's current limit is effectively being utilized in case of unbalanced faults as the numeric sum of positive and negative sequence current phasors is greater than the current limit of the converter but still the maximum phase current is below this level. It means that the proposed scheme offers better utilization of the converter's current handling capacity as compared to the conventional current limiting scheme. The subplot (d) presents the measured sequence powers at POC. It shows that the reactive power in negative sequence is increasing in unbalanced fault and its rate of change is dependent on the speed of the Q-V control for the negative sequence. Similarly, the subplot (e) presents the measured three phase currents on converter's side. For the unbalanced fault, it shows that the current in phase 'c' is greater than current in phase 'b' in the start of the fault. This is because the converter offers natural response against the negative sequence due to its voltage source behavior as the reference negative sequence voltage is very low and ramping up with the speed of the Q-V control. As the reference negative sequence voltage achieves a certain level, the current in phase 'b' is greater than current in phase 'c'. It is due to controlling the negative sequence injection.

From the above discussion, it can be concluded that the proposed GFM scheme offers stable response against large voltage variations in islanded operation. It can be further investigated against different fault levels.

The SCR of the grid at POC is selected as 1.5 to test the large signal stability of the proposed converter in a weak grid connection for different types of faults. Different types of faults are applied at POC with different grid frequencies to analyze the converter's stability in various conditions. The duration of the fault is selected as 10 seconds to analyze the synchronization of the converter during such conditions. A balanced three phase fault is applied at POC at 2 seconds. The fault is cleared at 10.2 seconds to study the post fault response. After achieving steady state levels, a L-L fault is introduced at 20.2 seconds. The reference active and reactive powers are 0.5 and 0.1 p.u. respectively. The response of the converter is plotted in Figure 4.31.

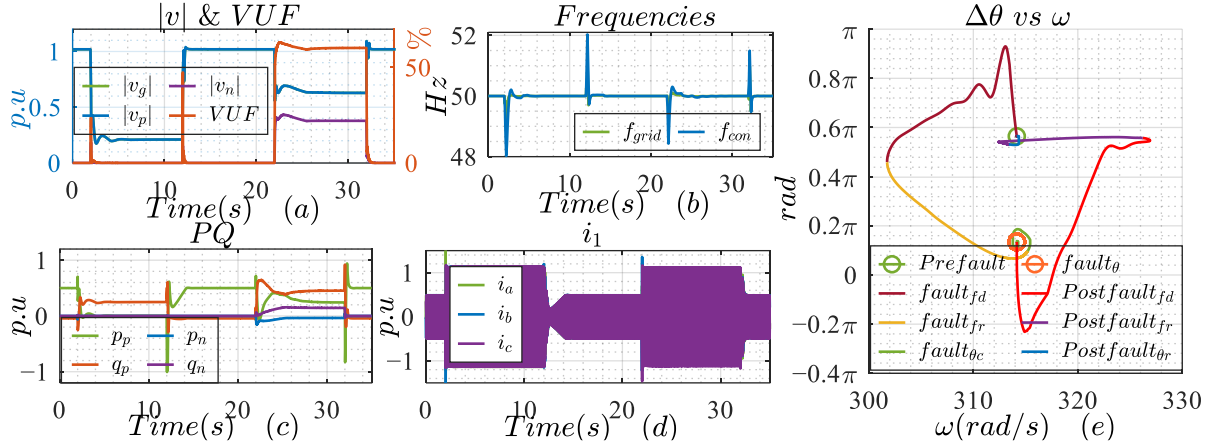


Figure 4.31: Large signal stability of GFM in nominal-frequency weak grid connection; (a) magnitude of sequence voltage phasors and VUF at POC, (b) frequencies of GFM and grid, (c) measured sequence real and reactive powers at POC, (d) measured phase currents on converter's side, (e) angular difference vs speed, the subscripts 'fd', 'fr', ' θ_c ', ' θ_r ' stands for frequency deviation, frequency restoration, angle convergence and angle restoration respectively

The subplot (a) of the above figure shows that the voltage at POC is recovered smoothly after clearing a fault. Moreover, the voltage is steady during the faults as well. The % VUF is initially high and then settles to a lower level. It is due to natural response of the converter initially during a fault and as the positive sequence power injections decrease and negative sequence power injections increase, the % VUF achieves a lower steady value. The subplot (b) presents the grid frequency and converter's frequency. It shows that both the frequencies are in close agreement and confirms the synchronization of the converter in case of severe voltage dips with limited current handling capability of the converter. Thus, with the proposed GFM control, the synchronization of the converter can be ensured even in case of very severe faults with weak grid connections.

The subplot (c) shows that during balanced three-phase fault, the positive sequence reactive power is prioritized and due to limited current handling capability, the active power drops to zero. As the fault is cleared, the power levels are also resumed to their pre-fault levels. During an unbalanced fault, the reactive power in the negative sequence is non-zero and it increases as the fault persists. It is due to the relatively slower Q-V control for the negative sequence. It also shows that the active power in the negative sequence is minimized, and reactive power is increased in case of unbalanced fault. The reactive power in negative sequence is less than the active power in the positive sequence during a fault even though the QNP priority scheme is activated. The difference in the power levels is due to the difference in sequence voltage phasors' magnitude. The subplot (d) shows the measured phase currents on converter's side of the LCL filter and confirms that no phase current exceeds the current limit of the converter.

The rotor angle stability is important for synchronous generators as it decides whether the system can regain a stable state after experiencing a fault or not. As the converter has no mechanical stored energy, the rotor angle concept is a bit different in voltage source converters. The subplot (e) of the above figure

shows the angular difference between converter's terminal voltage and voltage at POC. The converter's terminal voltage can be equated to the internal generated emf of the synchronous generator. Hence, the $\Delta\theta$ shown in subplot (e) is the virtual rotor angle for the VSCs. The subplot (e) shows the angle plot during the balanced three-phase fault. The pre-fault angle is stable against the stable converter's frequency. As the fault is introduced, initially, the frequency deviates from its nominal value. The subscript 'fd' stands for frequency deviation. The frequency is then restored in a short duration by the p-f control to ensure synchronization. The subscript 'fr' stands for frequency restoration. After restoring the frequency, a new angle difference is achieved which is lower than the pre fault level. The subscript ' θ_c ' stands for angle convergence. The lower $\Delta\theta$ confirms a lower active power flow between the two sources which is true in case of fault and can be confirmed from subplot (c). It is important to mention here that during the fault, a new stable $\Delta\theta$ is achieved which confirms the angle stability. As the fault is cleared, the frequency first deviates from its steady state value and then is restored to the initial level. The $\Delta\theta$ is changed and stabilized to its pre-fault level confirming the same real power injection as was before the fault. Thus, the subplots (a), (b) and (e) confirm the voltage, frequency, and angle stability (converter-driven stability) of the voltage source converter with the proposed control scheme in weak grid connections.

The same procedure is repeated to investigate the large signal stability in case of a weak grid with lower frequency. It is crucial because in such conditions, both the frequency and voltage support are demanded by the p-f and Q-V controls. A ramp frequency change is introduced from 2.5 to 4.5 seconds with a rate of change of -0.5 Hz/s. It results in a final frequency of 49 Hz at 3.5 seconds. A balanced fault is introduced at POC from 8 to 18 seconds and an unbalanced fault is introduced from 28 to 38 seconds. The response of the converter for such conditions is given in Figure 4.32.

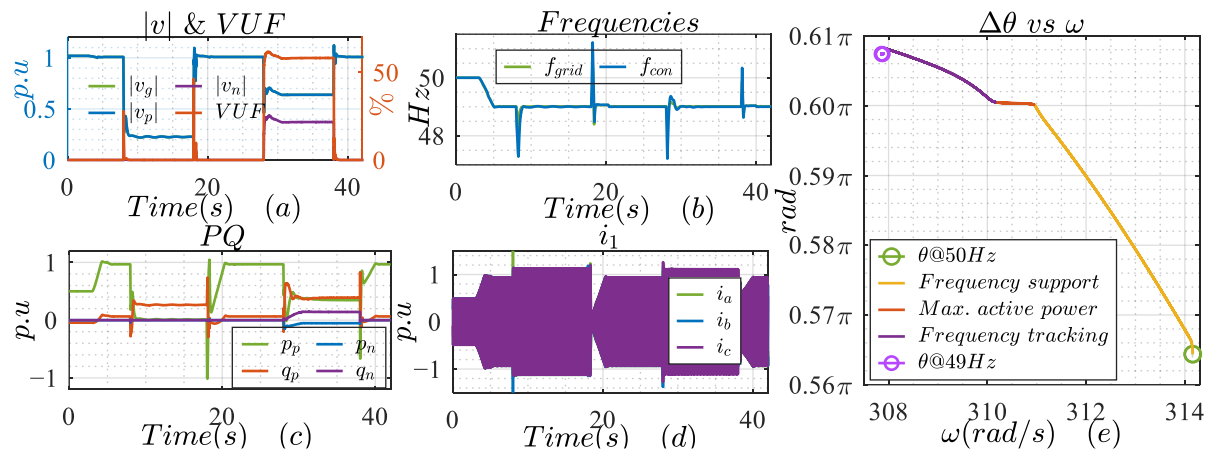


Figure 4.32: Large signal stability of GFM in low-frequency weak grid connection; (a) magnitude of sequence voltage phasors and VUF at POC, (b) frequencies of GFM and grid, (c) measured sequence real and reactive powers at POC, (d) measured phase currents on converter's side, (e) angular difference vs speed

The subplot (a) shows that the voltage achieves a different steady state level for different types of faults. The overall response is the same as the response for the 50 Hz weak grid. The subplot (b) shows a ramp frequency change from 2.5 to 3.5 seconds and the subplot (c) shows that during this frequency ramp,

the active power injection also increases smoothly till the frequency is reached 49.5 Hz. The droop gains of the converter are selected to inject the rated active power (1 p.u.) if the frequency drops 1 Hz from its nominal value but due to the reference reactive power of 0.5 p.u., in this case, the rated active power injection is achieved at 49.5 Hz. Below this frequency, the converter should keep its active power steady at the achieved level without losing the synchronization. Thus, at final value of 49 Hz, the converter is able to ensure the converter-driven stability, and voltage source behavior.

The injected power in case of fault is in agreement with the QNP priority injection scheme. Moreover, the active power is ramped up in post faults to avoid the loss of synchronization due to sudden voltage restoration. The angle stability can also be confirmed as it is done for the nominal frequency grid connection. Alternatively, it can also be confirmed from the steady power injections in normal and faulty durations as the divergent angular difference would have caused the full-scale oscillations in the injected active and reactive powers. The subplot (e) shows the angle difference vs speed for a ramp frequency change event. It shows that the $\Delta\theta$ is converged to a specific value for 50 Hz grid frequency. As the frequency ramp change is introduced, the $\Delta\theta$ keeps on rising which allows more real power injection. At around 49.5 Hz, the $\Delta\theta$ associates to the maximum real power injection and after that the grid frequency is tracked by the converter's p-f control and a new steady state level is achieved for the angular difference against steady frequency of 49 Hz.

Due to the voltage source behavior of the GFM, its connection with the stiff grid is a challenging task. A synchronized operation with the limited current handling capacity is particularly challenging during faults as the converter may lose synchronization in such cases. The same procedure is repeated for a stiff grid (SCR of 1000 at POC). The performance of the proposed scheme for a 50 Hz stiff grid and 49 Hz stiff grid connections is given in Figure 4.33 and Figure 4.34 respectively.

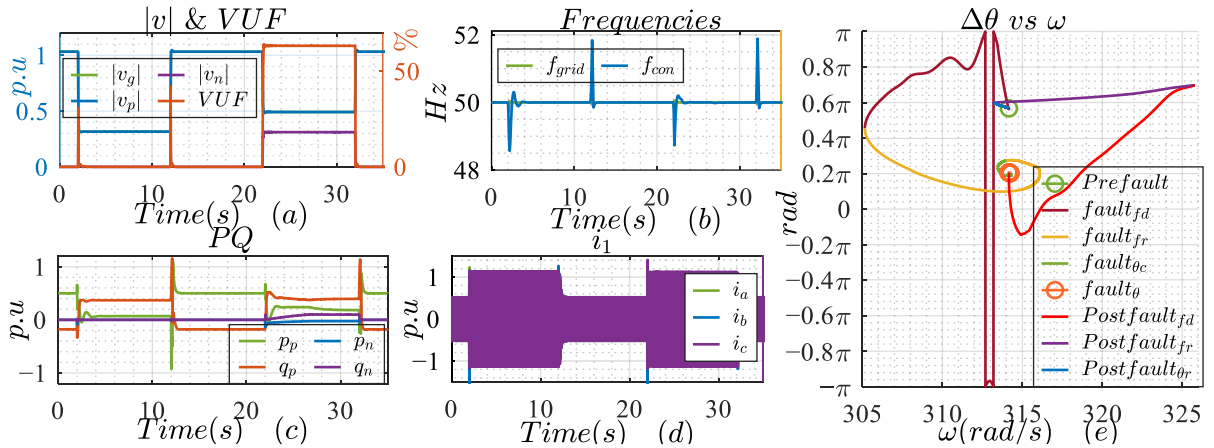


Figure 4.33: Large signal stability of GFM in nominal-frequency stiff grid connection; (a) magnitude of sequence voltage phasors and VUF at POC, (b) frequencies of GFM and grid, (c) measured sequence real and reactive powers at POC, (d) measured phase currents on converter's side, (e) angular difference vs speed, the subscripts 'fd', 'fr', 'θc', 'θr' stands for frequency deviation, frequency restoration, angle convergence and angle restoration respectively

The above figure confirms the stable operation of the proposed scheme in a stiff grid connection. The terminal voltage is stable. The frequency on the converter's side experiences a transient in initial fraction of seconds for fault and post fault conditions and finally achieves a steady value. The voltage angle difference also achieves a stable operating point in fault and post fault scenarios. The current limit of the converter is also ensured. The subplot (e) presents the angle stability of the converter against balanced fault.

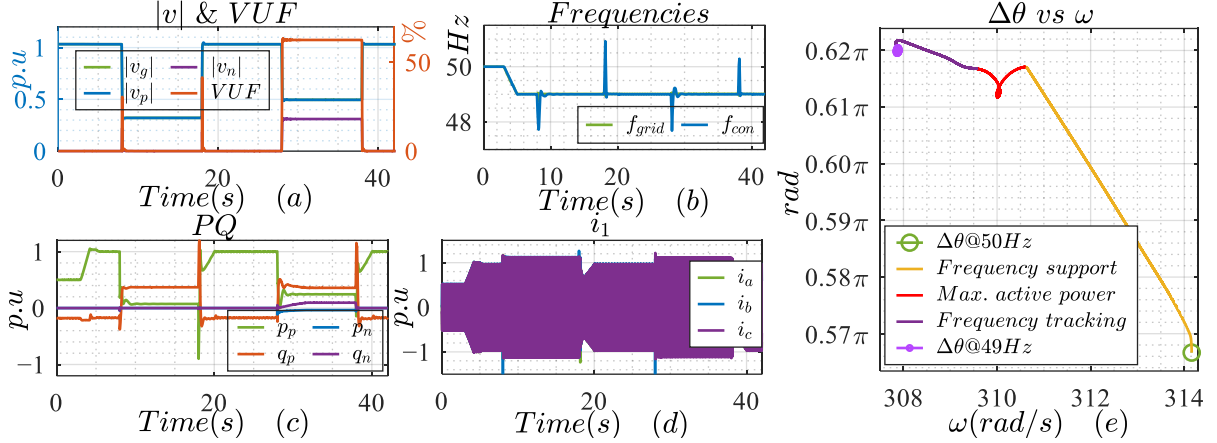


Figure 4.34: Large signal stability of GFM in low-frequency stiff grid connection; (a) magnitude of sequence voltage phasors and VUF at POC, (b) frequencies of GFM and grid, (c) measured sequence real and reactive powers at POC, (d) measured phase currents on converter's side, (e) angular difference vs speed

The above figure confirms the stable operation of the proposed scheme for a low frequency stiff grid connection. The subplot (e) shows that as the converter's maximum real power capacity is reached, a change in the angular difference is recorded but the control scheme is able to track the frequency quickly and ensure the synchronization with the grid.

The above performance analysis confirms the safe operation of the GFM in both islanded and grid connected operations. It can ensure the small signal and large signal stability for voltage, frequency and converter-driven stability in islanded, and weak to stiff grid. Moreover, it does not need any explicit measurement on the grid side to ensure stability.

4.4 Take Aways from Modeling and Analysis of GFM

The important conclusions from the above analysis are given below.

- The self synchronization technique offers fast and smooth connection with the grid as compared to the dedicated synchronization unit, however, the frequency fluctuations during the synchronization process are high. Self synchronization technique is robust provided the low pass filter and PI controller are properly tuned.
- Inclusions of additional frequency support and PI controller in conventional droop control of enhanced p-f loop help to support the low frequency grid with maximum active power injection while ensuring the synchronization.

- The enhanced p-f control also offers ramp increase in the additional frequency support and the reference real power in case of fault and post fault scenarios which helps in achieving smooth response under such conditions and avoids the loss of synchronization.
- The maximum real power injection is limited in case of faults to ensure that the sum of reference real power and additional frequency support is less than the allowed limit which is decided by the maximum power flow between two coupled ac sources in case of voltage dips.
- Due to the voltage source behavior of GFM, the slower response of Q-V control, actually, helps in reacting very quickly against any change in the operating condition at POC. Moreover, to address the unbalanced conditions, separate Q-V controls can be designed for positive and negative sequences.
- The enhanced Q-V control offers the controlled and uncontrolled negative sequence reactive power injection in case of unbalanced faults. The controlled negative sequence injection helps to reduce the real power oscillations while the uncontrolled negative sequence injection helps to reduce the voltage unbalance factor.
- Several power priority injection schemes can be designed for the GFM which not only helps in limiting the current but also helps to achieve the desired response with the limited current handling capability of the converter. However, the desired response is achieved with a certain time delay which is dependent on the speed of the Q-V controls. The initial response of the GFM is still like the natural response of the three-phase voltage source.
- The current limit of the converter can be ensured with the help of a virtual damping resistor which introduces additional reference voltage based on the measured current at POC. Moreover, cascaded voltage and current controllers can also be used for the direct current control.
- For a small signal stability in islanded operation, the proposed scheme offers smooth response against any load change and if the total load power exceeds the rated power of the converter, the response is dependent on the priority scheme. With PQN priority, there are less fluctuations in frequency as compared to the voltage. Thus, with PQN priority, the response of the GFM is closer to the response of the stiff-frequency grid.
- The small signal stability is largely decided by the grid in case of grid-connected mode, however, in weak grid connections, the converter's response has an impact on the stability and the analysis show that for unity SCR, a stable response for different reference powers in different grid's frequencies is achieved with the proposed GFM.
- In faulty situations, the proposed GFM ensures the voltage, frequency and angle stability while ensuring the safe operation of the converter in different modes and different operating conditions.

Thus, the key factors mentioned in section 4.1.1.3 are confirmed for the proposed GFM control. These parameters are given in Table 4.11.

Table 4.11: Performance of proposed GFM scheme against the defined key parameters

<i>Key Parameters</i>	<i>Performance</i>
It should maintain its voltage source behavior in all conditions.	✓
It should offer a stable response in all conditions.	✓
It should ensure the current limitation in all conditions.	✓
In case of LVRT conditions with rated frequency, it should be able to support the grid's voltage.	✓
In the case of LVRT with frequency dip, it should inject the maximum real power to the system while ensuring the synchronization with the grid to enhance the converter-driven stability.	✓
It should stay connected to the grid and offer stable response in case of high to low impedance faults.	✓
It should be able to provide selective voltage support in case of unbalanced faults.	✓
It should offer smooth transition from grid connected to islanded mode and vice versa.	✓
It should offer unified control for weak to stiff grid connections.	✓
It should also ensure the small and large signal stability in islanded, and grid connected mode.	✓

5. STABILITY OF MULTI-CONVERTER SYSTEMS

In the previous chapters, the design and performance of the individual GFL and GFM converters are discussed explicitly. The results confirm the stable operation of both the converters in different operating conditions. However, the performance analysis of the designed control schemes is verified in islanded, and grid connected operations with only one converter connected. In reality, there can be multiple converters connected in a micro-grid (MG). Thus, it is important to analyze the stability of these converters in a multi-converter system (MCS) as various dynamic interactions are possible between the converters in an MCS. Moreover, the injected power quality can also be degraded due to these interactions [119]. Another important aspect is the calculation of the short circuit ratio (SCR) of a converter connected system. Thus, in this chapter, the interactions of different converters will be analyzed in different operating conditions and the SCR will be discussed for a fully converter-based system.

5.1 Short Circuit Ratio

The short circuit ratio (SCR) is defined as the ratio of the short circuit power at a specific node to the rated power of the source/load connected at that node. It helps to define the grid's strength at a particular node. The higher SCR confirms that the system's frequency and voltage are less impacted by the load change of rated power at the specific node. Similarly, in a weak grid, such load/generation changes have a huge impact on the system's frequency and voltage. It also helps to categorize the grid as very weak, weak, or strong grid. If SCR is less than 3 at POC, it is categorized as a very weak grid and if it is between 3 and 5, then it is a weak grid [120]. The strong grid can have an SCR greater than 5 (preferably more than 7) at POC.

The GFM behaves like a controlled voltage source behind an impedance (Figure 2.22) and the GFL converter behaves like a controlled current source in parallel to an impedance (Figure 2.16). It is important to mention here that in a converter-connected network, the concept of short circuit power is different than its classical understanding. In [120], it is suggested to consider the GFM in the calculation of the SCP while the impact of GFL is ignored due to its current source behavior. The share of the GFM towards SCP is highly dependent on the actual operating conditions (type of disturbance). The GFL requires an active grid connection for its operation and the grid is mainly responsible for small signal stability even though the GFL converter can have a positive impact on the network's strength for small disturbances. Thus, the short circuit power of GFL in case of small disturbances is not calculated. Also in large disturbances, due to the controlled current source behavior, the share of GFL in SCP calculations is ignored. This is why in the following sub-sections, only the SCP of GFM is computed for small and large disturbances.

5.1.1 SCP of GFM in Small Disturbances

For small signal stability, the GFM can be considered as a very high short circuit power source that ensures the voltage and frequency stability in case of a load/generation change. The SCP of the converters in small disturbances (current limit of the converter is not reached) is different than the short circuit power in large disturbances (current limit of the converter is reached). It defines the resiliency of the system as higher SCP results in small change in terminal voltage due to the change in load. To calculate the resiliency of an islanded GFM in case of small disturbances, the following equivalent setup is used.

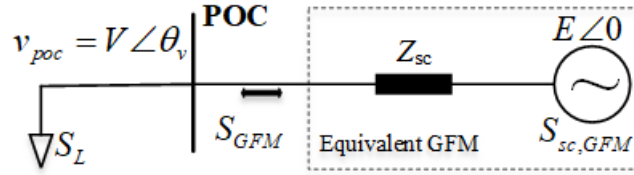


Figure 5.1: Equivalent network for SCP calculations of islanded GFM

A GFM controls active/reactive power injection at POC based on its operating mode. Thus, S_{GFM} is the rated apparent power of the GFM which can flow in either direction based on the operating condition. The change in terminal voltage, due to the change in load, defines the resiliency of the GFM as this is the only source available to control the voltage at POC. The minimum voltage change shows a strong source (GFM in this case). The SCP of the GFM in small disturbances can be computed by change in load and observing the change in terminal voltage phasor. The following expression can be used for the assessment of the SCP for islanded GFM. Its derivation is discussed in appendix N.

$$\left| \frac{\Delta S_L}{SCP} \right| = \left| \frac{\Delta v_{poc} + \left(|v_{1poc}|^2 - |v_{2poc}|^2 \right) / E}{E} \right| \quad (5.1)$$

Where the subscripts 1 and 2 are used to indicate the reading before the load change and after the load change respectively. It is important to mention here that the change in voltage at POC is in phasor form, thus, the phasor summation should be used to sum up the change in square of the magnitude voltages and the change in voltage phasor. The SCP of the GFM can be expressed in the form of its rated power. If the nominal voltage at the point of connection (E) is selected as the base voltage and the rated power of the GFM can be selected as the base power. The expression for the SCP of GFM in case of small disturbances is given in equation (5.2).

$$\frac{SCP}{S_{GFM}} = \left| \frac{\Delta S_{L,pu}}{\Delta v_{poc,pu} + \left(|v_{1poc,pu}|^2 - |v_{2poc,pu}|^2 \right)} \right| \quad (5.2)$$

The above expression shows that the SCP of the GFM is proportional to its rated power and the voltage sensitivity against the small disturbances. The X/R ratio for the short circuit impedance of the GFM can also be calculated if the voltage phasors at POC are known along with the angle of the power change. The expression for the X/R ratio of the short circuit impedance of islanded GFM is given below.

$$\left(\frac{X}{R}\right)_{Z_{sc}} = \tan^{-1}(\theta_{\Delta S_L} - \theta_x) \quad (5.3)$$

$$\therefore \theta_x = \angle\left(\Delta v_{poc,p.u} + \left(|v_{1poc,p.u}|^2 - |v_{2poc,p.u}|^2\right)\right)$$

The expressions for the SCP and the X/R ratio can be simplified by ignoring the difference of square of voltage magnitude at POC. The simplified expressions are given in equation (5.4).

$$\frac{SCP}{S_{GFM}} = \left| \frac{\Delta S_{L,p.u}}{\Delta v_{poc,p.u}} \right| \quad (5.4)$$

$$\left(\frac{X}{R}\right)_{Z_{sc}} = \tan^{-1}(\theta_{\Delta S_L} - \theta_{\Delta v_{poc}})$$

The voltage sensitivity depends on the control gains of Q-V control. Moreover, due to the active voltage control loop in GFM, the change in terminal voltage settles with times, thus, a time dependent trend of SCP can be drawn. For the assessment of SCP of islanded GFM, the improved design of GFM, discussed in chapter 4, is used. All the control gains are same as discussed in Table 4.9. To compare the detailed and simplified models (equation (5.2) and (5.4) respectively) for SCP calculation, a 10 % change in active and reactive load power is introduced at 0 seconds consecutively and the calculated normalized SCPs are plotted in Figure 5.2. For these plots, the dc current component, due to the switching of the inductor, is ignored.

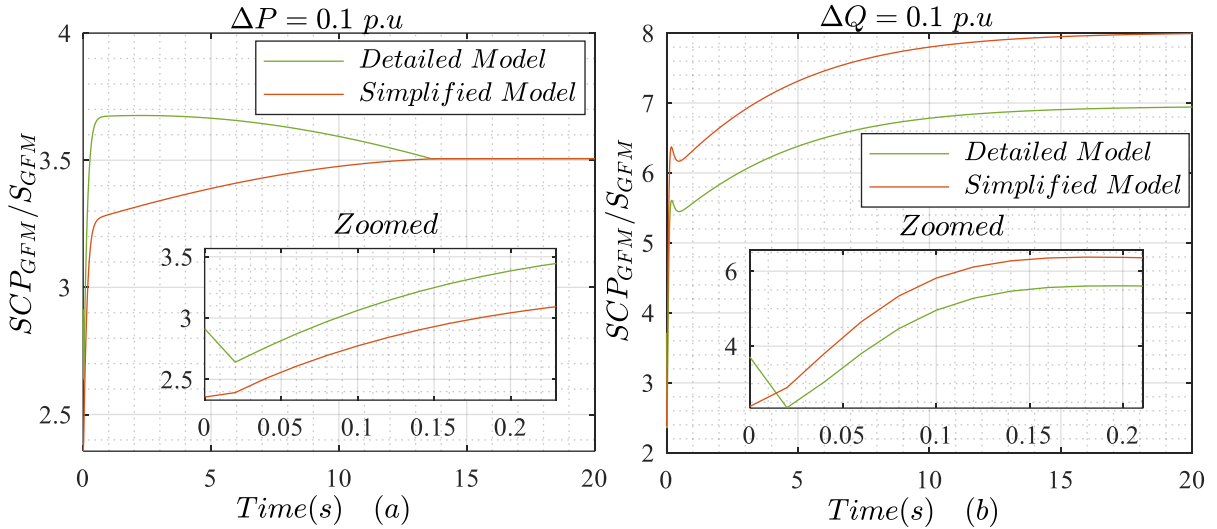


Figure 5.2: Ratio of SCP to the rated power of GFM in islanded conditions for small disturbances; (a) 10 % change in active power load, (b) 10 % change in reactive power load

The above figure shows that the SCP of the islanded GFM varies with time due to the active voltage control. As the voltage is recovered by Q-V controller, the final SCP settles to somewhat higher value than its initial value (after introducing the load change). Thus, in contrary to the slower GFM, a fast response of the GFM helps to steady SCP quickly. Moreover, the subplots (a) and (b) show that there is a considerable difference in the calculated SCPs by the detailed and simplified models both for the active and reactive power changes. Thus, the effect of the difference of square of voltage magnitudes

(before and after the load change) can't be ignored. Additionally, this factor has a positive impact on the SCP for the active load changes and negative impact on the SCP for the reactive load change. The reason for this is its phasor addition to the Δv_{poc} . Considering the dq-axis, the difference in the square of the voltage magnitudes is added to the d-axis component of Δv_{poc} . The change in active power load changes the distribution of the magnitude of the voltage phasor into its dq-components due to the sudden angle change whereas the change in reactive power majorly changes the magnitude of the voltage phasor and has less impact on its distribution into its dq-components. The change in voltage angle in case of reactive power change is due to the compensation of the filter's and coupling transformer's resistances. Its phasor representation is given in Figure 5.3.

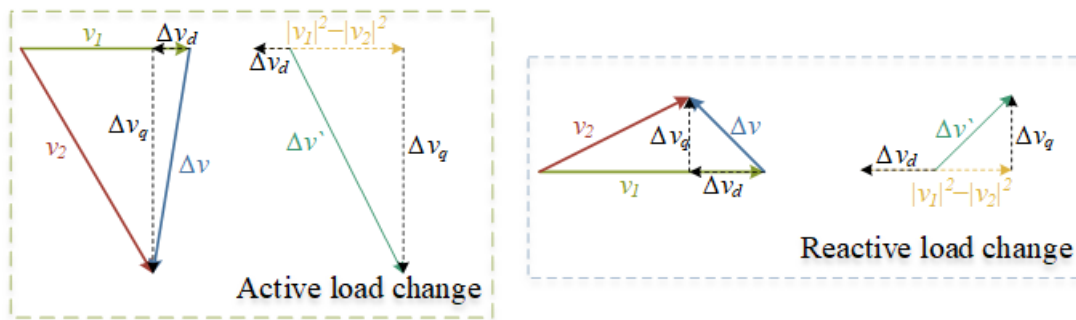


Figure 5.3: Phasor presentation of the voltage difference in case of active and reactive load change

The above figure shows that the active load change largely varies the voltage angle and has less impact on its magnitude. This results in a Δv with very high q-component and very small d-component. However, the d-component of the detailed model has an additional term which is the difference between the square of voltage magnitudes and this term compensates for the negative d-component which results in smaller resultant $\Delta v'$ and higher SCP.

Referring to subplot (a) of Figure 5.2, the detailed and the simplified models converge after some time. The reason for this is the recovery of the voltage magnitude to its initial value and the effect of difference of square of voltage magnitudes is diminished with time. As the voltage recovery is made by Q-V control, thus the convergence time is decided by the integral gain of Q-V control.

Referring to Figure 5.3, for the reactive load change, the magnitude of the voltage phasor varies largely and results in equal change in d- and q-components of the voltage phasor. In this case, the additional term in the d-component of the resultant $\Delta v'$ also compensates for the negative change in Δv_d but due to the higher magnitude difference between the final and initial voltage phasors, the magnitude of $\Delta v'$ is greater than the magnitude of Δv . Thus, detailed model results in smaller SCP than the simplified model (subplot (b) of Figure 5.2). Moreover, the magnitude voltage difference can't be minimized by the Q-V controller in this case, thus the calculated SCPs (by the simplified and detailed models) don't converge to a single value even in steady states.

From the above analysis, it is clear that the difference of the square of voltage magnitudes should not be ignored in the calculation of the SCP and it should be added vectorially to the voltage difference phasor. Thus, the plots afterwards will only be based on the detailed model. From equation (5.3), the X/R ratio of the short circuit impedance of the islanded GFM can also be calculated. Like the SCP, the X/R ratio is plotted for 10 % active and reactive load changes in Figure 5.4.

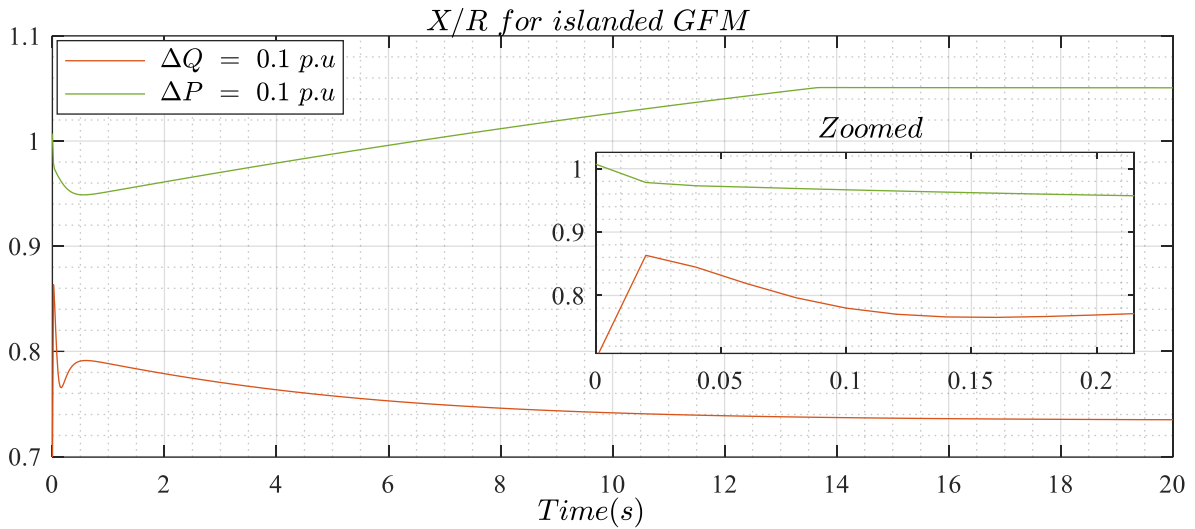


Figure 5.4: X/R ratio of the islanded GFM for active and reactive load changes

The above graph shows that the X/R ratio does not change drastically for active/ reactive load changes, but it also shows that the X/R ratio is less than unity. The initial values of SCP and X/R at 0 seconds can be ignored due to the averaging out the powers to eliminate the dc current component in case of inductor switching for reactive load change. Thus, the initial value may be selected after three cycles i.e., at 0.06 seconds for the 50 Hz system.

To analyze the impact of slow/fast Q-V controller, the integrator gain of the Q-V controller (K_{qp}) is increased 4 times and its impact is analyzed in case of 10 % change in active load.

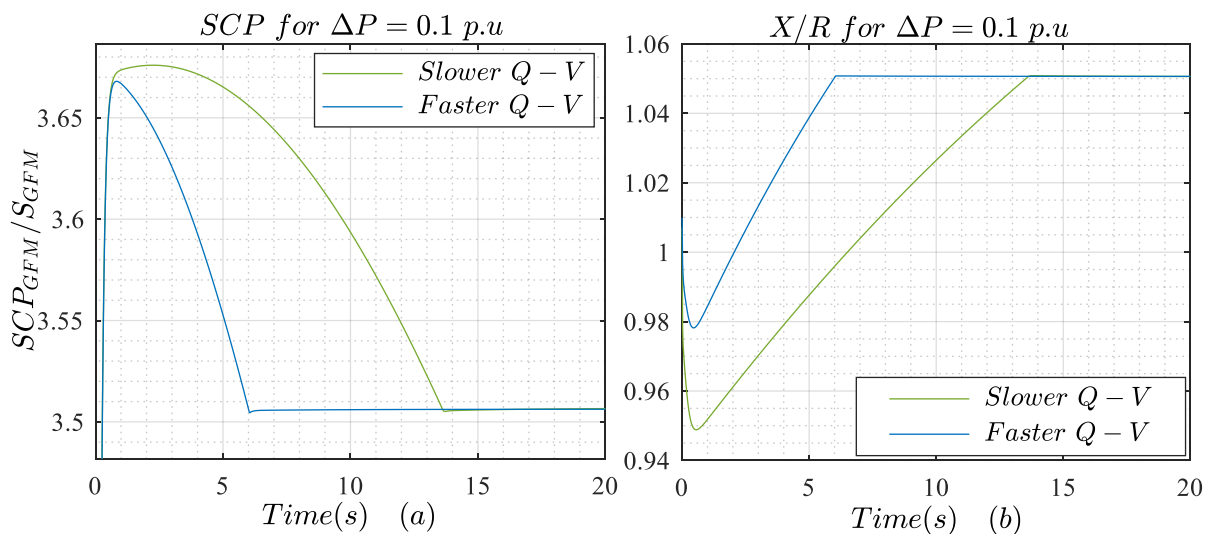


Figure 5.5: Impact of Q-V controller gain on the SCP and X/R ratio of the islanded GFM; (a) calculated SCP, (b) calculated X/R ratio

The above figure confirms that the faster Q-V controller helps to achieve the steady values more quickly. This is contrary to the recommendations for the GFM which demand a slower response. However, this effect of the slower/faster Q-V controller is dominant in case of active load change due to the voltage magnitude dependent additional term in the calculation of Δv . Moreover, from equation (5.2), it is clear that the calculated SCP is not dependent on the initial or final loading of the converter, but the current limit of the converter should not be reached due to the load change.

To decide the SCP of the GFM, the initial SCP (value at 60 milli-seconds) can be used as it is lower than the final value and if it is used in the calculation of the network's resilience, the actual network's strength will be more than the calculated one and can provide a safety margin. The other important question is that which of the SCP should be used as for active and reactive load changes, the SCP changes significantly. The scholar suggests deciding it based on the primary application of the GFM, e.g., if the GFM control scheme is used for a static synchronous compensator (STATCOM), the SCP for reactive load change should be used, and if GFM is used for frequency control (there is some other source to control the voltage), the SCP for active load change can be used. For generic applications, considering worst case scenario, minimum of the SCPs can be used in the calculations of the network's strength.

5.1.2 SCP of GFM in Large Disturbances

The short circuit power of the GFM can be considered equal to its power rating (ignoring the limited time over-current handling capability) in case of large disturbances. As the over-current capability of the converter (1.2 p.u.) is ignored, thus, the actual SCP will be slightly higher than the calculated one. A simple network is shown in Figure 5.6 for the calculation of the SCR in a converter-based network considering the large signal stability.

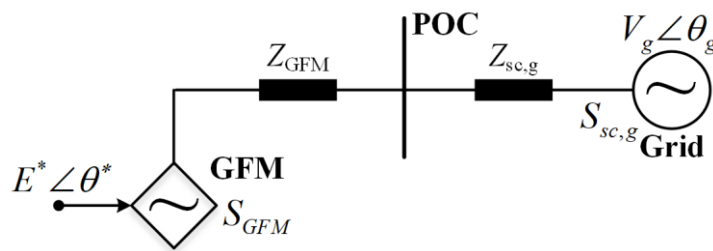


Figure 5.6: Direct coupling of grid and GFM

'S' represents the apparent power, 'Z' stands for impedance and subscript 'sc' stands for short circuit. In the above figure, the GFM is directly coupled to the grid at POC. The mathematical expression for the short circuit impedance, seen through POC, is given in equation (5.5).

$$Z_{poc} = Z_{GFM} \parallel Z_{sc,g} \quad (5.5)$$

If the rated power generation/consumption at POC is equal to the base power (S_b) and base voltage is same as nominal voltage level at POC then the SCR at POC can be defined as:

$$SCR_{poc} = \frac{S_{sc,poc}}{S_b} \rightarrow SCR_{poc} = \frac{1}{Z_{poc,pu}} \quad (5.6)$$

Where SCR stands for short circuit ratio and the subscript ‘p.u’ stands for per unit values. The above equation shows that the SCR is the inverse of the per unit short circuit impedance seen through POC. The mathematical expressions for the converter’s and grid’s short circuit impedances and the SCR are given in equation (5.7).

$$\begin{aligned} Z_{sc,g} &= \frac{V_g^2}{S_{sc,g}} \rightarrow Z_{sc,g,pu} = \frac{S_b}{S_{sc,g}} \\ Z_{GFM} &= \frac{V_g^2}{S_{GFM}} \rightarrow Z_{GFM,pu} = \frac{S_b}{S_{GFM}} \\ Z_{poc,pu} &= Z_{sc,g,pu} \parallel Z_{GFM,pu} \rightarrow Z_{poc,pu} = \frac{S_b}{S_{sc,g} + S_{GFM}} \\ SCR_{poc} &= \frac{1}{Z_{poc,pu}} \rightarrow SCR_{poc} = \frac{S_{sc,g} + S_{GFM}}{S_b} \end{aligned} \quad (5.7)$$

The above equation shows that the GFM has a positive impact on the SCR at POC. From the SCP calculations in case of small and large disturbances, it can be concluded that the share of the GFM to the SCP varies depending upon the actual conditions (small and large disturbances) and the minimum share of GFM in the SCP calculations is equal to its rated power. For small disturbances, the share of GFM towards network strength can be as high as 3–6 times of its rated power depending on the primary application of the GFM.

5.2 Analysis of Multi-Converter System

To decide the SCP for the GFL connection, Equation (5.7) is useful as it considers the minimum share of the GFM in the SCP, thus, the SCP in the normal conditions will be greater than the calculated one. Thus, this equation helps to decide the maximum rating of the GFL which can be connected at POC without causing its stability problems. Moreover, the minimum SCP at POC can also be calculated with the help of the above equation by selecting SCR as unity. The more generic network arrangement for a multi-converter system is given in Figure 5.7.

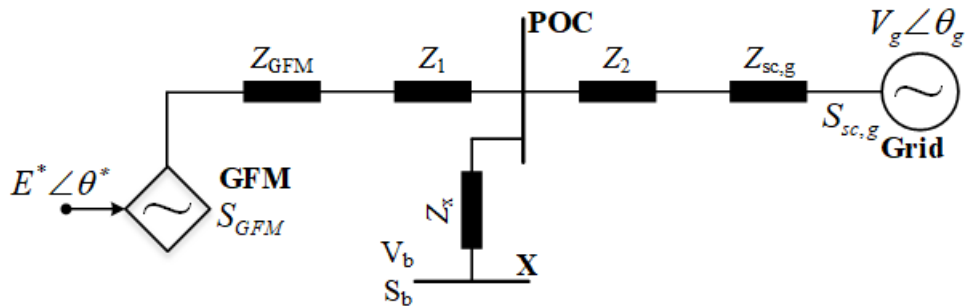


Figure 5.7: Generic multi-converter network

Z_1 , Z_2 and Z_X are the line impedances. The advantage of the above network is that the impact of a remotely connected converter can be taken into account. Similarly, if the grid's SCP is defined at some remote node, then it can be easily used to calculate the SCR to a node which is away from POC of the GFM and grid. The mathematical expression for the SCR at node 'X' for a base power of S_b is given in equation (5.8).

$$SCR_X = \frac{V^2}{S_b} \left\{ \frac{S_{GFM} B + S_{sc,g} A}{AB + Z_X (S_{GFM} B + S_{sc,g} A)} \right\}$$

$$A = V^2 + Z_1 S_{GFM} \quad (5.8)$$

$$B = V^2 + Z_2 S_{sc,g}$$

Where ' S_b ' denotes the rated power of the connected load/source at node 'X'. In the above equation, ' V ' is the nominal voltage at node 'X'. The SI units are used in the above equation. This equation can be used to calculate SCR at POC by selecting Z_X equal to zero. Similarly, SCP at POC and at node 'X' can also be calculated with the help of the above equation. It helps in deciding the maximum GFL rating to be connected at node 'X' to ensure the stable operation of the GFL. The above equation also shows that the impact of the GFM is marginalized by increasing the line impedance Z_1 . Similarly, the grid's share is reduced by increasing the Z_2 . It helps to calculate the SCR for a very strong to very weak coupling of the GFM and grid. A numerical example to calculate the SCP, at POC and node 'X', is given in appendix O.

Figure 5.8 shows a simple arrangement for a generic multi-converter system.

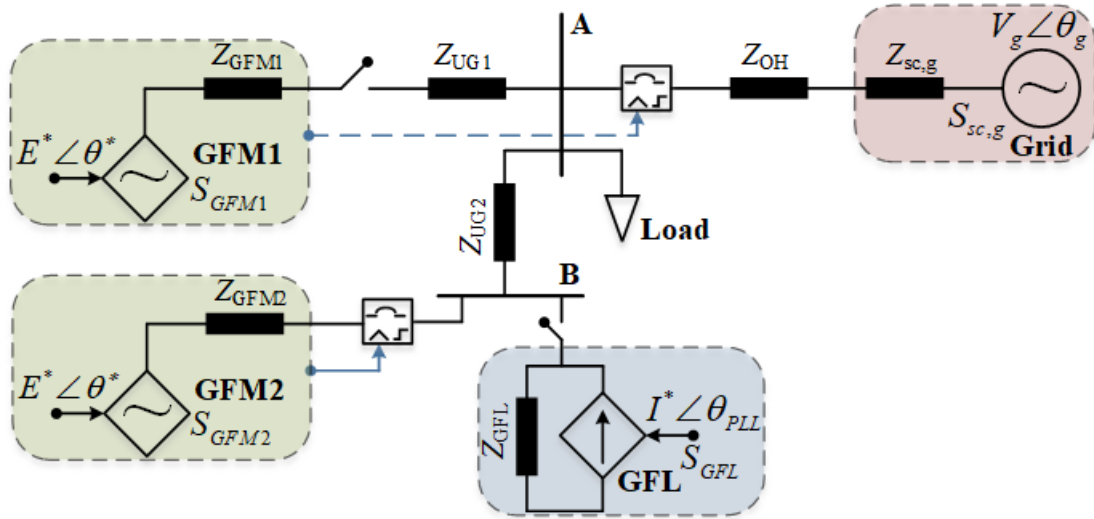


Figure 5.8: Simplified layout of multi-converter system

The subscript 'UG' and 'OH' stand for under ground cable and over-head transmission line respectively. The above figure shows a power network with multiple converters. These power sources can be connected/disconnected to simulate different arrangements for grid connected and islanded operations. The GFM1 represents a grid forming converter which is connected to the node A with the help of an underground cable having impedance of Z_{UG1} , the rating of this converter is varied between 100 and

400 kVA to analyze different schemes. The node 'B' represents the residential side of the feeder where two prosumers are connected, one having GFL converter and the other one having the GFM converter. The Z_{UG2} represents the underground cable impedance between node 'A' and 'B'. The $S_{sc,g}$ is the short circuit power of the grid which is defined at the grid station and the Z_{OH} is the overhead line's impedance from grid station to node 'A'. The rating of the residential sources is less as compared to the industrial side GFM. Thus, in islanded operation, the GFM1 acts as the main source and generates voltage and angle references for the rest of the sources. Based on the generic structure given in Figure 5.8, several combinations have been tested. The results are presented in the following sections.

5.2.1 GFM Vs Grid

In this comparison, the rated power of the GFM converter is set equal to the grid's SCP. For a fair comparison, the line impedances are not considered here. The SCP of the grid and rate power of the GFM1 are selected to be 200 kVA. A constant impedance load of 50 kW and 30 kVAR is connected at node 'A' at 5 seconds. The grid is connected to the node 'A' and other converters are switched off. A balanced fault is applied at node 'A' to analyze the response of the grid against this fault. The same procedure is repeated for the GFM1 converter with all other converters and grid disconnected from node 'A'. The results for the GFM and grid are given in Figure 5.9.

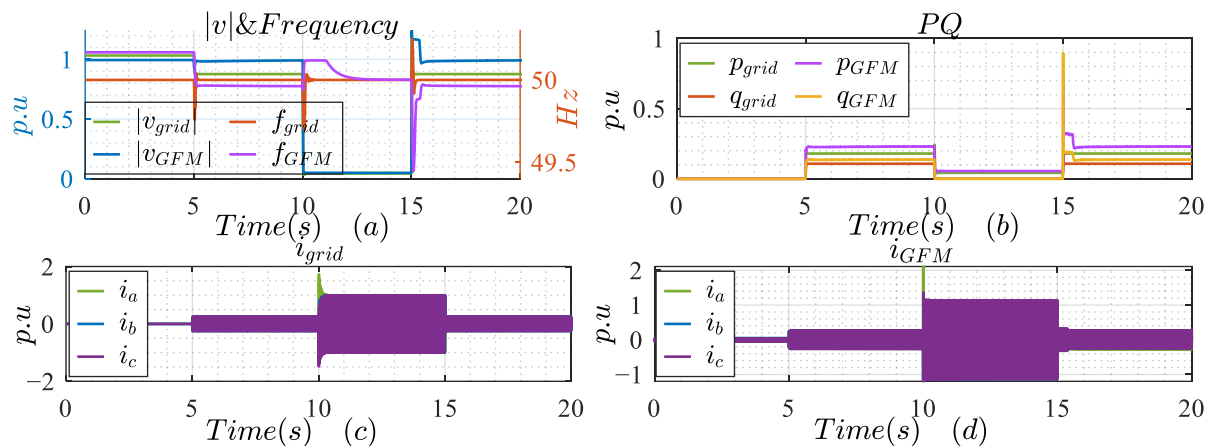


Figure 5.9: Comparison of GFM and grid; (a) terminal voltage and frequency, (b) real and reactive powers for GFM and grid, (c) grid's line current, (d) converter's line currents

From subplot (a), it is clear that the voltage at node 'A' for converter or grid connection is near to its nominal value in no load conditions. When a load is connected at 5 seconds, there is around 20 % drop in the voltage at node 'A' for the grid connection but for GFM, the voltage drop is minimal. It is due to the fact that the converter's control scheme includes voltage control whereas the grid is a constant voltage source without an excitation system. This reflects that the SCP of GFM in small disturbances is very high. At 10 seconds, a balanced fault is introduced at node 'A', voltage dip for GFM and grid is in good agreement with GFM offering 13.6 % more terminal voltage which means the GFM is stronger than the grid with SCP equal to the GFM's rated power. The reason for such behavior is the additional 20 % overcurrent injection capability of the converter in case of faults. From subplot (a), the frequency

graphs show that the post fault system's frequency is having more fluctuations in case of GFM as compared to the grid, but these fluctuations do not result in unstable response of the GFM.

The subplot (b) shows that measured powers at node 'A' for grid connected and GFM connected modes. It shows that the converter with its droop characteristics delivers more active and reactive power as compared to the grid when a load is connected at node 'A'. It is due to the better voltage profile in the case of GFM connected mode. Similarly, in fault duration, the GFM delivers more active power than the grid and there is no reactive power due to the resistive fault. The grid's line currents are plotted in subplot (c) which shows that the fault current is raised initially at the start of the fault and then it settles to 1 p.u. which is in accordance with its defined SCP. The subplot (d) shows the GFM's line currents which are limited to the maximum allowed current (1.2 p.u.). Due to the higher current in GFM, the better voltage profile and more active power injection is recorded for GFM in case of fault as compared to the grid.

Thus, it can be concluded that the GFM's share in the SCP calculation in an MCS varies largely depending upon the actual operating conditions (different for small and large disturbances) which is different than the classical understanding of SCP. However, the minimum share of GFM in SCP calculations should be updated with the short circuit power of GFM equal to its maximum current handling capacity times the rated power of the converter. If only the rated power of GFM is considered as its SCP, then the actual SCP will be more than the calculated one in an MCS having at least one or several GFMs. Thus, the concept of SCP with the classical definitions of short circuit power reveals significant shortcomings in case of multi converter systems. New concepts have to be developed in the future.

5.2.2 GFL and Grid

In this section, the impact of GFL connection, with the GFM and with very weak grid, is analyzed over the small and large signal stability of the system. The schematic diagram for this arrangement is given below.

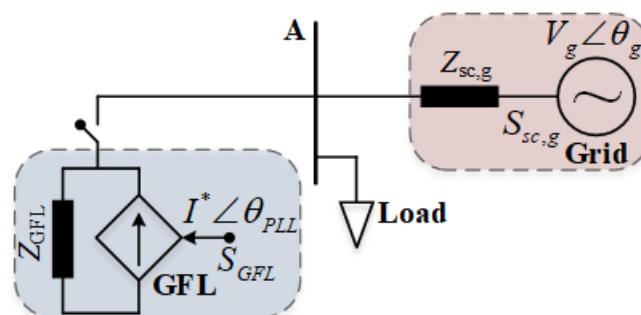


Figure 5.10: Schematic diagram for direct coupling of the GFL with the grid

The GFL connection stability is analyzed for unity SCR at node 'A'. The GFL is enabled at the start of the simulation and its real power injection is ramped up. At 5 seconds a load of 50 kW and 30 kVAR is

connected at node ‘A’ and a balanced fault is introduced at the same node on 10 seconds. The duration of the fault is 5 seconds. The reference real and reactive powers of GFL converter are 1.0 and 0 p.u. respectively. The pre-fault, fault and post-fault responses are analyzed. The GFL is connected with the grid having SCP equal to the rating of the GFL and line impedances are ignored.

The response of the GFL for such conditions is given in Figure 5.11.

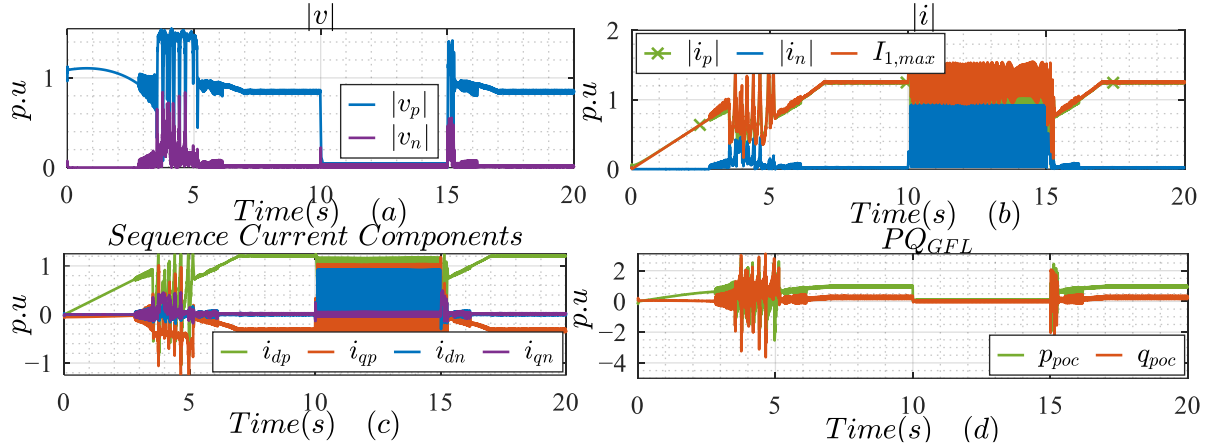


Figure 5.11: Response of GFL connection with the grid for unity SCR; (a) magnitude of sequence voltage phasors at POC, (b) magnitude of sequence current phasors at POC and maximum line current on converter’s side, (c) current components for positive and negative sequences measured on converter’s side of POC, (d) measured real and reactive power injections by GFL at POC

The above figure shows that the GFL response is not stable in pre-fault conditions for few seconds. It causes higher phase currents in this duration which could damage the converter’s switches. The PLL does not estimate the correct frequency in this duration which results in unstable response. However, at 5 seconds, a load is connected, and the converter’s response gets stable due to this load connection. This behavior validates the statement that the GFL converters may have negative impact on the SCP in case of small disturbances. Moreover, the subplot (c) shows that the constant reactive current injection in case of fault is also not achieved in this condition. Hence, the small and large signal stabilities of the GFL are poor for a unity SCR connection with the constant voltage source.

5.2.3 GFL and GFM

The same procedure is repeated for the GFL connection with a GFM connection of the same rating. The schematic diagram for the direct coupling of the GFL with the GFM is given in Figure 5.12.

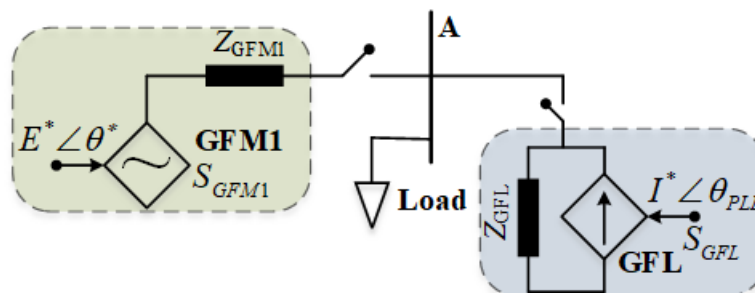


Figure 5.12: schematic diagram for direct coupling of the GFL with the GFM

The results of the above discussed arrangement are given in Figure 5.13.

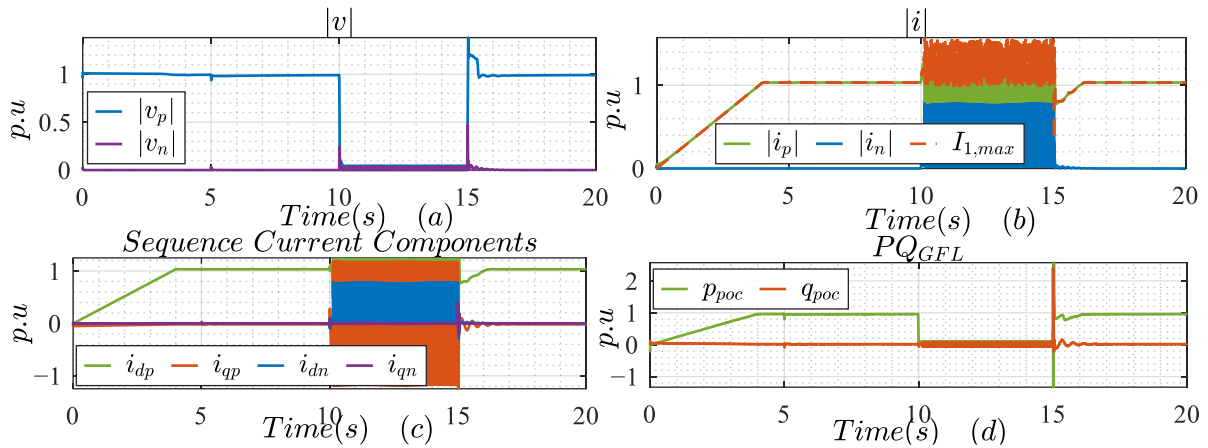


Figure 5.13: Response of GFL connection with GFM for unity SCR; (a) magnitude of sequence voltage phasors at POC, (b) magnitude of sequence current phasors at POC and maximum line current on GFL converter's side, (c) current components for positive and negative sequences measured on GFL converter's side of POC, (d) measured real and reactive power injections by GFL at POC

The above figure shows that the small signal stability of the GFL with the GFM connection is improved as compared to its grid's connection which validates that the GFM behaves as a strong SCP source against small disturbances. The reason for this is the active excitation control in the GFM which is missing with the very weak grid. However, in case of fault, the constant reactive current injection is not achieved which is due to the poor performance of the PLL. Thus, with the GFM connection, the pre-fault and post fault stability of GFL is improved as compared to its grid's connection. However, the large signal stability is poor for both the connections. The large signal stability is largely dependent on the SCR at the POC due to the negative admittance, in parallel to the network's admittance, introduced by the PLL. Thus, it is important to have the SCR larger than 2 at POC to ensure the stable GFL response in all conditions. The response of the GFL for SCR 2 at POC for grid and GFM connection is given in Figure 5.14.

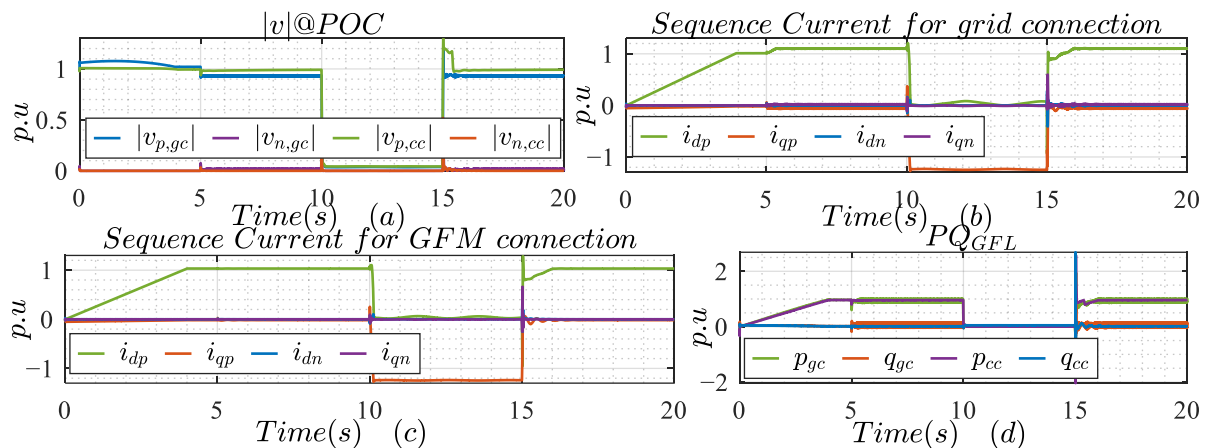


Figure 5.14: Response of GFL connection for SCR = 2; (a) magnitude of sequence voltage phasors at POC, (b) measured current components of GFL converter for grid connection, (c) measured current components of GFL converter for GFM connection, (d) measured real and reactive power injections by GFL at POC

In the above figure, the subscript ‘gc’ stands for grid connection and ‘cc’ stands for converter connection which is GFM in this case. The above figure shows that the large signal stability of the GFL is good for both the grid connection and converter’s connection. However, some undamped fluctuations in the injected powers are recorded for the grid connection of the GFL which is due to the absence of voltage control on the grid’s side. Moreover, the open loop reactive current injection mode is selected for the GFL due to which it does not support the voltage in normal conditions. The small signal stability for the GFM connection is ensured in this arrangement.

The same procedure is repeated to analyze the response of the GFL having the voltage control. The responses are plotted in Figure 5.15 for the grid and converter connections.

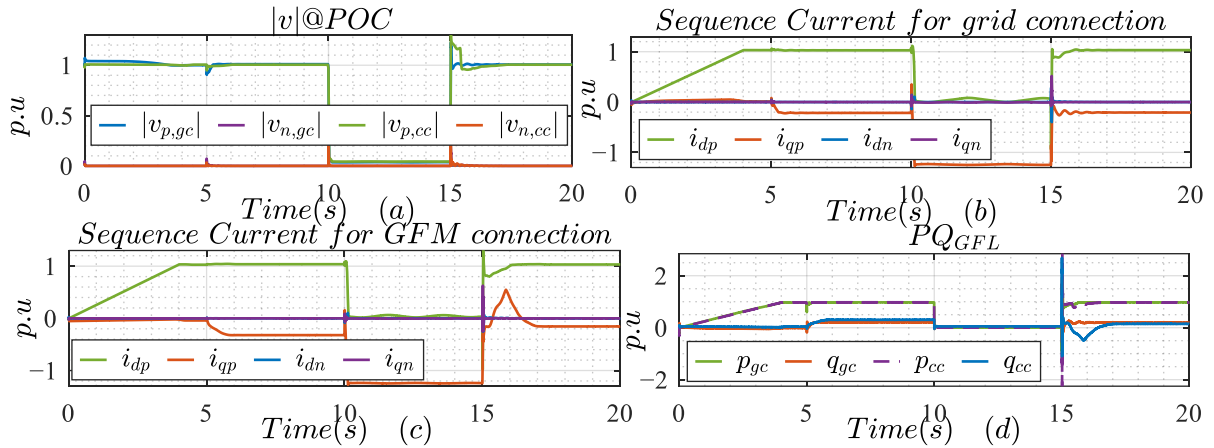


Figure 5.15: Response of GFL connection having voltage control for SCR = 2; (a) magnitude of sequence voltage phasors at POC, (b) measured current components of GFL converter for grid connection, (c) measured current components of GFL converter for GFM connection, (d) measured real and reactive power injections by GFL at POC

The above figure confirms the small and large signal stabilities of the GFL with voltage control for very weak grid connection, and for GFM connection. By comparing performance of the GFL in grid connected mode with and without voltage control mode, it shows that the injected power oscillations are also damped out for the GFL with the voltage control mode.

Hence it can be concluded from the analysis that the small and large signal stability is confirmed for the designed GFL if the SCR is at least 2. Moreover, the small signal stability is improved for a very weak grid connection if the GFL’s voltage control is activated.

The impact of line impedances is also investigated by considering a stronger grid. The line impedance is selected with the help of equation (5.8) to keep the SCR = 2 at POC. The grid’s SCP at the grid’s side of line impedance is selected four times higher than the rating of the GFL. Similarly, the rating of the GFM is also selected as four times higher than the rating of the GFL. To keep SCR = 2 at POC in each connection mode, the line impedance of 0.4Ω is introduced for the GFM and grid connections. It is important to mention here that only one source (from grid and GFM) is activated along with GFL for this investigation.

In case of GFL connection with the GFM, the performance of the GFL is same with and without line impedance if the SCR to connection point is same. In the case of grid connection, the performance of GFL depends on the type of line impedance. For inductive line, the performance of the GFL is same with and without line impedance if the SCR at connection point is same. However, for resistive line, the injected power experience oscillations for initial half a second on the load change of about 60 % of the capacity of the GFL which shows degraded performance in case of small disturbances.

5.2.4 Connection of Multiple GFMs

In the previous chapter, the performance of the GFM is analyzed both in grid connected and islanded operation. In this section, the small and large signal stability will be analyzed for a local grid comprised of two GFMs. In a grid connected operation, the small and large signal stability is ensured if the SCR at POC is 1.5 for the GFM connection. However, if another GFM operates as a grid then this ratio can be even decreased due to the voltage control of the master GFM which is missing in case of a grid. The layout of the test network for GFM connections is given in Figure 5.16.

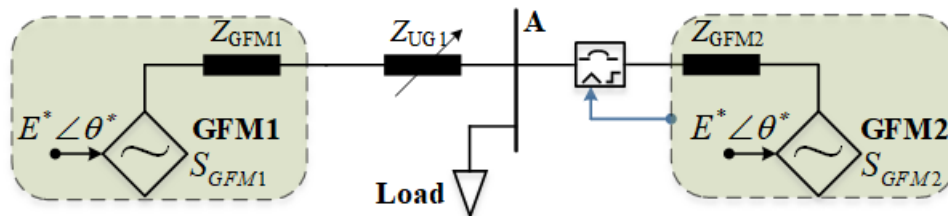


Figure 5.16: schematic diagram for the coupling of multiple GFMs

The responses of both the converters are given in Figure 5.17.

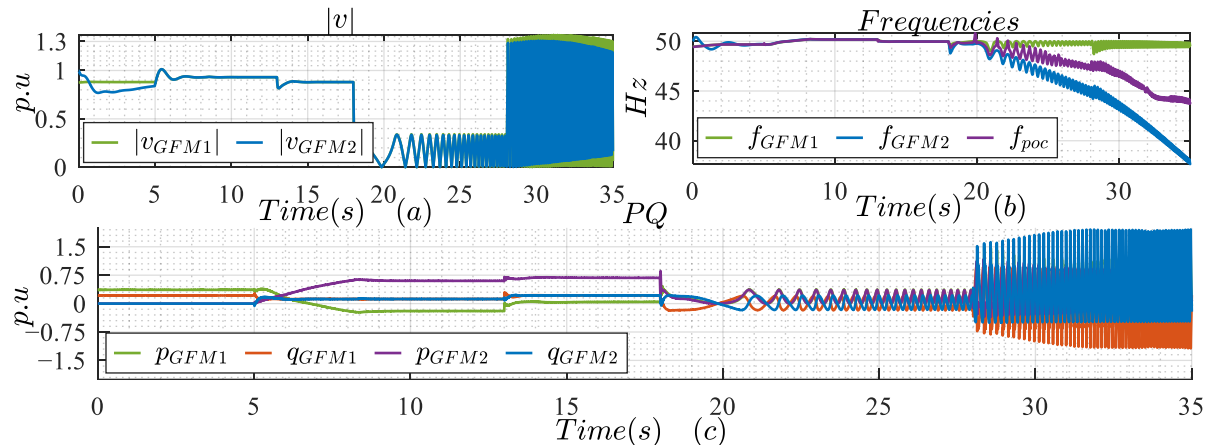


Figure 5.17: Response of GFM connection with another GFM acting as grid with SCR = 1 at POC; (a) magnitude of positive sequence voltage phasors for GFM1 and GFM2, (b) control frequencies of GFM1, GFM2, and measured frequency at POC, (c) measured active and reactive power injections at POC for GFM1 and GFM2

In this analysis, the GFM1 operates as a master/reference source. Its rated power is 100 kVA and the nominal line-line RMS voltage is 400 V. The line impedance (Z_{UG1}) is ignored in the first analysis. An active load of 50 kW and inductive load of 30 kVAR is connected at node A. Another GFM with the same ratings (GFM2) is synchronized to GFM1 and operates in grid connected mode with reference real power of 1 p.u. After the synchronization of the second source, the active and reactive loads are

doubled to analyze the small signal stability of the system. Moreover, a balanced fault is also introduced at node A for large signal stability analysis.

The synchronization process is started at the start of this simulation for GFM2, and it gets synchronized with the GFM1 in 5 seconds. From 0 to 5 seconds, the GFM1 is the only source to feed the load. This is the reason that in this duration, the frequency for the GFM1 is less than the nominal frequency (50 Hz) as the reference real power in islanded operation is set to zero. Both the active and reactive loads are fed by the GFM1, and it is also clear from subplot (c) of the above figure which presents the measured powers for both the converters. After the synchronization process is completed (at 5 seconds), the real power of the GFM2 starts to ramp up to its reference value. It is important to mention here that the measured real power of GFM2 is less than its reference value. It is due to the higher resultant frequency than the nominal frequency which has a negative droop effect on the injected real power. The measured real power for GFM1 is negative because of higher injected real power from GFM2 than the load connected at node A. The reactive load is equally shared by GFM1 and GFM2 in this duration.

To analyze the small signal stability of the system, the load is doubled at 13 seconds, the system frequency experiences a slight dip due to which the real power injection from the GFM2 is increased a bit. The real power injection from GFM1 is also increased as the total load connected at node 'A' is higher than the real power injection from GFM2. Thus, the rest of the power is delivered by GFM1. The reactive load is again equally shared by both the GFMs.

To analyze the large signal stability, a balanced three-phase fault is introduced at POC at 18 seconds with a duration of 10 seconds. The subplot (b) shows the frequency of the p-f loop for both the converters. It is the frequency of the internal voltage for the respective GFM but the resultant frequency at POC can be defined as the rate of change of the voltage angle which will be different than these frequencies if they are not the same. It helps to analyze the loss of synchronization between the GFMs. It confirms a loss of synchronization which causes oscillations in the real and reactive power injections and leads to voltage oscillations. The post fault response is also unstable. Thus, like a SG, the multiple GFMs system stability can be achieved if the fault is cleared before a critical clearance time. The calculation for this CCT is cumbersome for multiple GFMs system due to the complex control schemes involved. Due to resistive fault and absence of line impedances, the reactive power of GFM1 is opposite to the reactive power of GFM2 during the fault.

To improve the large signal stability, the low voltage ride through (LVRT) characteristic curve is defined to ensure the converter connection for 200 ms if the voltage drops to zero and the connection time is indefinite if the terminal voltage raised to 0.5 p.u. The curve is shown in Figure 5.18. It is important to mention here that the newly defined LVRT curve fulfills the standard LVRT requirement mentioned in [80].

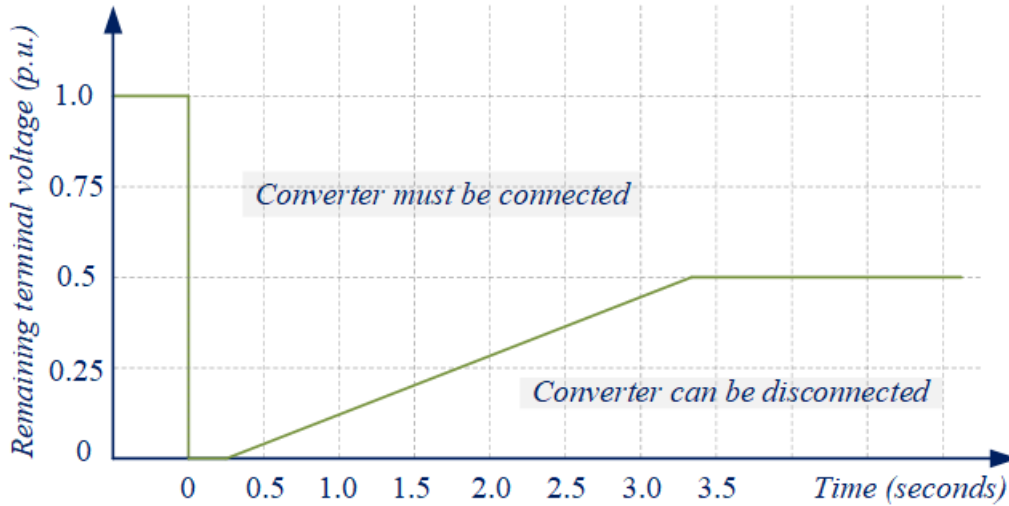


Figure 5.18: Designed LVRT curve for the GFM and GFL

The above analysis is repeated with the incorporation of the LVRT curve, the results are given in Figure 5.19.

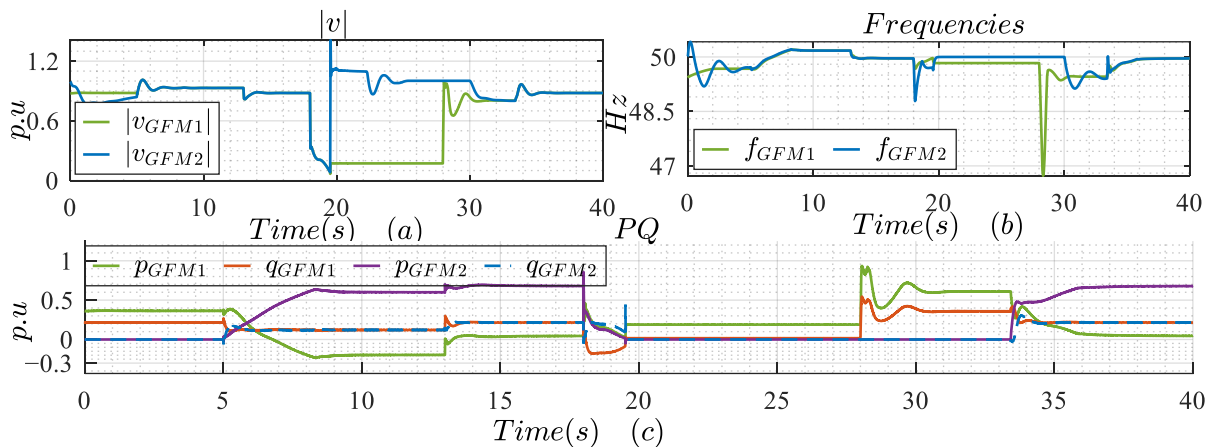


Figure 5.19: Response of GFM connection with another GFM acting as grid with $SCR = 1$ at POC with incorporation of the LVRT curve; (a) magnitude of positive sequence voltage phasors for GFM1 and GFM2, (b) control frequencies of GFM1, and GFM2, (c) measured active and reactive power injections at POC for GFM1 and GFM2

The above figure shows that the large signal stability is largely improved by incorporating the LVRT curve. The voltage drops to 0.1 p.u. in case of fault. After the applying the fault, the GFM2 is islanded in 1.5 seconds and both the converters are separated. Since the fault is on the GFM1 side, the voltage and frequency of the GFM2 are restored as the CB is opened. After the fault clearance, the synchronization process is initiated in two seconds. The above figure shows that the local network consisting of two GFMs is stable against small and large disturbances.

The next important factor is the calculation of minimum SCR for a GFM connection in a fully converter-based MG. The smaller SCR values cause larger synchronization time and more dip in the voltage during the synchronization process. However, the small and large signal stabilities are confirmed even

for very low SCRs. Keeping in mind the synchronization process, the SCR for a GFM connection with another GFM should be at least to 0.5.

5.2.5 Simultaneous Connection of GFL and GFM with the Grid

In this section, a network is studied which is comprised of a very weak grid, a GFM and a GFL. The SCR at POC for GFL is maintained to 2 with the help of both the grid and the GFM. The grid and GFM equally contribute to raise the SCR to 2 at POC for GFL. The layout of the scheme is given in the following figure.

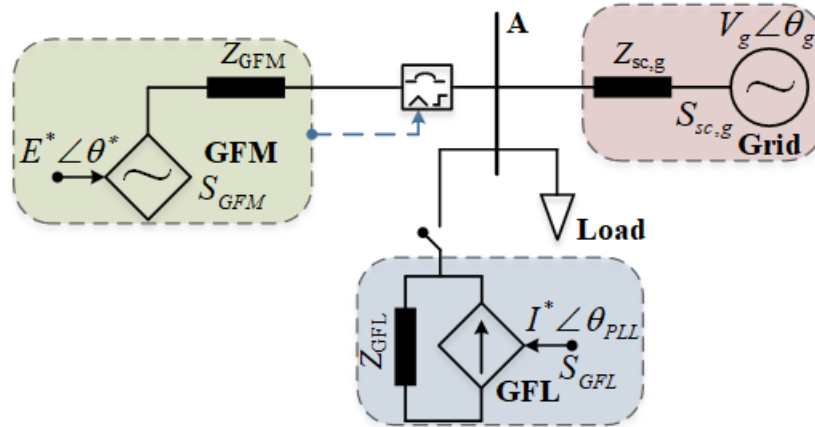


Figure 5.20: Direct coupling of GFM, GFL and the weak grid

The short circuit power of the grid is selected to be 150 kVA, a GFM of 100 kVA is synchronized with the grid and then a GFL of 125 kVA is enabled at node A. For simplicity, the line impedances are ignored. The GFL also incorporates an LVRT curve which is shown in Figure 5.18. The performance of the above discussed setup is presented in Figure 5.21.

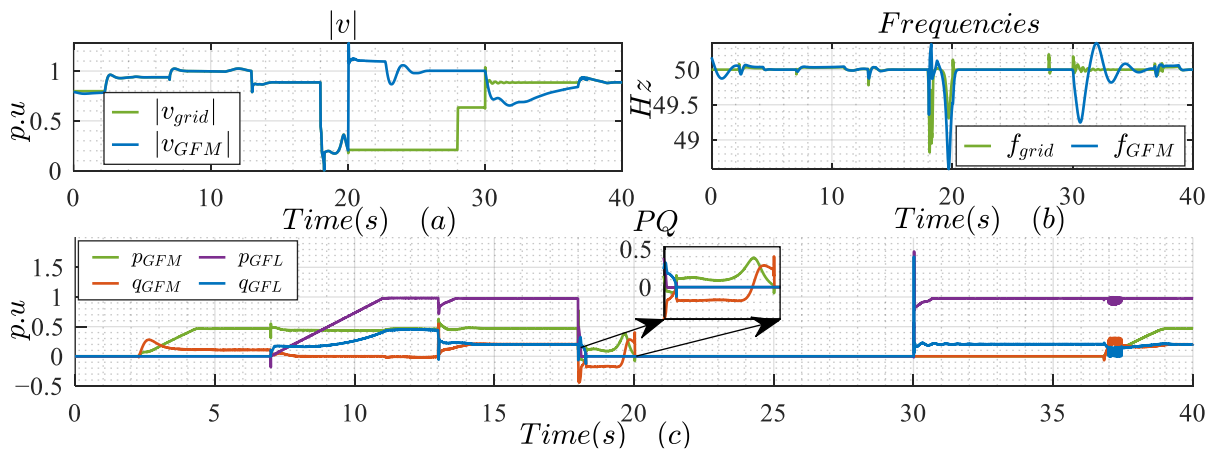


Figure 5.21: Combined response of GFM and GFL connection in a grid connected operation; (a) magnitude of positive sequence voltage phasors for grid and GFM, (b) frequencies of grid and GFM, (c) measured active and reactive power injections at node 'A' by GFM and GFL

The synchronization process for GFM is initiated at the start of the simulation and it is completed in 2 seconds. The reference real power for GFM and GFL is 0.5 and 1.0 p.u. respectively. The reference reactive powers for GFM and GFL are zero. However, the voltage control mode of GFL is activated.

The GFL is enabled at 7 seconds. To test the small signal stability of this system, a load of 50 kW and 30 kVAR is connected at node 'A' at 13 seconds. Finally, to test the large signal stability, a balanced three-phase fault is introduced at node 'A' at 18 seconds and the duration of the fault is set to be 10 seconds. After this, the post fault behavior of both the converters is also observed.

The subplot (a) of the above figure shows the magnitude of the positive sequence voltage phasor at node 'A' and at the terminal of the GFM (which can be different in case of islanded operations). The subplot (b) shows the grid's frequency and the frequency output of the p-f control of the GFM. The subplot (c) presents the real and reactive power injections by the GFM and GFL. From 0 to around 2 seconds, there is no power injection from either converter as the GFM is not yet synchronized and the GFL is not enabled. Around two seconds, the GFM is synchronized which can be confirmed from subplots (a) and (b). Due to the connection of the GFM, the terminal voltage at node 'A' is raised as the real and reactive powers are injected to the grid by the GFM. The reference real power is set to 0.5 p.u. and the subplot (c) shows that the measured value is ramped up and achieves a steady value close to the reference value. The reactive power is also injected to support the voltage with the proportionality constant of 2.

At 7 seconds, the GFL is enabled, and its reference real power is set to 1 p.u. and the reactive power is voltage controlled. The subplot (c) shows that the measured real power injection of GFL is ramped up to its reference value. The reactive power injection is also increased to support the terminal voltage. As both the GFM and GFL are connected at the same node, the voltage control for the GFL is faster than the control of GFM due to higher proportional and integral gains, thus, the reactive power injection from the GFL is more than the one from the GFM. From subplot (a) it is clear that in this duration, the terminal voltage is raised close to 1 p.u.

At 13 seconds, the load is connected to node 'A' which has a little impact on the real power injection of the GFM as the system's frequency is not changed. On the other hand, the reactive power injection of both the converters has changed noticeably. Due to such huge load connection to a very weak system, the terminal voltage is dropped to 0.88 p.u. The lower k-factor for GFL results in lower voltage support. As the voltage is less than the threshold voltage for the LVRT detection (0.9 p.u.), thus, the LVRT injection mode is activated which, in return, deactivated the normal voltage control mode of the GFL. Thus, the voltage support in this case is directly proportional to the terminal voltage drop and the proportionality constant which is selected as 2 in this case. Therefore, after load connection, the reactive power injection from the GFL is decreased and the reactive power injection from GFM is increased. The overall small signal stability of this setup is ensured as each converter achieves a new steady state power level after changing the system's load.

For the large signal stability investigation, a balanced fault is introduced at node 'A' at 18 seconds. During the fault duration, the GFL is disconnected in 300 ms and due to its disconnection, the terminal

voltage is recovered a bit, but it is less than 0.5 p.u. due to which the GFM is also disconnected from the grid in two seconds after the fault. In post fault phase, the GFL is smoothly reconnected to the grid in two seconds after the fault clearance and the synchronization process for the GFM is also initiated at the same time which is completed in 7 seconds. The subplot (c) shows a smooth reconnection of both the converters with the grid after the fault clearance.

5.3 Take Aways from the Multi-converter Systems' Analysis

The important conclusions from the above analysis are given below.

- The classical understanding of SCP is not applicable in a converter-based network. The share of converter's power rating in the calculation of SCP is highly dependent on the actual operating conditions.
- For small disturbances, the impact of GSL can be ignored due to its slower response whereas the GFM behaves as a high SCP source and its SCP can be as high as 3–6 times of its rated power. The actual SCP depends on the primary application of the GFM.
- For large disturbances, the rated power of GFM can be considered as its SCP and has a positive impact on the SCP calculations of the network whereas the GFL has no noticeable effect on the SCP.
- The GFL offers a stable response against small and large disturbances if the SCR is maintained at least two at the POC and its disconnection is allowed according to the proposed LVRT curve.
- The voltage control function of the GFL should be activated if there is no other source connected at that node. It helps to keep the voltage close to its rated value.
- In 400 V system, the faults are normally resistive, and the X/R ratio of the lines is also low, so, a lower reactive power injection is required. Thus, the proportionality constant for reactive current injection in case of faults should have lower value.
- The GFM offers stable response against small and large disturbances both in islanded and grid-connected modes. However, if a GFM is connected with other GFMs, the large signal stability is improved if the LVRT curve is used to ensure the minimum connection time.
- The SCR required for a GFM connection is very small. It can even be around 0.5. The lower values of SCR have less impact on the stability and more impact on the synchronization process and the voltage dip during the synchronization process.

Based on the above points, the operational limits for different converters in a multi-converter system are summarized below.

- For GFL connection, the SCR should be greater than or equal to 2.
- For GFM connection, the SCR at POC should be at least equal to 0.5.

6. ANALYSIS OF A MICRO GRID

In the previous chapter, the calculations for the SCR in a converter-based network are discussed along with the operational limits for the GFL and GFM in a multi-converter system. In most of the analysis, the direct coupling of the converters was discussed. In this chapter, a test network will be selected for a micro-grid and then different recommendations for the design of MG will be discussed. The minimum SCR at each node of the test network will be defined in a converter-based system. The load management system will be designed for the MG. The performance of the converters will also be discussed against small and large disturbances at the system's level. The splitting of the network in faulty situations will be discussed to achieve a stabilized response.

6.1 Selection of Test Network

Three different benchmark networks are discussed in section 2.4. The summary of these networks is given below.

Table 6.1: Summary of different benchmark networks

<i>Network</i>	<i>Total Nodes</i>	<i>Total Effective Length (km)</i>	<i>Total Load (MVA)</i>	<i>Load Type</i>	<i>Voltage (kV)</i>
IEEE-34 [104]	34	≈ 94	≈ 2	Unbalanced	24.9/4.16
European LV [102]	43	≈ 1.34	≈ 0.75	Balanced	0.4
Generic European Network [103]	92	≈ 5.7	≈ 0.52	Balanced	0.4

Since the purpose of this study is to investigate the performance of MG in small and large disturbances, benchmark networks having detailed line parameters (overhead/under-ground) are considered. However, the networks having on-load tap changing and the single-phase feeders are not considered here. Based on these limitations, the IEEE 34 bus system is not suitable for this study.

Generic European network is developed in Simulink, but the simulation is very slow. Thus, to have a reasonable simulation time, the load of some of the distributors can be lumped up. The simulation frequency is selected 16 kHz and due to these changes, the simulation speed is enhanced by roughly 10 times but, still, the simulation is quite slow due to large number of loads. Thus, this network is not considered further for the analysis.

On the other hand, the European LV distribution network has reasonable size, and its simulation is comparatively faster. Moreover, different types of feeders (residential, commercial, and industrial) and different types of line impedances (overhead lines and under-ground cables) involved in European LV distribution network help to design different MGs for different feeders. Hence the European distribution network is selected for the study of MG's stability. The details of the line impedances, transformers, loads and the medium voltage (MV) equivalent network are given in appendix B.

The detailed layout of the European LV distribution network is given in Figure 6.1.

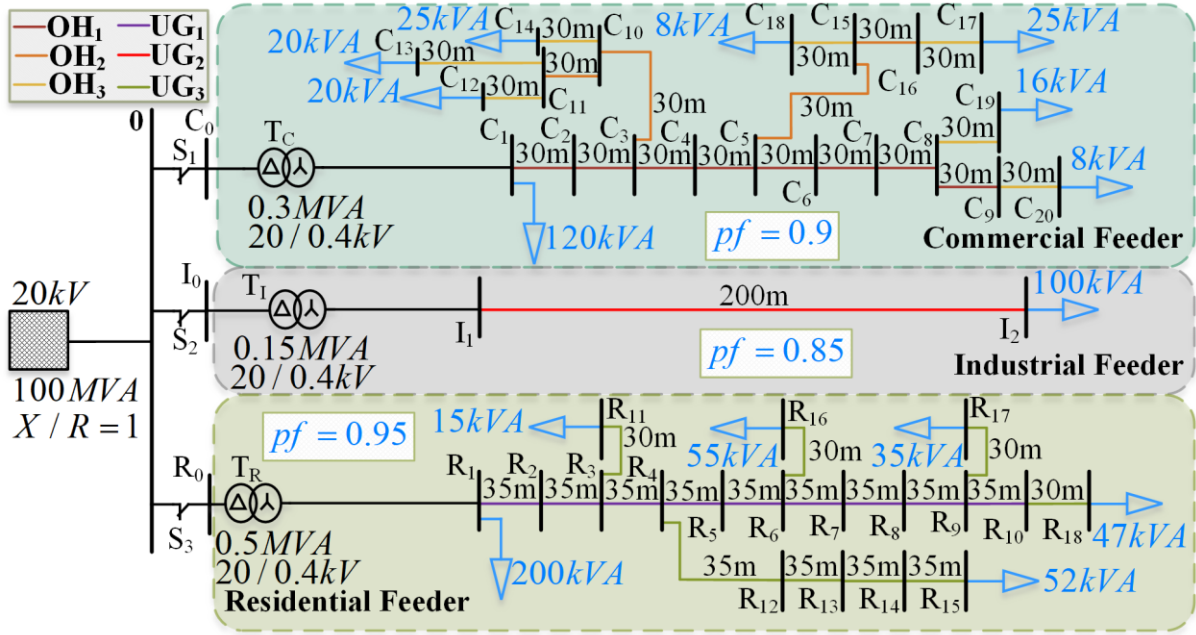


Figure 6.1: Detailed layout of conventional European LV distribution network

The ‘OH’ and ‘UG’ stands for overhead lines and underground cables respectively and their subscripts represent different models. Each feeder’s service area starts from the secondary side of the distribution transformer. Based on the defined loads, the commercial feeder’s transformer is loaded more than 80 % without considering the line losses. Similarly, T_I is loaded more than 67 % and T_R is loaded around 80 %.

For the sake of short circuit power calculations at each node, the MV grid’s impedances are referred to the voltage of the secondary side of the respective transformers. Considering the commercial feeder, the sum of short circuit impedance of the grid and impedance of the transformer T_C can be calculated by the following equation.

$$\begin{aligned}
 |Z_{sc}| &= \frac{400^2}{100 \times 10^6} = 0.016 \Omega \\
 \therefore \frac{X}{R} &= 1 \\
 Z_{sc} &= (1.1 + j1.1) m\Omega; \therefore Z_{T_C} = (5.3 + j21.3) m\Omega \\
 \Rightarrow Z_{sc,C1} &= (6.4 + j22.4) m\Omega \\
 \Rightarrow SCP_{C1} &= \frac{400^2}{|Z_{sc,C1}|} \approx 6.87 MVA \\
 \left(\frac{X}{R} \right)_{C1} &\approx 3.5
 \end{aligned} \tag{6.1}$$

By following the same procedure, the SCP at each node is given in Table 6.2.

Table 6.2: SCP at each node for European LV distribution network without any converter

Node	Z_{sc} (m Ω)	SCP (MVA)	(X/R)	Node	Z_{sc} (m Ω)	SCP (MVA)	(X/R)
------	------------------------	-----------	-------	------	------------------------	-----------	-------

<i>Residential Feeder</i>				<i>Commercial Feeder</i>			
R ₁	4.3+j13.9	10.97	3.22	C ₁	6.4+j22.4	6.86	3.49
R ₂	14.3+j20.2	6.47	1.42	C ₂	25.4+j39.2	3.43	1.55
R ₃	24.2+j26.5	4.46	1.10	C ₃	44.3+j56.1	2.24	1.27
R ₄	34.2+j32.7	3.38	0.96	C ₄	63.3+j72.9	1.66	1.15
R ₅	44.1+j39	2.72	0.88	C ₅	82.2+j89.7	1.32	1.10
R ₆	54.1+j45.3	2.27	0.84	C ₆	101.1+j106.5	1.09	1.05
R ₇	64+j51.5	1.95	0.81	C ₇	120.1+j123.3	0.93	1.03
R ₈	74+j57.8	1.71	0.78	C ₈	139+j140.1	0.81	1.01
R ₉	83.9+j64.1	1.52	0.76	C ₉	158+j156.9	0.72	0.99
R ₁₀	93.9+j70.3	1.37	0.75	C ₁₀	88.5+j77.6	1.36	0.88
R ₁₁	58.6+j40.4	2.25	0.69	C ₁₁	132.6+j99.1	0.97	0.75
R ₁₂	74.3+j49	1.8	0.66	C ₁₂	197.1+j122.2	0.69	0.62
R ₁₃	114.4+j65.2	1.22	0.57	C ₁₃	197.1+j122.2	0.69	0.62
R ₁₄	154.5+j81.5	0.92	0.53	C ₁₄	152.9+j100.7	0.87	0.66
R ₁₅	188.9+j95.4	0.76	0.51	C ₁₅	126.4+j111.2	0.95	0.88
R ₁₆	88.5+j59.2	1.5	0.67	C ₁₆	170.5+j132.7	0.74	0.78
R ₁₇	118.3+j78	1.13	0.66	C ₁₇	235+j155.8	0.57	0.66
R ₁₈	128.3+j84.2	1.04	0.66	C ₁₈	190.8+j134.3	0.69	0.71
<i>Industrial Feeder</i>				C ₁₉	203.5+j163.2	0.61	0.80
I ₁	11.8+j43.8	3.52	3.71	C ₂₀	222.4+j180	0.56	0.81
I ₂	102.1+j86.9	1.19	0.85				

The above table shows that the X/R ratio decreases as the length of the feeder is increased. Thus, the distant nodes have lower X/R values. The lower X/R values suggest keeping the lower proportionality constant for reactive current injection.

The SCP at each node helps to decide the maximum rating of the converter that can be connected to a particular node without compromising the stability of the system.

6.2 Selection of Size, Location, and Type of the Converters for Each Feeder

To decide the number of converters, their type, size, and location for each feeder, the first step is to decide the total load connected to the network. As each feeder is being treated as a separate MG, the total load of each feeder is considered to decide the total converter-based renewable power generation with option of autonomous islanded operation.

The next important task is to decide the ratio of the total installed power capacity of GFM to the total installed power capacity of GFL converters. It is important due to the fact that the GFMs contribute to the calculation of the SCP whereas GFL can't and secondly, the GFM can be connected with very low SCRs but for GFL connection, the SCR should be maintained to at least two. Additionally, the GFLs are mostly considered without having any energy storage element and connected to intermittent RES. Thus, in a fully converter-based MG, the total capacity of GFM should be greater than the total power capacity of GFLs and the exact limit also depends on the line impedances involved in the network. The

minimum value of this ratio is unity if all the line impedances are ignored. In reality, this should be greater than unity.

As far as the location of the converters is concerned. One limitation is imposed by the SCP at the particular node as the SCR for GFL connection should be greater than 2 and it should be at least 0.5 for GFM connection. The other important factor is that it should be close to the load. However, the type of primary energy source may be a limitation as well while deciding the location for the converter.

Some of the conditions in deciding the number of converters, their type, size, and location are expressed mathematically in the following equation.

$$\begin{aligned} \sum_{i=1}^n P_{GFM,i} + \sum_{j=1}^m P_{GFL,j} &\geq P_{load} \\ \frac{\sum_{i=1}^n P_{GFM,i}}{\sum_{j=1}^m P_{GFL,j}} &\geq 1 \\ \frac{SCP_x}{P_{GFL,x}} &\geq 2; \frac{SCP_x}{P_{GFM,x}} \geq 0.5 \end{aligned} \quad (6.2)$$

In the above expressions, the rating of the converter is expressed with ‘P’ and considered that the rating of the converter is the same as the real power capacity of the primary energy source. Thus, the converter can operate at unity power factor.

The selection of converters’ number, rating, type, and location for each feeder are discussed below.

6.2.1 Selection of Converters for Residential Feeder

The total power of the residential feeder is about 404 kVA and almost half of it is connected at R₁. Thus, the total converter-based power generation capacity for residential feeder is decided to be 500 kVA. The next important task is to decide the ratio of total capacity of GFM to GFL so that stability can be ensured. As the GFL does not contribute to the SCP and both the GFM and GFL are not connected to the same nodes so this ratio should be greater than 1 but the exact value is decided once the location of the GFM converters is decided. For reasonable simulation time, four converters for each feeder are considered. The power rating and location for each converter is decided to keep the system stable.

As major load is connected at R₁, thus, one GFM with 200 kVA rating is connected at this node. The potential nodes for the next GFM connection are R₁₅, R₁₆ and R₁₈ as heavy loads are connected at these nodes. To decide the location for the next GFM, the minimum SCP at the node should be at least half of the power rating of the newly connected GFM. Thus, the SCPs (considering large disturbances) at these nodes is calculated with the consideration of a 200 kVA GFM connected at R₁. The minimum SCP (for large disturbances) at nodes R₁₅, R₁₆ and R₁₈ is 160, 178 and 170 kVA respectively. Thus, a

100 kVA GFM is connected at R₁₈, the updated SCPs (for small and large disturbances) at different nodes are calculated. For small disturbance calculations, the X/R ratio is selected as unity (Figure 5.4) and the SCP for the GFM is considered to be 2.8 times the rated power of the GFM (Figure 5.2 Zoomed). The calculated SCPs for the small and large disturbances and the X/R ratio in case of small disturbances are given in Table 6.3. Subscripts '1' and '2' are used for small and large disturbances respectively and the rating of the GFL is decided based on the minimum SCP as stable operation in faulty conditions is also demanded. The rating of GFL is selected to ensure the minimum SCR of 2 at its point of connection.

Table 6.3: Short circuit power at each node of residential feeder for fully converter-based MG along with the power ratings of the GFL to ensure SCR = 2

<i>Node</i>	<i>SCP₁</i> (kVA)	<i>(X/R)₁</i>	<i>SCP₂</i> (kVA)	<i>S_{GFL@SCR=2}</i> (kVA)	<i>Node</i>	<i>SCP₁</i> (kVA)	<i>(X/R)₁</i>	<i>SCP₂</i> (kVA)	<i>S_{GFL@SCR=2}</i> (kVA)
R ₁	785	0.97	291	145.5	R ₂	767	0.96	289	144.5
R ₃	751	0.95	287	143.5	R ₄	737	0.94	285	142.5
R ₅	723	0.93	283	141.5	R ₆	712	0.93	281	140.5
R ₇	701	0.92	279	139.5	R ₈	691	0.92	277	138.5
R ₉	682	0.91	276	138.0	R ₁₀	675	0.91	274	137.0
R ₁₁	645	0.85	268	134.5	R ₁₂	620	0.83	264	132.0
R ₁₃	534	0.76	247	123.5	R ₁₄	469	0.71	231	115.5
R ₁₅	424	0.68	219	109.5	R ₁₆	616	0.84	264	132.0
R ₁₇	594	0.83	259	129.5	R ₁₈	656	0.90	269	134.5

The above table shows very high SCPs for the small disturbances which allows to connect more GFLs in the network if the stable operation in faulty conditions is not required. It also shows stable response of the network against small changes in loads. However, if the stable operation of GFLs is required in faulty conditions, its rating should be decided based on the SCP calculations for the large disturbances. The above table shows that the SCP₂ (in case of large disturbances) at each node is well above 200 kVA which allows the connection of a 100 kVA GFL converter at any of these nodes. As more load is connected to R₁₅ and R₁₆, thus, 100 kVA GFL converters can be connected at R₁₅ and R₁₆. In this way, the total number of converters is limited to four out of which two are GFM and two are GFL. The maximum rating of a single converter is not more than 200 kVA. The limitations for different deciding factors are summarized in the following table.

Table 6.4: Factors and associated limitations in deciding the converters for MG

<i>Factors</i>	<i>Limitations</i>
No. of converters	Increases degree of complexity and slows down the simulation.
No. of GFM converters	The number of GFM converters have no such limitations. However, angle stability becomes critical with large number of GFMs.
No. of GFL converters	There is no such limit on the number of converters if the SCR of 2 is ensured and the total power capacity of GFLs is less than the power rating of the GFMs.
Power rating of individual GFM	Physical constraint due to the primary energy source, maintaining the SCR=> 0.5 at point of connection.

Power rating of individual GFL	Physical constraint due to the primary energy source, maintaining the SCR => 2 at point of connection.
Ratio of GFM to GFL	This ratio should be greater than 1 if line impedances are ignored. In LV network, it should be at least 1.5.

6.2.2 Selection of Converters for Commercial Feeder

By using the same procedure, the converters' selection for the commercial feeder is performed. The total load of this feeder is 242 kVA. Thus, the total installed power capacity of the converters is selected to be 300 kVA. To keep the ratio of total installed power capacity of GFM to GFL equal to 1.5, the total GFM power capacity is selected to be 180 kVA and the total power capacity of GFL is 120 kVA. The total number of converters are four. Among these converters, a 150 kVA GFM converter is connected at C_1 as this node has the largest load connected in the feeder. The potential nodes for the next GFM converter are C_{12} , C_{13} , C_{14} , C_{17} and C_{19} . With the assumption of 150 kVA GFM at node C_1 , the minimum SCP at these nodes is 124, 124, 129, 119 and 122 kVA respectively.

To have voltage support at distant nodes, C_{19} is selected for the connection of next GFM with rated power of 30 kVA. To decide the location and capacity of GFL, the minimum SCP at different nodes of the commercial feeder is calculated by considering 150 kVA and 30 kVA GFM converters connected at C_1 and C_{19} respectively. The SCP (considering large disturbances only) and power ratings of GFL for each node are given in Table 6.5. These power ratings of the GFL ensure the SCR of 2 at a particular node.

Table 6.5: Short circuit power at each node of commercial feeder for fully converter-based MG along with the power ratings of the GFL to ensure SCR = 2

<i>Node</i>	<i>SCP (kVA)</i>	<i>S_{GFL@SCR=2} (kVA)</i>	<i>Node</i>	<i>SCP (kVA)</i>	<i>S_{GFL@SCR=2} (kVA)</i>
C_1	178	89.0	C_2	175	87.5
C_3	172	86.0	C_4	169	84.5
C_5	166	83.0	C_6	163	81.5
C_7	160	80.0	C_8	158	79.0
C_9	155	77.5	C_{10}	163	81.5
C_{11}	155	77.5	C_{12}	145	72.5
C_{13}	145	72.5	C_{14}	152	76.0
C_{15}	158	79.0	C_{16}	150	75.0
C_{17}	141	70.5	C_{18}	148	74.0
C_{19}	148	74.0	C_{20}	149	74.5

As more load is connected to C_{12} , C_{13} and C_{14} which are close to each other, thus, a 75 kVA GFL is connected to C_{11} which helps to improve the overall voltage profile. Another distant load is at C_{17} so a GFL of 45 kVA is proposed for this node. These two GFLs offer a combined power rating of 120 kVA. These conditions are mathematically shown below.

$$\begin{aligned}
 P_{load} &= 242kVA \\
 \sum_{i=1}^2 P_{GFM,i} + \sum_{j=1}^2 P_{GFL,j} &= 300kVA > P_{load} \\
 \frac{\sum_{i=1}^2 P_{GFM,i}}{\sum_{j=1}^2 P_{GFL,j}} &= 1.5 \\
 \frac{SCP_{C11}}{P_{GFL,C11}} > 2; \frac{SCP_{C17}}{P_{GFL,C17}} > 2; \frac{SCP_{C19}}{P_{GFM,C19}} > 0.5
 \end{aligned} \tag{6.3}$$

The industrial feeder is not considered in this study as it has a lumped load and one GFM of 100 kVA capacity should be able to supply it. The layout of the updated European LV distribution is given below.

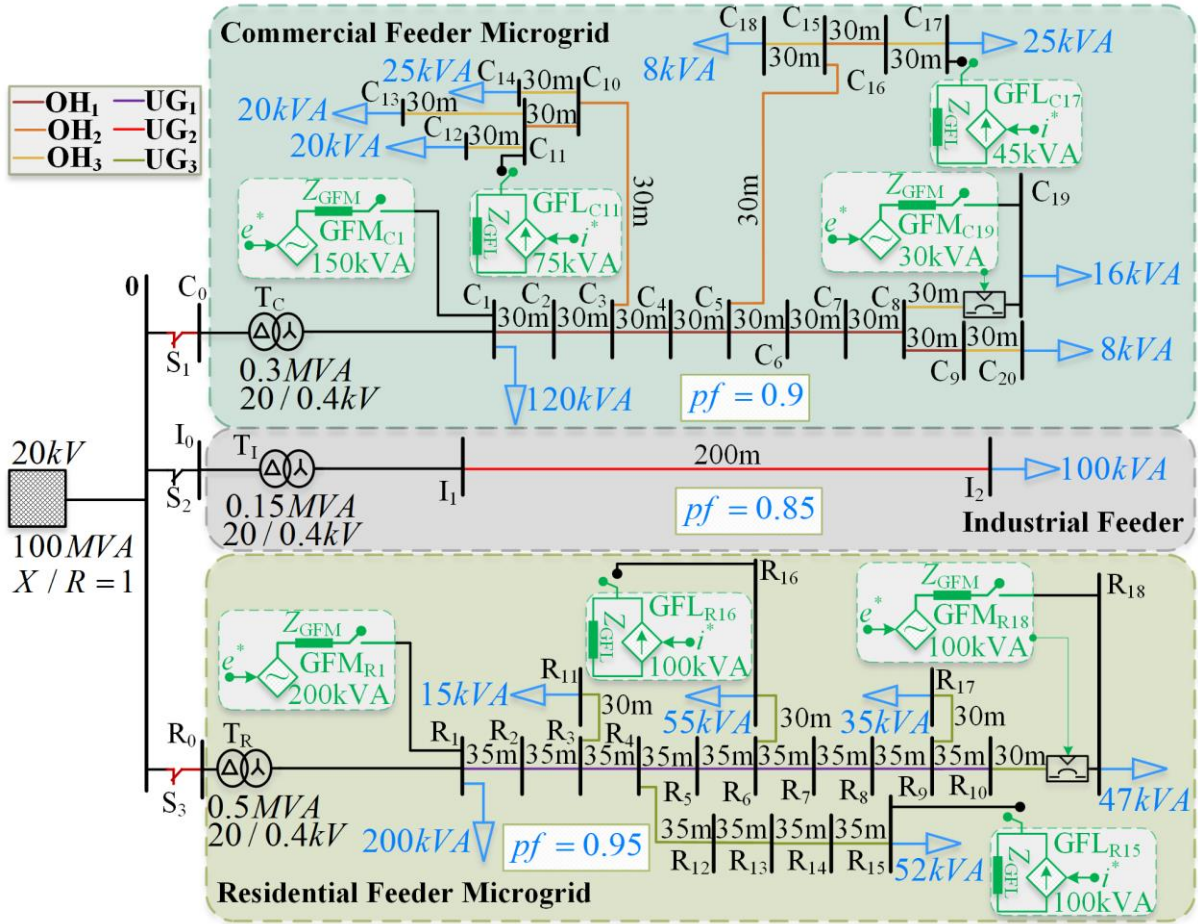


Figure 6.2: Layout of the updated European LV distribution network containing converters

6.3 Procedure for Black Start

The next important task is to define the procedure for the black start. As the GFM converter has the capability of black start, thus the lines are charged with the help of GFMs by disconnecting all the loads. Once the node voltages get stable, the GFLs can be connected, and then the loads are also connected to the network. It is important to mention here that the network splits up in case of faults so that some

loads can still be fed by the GFM if the fault is not located in their service area. With the arrangement shown in Figure 6.2, the load connected to C_{19} is fed by the connected GFM if the fault occurs at any of the rest of nodes. Similarly for residential MG, the loads connected to R_{18} is fed by the respective GFM if the fault occurs at any node other than R_{18} . On the fault clearance, if the GFM signal for resynchronization is turned on, it starts the resynchronization process after two seconds of the voltage restoration. Similarly, the GFL is also connected to the network after two seconds of the fault clearance. This time delay is introduced to stabilize the voltage before converters' connections. The sequence of load connection has an impact on the reactive power supply of the individual converters if the converters are operated in voltage control mode.

6.4 Initialization Process of the Residential MG

Initially, the GFM_{R1} is operated in the islanded mode to charge the lines and provides reference voltage and frequency for the rest of the converters. The synchronization process for the GFM_{R18} is initiated at 5 seconds which is soon synchronized with the GFM_{R1} . At 15 seconds, the GFL_{R15} is enabled, and it ramps up its injected real power to its reference real power. Similarly, at 25 seconds, the GFL_{R16} is also enabled and it reaches to its reference real power in almost 4 seconds. Both the GFLs work in voltage control mode. The reference real power for the GFLs and GFM_{R18} is set to 1 p.u. In general, it is assumed that the GFM converters are connected to an adequate energy source and storage system. However, limitations from the energy source or the storage systems are not considered in this analysis. The initialization performance of these sources without any load connection is given in Figure 6.3.

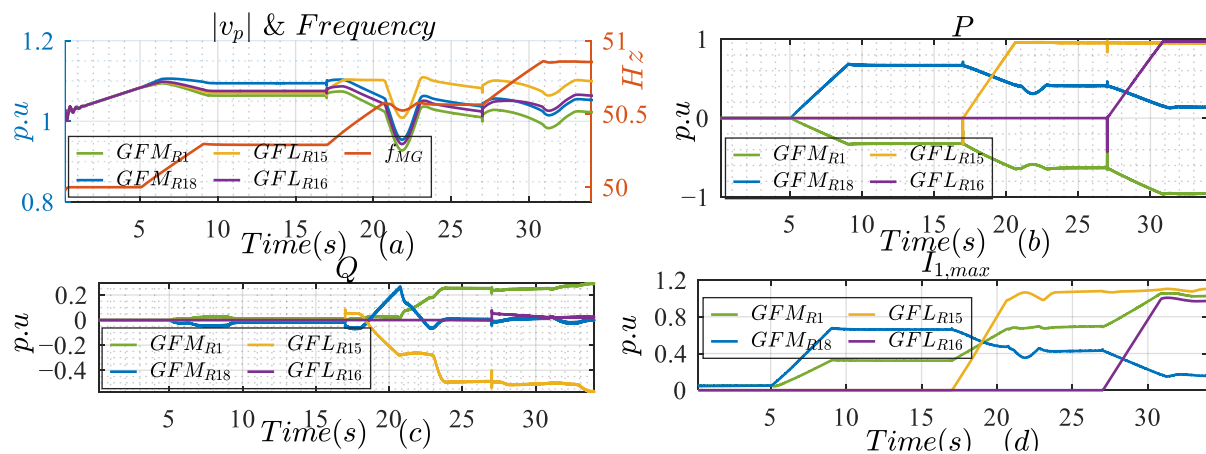


Figure 6.3: Initialization of the residential MG; (a) positive sequence voltage magnitude for different converters' nodes and system's frequency, (b) real power output of different converters, (c) reactive power output of different converters, (d) maximum phase current on the converter's side for each converter

It is important to mention here that the individual rated power of each converter is used as its base power to calculate its per unit values. The above figure shows that the system's frequency is 50 Hz from 0 to 5 seconds. It is the time period in which only the GFM_{R1} is connected to the system. Its reference power in islanded operation is set to zero and there is no load connected in this duration. Thus, the system's frequency is identical to the reference frequency and the real power output is zero in this duration.

Moreover, the line models used in the European LV distribution networks are the mutual inductance models having no shunt elements due to which no reactive power is involved in this duration. In subplot (d), there seems to be a very low current in GFM_{R1} in this duration. It is due to the fact that the maximum phase current shown in subplot (d) is on the converter's side of the LCL filter and there is a shunt resistor and capacitor involved between the converter's side and grid's side. Thus, the phase current on the grid's side is zero but there is some current on the converter's side to cancel the effect of the shunt elements of the filter. The initial ramp increase in the terminal voltage is due to the higher reference voltage which forced the internal reference voltage to ramp up.

At 5 seconds, the GFM_{R18} is synchronized with the GFM_{R1} . The reference real power of GFM_{R18} is 1 p.u. in grid connected mode and from subplot (b), it is clear that the real power of GFM_{R18} is ramped up and achieves a steady state value around 8 seconds. As there is no load connected to the system, GFM_{R1} absorbs the extra power to minimize the frequency change. From subplot (b), it is clear that the frequency ramps up as the real power output of the GFM_{R18} increases and achieves a new steady state value. Both the GFMs have a negative frequency droop due to which the GFM_{R18} is also operating below its reference real power. Due to the low X/R ratio of the lines in the residential feeder, the terminal voltage is also affected due to the real power transfer from GFM_{R18} to GFM_{R1} . The terminal voltage of GFM_{R18} goes above 1.1 p.u. which compels the GFM_{R18} controller to inject inductive reactive power. To keep the terminal voltage within limits, the GFM_{R18} absorbs the reactive power which should be delivered by the GFM_{R1} . From subplot (c), it is clear that the GFM_{R18} absorbs the reactive power while the GFM_{R1} delivers that power. In per unit, reactive power mismatch is clear, this is due to the different base powers of both the converters. The subplot (d) shows that the maximum phase current on the converter's side is within limits for both the converters and the GFM_{R18} is more loaded than the GFM_{R1} . This is due to the higher rating of the GFM_{R1} .

At 15 seconds, the GFL_{R15} is enabled. However, the controller waits for two seconds before feeding the real and reactive powers to the network. Thus, from the above figure, it is clear that the power injection from the GFL_{R15} starts around 17 seconds. As the real power of GFL_{R15} ramps up, its terminal voltage also starts to rise due to the low X/R ratio of the lines. Once reaching the upper voltage limit at R_{15} , the GFL_{R15} starts to absorb the reactive power to keep the terminal voltage within limits. After achieving the steady state level of the real power, the reactive power of the GFL_{R15} is stabilized, the reactive power of the GFM_{R18} comes back to its original level and the reactive power balance is achieved by the GFM_{R1} which increases its reactive power output. During this process, the terminal voltages experience a voltage dip and soon the steady state level is achieved. It is important to mention here that the GFLs have a PI controller for voltage control while the GFM uses a proportional controller for Q-V loop in grid connected mode and a PI controller in the islanded mode. Moreover, due to the activation of the GFL_{R15} , the system's frequency is increased as there is no load connected to the system and the GFMs frequency droop helps to oppose the change in frequency by reducing/absorbing the real power. It is

clear from subplot (d) which shows that the loading of the GFM_{R18} is decreased in this duration because its real power output is limited due to increase in frequency while the loading of the GFM_{R1} is increased. It is due to the fact that the GFM_{R1} is already receiving real power and due to the connection of a new power source, it needs to absorb more real power which increases the line current of the GFM_{R1} .

Similarly, the GFL_{R16} starts feeding the MG around 27 seconds. As its real power output increases, the terminal voltage is also increased at all the nodes and the terminal voltage at R_{15} soon reaches its upper limit which forces the GFL_{R15} to absorb more reactive power to keep the voltage within limit. Due to this, the terminal voltage of the other nodes is also decreased. The terminal voltage is also affected by the real power flow and as the GFL_{R16} is connected, the system's frequency jumped up to 50.86 Hz which forces the GFL_{R18} to further decrease its real power output which in turn also decrease the voltage drop between R_6 and R_{18} nodes. On the other hand, the extra real power coming from R_{16} increases the voltage drop from R_6 to R_1 . This voltage drop is compensated by injecting more reactive power from the GFM_{R1} . The loading of all the converters is within allowed limits even if all the converters are operated at their maximum reference real powers. The steady state voltage of different nodes is given in Figure 6.4.

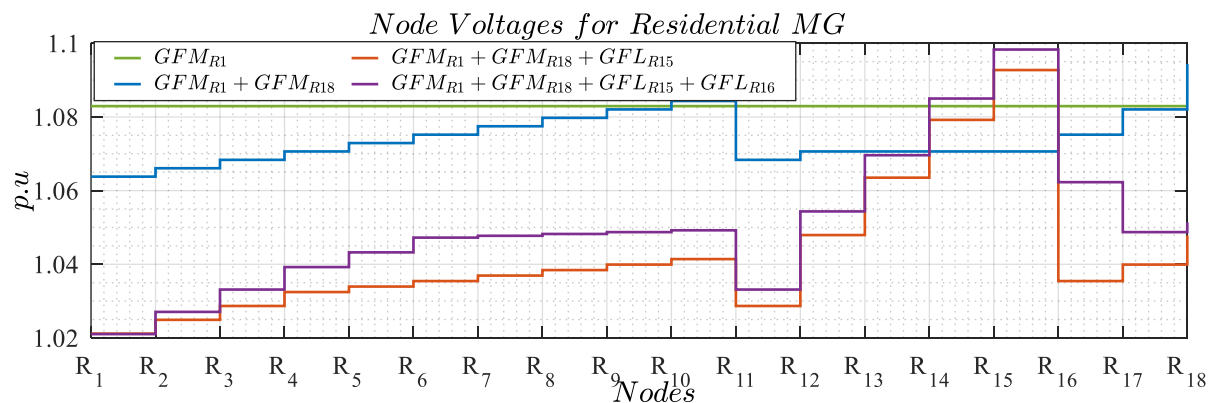


Figure 6.4: Steady state terminal voltage of different residential node during the initialization process

The above figure shows that the voltage profile of the residential feeder is fairly uniform during the initialization process. Due to the lower X/R ratio of the line, the real power flow largely impacts the voltage profile. The direction of power flow is also important to decide the terminal voltage of different nodes. The reference voltage for the residential MG is set to 1.05 p.u. With the increase in the total real power generation, the terminal voltage of R_1 decreases. It is due to the fact that most of the real power is balanced by the GFM connected at R_1 and the flow of real power is towards R_1 . For node R_{18} , the terminal voltage is raised when the GFM_{R18} is synchronized, and it starts to transfer real power to GFM_{R1} . It is due to the lower X/R ratio and flow of real power is from R_{18} to R_1 . As the GFLs are connected in the system, the real power flow from GFM_{R18} decreases due to the increase in the system's frequency which in turn decreases the terminal voltage at R_{18} . Similarly, the voltage profile for other nodes can also be explained.

The mean value and standard deviation help to define the range of the voltage in different phases. As, it is clear from Figure 6.4 that the terminal voltage is changed during the initialization process due to the connection of different power sources at different nodes. Thus, the mean value and the standard deviation helps to estimate the change in terminal voltage due to the connection of different power sources. The mathematical expressions for the mean value and standard deviations are given in equation (6.4).

$$V_{mean} = \frac{1}{N} \sum_{i=1}^N V_i$$

$$SD = \sqrt{\frac{1}{N} \sum_{i=1}^N (V_i - V_{mean})^2}$$
(6.4)

Where the ‘N’ is the number of events/samples and in this case, it is the number of stages for the initialization process i.e. 4. Moreover, subscript ‘mean’ represent the mean value of the respective parameter and SD stands for standard deviation. Based on the above expressions, the mean terminal voltage and the error bars of the residential MG are presented in Figure 6.5 for the initialization process.

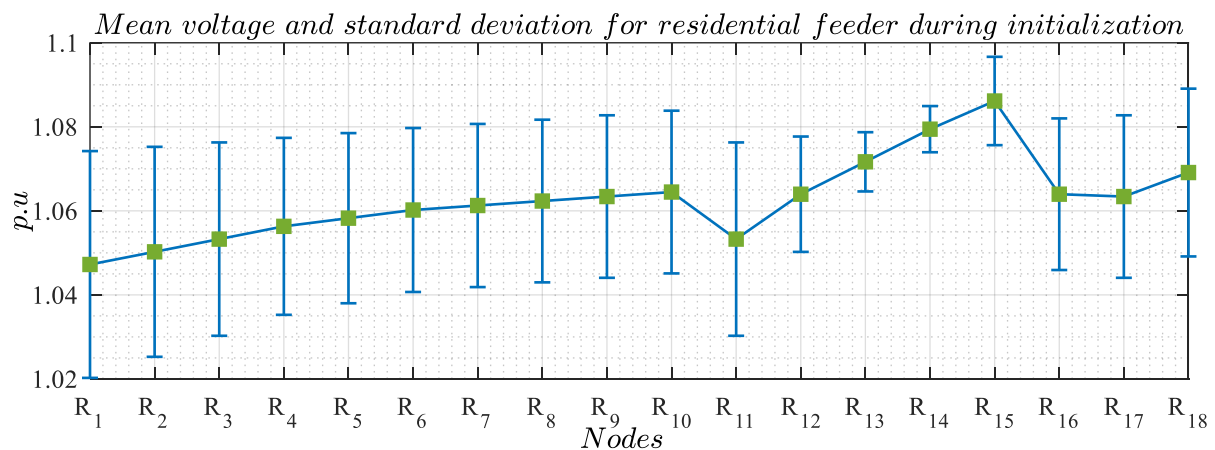


Figure 6.5: Mean voltage and standard deviation in terminal voltage for residential feeder during initialization process

The above figure shows that the standard deviation is quite low for all the nodes during the initialization process. In fact, the standard deviation is lower than the deadband of the voltage controllers and the terminal voltage of all the nodes is within defined limits during initialization process. Moreover, the mean value is different for different nodes, but it is highly dependent on the physical location of these nodes. As it is not a unidirectional power feeder and the location of the nodes is also not defined with its relative distance from node R₁, thus, it is hard to compare the terminal voltage of different nodes. However, the terminal voltages of the adjacent nodes are close to each other. As it is clear from the above figure, the minimum standard deviation is recorded for R₁₄ followed by R₁₃ and R₁₅ respectively.

The other connection schemes for initialization are also possible and can be explained in the same way. The main difference between different initialization schemes is the reactive power output of the individual converters because all the converters are operated in voltage control mode. Hence, if the

voltage is within limits due to initially connected converters, the other converters don't share the reactive load unless the terminal voltage deviates from its nominal range.

6.5 Load Management System for Residential MG

The switching sequence of the residential loads has an impact on the reactive power output of different converters and on the terminal voltage. In this section, two different switching sequence schemes are discussed. In this first scheme, the load at R_1 is connected first followed by the loads at R_{15} , R_{11} , R_{16} , R_{17} and R_{18} respectively. In the second scheme, the load connection sequence is reversed. The initialization phase is completed around two seconds i.e., the connected converters reach their reference power levels. At 5 seconds, the load at R_1 is connected to the network followed by the other loads according to the first scheme with a 15 second time delay. The response of the converters for the load connections with first scheme are given in Figure 6.6.

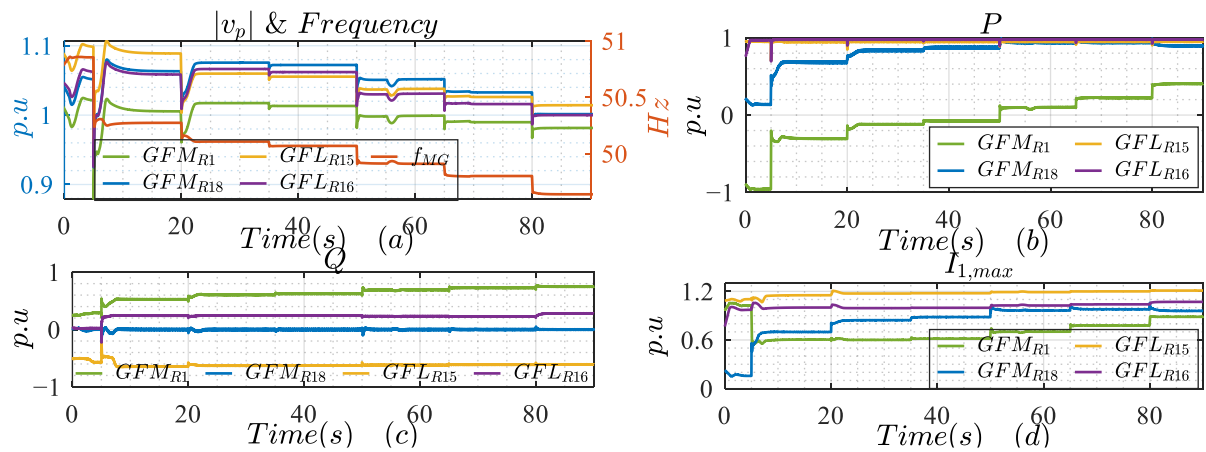


Figure 6.6: Response of the converters against load connections of the residential MG; (a) positive sequence voltage magnitude for different converters' nodes and system's frequency, (b) real power output of different converters, (c) reactive power output of different converters, (d) maximum phase current on the converter's side

As the load at R_1 is connected to the system, the terminal voltage experiences a dip, but the voltage remains within acceptable limits (subplot (a)). The terminal voltages get stable after experiencing a dip. The new steady output voltage at R_{18} is more than its previous value. It is due to the change in its real power output due to the frequency dip after connecting the load at R_1 . Similarly, the terminal voltage at R_1 settles at a relatively lower value due to the connection of relatively large load at R_1 . The terminal voltage at R_{15} also experiences a relatively smaller dip but the voltage at R_{16} regains its initial value. The change in voltage at R_{18} is mainly due to its real power change whereas the change in voltage for R_{15} is due to its reactive power consumption.

The load connected to the R_1 node is the largest load which drops the frequency of the system from 50.86 to 50.27 Hz. Due to the drop in frequency, the real power share from the GFMs is increased but the GFLs' real power is not changed, and it is due to the absence of the frequency support in the GFL's controller (subplot (b)). From subplot (c), it is clear that the reactive power output of GFM_{R1} is also

increased to feed the reactive load connected at R_1 . The reactive power of GFM_{R18} has not changed because its terminal voltage is still in nominal range. The GFL_{R15} consumes more reactive power to keep its terminal voltage below the maximum allowed limit and the GFL_{R16} supplies the reactive power to keep its voltage within defined limits. It is important to mention here that although the reactive power balance and the voltage control are a localized factors but due to the low X/R ratios, the terminal voltages are also highly affected by the real power flow. Moreover, due to closely located nodes, the effect of reactive power demand on R_1 is evident on the terminal voltage of the other nodes.

As far as the effect on the loading of the converters is concerned, all the converters experience an increase in the loading except the GFM_{R1} whose loading has decreased. It is due to the fact that the real power generation is more than the load and the GFM_{R1} is responsible to balance it by absorbing the additional real power. As the load is connected at R_1 , some real power is consumed by this load and the GFM_{R1} now needs to balance relatively less real power which decreases its loading. The slight change in the loading of the GFLs is due to a change in their reactive power upon the load connection at R_1 . Similarly, the loading of the GFM_{R18} is changed due to supplying more real power to the system as the frequency of the system has dropped.

The same trends are also evident for other load connections. The real power output of GFM_{R1} and GFM_{R18} increases with the increase in total load to the MG. However, after connecting the last load to the MG, the system's frequency drops and the real power of GFM_{R18} also drops a bit. It is due to the fact that the GFM_{R18} was already operating on its maximum real power capacity and with the connection of the load, its terminal voltage decreases due to which the controller limits its real power injection to ensure synchronization. The frequency and voltage are stable for these load connections. By following the same procedure, the other load connection schemes can also be tested. The steady state voltages at different nodes are plotted in Figure 6.7 for first load connection scheme.

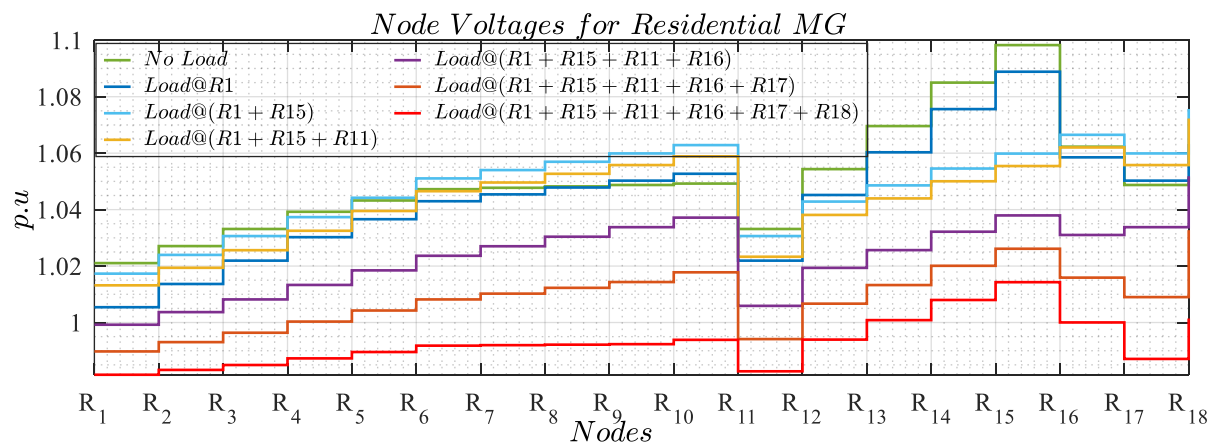


Figure 6.7: Steady state terminal voltage of different residential nodes against the first load connection scheme

The above figure shows that the terminal voltage of different nodes decreases as the loading on the system is increased. For most of the nodes, the maximum voltage is recorded in no load conditions and

the lowest terminal voltages are recorded when all the loads are connected to the MG. However, for some nodes, the different trends are also evident i.e. voltage at R_{10} is maximum if the loads at R_1 and R_{15} are connected to the system. It is due to the more active power flow from $GFM_{R_{18}}$ towards the GFM_{R_1} which is on the other side of the R_{10} node. However, after connecting more loads, its terminal voltage starts to decrease. The reactive power injection from the $GFM_{R_{18}}$ is still negligible and it is due to the fact that its terminal voltage remains within permissible range. The mean terminal voltages and their standard deviations for the residential MG are presented in Figure 6.8.

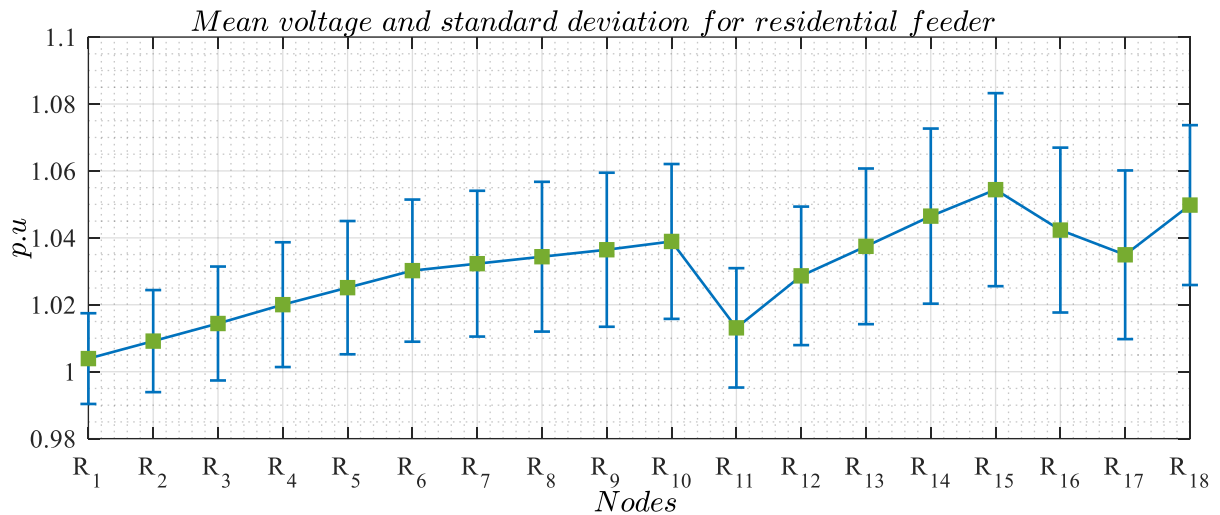


Figure 6.8: Mean voltage and standard deviation of terminal voltages for residential feeder against first load connection scheme

The above figure shows that the mean terminal voltage of all the nodes remains within permissible voltage limits during the connection of different loads to the MG. The change in terminal voltage during this process is also within limits. The minimum standard deviation is recorded for R_1 .

As stated before, the load connection scheme has an impact on the steady state voltage at different nodes. In the below figure, two load connection schemes are compared. In the first scheme, the load at R_1 is connected first followed by load at R_{15} , R_{11} , R_{16} , R_{17} and R_{18} respectively while in the second scheme the order to load connections is reversed i.e., the load at R_{18} is firstly connected to the MG followed by load at R_{17} , R_{16} , R_{11} , R_{15} and R_1 respectively.

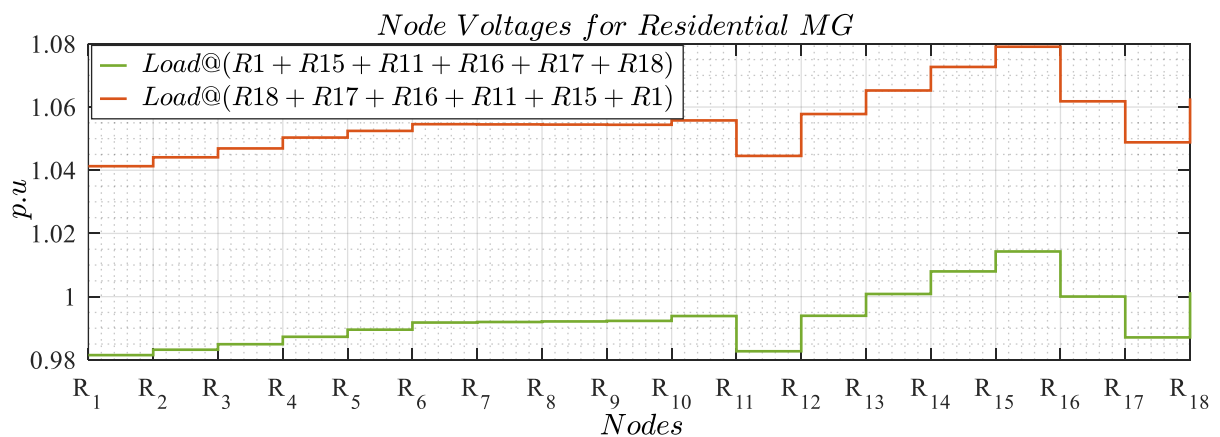


Figure 6.9: Steady state node voltages for different load connection schemes

The above figure clearly shows that the final steady state node voltages for both the load connection schemes are not the same. The reason for such a trend is the control of reactive power of different converters which is based on the terminal voltage and if the voltage is within permissible range of 2 %, no reactive power is supplied by the connected converters. Even though the terminal voltage is within permissible range for both the load connection schemes but it can highly affect the share of the reactive power of different converters. The other load connection schemes are also possible based on the priority loads. Hence, it can be helpful in the design phase of the MG to consider the location of the priority loads.

Even though the decentralized second level controller is used for the residential MG. However, a centralized load management system helps to connect/disconnect the loads based on their priority and operating conditions at connecting nodes. For this reason, a centralized load management system is designed. It requires frequency and terminal voltage to decide the connection/disconnection of the loads. For simplicity, only the critical and interruptible loads are considered here. The flow chart for the connection/dis-connection of the loads is given in Figure 6.10.

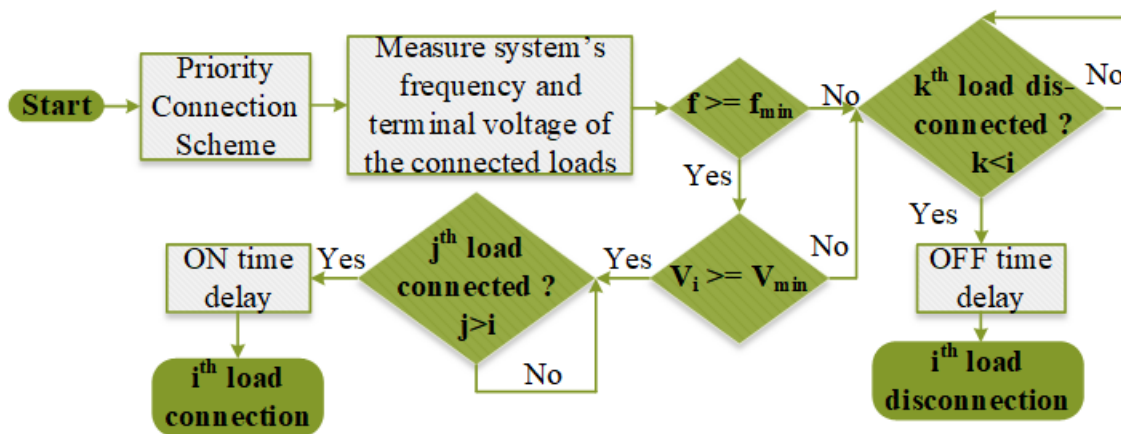


Figure 6.10: Flow chart for load management system

In the newly designed scheme, two different priority connection schemes are tested. One scheme prioritizes the load at R_1 followed by load at R_{11} , R_{15} , R_{16} , R_{17} and R_{18} respectively. In this scheme, the load at R_1 is connected to the network if the frequency of the system is greater than the defined minimum frequency and the terminal voltage is greater than its minimum threshold value. The next load is connected to the system with a defined time load delay if the operating conditions are met and the higher priority loads are already connected to the network. The same procedure is repeated for the other load connections as well.

If the system frequency drops below the minimum frequency or the terminal voltage drops below the minimum threshold, first the load with least priority is disconnected from the network. If the conditions persist, the second least priority load is disconnected after a defined time delay and so on. These time delays help to achieve the new operating point after the connection/dis-connection of the load. The same

procedure is used for the other priority connection schemes. In this above figure, the variable ‘i’ stands for the load which needs to be connected/disconnected, the ‘j’ represents the higher priority loads than i^{th} load and the ‘k’ represents the lower priority loads as compared to i^{th} load.

Moreover, to address the issue of successive switching of a load, this scheme also incorporates the reclosing function and if the load is connected and disconnected for multiple times (user defined) within certain time period then it is switched off permanently and can be switched on manually by resetting the recloser. It also introduces a certain time delay between the successive switching of a load to achieve the stable operating point before reconnecting the next load.

The performance of the load connection scheme is tested for the residential MG. The load at R_1 is given the highest priority followed by load at R_{11} , R_{15} , R_{16} , R_{17} and R_{18} respectively. The minimum frequency is set to 48 Hz and the minimum terminal voltage for the load connection is set to 0.8 p.u. Three reclosing attempts are allowed for each load. The time delay between successive load connections is set to 2 seconds and in case of successive load dis-connections, this time is reduced to 1 second. Upon the connection of a load, the frequency and terminal voltage may experience a dip and to address this problem, the load is not immediately disconnected but takes 0.2 seconds before the disconnection. For the sake of illustration, the recloser is not reset automatically for this simulation. Moreover, to test the performance of the load management scheme, the GFLs are operated in reference reactive power injection mode with reference reactive power set to zero. The performance of this scheme is given below.

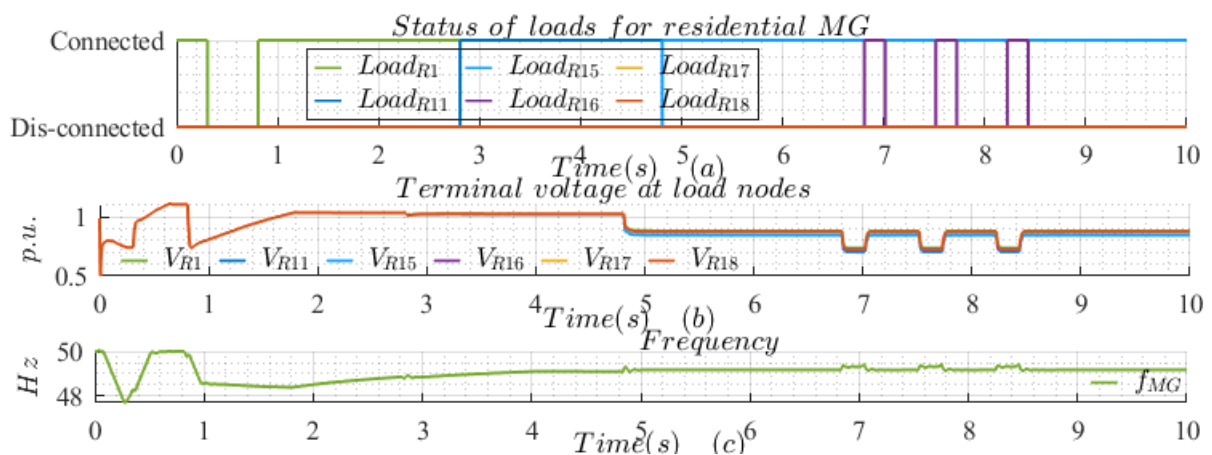


Figure 6.11: Performance of load connection/disconnection scheme; (a) load status, (b) terminal voltages at load nodes, (c) frequency of the MG

The above figure shows that the highest priority load is connected to the network as soon as its terminal voltage and system’s frequency are above their limits. However, due to the connection of the load, both the terminal voltage and the frequency experience a dip and falls below their limits. The load is disconnected after 0.2 seconds as the voltage and frequency were still below their limits. Due to the disconnection of the load, the voltage and frequency restores and after 0.5 seconds, the recloser again connects the load to the network. This time, the frequency does not drop below its allowed limit, and

the terminal voltage at R_1 is also raised above its threshold limit (0.8 p.u.) within 0.2 seconds after the load connection, thus, the load is not disconnected. After 2 seconds, the next priority load is connected to the system. It is not disconnected as the operating conditions are within defined limits. The load at R_{15} is connected to the network after the 2 seconds of the previous load connection. Even though a dip in terminal voltage is recorded but it is still within a defined limit, so the load is also not disconnected. After the next two seconds, the load at R_{16} is connected to the system. Due to this load connection, the terminal voltage drops below its allowed limit and the least priority load is disconnected after 0.2 seconds. The terminal voltage is restored after the disconnection of this load. The recloser again connects this load after 0.5 seconds but it causes the same voltage dip. Similarly, the recloser allows three attempts and afterwards this load (and the other least priority loads) is not automatically connected to the network. By using the same procedure, the other load priority orders can also be tested.

The above analysis shows the effectiveness of the load management system to achieve the stable response of the MG with limited real power generation capability.

6.6 Stability Analysis of the Residential Micro-Grid in Islanded Mode

In this section, the performance analysis of the residential feeder MG will be discussed. As the small signal stability is largely decided by the grid in the grid connected mode, thus, the small signal stability study is performed only for the islanded MG.

6.6.1 Small Signal Stability

6.6.1.1 Voltage Sensitivity Analysis

The voltage sensitivity analysis is performed for the islanded operation of the residential MG. Due to the lower X/R ratio, the terminal voltage is also sensitive to the real power flow, but it is more sensitive for the reactive power flow. The results for the voltage sensitivity are given in Figure 6.12.

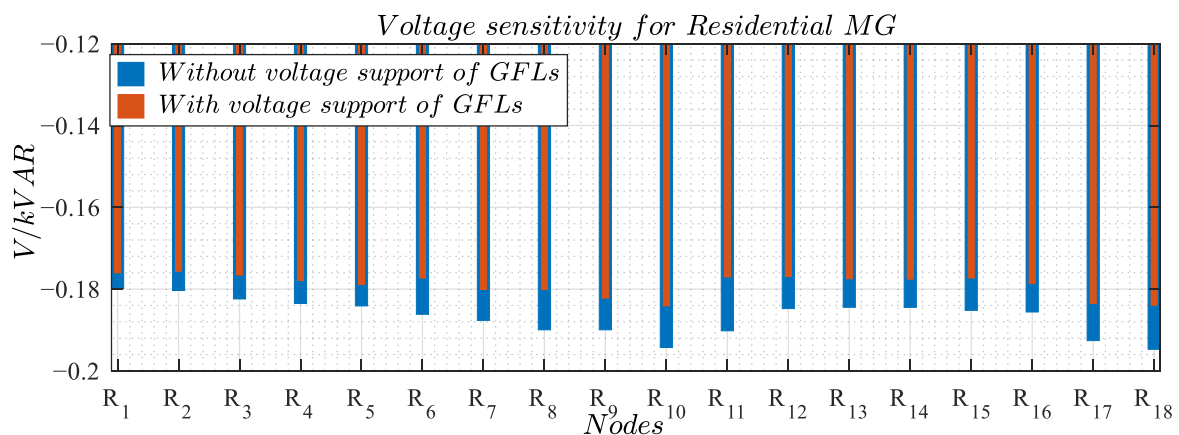


Figure 6.12: Voltage sensitivity analysis for residential MG

In this study, an additional inductive load is connected at a node and the change in its terminal voltage is recorded against this load. The same procedure is repeated for all the nodes of the residential MG. Hence, the degree of voltage sensitivity is computed against the change in the inductive load. As the GFL can operate in voltage support mode or constant reactive power injection mode, voltage sensitivity analysis is performed for both these modes.

It is important to mention here that the above bar chart is not stacked, rather each bar chart starts from zero for both the analysis and the converters' current limits are not reached during these analyses. The results show the change in line to neutral RMS voltage against the 1 kVAR increase in three-phase inductive load. The negative sign confirms the drop in terminal voltage as the reactive power demand is increased. Moreover, the above figure also confirms the higher resiliency if the GFLs are operated in voltage support mode. It increases the overall capacity of the MG to handle more reactive power. Based on the physical location of the nodes, the voltage sensitivity varies for different nodes. The nodes with converters connection are less sensitive due to their higher capacities to deal with change in reactive power demand. However, it is not the case for the node R_{18} where GFM_{R18} is connected. The reason for this is the proportional controller for the voltage controller in GFM_{R18} which contributes no reactive power share because its terminal voltage remains in the nominal range. Overall, the results confirm that the MG is less sensitive to reactive load change.

The voltage sensitivity can also be roughly calculated by using the SCP1 (corresponding to small disturbances) given in Table 6.3 and the mathematical expression given in equation (5.1). However, due to ignoring the phasor addition of the voltage difference phasor and the difference of the square of the voltage magnitudes before and after the load change, the calculated resiliency will be smaller than the actual one presented in above figure (without considering GFL). The other reason for this is the use of $SCP_{GFM}@t=0.06$ seconds for the calculations of SCPs of the residential network whereas the SCP of the GFM settles to some higher value eventually. Thus, the actual network's resiliency is always greater than the calculated one.

6.6.1.2 Frequency Sensitivity

In this section, the frequency stability analysis is discussed for the islanded residential MG. At steady state operation, an additional active load of about 10 % of the nominal load is connected to the MG and the change in the frequency is recorded. There can be different types of converter-based power sources in the MG having different droop constants, thus, it is important to characterize the system's frequency change based on the load change. For this reason, a 40 kW three-phase active load is connected to the MG at R_1 . The load is of constant impedance type; thus, its actual real power consumption is dependent on the terminal voltage. The system's frequency and the measured real power consumption for the additional load are plotted in Figure 6.13.

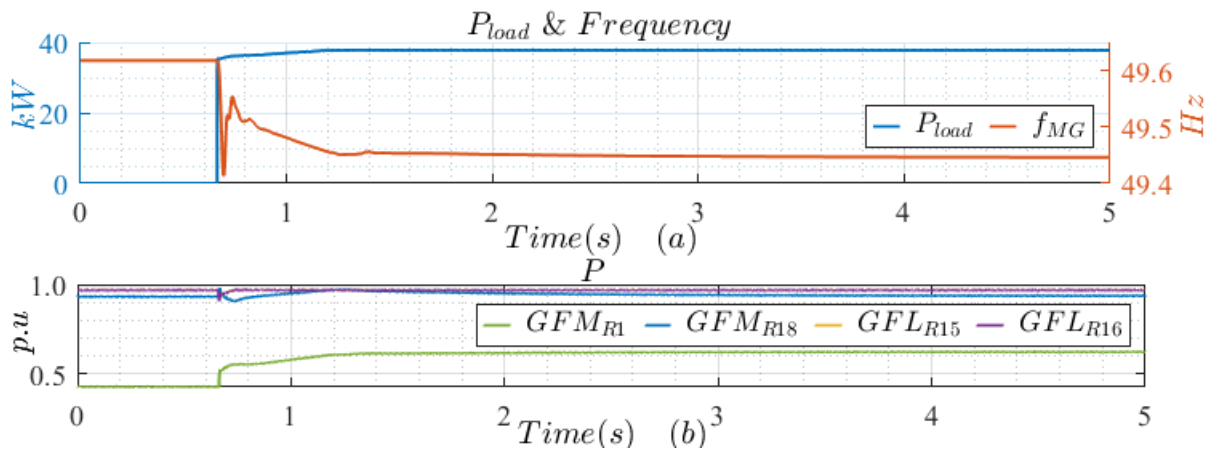


Figure 6.13: Frequency stability of the residential MG in islanded operation; (a) measured frequency and additional load change, (b) active power output of converter-based sources

The above figure shows a drop in frequency as the additional load is connected to the MG. A new operating frequency is achieved which depends on the actual load change and the frequency droop constants for different sources. From the above figure, it is clear that the frequency sensitivity for the residential MG is around -4.5 mHz/kW . This shows a stable frequency response against the active power load changes as long as the converters' current limits are not reached. The subplot (b) shows the impact of the load change on the output real power of the converters. The GFLs are insensitive to load change as the frequency support is not included in the control of GFL. Although the GFMs have the active power-frequency droop and respond to the frequency change but the output of the GFM_{R18} is not changed. The reason for this is that the GFM_{R18} operates in the grid connected mode and its reference real power is 1 p.u. As the additional load is connected, frequency drops below its steady state value which forces the GFMs to increase the real power output to support the frequency but the GFM_{R18} is already operating on its maximum real power capability. Thus, in such conditions, it ensures synchronization with the other sources and does not change its active power output. This is the reason that the maximum real power change is observed for the GFM_{R1} .

6.6.2 Large Signal Stability

The large signal stability of the MG is important in both grid connected and islanded mode. In this section, the large signal stability is discussed for the islanded operation of the MG. The stability of the MG is directly linked to the stable operation of the individual converters connected to the network. The converter-driven stability of the GFL is highly affected by the stability of the PLL. It is majorly because of the introduction of negative admittance, in parallel to the network's admittance, due to the PLL. The other important factor is the angle stability of the GFM which is related to the synchronization of the GFM in case of voltage dips. It becomes a critical factor due to the limited current handling capability of the GFM.

To investigate large signal stability, the fault duration is varied, and maximum fault duration is assessed during which no oscillations in the real/reactive power are observed i.e., the critical fault clearing times are assessed. Exemplarily, a balanced three-phase fault is introduced at node R_3 for the duration of 1.7 seconds and its impact is analyzed on the stability of the system. The fault is introduced at 0.5 seconds and ends at 2.2 seconds. The response of different converters is plotted in Figure 6.14.

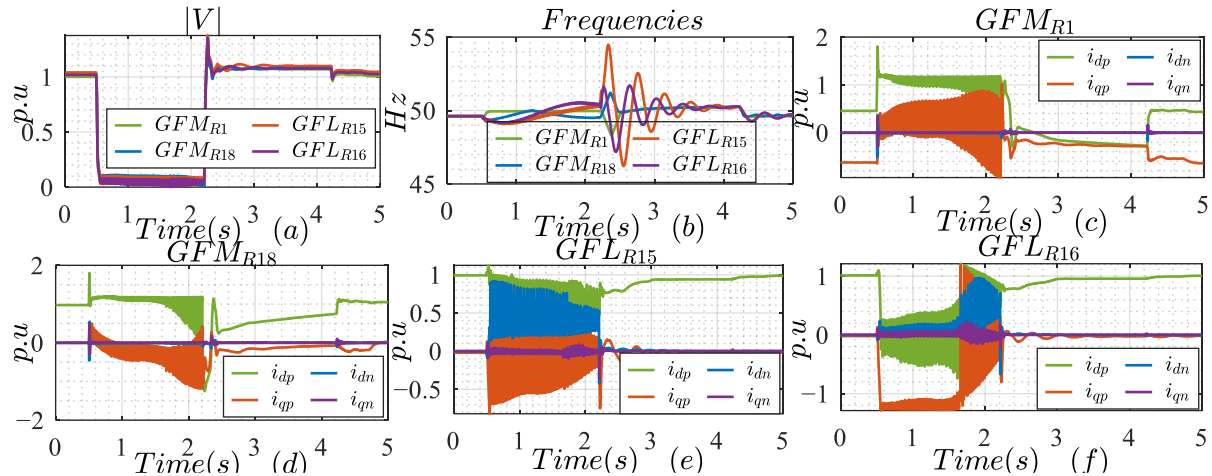


Figure 6.14: Response of different converters in case of three-phase balanced fault for islanded operation of the MG; (a) magnitude of the voltage phasor at each converter's terminal, (b) frequency estimation by each converter, (c) measured sequence current components for GFM at R_1 node, (d) measured sequence current components for GFM at R_{18} node, (e) measured sequence current components for GFL at R_{15} node, (f) measured sequence current components for GFL at R_{16} node

The above figure shows that the response of the different converters in the fault is poor. It is important to mention here that the converters achieve the initial stable operating point in the post fault scenario. However, during the fault, the converters are unable to achieve a stable operating point due to which the injected currents oscillate. The GFL converter's ideal response in such conditions is to inject the reactive current to support the grid's voltage. However, from subplots (e) and (f), it is clear that both the GFL converters are unable to inject the constant reactive current in such conditions. The reason for this is the relatively low SCP at the converters' terminal due to the absence of the grid. Moreover, as the fault is introduced between the GFM_{R_1} and the GFLs, thus, it decouples the system. As the fault is resistive in nature, the reactive power balance is automatically achieved by adjusting the voltage angle. The higher reactive current injection changes the voltage angle at the terminal of the GFL because there is no active grid available to stabilize the voltage angle. The change in voltage angle changes the current distribution which in turn again changes the voltage angle. This closed loop operation eventually causes an unstable response of the GFL. From subplot (b), it is clear that each PLL estimates a different operating frequency due to which their responses are also different from each other. By comparing subplot (e) and (f), it also shows that the GFL connected at R_{15} has more oscillations in the injected current as compared to the GFL at R_{16} .

The $GFM_{R_{18}}$ is operating in grid connected mode. It ensures the synchronization with the GFM_{R_1} in all operating conditions with limited current handling capability. The subplot (d) shows that the output of

the GFM_{R18} has also oscillations in faulty conditions. These oscillations are due to the oscillated current injection by the GFLs which has a huge impact on the terminal voltage at R_{18} in fault duration. As the fault is cleared at 2.2 seconds, the GFMs achieve synchronization quickly and the GFLs achieve a stable operating point in a reasonable time. The post fault frequency oscillations in the GFL are due to the slower PLL. As explained in the GFL design chapter that the slower PLL may cause oscillations in the measured frequency which in turn can cause different power injections than the reference power. Thus, it was suggested in the same chapter that a reference current can be adjusted to take into account the slowness of the PLL so that accurate powers are injected to the network. Hence, in this case, although the measured frequency has large oscillations in the post fault conditions but the measured current components have no such oscillations which is due to the adjustment in the reference currents. Moreover, a change in operating frequency is recorded at 4.2 seconds. This is due to the reconnection of one of the loads which was dis-connected by the load connection scheme discussed in subsection 6.5.

To achieve a stable response of the GFL in faulty conditions, there can be different remedies. A strong grid can ensure a stable response, but it is highly unlikely and economically not feasible to install high power GFMs to stabilize the GFLs in islanded mode. Thus, in islanded mode, one option is to relocate the GFLs to some other nodes where they could offer a better response. The same analysis is performed for relocating one GFL to R_4 and the other one to R_6 . This time, the response of the system in fault and post fault conditions is stable. The response of the system is plotted in the below given figure.

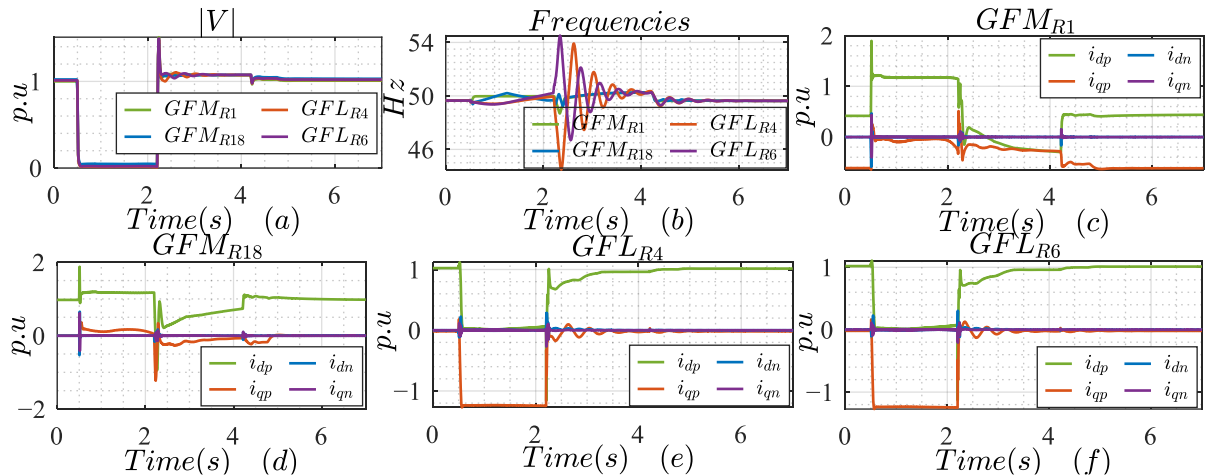


Figure 6.15: Response of different converters in case of three-phase balanced fault for islanded operation of the MG; (a) magnitude of the voltage phasor at each converter's terminal, (b) frequency estimation by each converter, (c) measured sequence current components for GFM at R_1 node, (d) measured sequence current components for GFM at R_{18} node, (e) measured sequence current components for GFL at R_4 node, (f) measured sequence current components for GFL at R_6 node

The above figure shows that the GFLs achieve a stable operating point even in case of fault. The GFLs injected current is according to the grid code recommendations. Moreover, in case of fault, the GFM_{R18} does not change its reactive power drastically as it offers the natural response of a voltage source and due to resistive fault and relatively lower X/R ratio of the line sections, it does not inject more reactive current for the voltage support. The same is true for the GFM_{R1} as well. This is the reason that both the

GFM's increase the active current component in case of a resistive fault in a relatively resistive network. The above figure also confirms the stable operation of all the converters in pre-fault, fault, and post fault scenarios.

The stable fault and post fault operation is dependent on the duration, type, and location of the fault, SCP at POC for the GFLs, length of the lines and their X/R ratio between different sources and fault, etc. It is difficult to estimate the exact fault duration which result in stable fault/post-fault operation. However, some qualitative relations can be developed. Based on this discussion, a new parameter is introduced for the sake of defining the large signal stability of the MG. This is termed as critical clearing time (CCT), but it is different from the CCT defined for the conventional power systems having some synchronous generators. Unlike the conventional power system, here, the CCT_q is defined as the maximum fault clearing time in which the GFLs confirm the stable current injection with grid supporting behavior. Another time (CCT_p) can also be defined which corresponds to the maximum fault clearing time to ensure no real power reversal for the GFLs connected in the system. This is important particularly for the GFLs which can't handle the real power reversal. The prime reason for the active and reactive current injection is the wrong assessment of the voltage angle by the PLL.

To investigate more about the impact of the fault location on the stability of the MG, the fault is introduced at other nodes and the CCT_q and CCT_p are recorded. It is important to mention here that the CCT_q and CCT_p can be different for different converters but to define the CCTs for the complete network, the minimum of them is recorded so that it could ensure that all the converters offer the same type of response. Moreover, the CCTs are important for the GFLs as the GFMs offer the natural response and may change the direction of the reactive power. Moreover, most of the GFMs offer frequency support so they also have energy storage elements on the dc side. Thus, the real power reversal is not a challenge for the GFMs. This is the reason that only the GFLs are considered here to define the CCTs for the MG. The CCTs for different fault locations are given in the following table.

Table 6.6: Critical clearing times for the large signal stability of the GFLs connected at R_4 and R_6

<i>Fault Location</i>	<i>CCT_p (ms)</i>	<i>CCT_q (ms)</i>	<i>Fault location</i>	<i>CCT_p (ms)</i>	<i>CCT_q (ms)</i>
R ₁	67.5	66.9	R ₂	74.2	73.8
R ₃	1772	1809	R ₄	1930.6	1991.4
R ₅	2548.5	2574.8	R ₆	4574.1	Inf
R ₇	Inf	Inf	R ₈	Inf	Inf
R ₉	Inf	Inf	R ₁₀	Inf	Inf
R ₁₁	1228	1227.7	R ₁₂	1244.1	1243.8
R ₁₃	950.8	950.6	R ₁₄	542.1	541.8
R ₁₅	448.2	448	R ₁₆	1488.1	1511.7
R ₁₇	1619.4	1654.3	R ₁₈	4390.2	Inf

In the above table, some entries show 'Inf' which stands for infinity. The fault duration is selected to be 5 seconds in this analysis and if the converters' response is stable in the complete fault duration, then it is recorded as 'Inf' in the above table.

The above table shows that the CCTs are increased as the fault location moves away from the node R_1 where the reference GFM converter is connected. However, the change in CCTs is not linear with the fault distance from the R_1 node. For the fault locations from R_1 to R_{10} , the fault current infeed from different paths is different depending upon the location of the fault and if the fault is introduced at the rest of the nodes, there are some common lines and more current passes through these lines. These lines also have lower X/R ratios and results in lesser CCTs as compared to the location excluding these common lines. For example, if the CCTs for the node R_3 and R_{11} are compared, it shows that the CCTs for R_{11} are lesser than the CCTs for R_3 fault which means that the fault at R_{11} is more critical than the fault at R_3 . Physically these two nodes have only one line section in between with lower X/R ratio. The same is true if the results for the fault at R_4 are compared with the results of fault at R_{12} . Thus, from these results, it is clear that the response of each converter depends on the line impedance from the point of connection up to the fault location. It is also dependent on the rating of the converter. This is the reason that if both GFL converters are connected at the same node, the CCTs will be changed. Hence, it is important to perform this analysis for the actual network configuration.

To confirm the dependence of the CCTs over the actual network configuration, the same process is repeated by first connecting both the GFL converters at R_4 and then at R_6 . Only three fault locations are selected for comparison i.e., on the end nodes of the feeder (R_1 and R_{18}), and the one with some common impedance involved (R_{12} if both converters are connected at R_4 and R_{16} if both converters are connected at R_6). The results are presented in Table 6.7.

Table 6.7: CCTs for connecting the GFLs at the same node

<i>Fault Location</i>	<i>CCT_p (ms)</i>	<i>CCT_q (ms)</i>	<i>Fault Location</i>	<i>CCT_p (ms)</i>	<i>CCT_q (ms)</i>
<i>Both the GFLs are connected at R₄</i>			<i>Both the GFLs are connected at R₆</i>		
R_1	65.3	64.8	R_1	63.1	62.3
R_{18}	1727.8	1727.6	R_{18}	1445.5	1445.3
R_{12}	1246.1	1245.8	R_{16}	1450.4	1450.1

The first two rows of the above table show that the CCTs are increased if the same rating of GFL is connected near to the reference GFM. The third-row results are not comparable as the line lengths from GFLs to the specific node are different. If the results of the above table are compared with the response given in Table 6.6, it shows that the distributed GFL results in longer CCTs as compared to the single point connection for the GFLs. However, it is also important to consider that the SCP at R_4 and R_6 is 285 and 281 kVA respectively and by connecting a 200 kVA GFL at these nodes resulted in SCR less than 2 which also has a negative effect on the stability of the GFL's response.

To conclude the above discussion, it can be stated that it's better to install the GFLs near to the reference GFM from large signal stability's perspective. The GFL connection should ensure the SCR to be at least 2 at the POC. Moreover, the CCTs are changed nonlinearly as the location of the fault is varied.

The above study confirms that the original configuration (one GFL connected at R_{15} and the other at R_{16}) may result in very poor large signal stability even though the SCR is ensured to be greater than 2 at the specified nodes. This is mainly due to adjusting the reference currents to take into account the slow response of the PLL. Thus, in this case, even though the PLL is slower, the reference currents are quickly adjusted if a change in the operating conditions is sensed. This adjustment in reference currents results in accurate reference powers at POC and helps to employ the current limiting schemes without considering the coupling of the currents components. However, it has a negative effect on the large signal stability of the converter.

The other possible option is to deactivate the reference current adjustments in case of faults. It can enhance the converter's large signal stability. The drawback to deactivating this adjustment is to compromise on the accuracy of the feeding powers at POC which can be acceptable in case of faulty conditions. Moreover, due to the absence of the reference current adjustment and slower PLL, the actual grid's voltage angle at POC is different than the assessed one which will result in oscillations in the active and reactive current components in case of faults. Due to these oscillations, the CCTs need to be calculated in this case as well.

To test the performance of the MG without reference current adjustments for GFLs, a three-phase balanced fault is introduced at R_3 and the GFLs are connected at R_{15} and R_{16} . The fault duration is 1.7 seconds, and it is introduced at 0.5 seconds. The response of different converters is plotted in Figure 6.16.

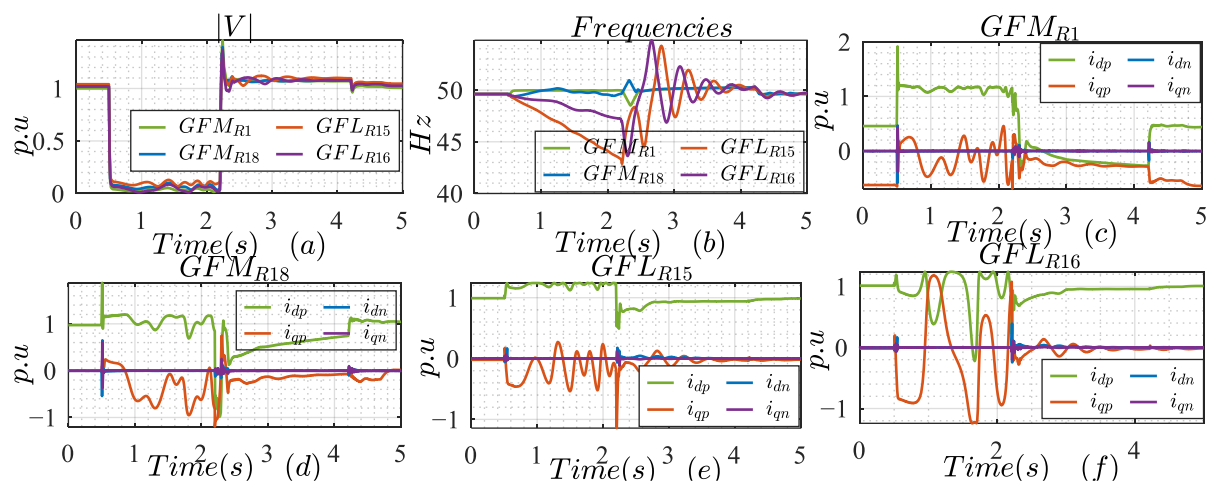


Figure 6.16: Response of different converters in case of three-phase balanced fault for islanded operation of the MG without reference current adjustment; (a) magnitude of the voltage phasor at each converter's terminal, (b) frequency estimation by each converter, (c) measured sequence current components for GFM at R_1 node, (d) measured sequence current components for GFM at R_{18} node, (e) measured sequence current components for GFL at R_{15} node, (f) measured sequence current components for GFL at R_{16} node

By comparing Figure 6.14 and Figure 6.16, it is clear that the GFLs without reference current adjustment result in longer CCTs and helps to improve the large signal stability of the MG. The subplots (e) and (f) show a better response of GFLs without reference current adjustments. Due to the relatively stable

response of GFLs, the GFM's response is also stable. With reference current adjustment, the CCT_p and CCT_q for the same fault were 55.6 and 55.5 ms respectively but without reference current adjustments, these are 1146 and 448.9 ms respectively. However, the drawback of slower PLL is clear from subplot (b) which shows wrong assessment of frequency by the GFLs during fault. Hence, this analysis shows that the large signal stability is improved by using a slower PLL. Thus, in this thesis, the location of the GFLs is not changed as it may be the result of different external factors, but the reference current adjustment is deactivated in case of faults to improve the large signal stability of the MG operating in islanded mode.

Most of the LVRT curves ensure the converter's connection for a minimum time period in case of a voltage dip. In [80], this time is mentioned to be 200 ms if the terminal voltage drops to zero volts. Thus, this is the minimum time for which the converter should ensure its connection with the network. Even though these conditions are important for the grid connection mode, the same may be used for the MG operation as well. Hence, it is important to compute the CCTs for the original network which should be at least greater than 200 ms for any fault location. The CCTs for the original network configuration (without reference current adjustments for the GFLs) are given below.

Table 6.8: Critical clearing times for the large signal stability of the GFLs without reference current adjustments connected at R_{15} and R_{16}

<i>Fault Location</i>	<i>CCT_p (ms)</i>	<i>CCT_q (ms)</i>	<i>Fault location</i>	<i>CCT_p (ms)</i>	<i>CCT_q (ms)</i>
R ₁	1486.6	421.2	R ₂	1101.7	431.9
R ₃	1136.6	447.4	R ₄	Inf	425
R ₅	Inf	384.3	R ₆	1342.5	364.4
R ₇	1795	362.5	R ₈	1638.3	360.9
R ₉	1083.1	359.3	R ₁₀	1054.8	357.5
R ₁₁	413.7	374.2	R ₁₂	346.2	479.3
R ₁₃	310.9	522.8	R ₁₄	298.5	507.2
R ₁₅	288.8	487.1	R ₁₆	381	363
R ₁₇	355.6	347.3	R ₁₈	974.6	331.3

The above table shows that the minimum $CCT_{p,q}$ for the said arrangement is greater than 200 ms. Due to the severity of the fault, the terminal voltages during fault are below 0.1 p.u. thus, according to the LVRT curves of the GFL, it should be connected to the network for at least 200 ms. Hence, if the fault is removed/isolated before the CCTs or the GFLs are disconnected from the network after fulfilling the LVRT curve then the stable operation of the MG can be ensured. To confirm the large signal stability of the network with the GFLs fulfilling the LVRT curve, a three-phase fault is introduced at R_3 at 0.5 seconds for a duration of 0.4 seconds. The response of different converters is given below.

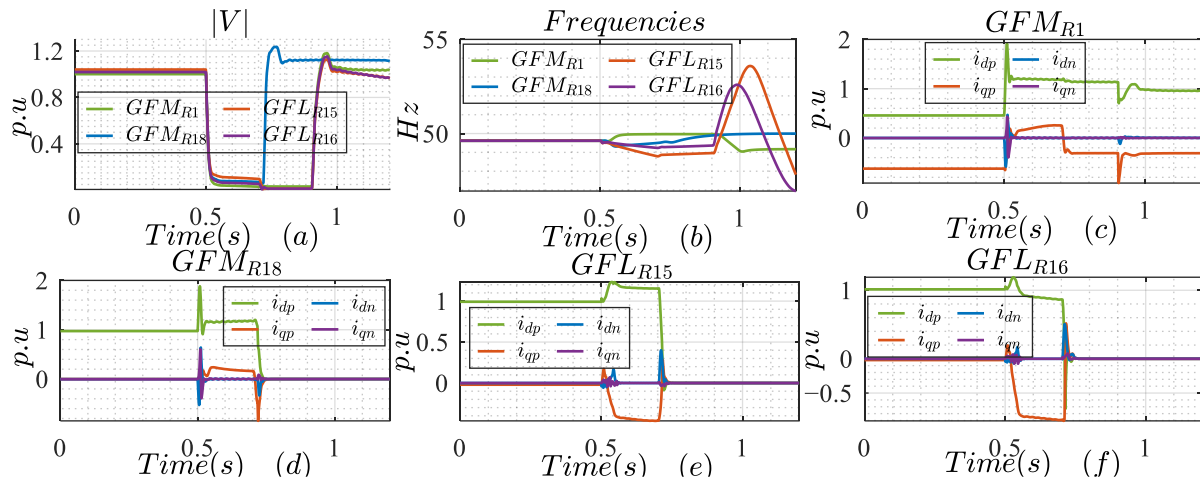


Figure 6.17: Response of different converters in case of three-phase balanced fault for islanded operation of the MG with LVRT curve and without reference current adjustment; (a) magnitude of the voltage phasor at each converter's terminal, (b) frequency estimation by each converter, (c) measured sequence current components for GFM at R_1 node, (d) measured sequence current components for GFM at R_{18} node, (e) measured sequence current components for GFL at R_{15} node, (f) measured sequence current components for GFL at R_{16} node

From the subplots (e) and (f), it is clear that the response of the GFLs is smooth in fault duration. Even though the fault lasted till 0.9 seconds but after fulfilling the minimum connection time (according to the LVRT curve), the GFLs disconnected from the network around 0.7 seconds. The reactive and active current components for both the converters did not experience oscillations which helped to improve the stability of the MG. Similarly, from subplot (d), it is clear that the GFM $_{R_{18}}$ is also tripped due to long duration of the fault as this converter also ensures the fulfillment of the LVRT curve and after the minimum required connection time, it is disconnected to avoid power oscillations due to synchronization loss. This is the reason that the terminal voltage for GFM $_{R_{18}}$ is restored before the fault clearance (subplot (a)). From subplot (b), it shows that the GFLs frequency assessment is not accurate, and this is mainly because of the absence of the reference current adjustments which overcome the disadvantage of the slower PLL.

After the fault clearance, the GFLs assessed frequency has large oscillations which are damped out gradually depending on the speed of the PLL. Anyhow, these oscillations do not affect the performance of the MG as the GFLs wait for two seconds before the reconnection so that the true frequency is assessed. As soon as the fault is cleared, the GFM $_{R_{18}}$ can also start its synchronization process and smoothly synchronize with the network.

The next step is to analyze the large signal stability of the MG against an unbalanced fault. The response of the MG in case of unbalanced fault is influenced by the operating modes of the GFL which are discussed in detail in the previous chapters. Mainly three factors of GFL affect the response of the MG in case of unbalanced faults i.e., whether the GFL is operated to minimize the VUF or to minimize the real power oscillations or to inject the reactive currents according to the grid codes. A combined scheme is also presented which results in minimum VUF along with minimum real power oscillations in case

of asymmetrical faults. The next important factor is the selection of the priority injection scheme which has a huge impact on the response of the system as the reference currents are normally high in faulty conditions and the current components with higher priority decide the response of the converter. The impact of these factors is discussed in detail in the chapter 3. In this section, the impact of these factors will be analyzed on the MG level.

For this analysis, a line-to-line fault is introduced at R_3 between phase ‘a’ and ‘b’. The fault is introduced at 0.5 seconds and the fault duration is 0.4 seconds. The GCR scheme is activated for the GFLs, and the NQP priority selection scheme is activated. Additionally, the DSVS scheme is selected to fully utilize the current capacity of the GFLs in case of fault. The response of the different converters in case of unbalanced faults is given in Figure 6.18.

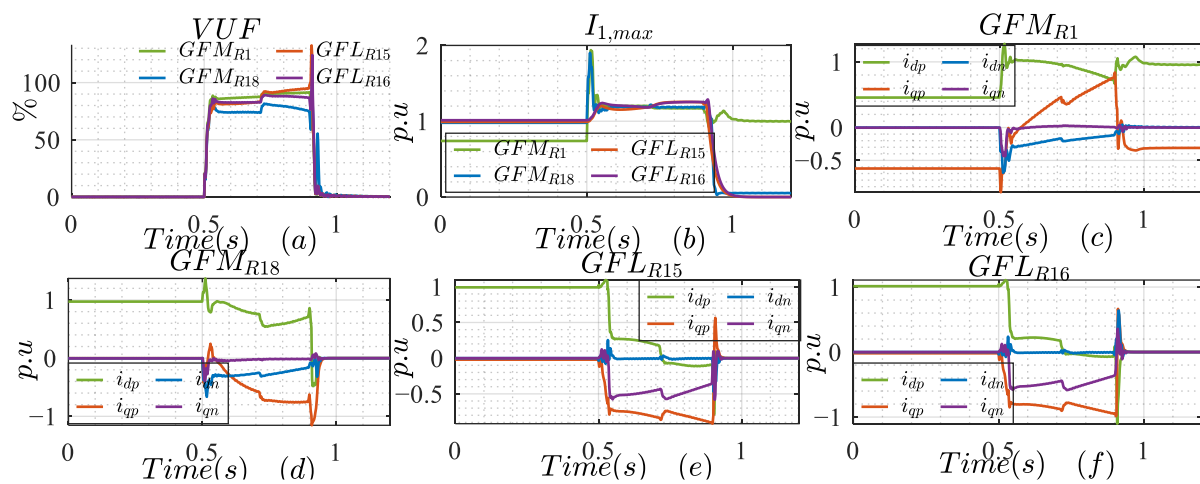


Figure 6.18: Response of different converters in case of unbalanced fault for islanded operation of the MG; (a) VUF at each converter's terminal, (b) maximum phase current on converter's side for each converter, (c) measured sequence current components for GFM at R_1 node, (d) measured sequence current components for GFM at R_{18} node, (e) measured sequence current components for GFL at R_{15} node, (f) measured sequence current components for GFL at R_{16} node

The above figure shows that the response of all the connected converters is stable against the L-L fault. The subplot (a) presents the %VUF at the converters' terminals which shows a change in VUF due to the changing response of different converters. A change in %VUF around 0.7 seconds is due to the least priority load disconnection. The subplot (b) confirms the safe operation of the converter during the fault. The first cycle fault current for the GFMs is greater than the current limit of the converter. It can be due to the wrong estimation of the angle between the positive and negative sequence current phasors and the error in frequency estimation may also result in inaccuracy in the measurement of maximum phase current. From the time domain response, it can be confirmed that the current in few phases may exceed the current limit of the converter but the duration of this current only lasts for one cycle. Ignoring the sub transient current exceeding, the maximum fault current for each converter is within its defined limits.

The subplots (c) and (d) present the measured sequence currents for GFM_{R1} and GFM_{R18} respectively. As the fault is purely resistive, to minimize the voltage difference among different phases, the GFMs injected the active current component in the negative sequence and the sign of the negative sequence active power for both the GFMs is the same.

The subplots (e) and (f) show the response of the GFL_{R15} and GFL_{R16} respectively. It shows that both the GFLs inject the current according to the grid code's recommendations (even though, it is not a binding to fulfill GCR in islanded mode). It also confirms the priority scheme as the reactive current components are prioritized over the active current component. However, the reactive current component in the positive sequence is higher than the reactive current component in the negative sequence even though the NQP priority injection scheme is activated. This is due to the fact that the change in negative sequence voltage phasor's magnitude is less and the injected i_{qn} corresponds to this change and the proportionality constant (k_n) which is selected to be 2 in this case. Thus, after prioritizing the i_{qn} , the rest of the current capacity is used for the i_{qp} and due to bigger change in the magnitude of the positive sequence voltage phasor, higher i_{qp} has resulted. Even though the proportionality constants ($k_{p,n}$) are selected to be 2 for the calculation of the reactive current in case faults, due to the limited current handling capacity of the converter and due to the prioritization of the negative sequence current components, the measured value of k_n is 2 but the measured k_p value is around 1.1.

For the sake of comparison of different modes of operation, a L-L fault is introduced at R_3 , and the negative sequence current phasor is prioritized for GFLs in faulty conditions. The performance of the GCR, OAI and OAI&MRPF schemes is compared for the real power oscillations and the mean real power. The following table shows the comparison of these schemes for each converter. Due to the continuous change in the terminal voltage, the mean real power and associated oscillations are also changed. Thus, for the sake of comparison, the values are computed against the same time for each current injection scheme.

Table 6.9: Comparison of different reference current schemes for the real power oscillations in faulty conditions

<i>Parameter</i>	<i>Amplitude of real power oscillations (p.u)</i>			<i>p_{mean} (p.u)</i>		
	<i>GCR</i>	<i>OAI</i>	<i>OAI&MRPF</i>	<i>GCR</i>	<i>OAI</i>	<i>OAI&MRPF</i>
GFM_{R1}	0.37	0.28	0.37	0.43	0.01	0.32
GFM_{R18}	0.51	0.16	0.43	-0.05	0.21	-0.01
GFL_{R15}	0.45	0.19	0.02	0.26	0.15	0.24
GFL_{R16}	0.45	0.11	0.02	0.25	0.14	0.29

The green color shows the best performance followed by the blue and red colors respectively. One of the primary targets in unbalanced conditions is to minimize the real power oscillations. The above table shows that the OAI&MRPF scheme offers minimum real power oscillations for the grid following converters, but it has very little effect on the GFMs. Even though the above stated schemes are used in GFLs, but they also affected the response of the GFMs as converters are electrically connected. Thus, from the perspective of the GFLs, the OAI&MRPF scheme offers minimum real power oscillations but

from the perspective of the MG, the overall real power oscillations are minimized with the OAI scheme. The mean real power comparison shows that the injected power from these sources is not zero for the minimum real power oscillations.

The next important factor in case of unbalanced conditions is to improve the voltage uniformity among different phases which is indicated with the help of % VUF. The above discussed three schemes are also compared for the minimum VUF at each node. The performance of each scheme is shown in Figure 6.19.

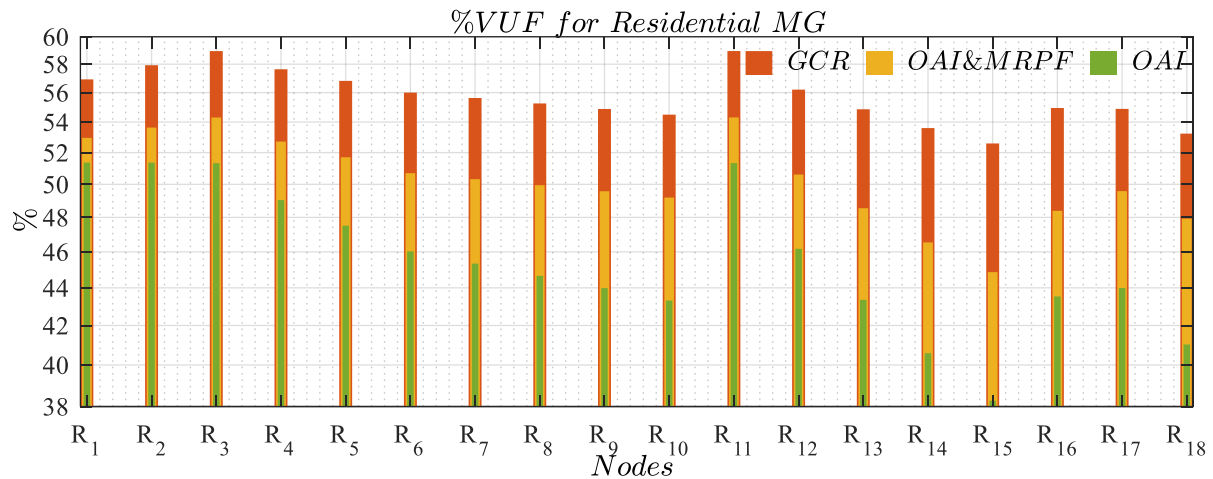


Figure 6.19: %VUF at each node in residential feeder against different reference current generation schemes for GFLs

It is important to mention here that the above bar chart is not stacked, rather each bar chart starts from zero against each reference current generation scheme. The above figure confirms that the minimum VUF has resulted at each node if the OAI scheme is implemented for the GFLs. It also confirms that the grid code recommendation of only reactive current injection in the negative sequence does not result in minimum VUF. Moreover, the OAI&MRPF scheme offers better results than GCR. However, its performance, for % VUF, is lower than the OAI scheme as this scheme minimizes the real power oscillations as well. It is important to mention here that even though these are the reference current generations schemes only for the GFLs but due to the weaker grid and higher proportion of the GFL based power in the system, the impact of these scheme is evident on the MG level.

The highlights of the large signal stability of the MG in islanded operation are given below.

- The GFM's offer stable operation in different faulty conditions.
- In weaker networks, the GFL's response in faulty conditions can be unstable which is due to the higher impact of the GFL's current injection on the phase angle of its terminal voltage.
- To improve the stability of the GFL in faulty conditions, either it should be located to the nodes with higher SCP and close to the reference converter/power source or the slower PLL without reference current adjustments should be used.

- Two CCTs can be defined for the converter-based system which ensure that there is no reversal of real and reactive powers if the fault is cleared before this time, or the converters are disconnected before this time.
- The CCTs are changed nonlinearly against the fault location and the fault impedance. Thus, these times need to be computed for each configuration. In general, if the GFLs are installed near to the reference voltage source, higher values for the CCTs are expected.
- The minimum connection time for the GFLs (according to the LVRT curve) should be less than the CCTs so that no fluctuations in the real/reactive current are experienced.
- In case of unbalanced faults, the OAI scheme for the GFLs results in minimum VUF, thus it improves the voltage uniformity among different phases. It also results in relatively lower oscillations in the injected real power from the GFLs which in turn also decreases the real power oscillations of the GFMs. Thus, the OAI scheme can be used to minimize the % VUF and the real power oscillations in case of unbalanced conditions.

6.7 Analysis of the Residential MG in Grid-connected Mode

6.7.1 Smooth Connection/disconnection to the Grid

In the grid connected (GC) operation mode, it is important to ensure the MG's smooth connection and dis-connection with the grid. To achieve the synchronization, the MG's frequency, and terminal voltage at point of connection need to be adjusted according to the grid's conditions. This can cause variation in operating frequency of the MG and the terminal voltage can also experience a dip which can cause the GFLs to operate in LVRT mode. To avoid such situations, one option can be to disconnect all the sources and the loads in the MG and then synchronize these sources one by one with the network. After the connection of these sources, the loads can be connected to the network again. The drawback of this scheme is the non-availability of the service to the loads during the synchronization process. The down time can be minimized by simultaneously connecting some sources and loads to the network. The other option is to deal the MG as a single prosumer and ensure that its sources operate in their defined range while synchronization process is initiated. This can confirm the uninterruptible power supply to the loads during the synchronization process. However, due to voltage dip and frequency change during synchronization, some of the loads can be disconnected by the load management system discussed in section 6.5.

The process of grid connection is relatively easier as it can be planned beforehand but the MG response in case of sudden grid loss is more critical. There can be different reasons which can force the sudden disconnection of the MG from the external power grid. In such conditions, the response of the MG is critical and should be investigated. The simplified layout diagram of the residential MG connection with the grid is shown in Figure 6.20.

the same frequency and phase angle as of grid (subplot (a)). The terminal voltage at R_1 is also changed to achieve the same voltage magnitude on both sides of the CB. The voltage dip at the load terminals is small enough to disconnect any load during the synchronization process. The subplot (b) shows the real power output of different converters. As the GFL converters don't have the frequency support capability, thus, their real power output is not changed drastically during this process. However, the real power output of the GFMs is changed to achieve the same frequency and phase angle on both sides of the CB.

The subplot (c) shows the reactive power output of the connected converters. It also shows the change in reactive power output of the GFMs during the synchronization process. The terminal voltage for the GFLs did not drop below 0.9 p.u. due to which no voltage support is provided by the GFLs during this process. To analyze the angular stability of the MG, the angular stability of the GFM_{R18} is investigated as it is supposed to be synchronized with the GFM_{R1} in both, grid connected and islanded, modes. The subplot (d) presents the angular stability for the GFM_{R18} which shows that an equilibrium point is achieved before the synchronization process is initiated. As the synchronization process is started, the operating frequency and the angular difference changes from the steady state value and it achieves a new equilibrium point on achieving the grid connection. In islanded mode, the operating frequency was different than 50 Hz but on achieving the grid connection, the operating frequency is changed to 50 Hz. The angle difference is relatively lower in both the modes as the GFM_{R18} requires to inject 1 p.u. real power in both modes of operation.

The above figure also shows that after connected with the grid, the terminal voltages, frequency, and converters' real and reactive powers are stable. The real power of the GFM_{R1} shows a ramp change from 0 to its reference value (which is 0.5 p.u in this study). This is ramped up to avoid the abrupt change in real power output of a GFM when it is synchronized with the grid. At 12 seconds, the MG is forcibly disconnected from the grid by disconnecting the CB between R_t and R_1 . Due to this sudden loss of grid, the terminal voltages experience a dip which is larger than 0.1 p.u. and hence the GFLs also inject the reactive power to support the voltage along with the GFMs. The real power output of the other converters also experiences small fluctuations but none of the load is disconnected in this process. This condition remains for about two seconds and the MG achieves its islanding mode's equilibrium point. The subplot (d) shows some oscillations in the operating frequency and the angular difference during this process until the stable operating point is achieved successfully.

It is important to mention here that the $|I_n|$ priority injection scheme is used for GFLs in the above analysis and the positive sequence current phasor's magnitude is limited in case of LVRT conditions, but its angle remains the same. In the process of synchronization, the terminal voltage of the GFLs may drop below 0.9 p.u. and the reactive current can be injected to support the voltage which may prolong the synchronization process, thus, during synchronization process, the $|I_n|$ or $|I_p|$ priority injection should

be used which limits the injected reactive current component as compared to the active current component.

6.7.2 Large Signal Stability in Grid Connected Mode

Due to the presence of a strong external grid, the small signal stability of the network is mainly decided by the grid and will not be discussed here. Thus, only the large signal stability of the network will be analyzed for the grid connected operation. A balanced fault is introduced at R_3 in the grid connected mode at 0.5 seconds with the fault duration of 1 second. The response of each converter is analyzed and given in Figure 6.22.

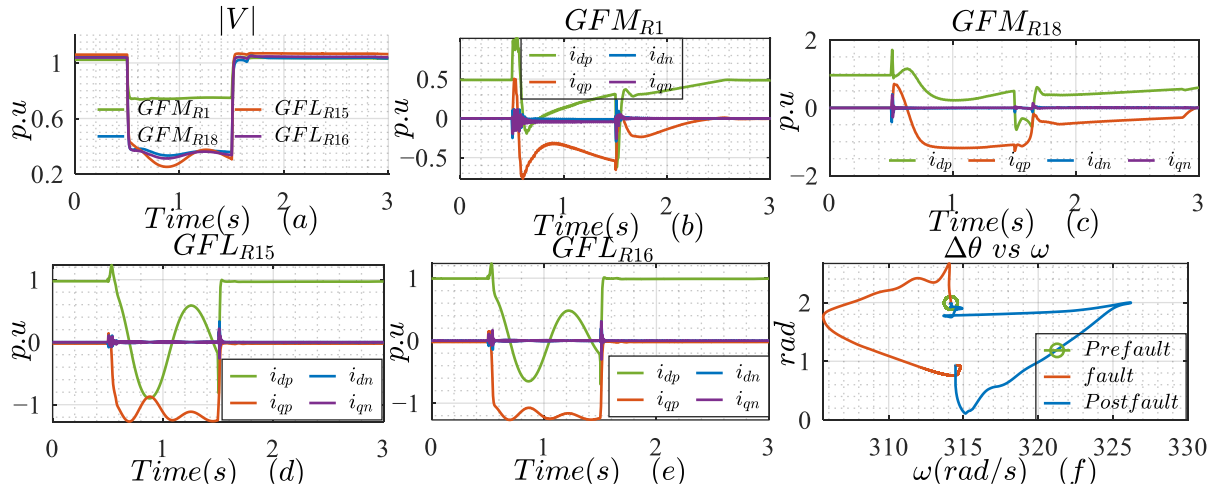


Figure 6.22: Response of different converters in case of three-phase balanced fault for grid connected operation of the MG without LVRT curve and reference current adjustment; (a) magnitude of the voltage phasor at each converter's terminal, (b) measured sequence current components for GFM at R_1 node, (c) measured sequence current components for GFM at R_{18} node, (d) measured sequence current components for GFL at R_{15} node, (e) measured sequence current components for GFL at R_{16} node, (f) angular difference vs speed for GFM_{R18}

The above figure shows that the CCT_q is increased due to the better terminal voltage in case of grid connected operation. However, from subplots (d) and (e), it is clear that the real power output of both the converters oscillates during the fault and it can be negative. It is due to an error in the estimated frequency by the PLL. Thus, the CCT_p is decreased as compared to the islanded operation. The reactive current of these converters does not change its sign during the fault and can support the voltage in LVRT situations. To address the lower CCT_p , either the dc side of the converter should be equipped with dc choppers which can handle this real power reversal, or the current adjustment should be activated when the MG mode is shifted from islanded to the grid connected. The subplot (f) shows the operating point for the GFM_{R18} in each operating phase, and it confirms that the stable operating point is successfully achieved in the post fault scenario.

Addressing the issue of CCT_p in grid connected mode, as discussed above, the adjustment in the reference current can help to enhance it because, in grid connected mode, there is strong power source available and the impact of the converter's current injection on the terminal voltage angle is minimized. Thus, in such conditions, the reference current adjustment can help to estimate the true voltage angle

and can inject non-fluctuated current components in faulty conditions. However, the drawback of this scheme is that the operating mode of the MG needs to be passed on to the GFL control that may be difficult for a MG where the power sources are far away from each other. The MG's operating mode can be decided based on the status of the CB connected between R_t and R_1 . The schematic diagram is given below.

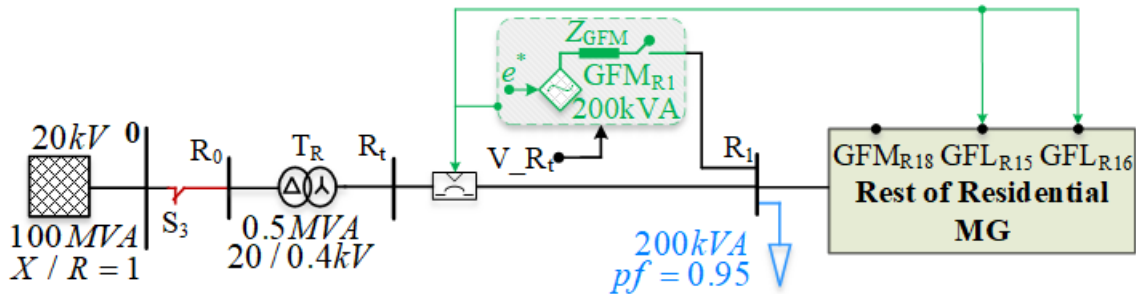


Figure 6.23: Schematic diagram of the grid connected MG with the mechanism of reference current adjustment of GFLs in LVRT conditions

As the above figure shows, the status of the CB is passed to the GFLs connected in the MG to activate the reference current adjustment for the true assessment of the terminal's voltage angle. The CCT_p can also be improved by using the $|I_p|$ or $|I_n|$ priority injection schemes as these schemes only changes the magnitude of the current phasors and does not disturb the ratio of the active to reactive current components which results in relatively higher active current component in the faulty conditions as compared to the priority injection schemes. However, the drawback of this approach is the relatively smaller reactive current in the faulty conditions which may result in a smaller proportionality constant ($k_{p,n}$). The performance comparison of these three approaches for the reference current handling of the GFL_{R15} is given in Figure 6.24. The same can be expected for the other GFLs connected to the network.

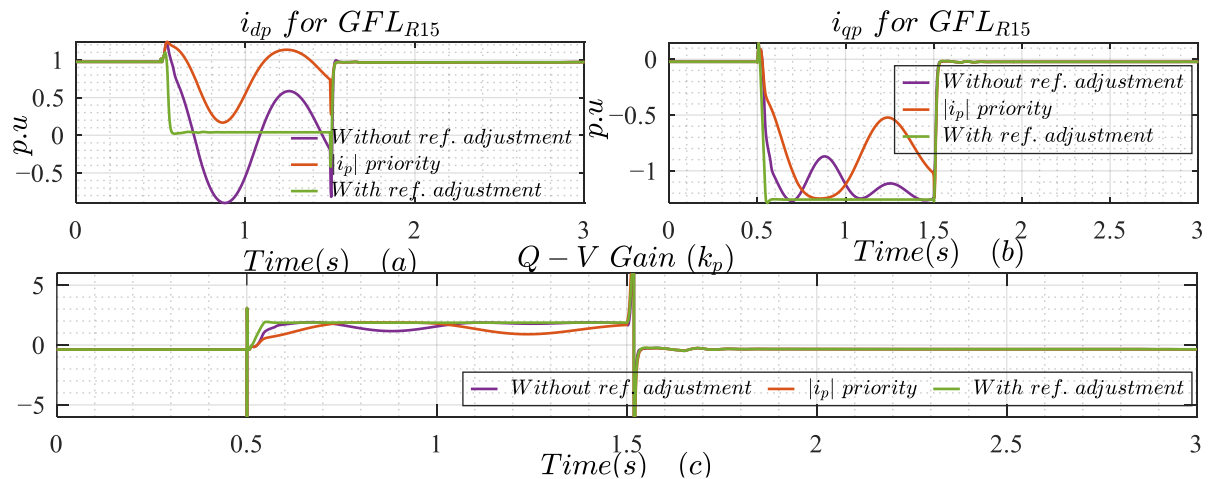


Figure 6.24: Comparison of the different reference current approaches of GFL for the grid connected MG; (a) active current component for the positive sequence, (b) reactive current component for the positive sequence, (c) proportionality constant for reactive current injection in the positive sequence in faulty conditions

The above figure shows that the CCT_p is enhanced for the $|I_p|$ priority injection and with the reference current adjustment approach. i_{dp} greater in case of $|i_p|$ priority scheme as compared to the reference

current adjustment scheme. However, the $|I_p|$ approach results in relatively smaller reactive current injection as compared to the other schemes as it limits the magnitude of the current phasor and in faulty conditions, the reference i_{dp} is greater than i_{qp} . The above graph also confirms that the current adjustment approach results in non-fluctuated current injections in the faulty conditions for grid connected mode. The performance of these schemes is same in the normal conditions.

The performance of the grid connected MG is also analyzed in case of unbalanced faults. The OAI scheme is used for GFLs' control in LVRT conditions along with the $|I_n|$ priority injection and conventional current limiting scheme. The response of the network against a line-to-line fault at R_3 is shown in Figure 6.25.

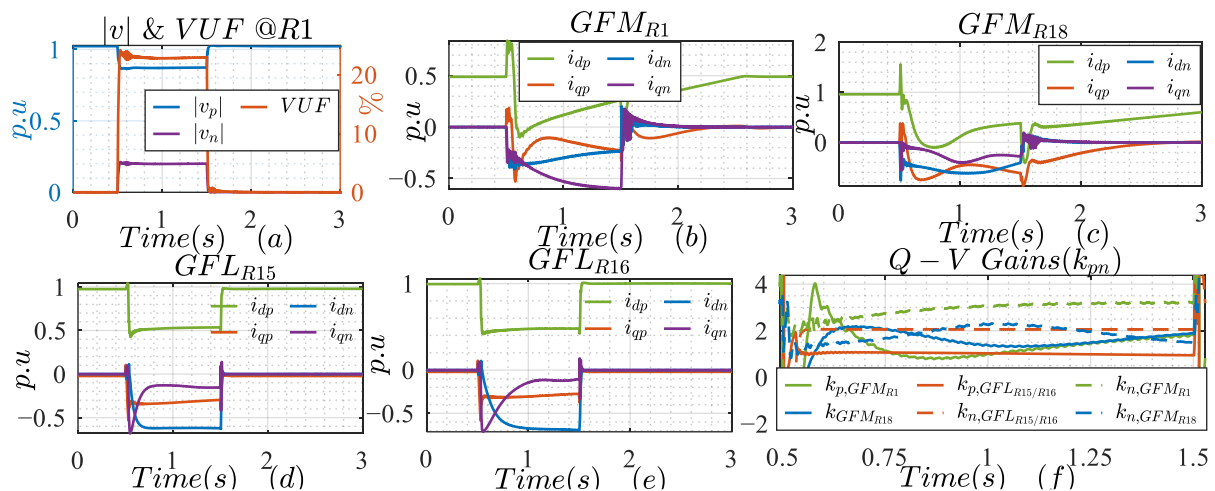


Figure 6.25: Response of different converters in case of L-L fault for grid connected operation of the MG with LVRT curve and GFLs' reference current adjustment; (a) magnitude of the sequence voltage phasors and % VUF at R1 node, (b) measured sequence current components for GFM at R1 node, (c) measured sequence current components for GFM at R18 node, (d) measured sequence current components for GFL at R15 node, (e) measured sequence current components for GFL at R16 node, (f) proportionality constants for reactive current injection in faulty conditions

The subplots (d) and (e) of the above figure show that the measured current components for GFLs are stable in the faulty duration. The active current component in negative sequence (for all the converters) is non-zero to achieve the minimum VUF. The current limits of all the converters are ensured. The response of the GFMs is the natural response of a three-phase voltage source. Even though the LVRT curve is implemented for all the converters, no converter is disconnected in the complete fault duration as the remaining terminal voltage is greater than the minimum voltage for converter's disconnection. The subplot (f) confirms the $|I_n|$ priority as the proportional gains for the negative sequence current injection for the GFLs are greater than the positive sequence proportional gains (k_p). It is important to mention here that the response of the GFMs is according to the natural response of the voltage source converters and they also offered higher (k_n) values in case of unbalanced faults and the same can be achieved by the GFLs with the OAI scheme and the $|I_n|$ priority.

To study the performance of the MG as a single unit with respect to the grid, a balanced fault is applied on the HV side of the transformer T_R at 0.5 seconds for a duration of 1 second. The response of the MG is analyzed at node R_t . To compute the per unit phase current, the total power rating of the MG converters (500 KVA) is considered as the base power. The response of the residential MG at R_t node is given in Figure 6.26.

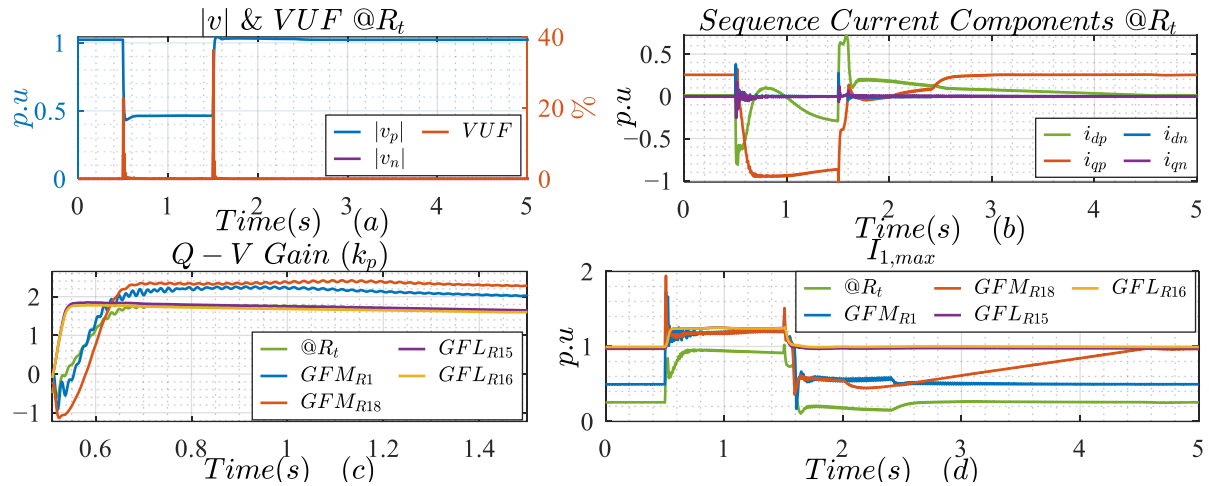


Figure 6.26: Response of the MG as single unit against a balanced fault on grid's side; (a) magnitude of the sequence voltage phasors and %VUF at R_t node, (b) measured sequence current components at R_t node, (c) proportionality constant for reactive current injection in the positive sequence in faulty conditions, (d) maximum measured phase currents at R_t node and of different converters

The above figure shows that the reactive power is fed from grid to the MG in normal conditions and in faulty conditions the reactive power is fed from MG to the grid's side. Due to this reactive power reversal, the direction of the reactive current is changed in subplot (b) in fault duration. The sign of active current in subplot (b) is opposite i.e., its positive sign means the active power flow from grid to the MG and the negative sign confirms the active power reversal. It also shows that reactive current injection is more as compared to the active current injection during the fault and the direction of the current flow is from MG to the grid which is according to the grid code recommendations.

The subplot (c) shows the proportional constant for reactive current injection in case of fault. It confirms that the reactive current injection at the start of the fault is according to the GFMs and eventually it stabilizes according to the GFL's proportional constant for reactive current injection. The subplot (d) shows that in fault duration, all the converters are operating at their current limits but the fault current fed to the fault is lower than the current rating of the MG. This is due to the partial load feeding during the fault as the loads are forcibly connected to the network during this analysis.

From the above discussion, it can be concluded that, as a single unit, the MG fulfills the grid code recommendations in faulty conditions. Moreover, to improve the load service, the LVRT curve of the GFM_{R1} can be changed to ensure the minimum connection time with the grid in case of fault and as the fault persists, it may open the CB between R_t and R_1 and the MG may operate in islanded mode to provide service to its connected loads. For this, the LVRT scheme for the GFM_{R1} is modified and is

activated if the terminal voltage drops below 0.8 p.u. which is still less than the grid code recommended value of 0.9 p.u. Moreover, the minimum connection time is increased with a rate of 3.3 s/p.u. as the terminal voltage is raised which results in longer connection time as compared to the grid code's minimum connection time in case of LVRT conditions. The performance of the MG against HV side balanced fault with duration of 5 seconds is given in Figure 6.27. The fault is introduced at 10.5 seconds.

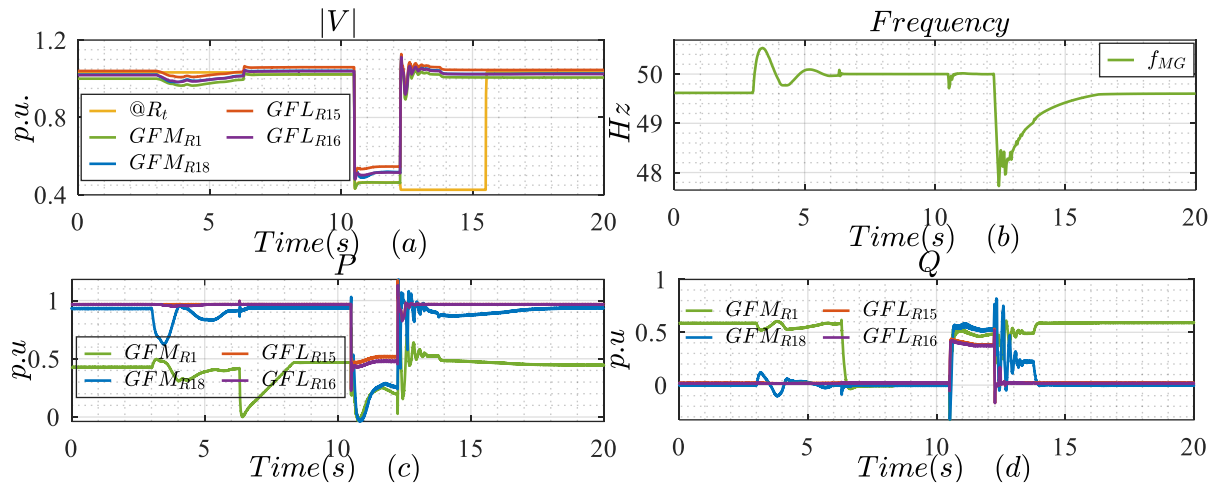


Figure 6.27: Automatic disconnection of the MG in case of a fault on grid's side; (a) magnitude of the sequence voltage phasors at converters' terminals and at R_t , (b) MG's operating frequency, (c) Real power output of connected converters, (d) Reactive power output of connected converters

The above figure shows that the MG is successfully and smoothly disconnected from the grid in case of fault on the HV side. The fault is introduced at 10.5 seconds and lasts till 15.5 seconds. The subplot (a) shows that terminal voltage at R_t experiences a further reduction in terminal voltage at 12.25 seconds and at the same time the terminal voltages at the converters' terminals are restored which is the indication of the loss of connection between the grid and the MG at 12.25 seconds. The same can also be noticed from subplot (b) where the operating frequency of the MG suddenly changes at 12.25 seconds and achieves the steady state value of the islanded MG i.e., the frequency before the grid connection (till three seconds). The sudden dip in frequency at 12.25 seconds can also be explained from the subplot (c) which shows that the real power output needs to be jumped up as the grid's connection is lost which causes some oscillations in the real and reactive output powers. These oscillations remain for just about one and a half second and soon the system achieves its steady state operation. The subplot (d) also shows that the reactive power supply from the GFM_{R1} is reduced to minimum as the MG is synchronized with the grid. This is due to the fact that the voltage is now being stabilized by the grid and in normal conditions the Q-V control of the GFM_{R1} does not inject the reactive power to the system. However, as the grid connection is lost at 12.25 seconds, the reactive power of GFM_{R1} is again stabilized at its previous level.

Thus, from the above analysis, it is confirmed that if the disconnection time for the reference converter is lower, the restoration of the electrical supply can be ensured if the fault is on the grid's side.

6.8 Take Aways from MG's Analysis.

The important conclusions from the above analysis are given below.

- In a fully converter-based MG, the total power capacity of GFMs should be greater than the total power capacity of GFLs and the exact limit also depends on the line impedances involved in the network.
- As far as the location of the converters is concerned in a MG, one limitation is imposed by the SCP at the particular node as the SCR for GFL connection should be greater than 2 and it should be at least 0.5 for GFM connection.
- For smooth initialization of the MG, the loads and converters should be connected to the network in a coordinated way. Even though the decentralized control is used for individual converters and explicit second level controller is not required for the MG, the centralized load management system helps to prioritize the loads and ensures the smooth operation of the MG.
- The voltage sensitivity of the MG can be improved by operating the individual converters in voltage control mode.
- The frequency sensitivity depends on the strength of the network and for the designed residential MG, its frequency sensitivity is much better in islanded mode.
- The large signal stability of the MG depends on several factors i.e., mode of operation, converter-driven stability of GFLs due to PLL, and converter-driven stability of GFM due to angle stability, etc. Largely the response of the GFLs affects the large signal stability of the MG.
- The minimum connection time for the GFLs (according to the LVRT curve) should be less than the CCTs so that no fluctuations in the real/reactive current are experienced.
- Different modes of operation of the GFL in case of unbalanced faults have huge impact on the resulted VUF and the real power oscillations. These effects are more dominant in islanded operation.
- By properly selecting the disconnection time for the converters in case of faults, the reliability and the stability of the remaining network can be enhanced.

7. DISCUSSION AND CONCLUSION

7.1 General Conclusions

With the increased penetration of the renewable energy sources and the market competitiveness for the MGs, the trend of MG is increasing. The fully converter-based MGs are the potential solution for the growing electrical systems. However, without proper design of the MG and careful tuning of the control schemes, the stability of the MG may face serious challenges, and it can pose negative effect on the safety of the individual converters and on the stability of the power system.

The stability of the GFL is highly affected by the SCP at POC, the performance of the PLL and the current component priority. For a weak grid, the impact of current injection by the GFL on the terminal's voltage angle is more which results in unstable response of the PLL. In such conditions, the converter-driven stability of the GFL can be improved by using a slower PLL and defining the critical fault clearing time until than no real/reactive power reversal has resulted due to slower PLL. It is particularly important for the GFLs which can't deal with the real power reversal. A novel GFL scheme is presented in this thesis which ensures the stable response of GFL and offers minimum VUF and real power oscillations in unbalanced conditions.

The GFM converter acts as a voltage source, and it is important to maintain its voltage source behavior in various operating conditions. It provides reference voltage phasor for the GFLs connected in the system. The smooth synchronization of the GFM with the MG is essential for the smooth operation of the network. Moreover, it should stay connected and synchronized in case of frequency drops even after achieving its maximum real power as the disconnection from the network in such conditions may cause further frequency drop. Thus, it is important for the stability of the MG that the GFM, after reaching to its real power limit, should ensure its synchronization with the MG. Some novel modifications in GFM control are proposed in this thesis which help to improve the angle stability in different operating conditions while offering priority injections in faulty conditions. This scheme offers stable response in islanded, and grid connected modes.

The small signal stability of the grid connected MG is of least importance as the grid is mainly responsible for it due to having relatively large inertia and higher grid's strength. On the other hand, both the small and large signal stabilities are important in the islanded operation of the MG. The frequency sensitivity in islanded operation is mainly affected by the droop gains of the GFMs connected in the MG. The voltage sensitivity is a localized parameter and can be largely affected by the reactive power injection mode of the GFLs. Moreover, due to the relatively lower X/R ratios in the LV networks, the coupling of the voltage with the real power can't be ignored. Due to the lower network's strength, the response of the GFLs is critical for the large signal stability of the MG. However, a stable operation

of the MG can be achieved in different operating conditions by carefully selecting the control modes for the converters.

For large signal stability improvement, the reference current adjustment for the GFLs should be based on the islanded/grid-connected mode's operation. This can be easily decided based on the status of the coupling CB if the MG is connected with the external grid as a single point connection. On the MG's level, the VUF and oscillations in real power can be damped to a great proportion if the OAI&MRPF reference current generation scheme is used for the connected GFLs. Additionally, by properly designing the LVRT curve for the reference GFM, the MG can be disconnected from the grid if the fault is on the grid's side and can shorten the loss of service time for the connected loads. Moreover, even though the decentralized control of the MG is quite useful, but the centralized load management system should be designed to prioritize the loads in case of limited available power. It is also useful for the smooth initialization of the MG.

7.2 Specific Conclusions Addressing the Formulated Research Questions

ROI: How to achieve a stable response of GFL, ensuring and maximizing the utility of current limit of the converter and prioritizing certain current components?

For stable GFL operation, true sequence estimation is important in unbalanced conditions, and it can be fairly achieved by using IDSM or SOGI based sequence extraction schemes. Due to the inclusion of negative admittance by PLL in parallel to the network's admittance, a slower PLL should be used in the control of GFL and SCR at POC should be maintained to at least 2. It is important to mention that the SCP (corresponding to large disturbance) of the GFM should be considered for calculating the SCR for the GFL connection. Moreover, due to the limited current handling capability of the converters in faulty conditions, some current components should be prioritized in such conditions to achieve the desired response without exceeding the current limits. Five different priority injection schemes are discussed in this thesis and their comparison is presented to achieve the minimum VUF. For GCR based reference currents, the NQP and $|I_n|$ priority schemes result in minimum VUF. The other important aspect for GFLs is to maximize the utility of its current handling capability especially in case of unbalanced faults. For achieving this, several current limiting schemes are designed in this thesis and their performance comparison is presented. The DSVS scheme results in maximum utilization of the converter's current capacity. Moreover, the true detection of the LVRT conditions is also important for the timely response and based on the definition of LVRT conditions in grid codes, it can be accurately assessed with the help of the magnitude of the positive and negative sequence voltage phasors and the angle between them. Based on this, the SBS offers timely and accurate detection of the LVRT conditions.

RO2: How to enhance the voltage uniformity and minimize real power oscillations in case of unbalanced faults?

Several reference current generation schemes are discussed in this thesis for GFL. A comparative study is presented; proving that the GCR based reference currents don't result in minimum VUF. Moreover, due to the three-phase, three-leg converter's arrangement, it is not possible to achieve simultaneous stable real and reactive power injections in case of unbalanced conditions. They have oscillating term with the double of the fundamental frequency. However, with proper reference current generation, the oscillations of real power can be minimized along with achieving the minimum VUF. In this way, reference currents can be optimized against two objective parameters which not only enhances the degree of uniformity among different phases, but it also minimizes the real power oscillations which may have a negative effect on the nearby connecting GFM. The OAI&MRPF scheme is developed in this thesis to achieve minimum real power oscillations along with minimum VUF in case of unbalanced faults.

RO3: How to design a unified GFM scheme for weak to stiff grid connections ensuring synchronization in fault and post fault conditions?

Some modifications in the conventional GFM scheme are proposed in this thesis to design a unified control scheme for weak to stiff grid connections ensuring the angle stability. The enhanced real power-frequency control offers the ramp power changes for smooth transition, ensures the maximum real power injection in case of frequency dips while ensuring the synchronization, improves the post fault recovery, and ensures the angle stability in different operational phases. Moreover, the enhanced Q-V control offers the controlled and uncontrolled negative sequence reactive power injections in case of unbalanced faults. The controlled negative sequence injection helps to reduce the real power oscillations while the uncontrolled negative sequence injection helps to reduce the voltage unbalance factor. Additionally, several priority injection schemes are designed for the GFM which not only help in limiting the current but also help to achieve the desired response with the limited current handling capability of the converter. However, the desired response is achieved with a certain time delay which is dependent on the speed of the Q-V controls. The initial response of the GFM is still the natural response of a three-phase voltage source.

RO4: What is the impact of different converter's control schemes on the short circuit power?

The classical understanding of SCP is not applicable in a converter-based network. The share of converter in the calculation of SCP is highly dependent on the type of the converter and the actual operating conditions. For small disturbances (current limit of the converter is not reached), the GFM behaves as a high SCP source and may offer 3-6 times higher SCP than its rated power whereas the GFL may have a negative impact on the SCP. Whereas for large disturbances (converter's current limit

is reached), the rated power of GFM can be considered as its SCP and has a positive impact on the SCP calculations of the network whereas the GFL has no noticeable effect on the SCP.

RQ5: What should be the ratio of GFM to GFL based power for stable operation of the MG?

The GFMs mainly define the SCP of the fully converter-based MG at any node whereas the GFL requires a minimum SCR equal to 2 for its stable operation which limits the total GFL's based power in a MG. For a lossless network, the ratio of total GFM to GFL based installed power should be at least one but, in reality, it should be greater than unity (1.5 is considered here) and the sum of GFM and GFL based installed power should be greater than the total expected load.

RQ6: What should be the characteristics of the load management system for the smooth operation of the MG?

A properly designed centralized load management system helps to achieve the stable operation of the MG by connecting/disconnecting loads based on their priority. It also enhances the reliability of the power supply for the priority loads. It should introduce definite time delays between successive connection/dis-connection events, allowing the frequency and voltage of the system to get stable before the next event. It should ensure that the frequency and voltage of the system remain in a defined range and should disconnect the least priority loads if these parameters are not in this range.

7.3 Future Recommendations

The possible future contributions are given below.

- i. The characteristics of the primary energy source should be investigated with the proposed control schemes.
- ii. The reference power for each converter can be defined based on the unit commitment and economic dispatch which largely affects the terminal voltages due to the lower X/R ratio of the lines.
- iii. The presented control schemes should be tested, and response should be verified in hardware in loop testing. Moreover, the delay and error in the measurement should be considered for the design of the centralized load management system.
- iv. A dedicated protection scheme should be designed to enhance the safety of the system against low voltages.

REFERENCES

- [1] "Energy Policy Review," IEA, Paris, 2020. Accessed: 09 October 2024. [Online]. Available: <https://www.iea.org/reports/austria-2020>
- [2] "Renewables 2022 Global Status Report," in "REN21, 2022," REN21 Secretariat, Paris, 2022. Accessed: 09 October 2024. [Online]. Available: https://www.ren21.net/wp-content/uploads/2019/05/GSR2022_Full_Report.pdf
- [3] Z. K. Shuai *et al.*, "Microgrid stability: Classification and a review," (in English), *Renew Sust Energ Rev*, vol. 58, pp. 167-179, May 2016, doi: 10.1016/j.rser.2015.12.201.
- [4] IEA, "Renewables 2023," IEA, Paris, 2023. Accessed: 09 October 2024. [Online]. Available: <https://www.iea.org/reports/renewables-2023>
- [5] J. H. Kueffner, "Wind Hybrid Power System for Antarctica Inmarsat Link," in *INTELEC '86 - International Telecommunications Energy Conference*, 19-22 Oct. 1986 1986, pp. 297-298, doi: 10.1109/INTLEC.1986.4794440.
- [6] K. Jopp, "The future belongs to decentralized electricity grids," (in German), *Brennst Waerme Kraft*, vol. 52, no. 9, p. 21, 2000.
- [7] B. Lasseter, "Microgrids [distributed power generation]," in *2001 IEEE Power Engineering Society Winter Meeting, PES 2001 - Conference Proceedings*, 2001, vol. 1: Institute of Electrical and Electronics Engineers Inc., pp. 146-149, doi: 10.1109/PESW.2001.917020.
- [8] P. M. Costa and M. A. Matos, "Reliability of distribution networks with microgrids," in *2005 IEEE Russia Power Tech, PowerTech*, 2005, doi: 10.1109/PTC.2005.4524611.
- [9] J. A. P. Lopes, C. L. Moreira, and A. G. Madureira, "Defining control strategies for analysing microgrids islanded operation," in *2005 IEEE Russia Power Tech, PowerTech*, 2005, doi: 10.1109/PTC.2005.4524548.
- [10] A. Kwasinski and P. T. Krein, "A microgrid-based telecom power system using modular multiple-input DC-DC converters," in *INTELEC, International Telecommunications Energy Conference (Proceedings)*, 2005, pp. 515-520, doi: 10.1109/INTLEC.2005.335152.
- [11] A. P. Agalgaonkar, C. V. Dobariya, M. G. Kanabar, S. A. Khaparde, and S. V. Kulkarni, "Optimal sizing of distributed generators in MicroGrid," in *2006 IEEE Power India Conference*, 2005, vol. 2005, pp. 901-908, doi: 10.1109/POWERI.2006.1632627.
- [12] J. A. Peças Lopes *et al.*, "Control strategies for MicroGrids emergency operation," in *2005 International Conference on Future Power Systems*, 2005, vol. 2005, doi: 10.1109/FPS.2005.204226.
- [13] "Microgrid Market Size, Share, and Trends 2024 to 2033," Precedence Research, 2023. Accessed: 09 October 2024. [Online]. Available: <https://www.precedenceresearch.com/microgrid-market>
- [14] "Market size of microgrids worldwide from 2017 to 2021, with a forecast from 2022 to 2028 (in billion U.S. dollars)." Precision Business Insights. <https://www.statista.com/statistics/1313998/global-microgrid-market-size/> (accessed 09 October 2024).
- [15] "U.S. Department of Energy Combined Heat and Power and Microgrid Installation Databases." <https://doe.icfwebservices.com/downloads/microgrid> (accessed 09 October 2024).
- [16] C. Marnay *et al.*, "Microgrid Evolution Roadmap," in *2015 International Symposium on Smart Electric Distribution Systems and Technologies (EDST)*, 8-11 Sept. 2015 2015, pp. 139-144, doi: 10.1109/SEDST.2015.7315197. [Online]. Available: <https://ieeexplore.ieee.org/document/7315197/>
- [17] "IEEE Standard for the Specification of Microgrid Controllers," *IEEE Std 2030.7-2017*, pp. 1-43, 2018, doi: 10.1109/ieeestd.2018.8340204.
- [18] M. Uddin, H. Mo, D. Dong, S. Elsayah, J. Zhu, and J. M. Guerrero, "Microgrids: A review, outstanding issues and future trends," *Energy Strategy Reviews*, vol. 49, 2023/09/01/ 2023, doi: 10.1016/j.esr.2023.101127.
- [19] G. Shahgholian, "A brief review on microgrids: Operation, applications, modeling, and control," *Int T Electr Energy*, vol. 31, no. 6, p. e12885, 2021/06/01 2021, doi: 10.1002/2050-7038.12885.
- [20] D. W. Gao, "Applications of ESS in Renewable Energy Microgrids," in *Energy Storage for Sustainable Microgrid*, D. W. Gao Ed. Oxford: Academic Press, 2015, pp. 35-77.
- [21] D. E. Olivares *et al.*, "Trends in Microgrid Control," (in English), *IEEE Transactions on Smart Grid*, vol. 5, no. 4, pp. 1905-1919, Jul 2014, doi: 10.1109/tsg.2013.2295514.
- [22] B. Mitra *et al.*, *Development and Role of Microgrids Surrounding Modernized Irrigation District*. 2020.
- [23] S. Shahzad, M. A. Abbasi, H. Ali, M. Iqbal, R. Munir, and H. Kilic, "Possibilities, Challenges, and Future Opportunities of Microgrids: A Review," *Sustainability*, vol. 15, no. 8, doi: 10.3390/su15086366.
- [24] K. A. Skeen and G. K. Venayagamoorthy, "Network of Microgrids: Opportunities and Challenges," in *2023 IEEE PES Grid Edge Technologies Conference & Exposition (Grid Edge)*, 10-13 April 2023 2023, pp. 1-5, doi: 10.1109/GridEdge54130.2023.10102727. [Online]. Available: <https://ieeexplore.ieee.org/document/10102727/>

- [25] A. Hirsch, Y. Parag, and J. Guerrero, "Microgrids: A review of technologies, key drivers, and outstanding issues," *Renewable and Sustainable Energy Reviews*, vol. 90, pp. 402-411, 2018/07/01/ 2018, doi: 10.1016/j.rser.2018.03.040.
- [26] F. Sioshansi, "The evolution of California's variable renewable generation," in *Variable Generation, Flexible Demand*, F. Sioshansi Ed.: Academic Press, 2021, pp. 3-24.
- [27] V. Motjoadi, M. G. Kilimi, P. N. Bokoro, and K. Roro, "On the review of microgrid systems: benefits, control techniques, and risk analysis," in *2021 IEEE AFRICON*, 13-15 Sept. 2021 2021, pp. 1-7, doi: 10.1109/AFRICON51333.2021.9570935. [Online]. Available: <https://ieeexplore.ieee.org/document/9570935/>
- [28] V. Saravanan, K. M. Venkatachalam, M. Arumugam, M. A. K. Borelessa, and K. T. M. U. Hemapala, "Overview of microgrid systems," *International Journal of Advances in Applied Sciences*, vol. 10, no. 4, 2021, doi: 10.11591/ijaas.v10.i4.pp378-391.
- [29] E. Espina, J. Llanos, C. Burgos-Mellado, R. Cardenas-Dobson, M. Martinez-Gomez, and D. Saez, "Distributed Control Strategies for Microgrids: An Overview," *Ieee Access*, vol. 8, pp. 193412-193448, 2020, doi: 10.1109/access.2020.3032378.
- [30] N. Singh, I. Elamvazuthi, P. Nallagownden, G. Ramasamy, and A. Jangra, "Routing Based Multi-Agent System for Network Reliability in the Smart Microgrid," *Sensors*, vol. 20, no. 10, doi: 10.3390/s20102992.
- [31] L. He, S. Zhang, Y. Chen, L. Ren, and J. Li, "Techno-economic potential of a renewable energy-based microgrid system for a sustainable large-scale residential community in Beijing, China," *Renewable and Sustainable Energy Reviews*, vol. 93, pp. 631-641, 2018/10/01/ 2018, doi: 10.1016/j.rser.2018.05.053.
- [32] E. Unamuno and J. A. Barrena, "Hybrid ac/dc microgrids—Part I: Review and classification of topologies," *Renewable and Sustainable Energy Reviews*, vol. 52, pp. 1251-1259, 2015/12/01/ 2015, doi: 10.1016/j.rser.2015.07.194.
- [33] S. Charadi, Y. Chaibi, A. Redouane, A. Allouhi, A. El Hasnaoui, and H. Mahmoudi, "Efficiency and energy-loss analysis for hybrid AC / DC distribution systems and microgrids: A review," (in English), *Int T Electr Energy*, Review vol. 31, no. 12, 2021, Art no. e13203, doi: 10.1002/2050-7038.13203.
- [34] M. Saleh, Y. Esa, M. E. Hariri, and A. Mohamed, "Impact of Information and Communication Technology Limitations on Microgrid Operation," *Energies*, vol. 12, no. 15, doi: 10.3390/en12152926.
- [35] A. Mohammed, S. S. Refaat, S. Bayhan, and H. Abu-Rub, "AC Microgrid Control and Management Strategies: Evaluation and Review," (in English), *IEEE Power Electron. Mag.*, Review vol. 6, no. 2, pp. 18-31, 2019, Art no. 8739061, doi: 10.1109/mpel.2019.2910292.
- [36] G. San, W. Zhang, X. Guo, C. Hua, H. Xin, and F. Blaabjerg, "Large-disturbance stability for power-converter-dominated microgrid: A review," *Renewable and Sustainable Energy Reviews*, vol. 127, 2020/07/01/ 2020, doi: 10.1016/j.rser.2020.109859.
- [37] D. K. J. S. Jayamaha, N. W. A. Lidula, and A. D. Rajapakse, "Protection and grounding methods in DC microgrids: Comprehensive review and analysis," *Renewable and Sustainable Energy Reviews*, vol. 120, 2020/03/01/ 2020, doi: 10.1016/j.rser.2019.109631.
- [38] M. Farrokhhabadi *et al.*, "Microgrid Stability Definitions, Analysis, and Examples," *IEEE Transactions on Power Systems*, vol. 35, no. 1, pp. 13-29, 2020, doi: 10.1109/tpwrs.2019.2925703.
- [39] P. Kundur *et al.*, "Definition and Classification of Power System Stability IEEE/CIGRE Joint Task Force on Stability Terms and Definitions," (in English), *IEEE Transactions on Power Systems*, Article vol. 19, no. 3, pp. 1387-1401, 2004, doi: 10.1109/tpwrs.2004.825981.
- [40] N. Hatziargyriou *et al.*, *Stability Definitions and Characterization of Dynamic Behavior in Systems with High Penetration of Power Electronic Interfaced Technologies*. 2020.
- [41] N. Hatziargyriou *et al.*, "Definition and Classification of Power System Stability – Revisited & Extended," *IEEE Transactions on Power Systems*, vol. 36, no. 4, pp. 3271-3281, 2021, doi: 10.1109/tpwrs.2020.3041774.
- [42] L. Herrera, E. Inoa, F. Guo, J. Wang, and H. Tang, "Small-Signal Modeling and Networked Control of a PHEV Charging Facility," *IEEE Transactions on Industry Applications*, vol. 50, no. 2, pp. 1121-1130, 2014, doi: 10.1109/tia.2013.2272912.
- [43] M. A. Aboushal and M. M. Z. Moustafa, "A new unified control strategy for inverter-based micro-grid using hybrid droop scheme," *Alexandria Engineering Journal*, vol. 58, no. 4, pp. 1229-1245, 2019/12/01/ 2019, doi: 10.1016/j.aej.2019.10.006.
- [44] R. Majumder, B. Chaudhuri, A. Ghosh, R. Majumder, G. Ledwich, and F. Zare, "Improvement of stability and load sharing in an autonomous microgrid using supplementary droop control loop," in *IEEE PES General Meeting*, 25-29 July 2010 2010, pp. 1-1, doi: 10.1109/PES.2010.5589665. [Online]. Available: <https://ieeexplore.ieee.org/document/5589665/>

- [45] S. Eberlein and K. Rudion, "Small-signal stability modelling, sensitivity analysis and optimization of droop controlled inverters in LV microgrids," (in English), *Int J Elec Power*, vol. 125, 2021, doi: 10.1016/j.ijepes.2020.106404.
- [46] L. L. Yuan, A. Krishnan, and F. Y. S. Eddy, "Design of a Droop Control Scheme for Programmable Sources in a Microgrid Testbed," *IFAC-PapersOnLine*, vol. 51, no. 28, pp. 714-719, 2018/01/01/ 2018, doi: 10.1016/j.ifacol.2018.11.789.
- [47] M. Zhu, H. Li, and X. Li, "Improved state-space model and analysis of islanding inverter-based microgrid," in *2013 IEEE International Symposium on Industrial Electronics*, 28-31 May 2013 2013, pp. 1-5, doi: 10.1109/ISIE.2013.6563600. [Online]. Available: <https://ieeexplore.ieee.org/document/6563600/>
- [48] C. N. Rowe, T. J. Summers, R. E. Betz, D. J. Cornforth, and T. G. Moore, "Arctan Power-Frequency Droop for Improved Microgrid Stability," *Ieee T Power Electr*, vol. 28, no. 8, pp. 3747-3759, 2013, doi: 10.1109/tpel.2012.2230190.
- [49] N. Soni, S. Doolla, and M. C. Chandorkar, "Improvement of Transient Response in Microgrids Using Virtual Inertia," *IEEE Transactions on Power Delivery*, vol. 28, no. 3, pp. 1830-1838, 2013, doi: 10.1109/tpwr.2013.2264738.
- [50] M. N. Ambia, A. Al-Durra, C. Caruana, and S. M. Mueeen, "Stability enhancement of a hybrid microgrid system in grid fault condition," in *2012 15th International Conference on Electrical Machines and Systems (ICEMS)*, 21-24 Oct. 2012 2012, pp. 1-6.
- [51] A. Karimi *et al.*, "Inertia Response Improvement in AC Microgrids: A Fuzzy-Based Virtual Synchronous Generator Control," *Ieee T Power Electr*, vol. 35, no. 4, pp. 4321-4331, 2020, doi: 10.1109/tpel.2019.2937397.
- [52] G. F. Silva, A. Donaire, M. M. Seron, A. McFadyen, and J. Ford, "String Stability in Microgrids Using Frequency Controlled Inverter Chains," *IEEE Control Systems Letters*, vol. 6, pp. 1484-1489, 2022, doi: 10.1109/lcsys.2021.3114143.
- [53] F. Zheng, C. Deng, L. Chen, S. Li, Y. Liu, and Y. Liao, "Transient Performance Improvement of Microgrid by a Resistive Superconducting Fault Current Limiter," (in English), *IEEE Transactions on Applied Superconductivity*, vol. 25, no. 3, pp. 1-5, Jun 2015, doi: 10.1109/tasc.2015.2391120.
- [54] D. B. Rathnayake *et al.*, "Grid Forming Inverter Modeling, Control, and Applications," *Ieee Access*, vol. 9, pp. 114781-114807, 2021, doi: 10.1109/ACCESS.2021.3104617.
- [55] Y. Li, Y. Gu, and T. C. Green, "Revisiting Grid-Forming and Grid-Following Inverters: A Duality Theory," *IEEE Transactions on Power Systems*, vol. 37, no. 6, pp. 4541-4554, 2022, doi: 10.1109/tpwrs.2022.3151851.
- [56] Y. Lin *et al.*, "Research Roadmap on Grid-Forming Inverters," United States, 2020-11-11 2020. Accessed: 09 October 2024. [Online]. Available: <https://www.nrel.gov/docs/fy21osti/73476.pdf>
- [57] R. Aboelsaud, A. Ibrahim, and A. G. Garganeev, "Review of three-phase inverters control for unbalanced load compensation," *International Journal of Power Electronics and Drive Systems (IJPEDS)*, vol. 10, no. 1, 03/01 2019, doi: 10.11591/ijpeds.v10.i1.pp242-255.
- [58] J. Rocabert, A. Luna, F. Blaabjerg, and P. Rodríguez, "Control of Power Converters in AC Microgrids," *Ieee T Power Electr*, vol. 27, no. 11, pp. 4734-4749, 2012, doi: 10.1109/tpel.2012.2199334.
- [59] P. Hackl, Z. Zhang, and R. Schuerhuber, "Unsymmetrical fault behavior of PLL based grid-connected converters," in *2022 24th European Conference on Power Electronics and Applications (EPE'22 ECCE Europe)*, 5-9 Sept. 2022 2022, pp. 1-10.
- [60] Y. Zhao, A. An, Y. Xu, Q. Wang, and M. Wang, "Model predictive control of grid-connected PV power generation system considering optimal MPPT control of PV modules," *Protection and Control of Modern Power Systems*, vol. 6, no. 1, p. 32, 2021/10/14 2021, doi: 10.1186/s41601-021-00210-1.
- [61] P. Sorensen, J. Fortmann, F. Jiménez Búendía, J. Bech, A. Morales, and C. Ivanov, *Final Draft International Standard IEC 61400-27-1: Electrical simulation models of wind turbines*. 2014.
- [62] K. Yamashita *et al.*, *Modelling of inverter-based generation for power system dynamic studies*. 2018.
- [63] S. Martín-Martínez, E. Gómez-Lázaro, A. Molina-García, A. Viguera-Rodríguez, M. Milligan, and E. Muljadi, "Participation of wind power plants in the Spanish power system during events," in *2012 IEEE Power and Energy Society General Meeting*, 22-26 July 2012 2012, pp. 1-8, doi: 10.1109/PESGM.2012.6345017. [Online]. Available: <https://ieeexplore.ieee.org/document/6345017/>
- [64] M. H. J. Bollen, IEEE Industry Applications Society., IEEE Power Electronics Society., and IEEE Power Engineering Society., *Understanding power quality problems : voltage sags and interruptions* (IEEE Press series on power engineering). New York: IEEE Press, 2000, pp. xvii, 543 p.
- [65] J. Pinto, A. Carvalho, A. Rocha, and A. Araújo, "Comparison of DSOGI-Based PLL for Phase Estimation in Three-Phase Weak Grids," (in English), *Electricity*, vol. 2, no. 3, pp. 244-270, Sep 2021, doi: 10.3390/electricity2030015.

- [66] J. Svensson, M. Bongiorno, and A. Sannino, "Practical Implementation of Delayed Signal Cancellation Method for Phase-Sequence Separation," *IEEE Transactions on Power Delivery*, vol. 22, no. 1, pp. 18-26, 2007, doi: 10.1109/tpwr.2006.881469.
- [67] J. A. L. Ghijselen and A. P. M. VandenBossche, "Exact Voltage Unbalance Assessment Without Phase Measurements," *IEEE Transactions on Power Systems*, vol. 20, no. 1, pp. 519-520, 2005, doi: 10.1109/tpwrs.2004.841145.
- [68] A. Meligy, T. Qoria, and I. Colak, "Assessment of Sequence Extraction Methods Applied to MMC-SDBC STATCOM Under Distorted Grid Conditions," *IEEE Transactions on Power Delivery*, vol. 37, no. 6, pp. 4923-4932, 2022, doi: 10.1109/tpwr.2022.3162959.
- [69] L. Du, L. Xiong, M. Li, Z. Tang, L. Xiu, and X. Ma, "Fast positive sequence component detection schemes based on delay operational period filter," *Csee J Power Energy*, pp. 1-8, 2020, doi: 10.17775/cseejpes.2019.02810.
- [70] "Technical Requirements for the Connection and Operation of Customer Installations to the Medium-Voltage Network," VDE-AR-N 4110;VDE: Frankfurt, Germany, 2018. Accessed: 09 October 2024. [Online]. Available: <https://www.vde.com/en/fnn/topics/technical-connection-rules/tcr-for-medium-voltage>
- [71] M. Graungaard Taul, X. Wang, P. Davari, and F. Blaabjerg, "Current Reference Generation Based on Next-Generation Grid Code Requirements of Grid-Tied Converters During Asymmetrical Faults," *Ieee J Em Sel Top P*, vol. 8, no. 4, pp. 3784-3797, 2020, doi: 10.1109/jestpe.2019.2931726.
- [72] M. M. Shabestary and Y. A.-R. I. Mohamed, "Asymmetrical Ride-Through and Grid Support in Converter-Interfaced DG Units Under Unbalanced Conditions," *Ieee T Ind Electron*, vol. 66, no. 2, pp. 1130-1141, 2019, doi: 10.1109/tie.2018.2835371.
- [73] A. Camacho, M. Castilla, J. Miret, A. Borrell, and L. G. de Vicuna, "Active and Reactive Power Strategies With Peak Current Limitation for Distributed Generation Inverters During Unbalanced Grid Faults," *Ieee T Ind Electron*, vol. 62, no. 3, pp. 1515-1525, 2015, doi: 10.1109/tie.2014.2347266.
- [74] M. B. Shamsheh, R. Inzunza, I. Fukasawa, T. Tanaka, and T. Ambo, "Grid Support During Asymmetrical Faults using Negative Sequence Current Injection," in *2019 IEEE 4th International Future Energy Electronics Conference (IFEEEC)*, 25-28 Nov. 2019 2019, pp. 1-6, doi: 10.1109/IFEEEC47410.2019.9015036. [Online]. Available: <https://ieeexplore.ieee.org/document/9015036/>
- [75] A. Camacho, M. Castilla, J. Miret, M. Velasco, and R. Guzman, "Positive-Sequence Voltage Control, Full Negative-Sequence Cancellation, and Current Limitation for Static Compensators," *Ieee J Em Sel Top P*, vol. 9, no. 6, pp. 6613-6623, 2021, doi: 10.1109/jestpe.2021.3066681.
- [76] A. Moawwad, M. S. El Moursi, and W. Xiao, "A Novel Transient Control Strategy for VSC-HVDC Connecting Offshore Wind Power Plant," *Ieee T Sustain Energ*, vol. 5, no. 4, pp. 1056-1069, 2014, doi: 10.1109/tste.2014.2325951.
- [77] A. Moawwad, M. E. Moursi, and X. Weidong, "A novel transient control strategy for VSC-HVDC connecting offshore wind power plant," in *2015 IEEE Power & Energy Society General Meeting*, 26-30 July 2015 2015, pp. 1-1, doi: 10.1109/PESGM.2015.7285804. [Online]. Available: <https://ieeexplore.ieee.org/document/7285804/>
- [78] G. M. S. Azevedo, J. Rocabert, M. C. Cavalcanti, F. A. S. Neves, and P. Rodriguez, "A Negative-sequence Current Injection Method to Mitigate Voltage Imbalances in Microgrids," *Eletrônica de Potência*, vol. 16, no. 4, pp. 296-303, 11/01 2011, doi: 10.18618/rep.20114.296303.
- [79] V. A. F. Almeida, G. N. Taranto, and J. M. T. Marinho, "Phasor-domain Dynamic Model of Asymmetric Current Injection Controller for Converter-interfaced Generator," *Journal of Modern Power Systems and Clean Energy*, vol. 9, no. 6, pp. 1269-1278, 2021, doi: 10.35833/mpce.2021.000407.
- [80] M. T. Villén, M. P. Comech, E. Martinez Carrasco, and A. A. Prada Hurtado, "Influence of Negative Sequence Injection Strategies on Faulted Phase Selector Performance," *Energies*, vol. 15, no. 16, doi: 10.3390/en15166018.
- [81] X. Li, Z. Wang, L. Zhu, L. Guo, and C. Wang, "Analytical Dual-Sequence Current Injections Feasible Region of Weak-Grid Connected VSC Under Asymmetric Grid Faults," *IEEE Transactions on Power Systems*, vol. 38, no. 6, pp. 5546-5559, 2023, doi: 10.1109/tpwrs.2022.3226560.
- [82] J. Jundi, Y. Guangya, and A. H. Nielsen, "Investigation of grid-connected voltage source converter performance under unbalanced faults," in *2016 IEEE PES Asia-Pacific Power and Energy Engineering Conference (APPEEC)*, 25-28 Oct. 2016 2016, pp. 609-613, doi: 10.1109/APPEEC.2016.7779576. [Online]. Available: <https://ieeexplore.ieee.org/document/7779576/>
- [83] L. Wang *et al.*, "Research on Ride-Through Control of Power Conversion System in Energy Storage Converter Under Unbalanced Grid Voltage Fault Condition," in *2022 China International Conference on Electricity Distribution (CICED)*, 7-8 Sept. 2022 2022, pp. 925-929, doi:

- 10.1109/CICED56215.2022.9929038. [Online]. Available: <https://ieeexplore.ieee.org/document/9929038/>
- [84] H. Wang, Y. Liu, and N. R. Watson, "Enhanced Grid-tie Converter Control Under Unbalanced Conditions with no PLL," in *2022 7th IEEE Workshop on the Electronic Grid (eGRID)*, 29 Nov.-2 Dec. 2022, pp. 1-5, doi: 10.1109/eGRID57376.2022.9990009. [Online]. Available: <https://ieeexplore.ieee.org/document/9990009/>
- [85] S. Pal, M. Mishra, A. Verma, P. R. Kasari, B. Das, and A. Chakraborti, "Control of Grid Connected Converters Under Unbalanced Grid Faults," in *2018 IEEE International Conference on Power Electronics, Drives and Energy Systems (PEDES)*, 18-21 Dec. 2018, pp. 1-6, doi: 10.1109/PEDES.2018.8707567. [Online]. Available: <https://ieeexplore.ieee.org/document/8707567/>
- [86] R. Rosso, X. Wang, M. Liserre, X. Lu, and S. Engelken, "Grid-Forming Converters: Control Approaches, Grid-Synchronization, and Future Trends—A Review," *IEEE Open Journal of Industry Applications*, vol. 2, pp. 93-109, 2021, doi: 10.1109/ojia.2021.3074028.
- [87] D. Pattabiraman, R. H. Lasseter, and T. M. Jahns, "Impact of Phase-Locked Loop Control on the Stability of a High Inverter Penetration Power System," in *2019 IEEE Power & Energy Society General Meeting (PESGM)*, 4-8 Aug. 2019, pp. 1-5, doi: 10.1109/PESGM40551.2019.8973657. [Online]. Available: <https://ieeexplore.ieee.org/document/8973657/>
- [88] U. Markovic, O. Stanojev, P. Aristidou, E. Vrettos, D. Callaway, and G. Hug, "Understanding Small-Signal Stability of Low-Inertia Systems," *IEEE Transactions on Power Systems*, vol. 36, no. 5, pp. 3997-4017, 2021, doi: 10.1109/tpwrs.2021.3061434.
- [89] B. Fan, T. Liu, F. Zhao, H. Wu, and X. Wang, "A Review of Current-Limiting Control of Grid-Forming Inverters Under Symmetrical Disturbances," *IEEE Open Journal of Power Electronics*, vol. 3, pp. 955-969, 2022, doi: 10.1109/ojpe.2022.3227507.
- [90] J. Hu, Y. Chi, X. Tian, Y. Li, Y. Xiao, and F. Cheng, "A survey on development and prospect of wind turbines virtual synchronous control technology," *Energy Reports*, vol. 8, pp. 75-83, 2022/04/01/ 2022, doi: 10.1016/j.egyr.2021.11.005.
- [91] Q.-C. Zhong and G. Weiss, "Synchronverters: Inverters That Mimic Synchronous Generators," *Ieee T Ind Electron*, vol. 58, no. 4, pp. 1259-1267, 2011, doi: 10.1109/tie.2010.2048839.
- [92] S. Yazdani, M. Ferdowsi, M. Davari, and P. Shamsi, "Advanced Current-Limiting and Power-Sharing Control in a PV-Based Grid-Forming Inverter Under Unbalanced Grid Conditions," *Ieee J Em Sel Top P*, vol. 8, no. 2, pp. 1084-1096, 2020, doi: 10.1109/JESTPE.2019.2959006.
- [93] N. Baeckeland, D. Venkatramanan, M. Kleemann, and S. Dhople, "Stationary-Frame Grid-Forming Inverter Control Architectures for Unbalanced Fault-Current Limiting," *IEEE Transactions on Energy Conversion*, vol. 37, no. 4, pp. 2813-2825, 2022, doi: 10.1109/TEC.2022.3203656.
- [94] L.-Y. Lu and C.-C. Chu, "Consensus-Based Secondary Frequency and Voltage Droop Control of Virtual Synchronous Generators for Isolated AC Micro-Grids," *Ieee J Em Sel Top C*, vol. 5, no. 3, pp. 443-455, 2015, doi: 10.1109/jetcas.2015.2462093.
- [95] S. M. Ashabani and Y. A.-R. I. Mohamed, "General Interface for Power Management of Micro-Grids Using Nonlinear Cooperative Droop Control," *IEEE Transactions on Power Systems*, vol. 28, no. 3, pp. 2929-2941, 2013, doi: 10.1109/tpwrs.2013.2254729.
- [96] W. Schulze, P. Weber, M. Suriyah, and T. Leibfried, "Grid-forming synchronverter-based control method with current limiting method for grid-side converters of converter-based generation plants," in *21st Wind & Solar Integration Workshop (WIW 2022)*, 12-14 Oct. 22 2022, vol. 2022, pp. 394-401, doi: 10.1049/icp.2022.2802.
- [97] Z. Qing-Chang, N. Phi-Long, M. Zhenyu, and S. Wanxing, "Self-Synchronized Synchronverters: Inverters Without a Dedicated Synchronization Unit," *Ieee T Power Electr*, vol. 29, no. 2, pp. 617-630, 2014, doi: 10.1109/tpe.2013.2258684.
- [98] J. M. Ramirez, E. T. Montalvo, and C. I. Nuño, "Modelling, synchronisation, and implementation of the virtual synchronous generator: a study of its reactive power handling," *Electrical Engineering*, vol. 102, no. 3, pp. 1605-1619, 2020/09/01 2020, doi: 10.1007/s00202-020-00980-1.
- [99] A. P. Asensio, S. A. Gomez, J. L. Rodriguez-Amenedo, and M. A. Cardiel-Alvarez, "Reactive Power Synchronization Method for Voltage-Sourced Converters," *Ieee T Sustain Energ*, vol. 10, no. 3, pp. 1430-1438, 2019, doi: 10.1109/tste.2019.2911453.
- [100] R. Rosso, S. Engelken, and M. Liserre, "On The Implementation of an FRT Strategy for Grid-Forming Converters Under Symmetrical and Asymmetrical Grid Faults," *IEEE Transactions on Industry Applications*, vol. 57, no. 5, pp. 4385-4397, 2021, doi: 10.1109/tia.2021.3095025.
- [101] K. P. Schneider *et al.*, "Analytic Considerations and Design Basis for the IEEE Distribution Test Feeders," *IEEE Transactions on Power Systems*, vol. 33, no. 3, pp. 3181-3188, 2018, doi: 10.1109/TPWRS.2017.2760011.

- [102] K. Strunz, E. Abbasi, R. Fletcher, N. Hatziaargyriou, R. Iravani, and G. Joos, *TF C6.04.02: TB 575-Benchmark Systems for Network Integration of Renewable and Distributed Energy Resources*. 2014.
- [103] A. Traupmann and T. Kienberger, "Test Grids for the Integration of RES—A Contribution for the European Context," *Energies*, vol. 13, no. 20, 2020, doi: 10.3390/en13205431.
- [104] N. Mwakabuta and A. Sekar, "Comparative Study of the IEEE 34 Node Test Feeder under Practical Simplifications," in *2007 39th North American Power Symposium*, 30 Sept.-2 Oct. 2007 2007, pp. 484-491, doi: 10.1109/NAPS.2007.4402354. [Online]. Available: <https://ieeexplore.ieee.org/document/4402354/>
- [105] A. J. O. Owuor, J. L. Munda, and A. A. Jimoh, "The IEEE 34 node radial test feeder as a simulation testbench for Distributed Generation," in *IEEE Africon '11*, 13-15 Sept. 2011 2011, pp. 1-6, doi: 10.1109/AFRCON.2011.6072095. [Online]. Available: <https://ieeexplore.ieee.org/document/6072095/>
- [106] S. Hasan, Suherman, D. P. Saragi, Y. Siregar, and M. Al-Akaidi, "The LCL filter design for three phase DC-AC voltage converter," *Journal of Physics: Conference Series*, vol. 1783, no. 1, 2021/02/01 2021, doi: 10.1088/1742-6596/1783/1/012067.
- [107] M. B. Said-Romdhane, M. W. Naouar, I. S. Belkhdja, and E. Monmasson, "An Improved LCL Filter Design in Order to Ensure Stability without Damping and Despite Large Grid Impedance Variations," *Energies*, vol. 10, no. 3, doi: 10.3390/en10030336.
- [108] L. F. Wu and C. Z. Zhang, "Research on LCL filter considering grid impedance," *IOP Conference Series: Earth and Environmental Science*, vol. 354, no. 1, 2019/10/01 2019, doi: 10.1088/1755-1315/354/1/012098.
- [109] I. Chtouki, M. Zazi, M. Feddi, and M. Rayyam, "LCL filter with passive damping for PV system connected to the network," in *2016 International Renewable and Sustainable Energy Conference (IRSEC)*, 14-17 Nov. 2016 2016, pp. 692-697, doi: 10.1109/IRSEC.2016.7984020. [Online]. Available: <https://ieeexplore.ieee.org/document/7984020/>
- [110] C. J. O'Rourke, M. M. Qasim, M. R. Overlin, and J. L. Kirtley, "A Geometric Interpretation of Reference Frames and Transformations: dq0, Clarke, and Park," *IEEE Transactions on Energy Conversion*, vol. 34, no. 4, pp. 2070-2083, 2019, doi: 10.1109/tec.2019.2941175.
- [111] P. Salmerón Revuelta, S. Pérez Litrán, and J. Prieto Thomas, "Instantaneous Reactive Power Theory," in *Active Power Line Conditioners*, P. Salmerón Revuelta, S. Pérez Litrán, and J. Prieto Thomas Eds. San Diego: Academic Press, 2016, pp. 51-105.
- [112] P. Bansal, S. Dixit, S. Gupta, M. A. Alotaibi, H. Malik, and F. Pedro García Márquez, "A robust modified notch filter based SOGI-PLL approach to control multilevel inverter under distorted grid," *Ain Shams Engineering Journal*, vol. 15, no. 5, 2024/05/01/ 2024, doi: 10.1016/j.asej.2024.102675.
- [113] M. Abubakar, H. Akbari, and H. Renner, "Development of Reference Current Calculation Scheme for Grid-Side Converter during Unbalanced Faults," in *2022 Second International Conference on Sustainable Mobility Applications, Renewables and Technology (SMART)*, 23-25 Nov. 2022 2022, pp. 1-9, doi: 10.1109/SMART55236.2022.9990338. [Online]. Available: <https://ieeexplore.ieee.org/document/9990338/>
- [114] M. Abubakar, P. Hackl, H. Renner, and R. Schürhuber, "Investigation of Optimal Share of Active and Reactive Current Injection in Negative Sequence in Case of Unbalanced Faults in Grid Following Converter," presented at the Cigre B4 Colloquium 2023, Vienna, Austria, 2023. [Online]. Available: <https://www.e-cigre.org/publications/detail/coll-vie-2023-colloquium-vienna-2023.html>
- [115] M. Abubakar, H. Renner, and R. Schürhuber, "Development of a Novel Control Scheme for Grid-Following Converter under Asymmetrical Faults," *Energies*, vol. 16, no. 3, 2023, doi: 10.3390/en16031276.
- [116] M. Abubakar, H. Renner, and R. Schürhuber, "Development of a Novel Control Scheme to Achieve the Minimum Unbalance Factor and Real Power Fluctuations under Asymmetrical Faults," *Energies*, vol. 16, no. 22, doi: 10.3390/en16227511.
- [117] B. Bahrani, "Power-Synchronized Grid-Following Inverter Without a Phase-Locked Loop," *Ieee Access*, vol. 9, pp. 112163-112176, 08/05 2021, doi: 10.1109/access.2021.3102631.
- [118] ACER. "NC RfG DC Recommendation: Annex 1 – Amended RfG Regulation." European Union Agency for the Cooperation of Energy Regulators. https://www.acer.europa.eu/sites/default/files/documents/Recommendations_annex/ACER_Recommendation_03-2023_Annex_1_NC_RfG_clean.pdf (accessed 9 Sep. 2024).
- [119] A. Emadi and M. Ehsani, "Multi-converter power electronic systems: definition and applications," in *2001 IEEE 32nd Annual Power Electronics Specialists Conference (IEEE Cat. No.01CH37230)*, 17-21 June 2001 2001, vol. 2, pp. 1230-1236 vol.2, doi: 10.1109/PESC.2001.954287. [Online]. Available: <https://ieeexplore.ieee.org/document/954287/>
- [120] CIGRÉ, "Connection of Wind Farms to Weak AC Networks," CIGRÉ, 9782858733743, 2016. [Online]. Available: <https://books.google.at/books?id=g32uswEACAAJ>

APPENDICES

A. DATA FOR GENERIC EUROPEAN NETWORK

Appendix Table A.1: Summary of generic European network

	Lower Half	Upper Half	Total
Total effective length (m)	2763.76	3011.68	5775.44
Total real load (kW)	247.22	257.26	504.48
Total reactive load (kVAR)	50.21	52.24	102.45
Total generation (kW)	132.8	121.2	254



For total values of a distributor

For total values of a sub-distributor

For common elements in a distributor/sub-distributor

Appendix Table A.2: Details of generic European network

Line	From	To	Length (m)	R,X (Ω /km)	Node	Load (kW, kVar)		Gen (kW, kVar)					
						P (kW)	Q (kVar)	P	Q				
T01	K00	K01	0(Trans)					630 kVA					
L12	K01	K02	73.12	0.167, 0.08	K02	6.11	1.24			Distributor# 1			
L23	K02	K03	28.27		K03	5.55	1.13	4.5	0				
L34	K03	K04	33.07		K04								
L45	K04	K05	76.38		K05	4.87	0.99						
Dis.1 L			210.84		Dis.1 Total	22.08	4.49	4.5	0				
L16	K01	K06	57.56	0.167, 0.08	K06	7.6	1.54	10.4	0	Distributor# 2			
L67	K06	K07	73.94		K07								
L78	K07	K08	26.42		K08	5.55	1.13						
L89	K08	K09	76.73		K09	8.02	1.63	5.6	0				
L910	K09	K10	22.51		K10	5.55	1.13						
L1011	K10	K11	30.93		K11	6.26	1.27	3.9	0				
L1112	K11	K12	44.64		K12	4.17	0.85	10.7	0				
Dis.2 L			332.73	Dis.2 Total	44.75	9.09	30.6	0					
L117	K01	K17	55.01	0.167, 0.08	K17	7.5	1.52	7.2	0	Distributor# 3			
L1718	K17	K18	53.11		K18	5.55	1.13						
L1813	K18	K13	41.27		K13	5	1.02	9.9	0				
L1314	K13	K14	55.01		K14	7.5	1.52	6.1	0				
L1415	K14	K15	65.03		K15	6.57	1.33						
Dis.3 L			269.43	Dis.3 Total	32.12	6.52	23.2	0					
L119	K01	K19	79.77	0.167, 0.08	K19	6.11	1.24	3.1	0	Sub-Dist. 4a			
L1920	K19	K20	63.17		K20	4.17	0.85						
L2021	K20	K21	73.19		K21	6.66	1.35						
L2122	K21	K22	40.79		K22	5	1.02						
L2223	K22	K23	78.28		K23	3	0.61						
L2316	K23	K16	33.06		K16	6.11	1.24	2	0				

Lower Half

Dis.4a L			368.26		Dis.4a Total	31.05	6.31	5.1	0			
L119	K01	K19	79.77	0.167, 0.08	K19	6.11	1.24	3.1	0	Sub-Dist. 4b		
L1920	K19	K20	63.17		K20	4.17	0.85					
L2031	K20	K31	22.56		K31	5	1.02					
L3132	K31	K32	63.77		K32	2	0.41	6.7	0			
L3233	K32	K33	33.46		K33	6.26	1.27					
L3334	K33	K34	36.14		K34	5.55	1.13					
Dis.4b L			298.87		Dis.4b Total	29.09	5.92	9.8	0			
Dis.4 Eff L			524.19		Dis.4 Total	49.86	10.14	11.8	0			
L127	K01	K27	47.28	0.167, 0.08	K27	6.26	1.27			Sub-Dist. 5a		
L2728	K27	K28	63.57		K28	7.22	1.47					
L2824	K28	K24	38.53		K24	6.57	1.33	6.8	0			
L2425	K24	K25	27.54		K25	6.66	1.35					
L2526	K25	K26	20.59		K26	4.17	0.85					
Dis.5a L			197.51		Dis.5a Total	30.88	6.27	6.8	0			
L127	K01	K27	47.28	0.167, 0.08	K27	6.26	1.27			Sub-Dist. 5b		
L2728	K27	K28	63.57		K28	7.22	1.47					
L2824	K28	K24	38.53		K24	6.57	1.33	6.8	0			
L2429	K24	K29	75.34		K29	6.11	1.24	4.9	0			
Dis.5b L			224.72		Dis.5b Total	26.16	5.31	11.7	0			
Dis.5 Eff L			272.85		Dis.5 Total	36.99	7.51	11.7	0			
L130	K01	K30	66.97	0.167, 0.08	K30	4	0.81	9	0	Distributor# 6		
L3085	K30	K85	106.37	0.249, 0.08	K85							
L8589	K85	K89	149.82		K89							
L8988	K89	K88	189.03		K88							
L8887	K88	K87	139.04		K87							
L8786	K87	K86	157.16		K86	9.2	0					
Dis.6 L			808.39		Dis.6 Total	24	4.86	18.2	0			
L138	K01	K38	42.69	0.167, 0.08	K38	4	0.81	1.6	0	Sub-Dist. 7a		
L3835	K38	K35	34.19	0.063, 0.079	K35	5	1.02	9.7	0			
L3536	K35	K36	30.63	0.167, 0.08	K36	7.22	1.47	3.2	0			
L3637	K36	K37	69.78		K37	3	0.61	8.5	0			
Dis.7a L			177.29		Dis.7a Total	19.22	3.91	23	0			
L138	K01	K38	42.69	0.167, 0.08	K38	4	0.81	1.6	0	Sub-Dist. 7b		
L3835	K38	K35	34.19	0.063, 0.079	K35	5	1.02	9.7	0			
L3539	K35	K39	66.02	0.167, 0.08	K39	7.6	1.54					
L3940	K39	K40	76.07		K40							
L4041	K40	K41	25.95		K41	3	0.61	9.8	0			
Dis.7b L			244.92		Dis.7b Total	27.2	5.52	21.1	0			
Dis.7 Eff L			345.33		Dis.7 Total	37.42	7.6	32.8	0			
L142	K01	K42	68.03	0.063, 0.079	K42	5.55	1.13	8.5	0	Sub-Dist. 8a		
L4243	K42	K43	68.79	0.167, 0.08	K43	7.97	1.62					
L4344	K43	K44	47.1		K44	4.17	0.85					
L4445	K44	K45	33.66		K45	7.5	1.52					
L4546	K45	K46	57.04		K46							
											Distributor# 8	

Dis.8a L			274.62		Dis.8a Total	32.69	6.64	8.5	0				
L142	K01	K42	68.03	0.063, 0.079	K42	5.55	1.13	8.5	0	Sub-Dist. 8b			
L4248	K42	K48	64.75	0.167, 0.08	K48	2	0.41						
L4847	K48	K47	36.5		K47	7.22	1.47	11.4	0				
L4746	K47	K46	51.8		K46	7.5	1.52						
Dis.8b L			221.08		Dis.8b Total	22.27	4.53	19.9	0				
Dis.8 Eff L			427.67		Dis.8 Total	41.91	8.52	19.9	0				
L149	K01	K49	67.02	0.167, 0.08	K49	5.56	1.13			Distributor# 9			
L4950	K49	K50	61.03		K50	7.97	1.62	2	0				
L5051	K50	K51	79.35		K51	6.57	1.33						
L5152	K51	K52	68.13		K52	5.56	1.13	11	0				
L5253	K52	K53	52.14		K53	7.22	1.47	6.6	0				
Dis.9 L			327.67		Dis.9 Total	32.88	6.68	19.6	0				
L154	K01	K54	21.09	0.167, 0.08	K54	4.17	0.85			Distributor# 10			
L5455	K54	K55	76.36		K55	6.11	1.24	7.8	0				
L5582	K55	K82	56.4	0.249, 0.08	K82	4	0.81						
L8281	K82	K81	88.5		K81								
L8180	K81	K80	147.91		K80								
L8084	K80	K84	91.9		K84								
L8483	K84	K83	74.62	K83			1.7	0					
Dis.10 L			556.78		Dis.10 Total	30.28	6.14	9.5	0				
L156	K01	K56	32.61	0.167, 0.08	K56	7.6	1.54			Distributor# 11			
L5657	K56	K57	50.61		K57	7.5	1.52	4.5	0				
L5758	K57	K58	74.38		K58	4.87	0.99						
L5859	K58	K59	57.74		K59	6.57	1.33	1.9	0				
Dis.11 L			215.34		Dis.11 Total	26.54	5.38	6.4	0				
L160	K01	K60	68.7	0.167, 0.08	K60	5.56	1.13	2.6	0	Distributor# 12			
L6061	K60	K61	49.14		K61	8.02	1.63	5.1	0				
L6192	K61	K92	91.88	0.249, 0.08	K92	4	0.81						
L9291	K92	K91	219.97		K91								
L9190	K91	K90	146.86		K90						9.9	0	
Dis.12 L			576.55		Dis.12 Total	25.58	5.19	17.6	0				
L162	K01	K62	62.81	0.063, 0.079	K62	4	0.81			Sub-Dist. 13a			
L6263	K62	K63	75.05		K63	4.17	0.85	7.8	0				
L6364	K63	K64	75.64	0.167, 0.08	K64	7.5	1.52						
Dis.13a L			213.5		Dis.13a Total	15.67	3.18	7.8	0				
L162	K01	K62	62.81	0.063, 0.079	K62	4	0.81			Sub-Dist. 13b			
L6263	K62	K63	75.05		K63	4.17	0.85	7.8	0				
L6365	K63	K65	57.1	0.167, 0.08	K65	4	0.81						
L6566	K65	K66	40.6		K66	6.11	1.24						
L6667	K66	K67	76.16		K67	7.5	1.52	12	0				
L6768	K67	K68	27.49		K68	7.03	1.43	6.7	0				
Dis.13b1 L			201.35		Dis.13b1 Total	24.64	5	18.7	0				
L162	K01	K62	62.81	0.063, 0.079	K62	4	0.81			Sub			
L6263	K62	K63	75.05		K63	4.17	0.85	7.8	0				

B. DATA FOR EUROPEAN LV DISTRIBUTION NETWORK

The data for the line impedances is given below.

Appendix Table B.1: Phase impedance matrix of overhead line of European LV distribution network, Ref. [102]

Conductor ID/ Installation		Phase impedance matrix after Kron reduction (Ω/km)		
		A	B	C
OH1/3-ph	A	$0.616+j0.588$	$0.131+j0.306$	$0.141+j0.245$
	B	$0.131+j0.306$	$0.628+j0.566$	$0.147+j0.276$
	C	$0.141+j0.245$	$0.147+j0.276$	$0.650+j0.527$
OH2/3-ph	A	$1.457+j0.728$	$0.143+j0.417$	$0.152+j0.367$
	B	$0.143+j0.417$	$1.469+j0.720$	$0.159+j0.405$
	C	$0.152+j0.367$	$0.159+j0.405$	$1.490+j0.704$
OH3/3-ph	A	$2.137+j0.776$	$0.125+j0.453$	$0.133+j0.406$
	B	$0.125+j0.453$	$2.146+j0.771$	$0.138+j0.447$
	C	$0.133+j0.406$	$0.138+j0.447$	$2.163+j0.762$

Appendix Table B.2: Phase impedance matrix of underground cables of European LV distribution network, Ref. [102]

Conductor ID/ Installation		Phase impedance matrix after Kron reduction (Ω/km)		
		A	B	C
UG1/3-ph	A	$0.287+j0.167$	$0.121+j0.110$	$0.125+j0.070$
	B	$0.121+j0.110$	$0.279+j0.203$	$0.121+j0.110$
	C	$0.125+j0.070$	$0.121+j0.110$	$0.287+j0.167$
UG2/3-ph	A	$0.455+j0.204$	$0.185+j0.146$	$0.190+j0.107$
	B	$0.185+j0.146$	$0.444+j0.238$	$0.185+j0.146$
	C	$0.190+j0.107$	$0.185+j0.146$	$0.455+j0.204$
UG3/3-ph	A	$1.152+j0.458$	$0.321+j0.390$	$0.330+j0.359$
	B	$0.321+j0.390$	$1.134+j0.477$	$0.321+j0.390$
	C	$0.330+j0.359$	$0.321+j0.390$	$1.152+j0.458$

Appendix Table B.3: Line parameters of residential feeder of European LV distribution network, Ref. [102]

Line Segment	Node from	Node to	Conductor ID	Length (m)	Installation
1	R ₁	R ₂	UG1	35	UG 3-ph
2	R ₂	R ₃		35	UG 3-ph
3	R ₃	R ₄		35	UG 3-ph
4	R ₄	R ₅		35	UG 3-ph
5	R ₅	R ₆		35	UG 3-ph
6	R ₆	R ₇		35	UG 3-ph
7	R ₇	R ₈		35	UG 3-ph
8	R ₈	R ₉		35	UG 3-ph
9	R ₉	R ₁₀		35	UG 3-ph
10	R ₃	R ₁₁		UG3	30
11	R ₄	R ₁₂	35		UG 3-ph
12	R ₁₂	R ₁₃	35		UG 3-ph
13	R ₁₃	R ₁₄	35		UG 3-ph
14	R ₁₄	R ₁₅	30		UG 3-ph
15	R ₆	R ₁₆	30		UG 3-ph
16	R ₉	R ₁₇	30		UG 3-ph
17	R ₁₀	R ₁₈	30	UG 3-ph	

Appendix Table B.4: Transformer parameters of European LV distribution network, Ref. [102]

Node from	Node to	Connection	V ₁	V ₂	Z _{tr} (V ₂ side)	S _{rated}
-----------	---------	------------	----------------	----------------	---------------------------------------	--------------------

			kV	kV	m Ω	KVA
R ₀	R ₁	3-ph Dyn1	20	0.4	3.2+j12.8	500
I ₀	I ₁				10.7+j42.7	150
C ₀	C ₁				5.3+j21.3	300

Appendix Table B.5: MV equivalent network parameters of European LV distribution, Ref. [102]

Nominal system voltage kV	Short circuit power (Ssc) MVA	R/X ratio
20 LL	100	1

Appendix Table B.6: Line parameters of industrial feeder of European LV distribution network, Ref. [102]

Line Segment	Node from	Node to	Conductor ID	Length (m)	Installation
1	I ₁	I ₂	UG2	200	UG 3-ph

Appendix Table B.7: Line parameters of commercial feeder of European LV distribution network, Ref. [102]

Line Segment	Node from	Node to	Conductor ID	Length (m)	Installation
1	C ₁	C ₂	OH1	30	OH 3-ph
2	C ₂	C ₃		30	OH 3-ph
3	C ₃	C ₄		30	OH 3-ph
4	C ₄	C ₅		30	OH 3-ph
5	C ₅	C ₆		30	OH 3-ph
6	C ₆	C ₇		30	OH 3-ph
7	C ₇	C ₈		30	OH 3-ph
8	C ₈	C ₉		30	OH 3-ph
9	C ₃	C ₁₀	OH2	30	OH 3-ph
10	C ₁₀	C ₁₁		30	OH 3-ph
11	C ₁₁	C ₁₂	OH3	30	OH 3-ph
12	C ₁₁	C ₁₃		30	OH 3-ph
13	C ₁₀	C ₁₄		30	OH 3-ph
14	C ₅	C ₁₅		30	OH 3-ph
15	C ₁₅	C ₁₆		30	OH 3-ph
16	C ₁₆	C ₁₇		30	OH 3-ph

Appendix Table B.8: Load parameters of European LV distribution network, Ref. [102]

Node	Apparent Power (kVA)	Power factor (pf)-lagging
R ₁	200	0.95
R ₁₁	15	0.95
R ₁₅	52	0.95
R ₁₆	55	0.95
R ₁₇	35	0.95
R ₁₈	47	0.95
I ₂	100	0.85
C ₁	120	0.90
C ₁₂	20	0.90
C ₁₃	20	0.90
C ₁₄	25	0.90
C ₁₇	25	0.90
C ₁₈	8	0.90
C ₁₉	16	0.90
C ₂₀	8	0.90

C. DERIVATION OF TRANSFER FUNCTION FOR LCL FILTER

Considering the $v_g = 0$, the following equations can be derived from Figure 3.3 (b).

$$\begin{aligned}
\frac{R_d C_f s + 1}{s C_f} i_c &= (R_2^g + s L_2^g) i_g \xrightarrow{i_c = i_1 - i_g} \frac{R_d C_f s + 1}{s C_f} (i_1 - i_g) = (R_2^g + s L_2^g) i_g \\
\Rightarrow \\
\frac{R_d C_f s + 1}{s C_f} i_1 &= \left[\left(\frac{R_d C_f s + 1}{s C_f} \right) + (R_2^g + s L_2^g) \right] i_g \\
\therefore i_1 &= \frac{v_i - v_c}{R_1 + s L_1} \\
\Rightarrow \frac{R_d C_f s + 1}{(R_1 + s L_1)} [v_i - (R_2^g + s L_2^g) i_g] &= [s C_f (R_2^g + s L_2^g) + (R_d C_f s + 1)] i_g
\end{aligned} \tag{C.1}$$

Rearranging the equation (C.1) for i_g/v_i , the new expressions are given in equation (C.2).

$$\begin{aligned}
(R_d C_f s + 1) v_i &= \left[\left\{ s C_f (R_2^g + s L_2^g) + (R_d C_f s + 1) \right\} (R_1 + s L_1) + (R_d C_f s + 1) (R_2^g + s L_2^g) \right] i_g \\
H(s) = \frac{i_g}{v_i} &= \frac{(R_d C_f s + 1)}{\left[\left\{ s C_f (R_2^g + s L_2^g) + (R_d C_f s + 1) \right\} (R_1 + s L_1) + (R_d C_f s + 1) (R_2^g + s L_2^g) \right]} \\
\Rightarrow \\
H(s) &= \frac{R_d C_f s + 1}{y_1 s^3 + y_2 s^2 + y_3 s + y_4} \\
\therefore \begin{cases} y_1 = L_1 L_2^g C_f; & y_2 = L_2^g C_f (R_1 + R_d) + L_1 C_f (R_2^g + R_d) \\ y_3 = R_d C_f (R_1 + R_2^g) + R_1 R_2^g C_f + L_1 + L_2^g; & y_4 = R_1 + R_2^g \end{cases}
\end{aligned} \tag{C.2}$$

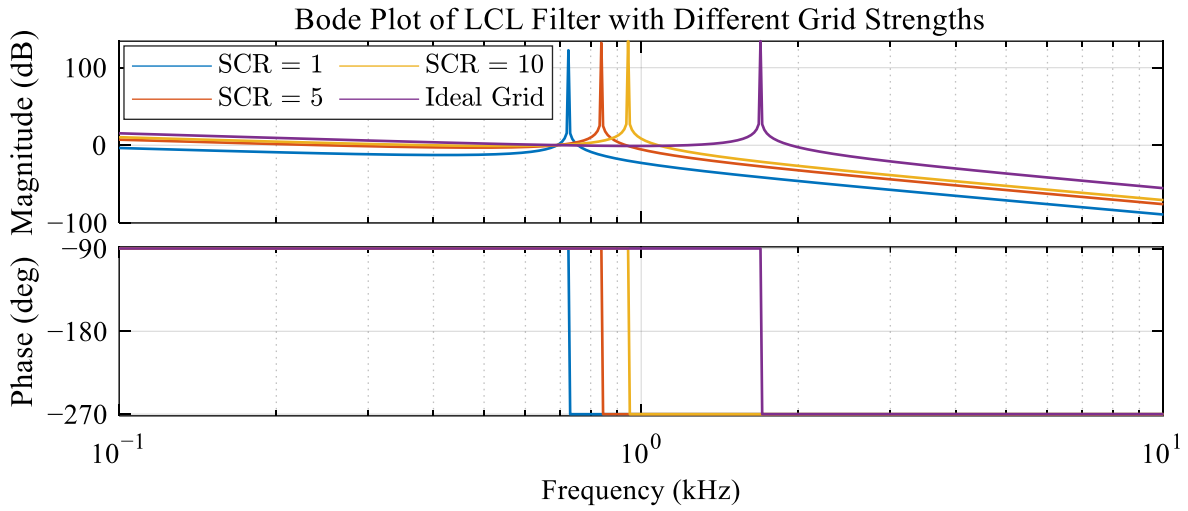
D. PERFORMANCE OF LCL FILTER

To discuss the performance of the designed LCL filter, the converter's specifications and the filter parameters are presented in Appendix Table D.1.

Appendix Table D.1: LCL filter's parameters

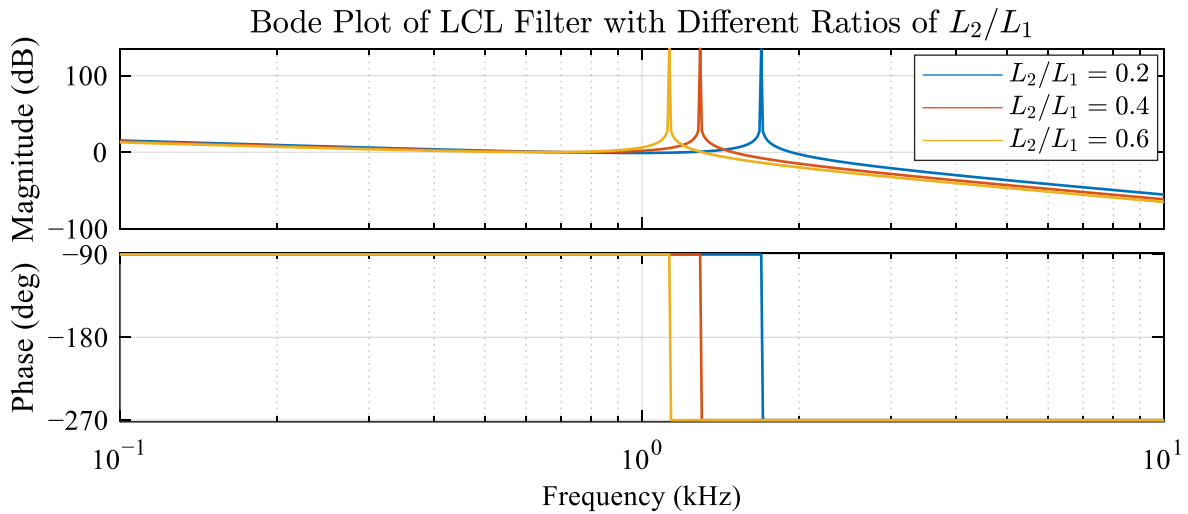
Given	$V_{L-L,RMS}$ (V)	S (kVA)	f_{sw} (kHz)	f_g (Hz)	v_{dc}	$r = (L_2/L_1)$
Parameters	260	100	10	50	425	0.2
Derived	L_1 (mH)	L_2 (mH)	f_{res} (kHz)	C_f (mF)	R_d (Ω)	
Parameters	0.226	0.0451	1.692	0.2354	0.133	

The resonance frequency satisfies the criteria discussed in equation (3.6). The resonant frequency is largely affected by grid strength, the ratio of L_2/L_1 , and the damping resistor.



Appendix Figure D.1: Effect of L_g on resonance frequency

Appendix Figure D.2 presents the effect of the ratio of L_2/L_1 on the resonant frequency of the LCL filter.

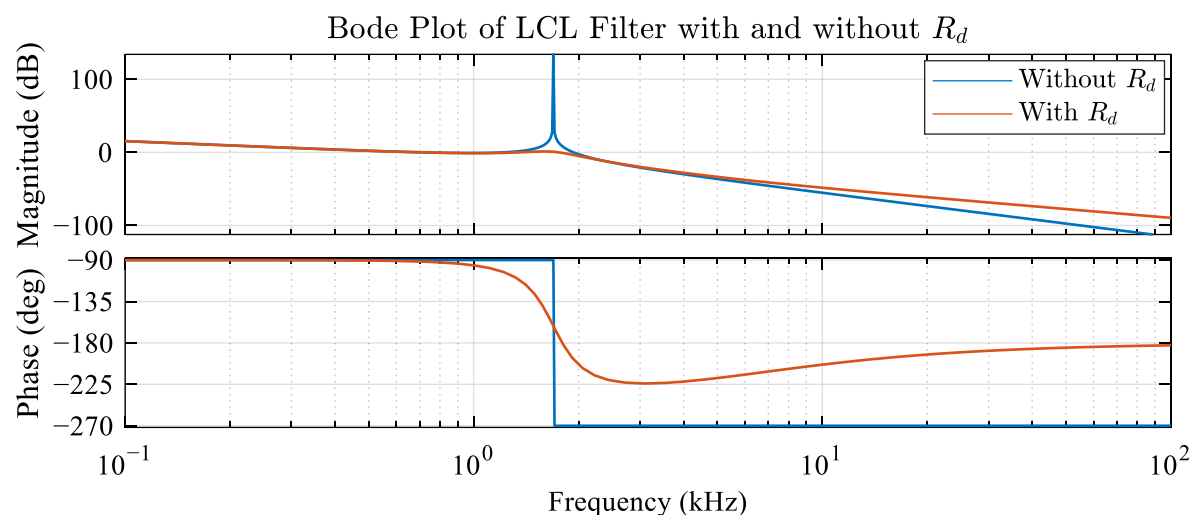


Appendix Figure D.2: Effect of L_2/L_1 on resonance frequency

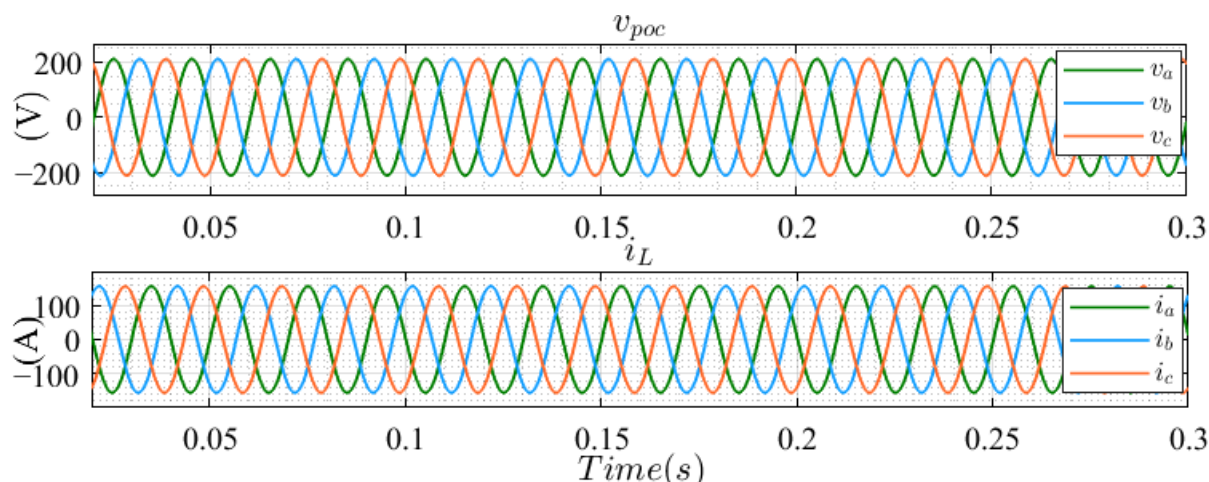
In Appendix Figure D.1, the impact of grid's inductance is presented on the resonance frequency. It shows that grid's inductance has a negative effect on the resonance frequency which means that the resonant peak occurs at lower frequency for weak grids. The grid strength can be represented with the short circuit ratio (SCR) which is the ratio between the short circuit power of the grid at POC to the rated power of the converter. To design a filter which could result in better response for typical SCRs, the resonant frequency needs to be shifted towards its upper limit so that the impact of grid's inductance could be accommodated.

Appendix Figure D.2 shows that the lesser ratio results in higher resonance frequency. This can be used to cancel/minimize the effect of grid's inductance on the resonance frequency. This is why in this design; minimum value of this ratio is selected (0.2).

From Appendix Figure D.1 and Appendix Figure D.2, it is clear that the resonance peak is very high and to suppress this peak, a damping resistor can be used in series with the filter's capacitor. Appendix Figure D.3 shows that the inclusion of damping resistor largely damps the resonance peak.



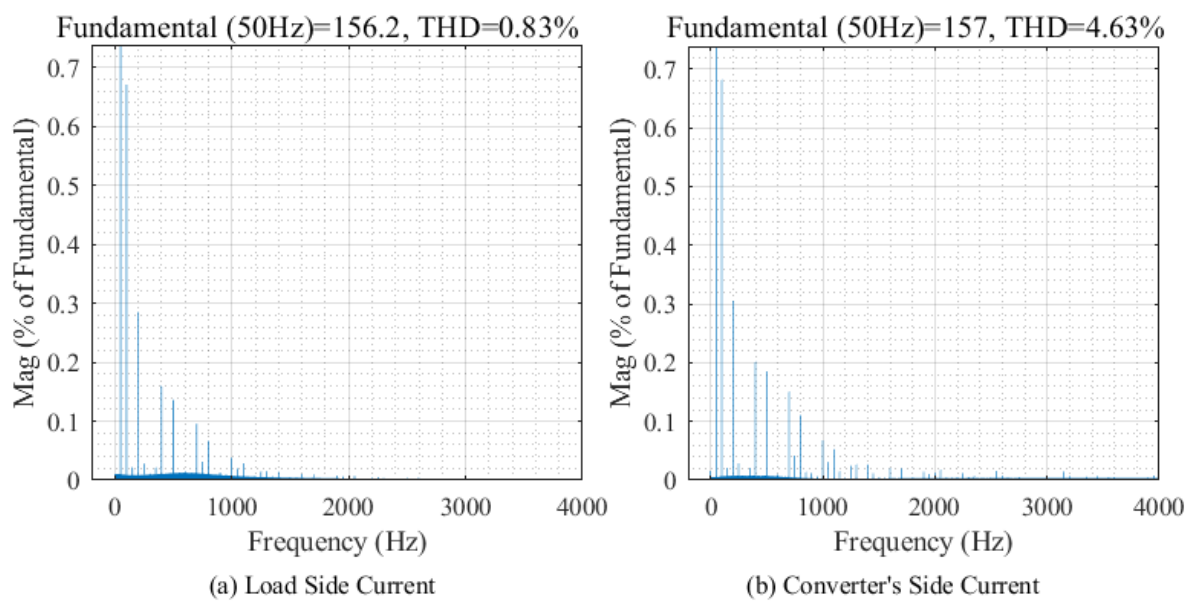
Appendix Figure D.3: Effect of R_d on resonance peak



Appendix Figure D.4: Three-phase voltage and current on load side

In LCL filter design, the ratio of L_2/L_1 is kept minimum and the R_d is introduced for the resonance peak reduction. To test the performance of the designed LCL filter in a converter-based system, the setup shown in Figure 3.3 (a) is used. The coupling transformer is ignored, and a load is connected instead of the grid. A simple reference voltage control is used for the converter. The other parameters are given in Appendix Table D.1. The three-phase voltage and current are given in Appendix Figure D.4.

In Appendix Figure D.4, i_L represents the load side current in the above figure. The above figure confirms the good performance of the LCL filter with a converter-based power source. The Fast Fourier Transform (FFT) analysis for the converter side and load side current is given in Appendix Figure D.5, which confirms the low THD for the load side current as compared to the converter's side current and both the THDs are less than 5 %.



Appendix Figure D.5: FFT analysis for load and converter's side current

E. LINEARIZATION AND LAPLACE TRANSFORMATION OF DIFFERENTIAL EQUATIONS

From the first part of equation (3.29), the variables are expressed in dq-domain with a rotating unity magnitude vector. The updated expressions are given below.

$$\begin{aligned}
L_1 \frac{d(i_{1,dq}(t)e^{j\omega t})}{dt} + R_1(i_{1,dq}(t)e^{j\omega t}) &= (v_{i,dq}(t)e^{j\omega t}) - (v_{c,dq}(t)e^{j\omega t}) \\
L_1 \frac{di_{1,dq}(t)}{dt} e^{j\omega t} + j\omega L_1 i_{1,dq}(t)e^{j\omega t} + R_1(i_{1,dq}(t)e^{j\omega t}) &= (v_{i,dq}(t)e^{j\omega t}) - (v_{c,dq}(t)e^{j\omega t}) \\
L_1 \frac{di_{1,dq}(t)}{dt} + j\omega L_1 i_{1,dq}(t) + R_1 i_{1,dq}(t) &= v_{i,dq}(t) - v_{c,dq}(t) \\
\Rightarrow \text{Linearization} \\
L_1 \frac{d\Delta i_{1,dq}(t)}{dt} + j\omega L_1 \Delta i_{1,dq}(t) + R_1 \Delta i_{1,dq}(t) &= \Delta v_{i,dq}(t) - \Delta v_{c,dq}(t)
\end{aligned} \tag{E.1}$$

By taking the Laplace transformation of equation (E.1).

$$\begin{aligned}
L_1 s \Delta i_{1,dq}(s) + j\omega L_1 \Delta i_{1,dq}(s) + R_1 \Delta i_{1,dq}(s) &= \Delta v_{i,dq}(s) - \Delta v_{c,dq}(s) \\
(L_1 s + R_1) \Delta i_{1,dq}(s) &= -j\omega L_1 \Delta i_{1,dq}(s) + \Delta v_{i,dq}(s) - \Delta v_{c,dq}(s) \\
\Delta i_{1,dq}(s) &= \frac{1}{L_1 s + R_1} (-j\omega L_1 \Delta i_{1,dq}(s) + \Delta v_{i,dq}(s) - \Delta v_{c,dq}(s)) \\
\Rightarrow \\
\Delta i_{1d}(s) &= \frac{1}{L_1 s + R_1} (L_1 \omega \Delta i_{1q}(s) + \Delta v_{id}(s) - \Delta v_{cd}(s)) \\
\Delta i_{1q}(s) &= \frac{1}{L_1 s + R_1} (-L_1 \omega \Delta i_{1d}(s) + \Delta v_{iq}(s) - \Delta v_{cq}(s))
\end{aligned} \tag{E.2}$$

F. STATIONARY REFERENCE FRAME COMPONENTS IN UNBALANCED CONDITIONS

If the phase voltages are 120° apart from each other but have different amplitudes, then the stationary reference component can be expressed as given below.

$$\begin{aligned} v_\alpha(t) &= \frac{1}{6}(4|v_a| + |v_b| + |v_c|)\cos(\omega t + \theta_v) + \frac{1}{2\sqrt{3}}(|v_c| - |v_b|)\sin(\omega t + \theta_v) \\ v_\beta(t) &= \frac{1}{2\sqrt{3}}(|v_c| - |v_b|)\cos(\omega t + \theta_v) + \frac{1}{2}(|v_c| + |v_b|)\sin(\omega t + \theta_v) \end{aligned} \quad (\text{F.1})$$

The above equation converges to a balanced orthogonal system if the three-phase voltages are balanced.

$$\begin{aligned} v_\alpha(t) &= |v|\cos(\omega t + \theta_v) \\ v_\beta(t) &= |v|\sin(\omega t + \theta_v) \end{aligned} \quad (\text{F.2})$$

G. POSITIVE AND NEGATIVE SEQUENCE COMPONENTS IN STATIONARY REFERENCE FRAME

The derivation of the expressions of stationary reference components of positive and negative sequence are given below in terms of measured voltage at POC in stationary reference component.

$$\begin{aligned}
 v_{\alpha}(t) &= v_{\alpha p}(t) + v_{\alpha n}(t) = |v_p| \cos(\omega t + \theta_{vp}) + |v_n| \cos(-\omega t - \theta_{vn}) \\
 v_{\beta}(t) &= v_{\beta p}(t) + v_{\beta n}(t) = |v_p| \sin(\omega t + \theta_{vp}) + |v_n| \sin(-\omega t - \theta_{vn}) \\
 \begin{cases} v_{\alpha}^T(t) = |v_p| \cos(\omega t + \theta_{vp} + 90) + |v_n| \cos(-\omega t - \theta_{vn} - 90) \\ v_{\beta}^T(t) = |v_p| \sin(\omega t + \theta_{vp} + 90) + |v_n| \sin(-\omega t - \theta_{vn} - 90) \end{cases} & \quad (G.1) \\
 \begin{cases} v_{\alpha}^T(t) = -|v_p| \sin(\omega t + \theta_{vp}) + |v_n| \sin(-\omega t - \theta_{vn}) \\ v_{\beta}^T(t) = |v_p| \cos(\omega t + \theta_{vp}) - |v_n| \cos(-\omega t - \theta_{vn}) \end{cases} \\
 \begin{cases} v_{\alpha}^T(t) = -v_{\beta p}(t) + v_{\beta n}(t) \\ v_{\beta}^T(t) = v_{\alpha p}(t) - v_{\alpha n}(t) \end{cases}
 \end{aligned}$$

The expressions of $\alpha\beta$ components of the measured voltage are presented in its sequence components. Similarly, the orthogonal of the $\alpha\beta$ components are also represented in the form of sequence components. By using these two sets of equations, the $\alpha\beta$ components in the positive and negative sequence systems can be presented in the form of stationary measured components and their orthogonal.

$$\begin{aligned}
 \begin{cases} v_{\alpha}(t) = v_{\alpha p}(t) + v_{\alpha n}(t) \\ v_{\beta}^T(t) = v_{\alpha p}(t) - v_{\alpha n}(t) \end{cases} & \rightarrow \begin{bmatrix} v_{\alpha p}(t) \\ v_{\alpha n}(t) \end{bmatrix} = \frac{1}{2} \begin{bmatrix} v_{\alpha}(t) + v_{\beta}^T(t) \\ v_{\alpha}(t) - v_{\beta}^T(t) \end{bmatrix} \\
 \begin{cases} v_{\beta}(t) = v_{\beta p}(t) + v_{\beta n}(t) \\ v_{\alpha}^T(t) = -v_{\beta p}(t) + v_{\beta n}(t) \end{cases} & \rightarrow \begin{bmatrix} v_{\beta p}(t) \\ v_{\beta n}(t) \end{bmatrix} = \frac{1}{2} \begin{bmatrix} v_{\beta}(t) - v_{\alpha}^T(t) \\ v_{\beta}(t) + v_{\alpha}^T(t) \end{bmatrix}
 \end{aligned} \quad (G.2)$$

H. DERIVATION OF DSM FOR SEQUENCE EXTRACTION

$$\begin{aligned}
v_\alpha(t) &= v_{\alpha p}(t) + v_{\alpha n}(t) = |v_p| \cos(\omega t + \theta_{vp}) + |v_n| \cos(-\omega t - \theta_{vn}) \\
v_\alpha(t + T_s) &= |v_p| \cos(\omega(t + T_s) + \theta_{vp}) + |v_n| \cos(-\omega(t + T_s) - \theta_{vn}) \\
v_\alpha(t + T_s) &= |v_p| \cos(\omega t + \theta_{vp} + \omega T_s) + |v_n| \cos(-\omega t - \theta_{vn} - \omega T_s) \\
&\begin{cases} \cos(a + b) = \cos(a)\cos(b) - \sin(a)\sin(b) \\ \therefore v_{\alpha p}(t) = |v_p| \cos(\omega t + \theta_{vp}); v_{\alpha n}(t) = |v_n| \cos(-\omega t - \theta_{vn}) \\ v_{\beta p}(t) = |v_p| \sin(\omega t + \theta_{vp}); v_{\beta n}(t) = |v_n| \sin(-\omega t - \theta_{vn}) \end{cases} \tag{H.1} \\
&\Rightarrow \\
v_\alpha(t + T_s) &= v_\alpha(t) \cos(\omega T_s) - v_{\beta p}(t) \sin(\omega T_s) + v_{\beta n}(t) \sin(\omega T_s)
\end{aligned}$$

Similarly, the expressions for the other unit delays can also be derived.

I. DERIVATION OF SSB BASED FAULT DETECTION METHOD

The general expression for the magnitude of the line-to-line voltage is given in equation (3.55). If v_y is known, the same equation can be used to calculate v_x . The expressions are given below.

$$|v_x| = \frac{-|v_y| \pm \sqrt{9.72 - 3|v_y|^2}}{2} \quad (\text{I.1})$$

Only the positive value from the above solution is considered as the magnitude of the phase voltage can't be negative. As an example, v_x is considered as v_a and v_y as v_b . v_c is considered as healthy phase (1 p.u.).

The expressions for the magnitudes of the positive and negative sequence voltage phasors are given below. The phase voltages are considered as 120° apart from each other.

$$\begin{aligned} |v_p| &= \frac{|v_a| + |v_b| + |v_c|}{3} \\ v_n &= \frac{|v_a| + |v_b|(-0.5 + 0.866j) + |v_c|(-0.5 - 0.866j)}{3} \\ |v_n| &= \frac{\sqrt{(|v_a| - 0.5(|v_b| + |v_c|))^2 + (0.866(|v_b| - |v_c|))^2}}{3} \end{aligned} \quad (\text{I.2})$$

The magnitude of v_b varies and the magnitude of v_a is calculated with the help of equation (I.1) and then the magnitudes of phase voltages are passed to equation (I.2) to calculate magnitudes of the positive and negative sequence voltage phasors. The results are tabulated in the following table. All the values are in per unit in the following table.

Appendix Table I.1: Tabulated results for SSB fault detection method

Inputs		Calculated with help of (I.1)	Calculated with help of (I.2)	
$ v_c $	$ v_b $	$ v_a $	$ v_p $	$ v_n $
1.0	1.0	0.796	0.932	0.068
1.0	0.95	0.849	0.933	0.044
1.0	0.9	0.9	0.933	0.033
0.9	0.9	0.9	0.9	0

From the above table, the following conditions can be derived for fault detection.

$$fault_flag = \begin{cases} True & \text{if } |v_p| \leq 90\% \text{ or } (|v_p| \leq 93\% \ \& \ |v_n| \geq 3.33\%) \\ False & \text{if } |v_p| > 93\% \text{ or } (|v_p| > 90\% \ \& \ |v_n| < 3.33\%) \end{cases} \quad (\text{I.3})$$

It is important to mention here that the conditions on the right most side of the above equation are valid only if the three-phase voltages are 120° apart from each other and one phase is healthy (1.0 p.u.).

J. DERIVATION OF SBS BASED FAULT DETECTION METHOD

The derivation of the SBS method is given below.

$$\begin{aligned}
 v_{ab}(t) &= \frac{\sqrt{3}}{2} v_{\alpha}(t) - \frac{1}{2} v_{\beta}(t) = \frac{1}{2} \left\{ \sqrt{3} (v_{\alpha_p}(t) + v_{\alpha_n}(t)) - (v_{\beta_p}(t) + v_{\beta_n}(t)) \right\} \\
 &\begin{cases} v_{\alpha_p}(t) = |v_p| \cos(\omega t + \theta_{vp}); v_{\alpha_n}(t) = |v_n| \cos(-\omega t - \theta_{vn}) \\ v_{\beta_p}(t) = |v_p| \sin(\omega t + \theta_{vp}); v_{\beta_n}(t) = |v_n| \sin(-\omega t - \theta_{vn}) \end{cases} \\
 \therefore &\begin{cases} \cos(a+b) = \cos(a)\cos(b) - \sin(a)\sin(b) \\ \sin(a+b) = \sin(a)\cos(b) + \cos(a)\sin(b) \end{cases} \\
 v_{ab}(t) &= \frac{1}{2} \{ A \cos(\omega t) + B \sin(\omega t) \} \\
 &\begin{cases} A = \sqrt{3} |v_p| \cos \theta_{vp} + \sqrt{3} |v_n| \cos \theta_{vn} - |v_p| \sin \theta_{vp} + |v_n| \sin \theta_{vn} \\ B = |v_n| \cos \theta_{vn} - |v_p| \cos \theta_{vp} - \sqrt{3} |v_n| \sin \theta_{vn} - \sqrt{3} |v_p| \sin \theta_{vp} \end{cases} \tag{J.1} \\
 |v_{ab}| &= \frac{1}{2} \sqrt{A^2 + B^2} \\
 A^2 + B^2 &= 4 |v_p|^2 + 4 |v_n|^2 + 4 |v_p| |v_n| \left\{ \cos(\theta_{vp} - \theta_{vn}) - \sqrt{3} \sin(\theta_{vp} - \theta_{vn}) \right\} \\
 |v_{ab}| &= \sqrt{|v_p|^2 + |v_n|^2 + |v_p| |v_n| \left\{ \cos(\theta_{vp} - \theta_{vn}) - \sqrt{3} \sin(\theta_{vp} - \theta_{vn}) \right\}}
 \end{aligned}$$

The expressions for other line-line voltages can be derived with the same steps.

K. EXPRESSIONS FOR REAL AND REACTIVE POWER IN UNBALANCED CONDITIONS

The derivation for the expressions for the real and reactive power in the unbalanced conditions is given below.

$$\begin{aligned} \therefore \begin{cases} v = (v_{\alpha p}(t) + v_{\alpha n}(t)) + j(v_{\beta p}(t) + v_{\beta n}(t)) \\ i^* = (i_{\alpha p}(t) + i_{\alpha n}(t)) - j(i_{\beta p}(t) + i_{\beta n}(t)) \end{cases} \\ \therefore \begin{cases} p = \text{real}(vi^*) \\ q = \text{imag}(vi^*) \end{cases} \end{aligned} \quad (\text{K.1})$$

$$\begin{bmatrix} p \\ q \end{bmatrix} = \begin{bmatrix} v_{\alpha p}(t) + v_{\alpha n}(t) & v_{\beta p}(t) + v_{\beta n}(t) \\ v_{\beta p}(t) + v_{\beta n}(t) & -(v_{\alpha p}(t) + v_{\alpha n}(t)) \end{bmatrix} \begin{bmatrix} i_{\alpha p}(t) + i_{\alpha n}(t) \\ i_{\beta p}(t) + i_{\beta n}(t) \end{bmatrix}$$

The expressions for the $\alpha\beta$ -components of the voltage and current can be expressed in terms of the magnitude of the phasor and its angle.

$$\begin{aligned} \therefore \begin{cases} p = (v_{\alpha p}(t) + v_{\alpha n}(t))(i_{\alpha p}(t) + i_{\alpha n}(t)) + (v_{\beta p}(t) + v_{\beta n}(t))(i_{\beta p}(t) + i_{\beta n}(t)) \\ q = (v_{\beta p}(t) + v_{\beta n}(t))(i_{\alpha p}(t) + i_{\alpha n}(t)) - (v_{\alpha p}(t) + v_{\alpha n}(t))(i_{\beta p}(t) + i_{\beta n}(t)) \end{cases} \\ \therefore \begin{cases} x_{\alpha}y_{\alpha} + x_{\beta}y_{\beta} = |x||y|\cos(\theta_x - \theta_y) \\ x_{\beta}y_{\alpha} - x_{\alpha}y_{\beta} = |x||y|\sin(\theta_x - \theta_y) \end{cases} \\ \Rightarrow \\ p_o = v_{\alpha p}(t)i_{\alpha p}(t) + v_{\beta p}(t)i_{\beta p}(t) + v_{\alpha n}(t)i_{\alpha n}(t) + v_{\beta n}(t)i_{\beta n}(t) \quad (\text{K.2}) \\ \Rightarrow p_o = |v_p||i_p|\cos(\theta_{vp} - \theta_{ip}) + |v_n||i_n|\cos(\theta_{vn} - \theta_{in}) \\ q_o = v_{\beta p}(t)i_{\alpha p}(t) - v_{\alpha p}(t)i_{\beta p}(t) + v_{\beta n}(t)i_{\alpha n}(t) - v_{\alpha n}(t)i_{\beta n}(t) \\ \Rightarrow q_o = |v_p||i_p|\sin(\theta_{vp} - \theta_{ip}) + |v_n||i_n|\sin(\theta_{vn} - \theta_{in}) \end{aligned}$$

Similarly, if the two components of opposite rotating sequences are multiplied, the resultant is a rotating term with double of their frequency.

$$\begin{aligned} \therefore \begin{cases} x_{\alpha p} = |x|\cos(\omega t + \theta_x); x_{\beta p} = |x|\sin(\omega t + \theta_x) \\ y_{\alpha n} = |y|\cos(-\omega t - \theta_y); y_{\beta n} = |y|\sin(-\omega t - \theta_y) \end{cases} \\ \Rightarrow \end{aligned} \quad (\text{K.3})$$

$$\begin{cases} x_{\alpha p}y_{\alpha n} + x_{\beta p}y_{\beta n} = |x||y|\cos(2\omega t + \theta_x + \theta_y) \\ x_{\beta p}y_{\alpha n} - x_{\alpha p}y_{\beta n} = |x||y|\sin(2\omega t + \theta_x + \theta_y) \end{cases}$$

With the help of equation (K.2) and (K.3) the following expressions can be derived.

$$\begin{aligned}
p &= p_o + \tilde{p} \\
q &= q_o + \tilde{q} \\
\begin{bmatrix} p_o \\ \tilde{p} \\ q_o \\ \tilde{q} \end{bmatrix} &= \begin{bmatrix} v_{\alpha p}(t) & v_{\beta p}(t) & v_{\alpha n}(t) & v_{\beta n}(t) \\ v_{\alpha n}(t) & v_{\beta n}(t) & v_{\alpha p}(t) & v_{\beta p}(t) \\ v_{\beta p}(t) & -v_{\alpha p}(t) & v_{\beta n}(t) & -v_{\alpha n}(t) \\ v_{\beta n}(t) & -v_{\alpha n}(t) & v_{\beta p}(t) & -v_{\alpha p}(t) \end{bmatrix} \begin{bmatrix} i_{\alpha p}(t) \\ i_{\beta p}(t) \\ i_{\alpha n}(t) \\ i_{\beta n}(t) \end{bmatrix} \\
p_o &= |v_p| |i_p| \cos(\theta_{vp} - \theta_{ip}) + |v_n| |i_n| \cos(\theta_{vn} - \theta_{in}) \\
\tilde{p} &= |v_n| |i_p| \cos(2\omega t + \theta_{vn} + \theta_{ip}) + |v_p| |i_n| \cos(2\omega t + \theta_{vp} + \theta_{in}) \\
q_o &= |v_p| |i_p| \sin(\theta_{vp} - \theta_{ip}) + |v_n| |i_n| \sin(\theta_{vn} - \theta_{in}) \\
\tilde{q} &= |v_p| |i_n| \sin(2\omega t + \theta_{vp} + \theta_{in}) - |v_n| |i_p| \sin(2\omega t + \theta_{vn} + \theta_{ip})
\end{aligned} \tag{K.4}$$

L. DERIVATION FOR MAGNITUDE OF RESULTANT CURRENT PHASOR

$$i_{\alpha\beta}(t) = |i_p| e^{j(\omega t + \theta_{vp} + \theta_{ip})} + |i_n| e^{-j(\omega t + \theta_{vn} - \theta_{in})}$$

$$i_{\alpha\beta}(t) = |i_p| e^{j\theta_{ip}} e^{j(\omega t + \theta_{vp})} + |i_n| e^{j\theta_{in}} e^{-j(\omega t + \theta_{vn})}$$

$$i_{dq,p} = |i_p| e^{j\theta_{ip}} ; i_{dq,n} = |i_n| e^{j\theta_{in}}$$

$$i' = i_{\alpha\beta}(t) e^{-j(\omega t + \theta_{vp})} = i_{dq,p} + i_{dq,n} e^{-j(2\omega t + \theta_{vp} + \theta_{vn})}$$

$$\therefore \delta(t) = 2\omega t + \theta_{vp} + \theta_{vn}$$

$$real(i') = i_{dp} + i_{dn} \cos(\delta(t)) + i_{qn} \sin(\delta(t))$$

(L.1)

$$imag(i') = i_{qp} + i_{qn} \cos(\delta(t)) - i_{dn} \sin(\delta(t))$$

$$|i_{\alpha\beta}(t)| = |i'|$$

$$\Rightarrow$$

$$|i|^2 = |i_p|^2 + |i_n|^2 + 2(i_{dp}i_{dn} + i_{qp}i_{qn})\cos(\delta(t)) + 2(i_{dp}i_{qn} - i_{qp}i_{dn})\sin(\delta(t))$$

M. DERIVATION OF LINE CURRENT EXPRESSIONS IN TERM OF SEQUENCE COMPONENTS

$$\begin{aligned}
i_{\alpha\beta}(t) &= i_{dq,p} e^{j(\omega t + \theta_{vp})} + i_{dq,n} e^{-j(\omega t + \theta_{vn})} \\
i_{\alpha\beta}(t) &= (i_{dp} + j i_{qp}) \left\{ \cos(\omega t + \theta_{vp}) + j \sin(\omega t + \theta_{vp}) \right\} \\
&\quad + (i_{dn} + j i_{qn}) \left\{ \cos(\omega t + \theta_{vn}) - j \sin(\omega t + \theta_{vn}) \right\} \\
\begin{cases} i_{\alpha}(t) = i_{dp} \cos(\omega t + \theta_{vp}) - i_{qp} \sin(\omega t + \theta_{vp}) + i_{dn} \cos(\omega t + \theta_{vn}) + i_{qn} \sin(\omega t + \theta_{vn}) \\ i_{\beta}(t) = i_{qp} \cos(\omega t + \theta_{vp}) + i_{dp} \sin(\omega t + \theta_{vp}) + i_{qn} \cos(\omega t + \theta_{vn}) - i_{dn} \sin(\omega t + \theta_{vn}) \end{cases} \\
\therefore \begin{cases} \cos(A+B) = \cos A \cos B - \sin A \sin B \\ \sin(A+B) = \sin A \cos B + \cos A \sin B \end{cases} \\
\Rightarrow \begin{bmatrix} i_{\alpha}(t) \\ i_{\beta}(t) \end{bmatrix} &= \begin{bmatrix} k_1 & k_2 \\ k_3 & k_4 \end{bmatrix} \begin{bmatrix} \cos(\omega t) \\ \sin(\omega t) \end{bmatrix} \\
\begin{bmatrix} k_1 \\ k_2 \\ k_3 \\ k_4 \end{bmatrix} &= \begin{bmatrix} i_{dp} & -i_{qp} & i_{dn} & i_{qn} \\ -i_{qp} & -i_{dp} & i_{qn} & -i_{dn} \\ i_{qp} & i_{dp} & i_{qn} & -i_{dn} \\ i_{dp} & -i_{qp} & -i_{dn} & -i_{qn} \end{bmatrix} \begin{bmatrix} \cos \theta_{vp} \\ \sin \theta_{vp} \\ \cos \theta_{vn} \\ \sin \theta_{vn} \end{bmatrix} \tag{M.1}
\end{aligned}$$

By converting $\alpha\beta$ to abc , the expressions for i_{abc} can be derived.

$$i_a(t) = i_{\alpha}(t); i_b(t) = \frac{1}{2} \left\{ -i_{\alpha}(t) + \sqrt{3} i_{\beta}(t) \right\}; i_c(t) = \frac{-1}{2} \left\{ i_{\alpha}(t) + \sqrt{3} i_{\beta}(t) \right\}$$

$$i_a(t) = A_1 \cos(\omega t) + B_1 \sin(\omega t)$$

$$A_1 = i_{dp} \cos \theta_{vp} - i_{qp} \sin \theta_{vp} + i_{dn} \cos \theta_{vn} + i_{qn} \sin \theta_{vn}$$

$$B_1 = -i_{qp} \cos \theta_{vp} - i_{dp} \sin \theta_{vp} + i_{qn} \cos \theta_{vn} - i_{dn} \sin \theta_{vn}$$

same procedure for other phases

$$\Rightarrow i_{abc}(t) = \frac{A}{2} \cos(\omega t) + \frac{B}{2} \sin(\omega t)$$

$$\begin{aligned}
A &= \begin{bmatrix} 2i_{dp} & -2i_{qp} & 2i_{dn} & 2i_{qn} \\ (\sqrt{3}i_{qp} - i_{dp}) & (\sqrt{3}i_{dp} + i_{qp}) & (\sqrt{3}i_{qn} - i_{dn}) & -(\sqrt{3}i_{dn} + i_{qn}) \\ -(\sqrt{3}i_{qp} + i_{dp}) & -(\sqrt{3}i_{dp} - i_{qp}) & -(\sqrt{3}i_{qn} + i_{dn}) & (\sqrt{3}i_{dn} - i_{qn}) \end{bmatrix} \begin{bmatrix} \cos \theta_{vp} \\ \sin \theta_{vp} \\ \cos \theta_{vn} \\ \sin \theta_{vn} \end{bmatrix} \\
B &= \begin{bmatrix} -2i_{qp} & -2i_{dp} & 2i_{qn} & -2i_{dn} \\ (\sqrt{3}i_{dp} + i_{qp}) & -(\sqrt{3}i_{qp} - i_{dp}) & -(\sqrt{3}i_{dn} + i_{qn}) & -(\sqrt{3}i_{qn} - i_{dn}) \\ -(\sqrt{3}i_{dp} - i_{qp}) & (\sqrt{3}i_{qp} + i_{dp}) & (\sqrt{3}i_{dn} - i_{qn}) & (\sqrt{3}i_{qn} + i_{dn}) \end{bmatrix} \begin{bmatrix} \cos \theta_{vp} \\ \sin \theta_{vp} \\ \cos \theta_{vn} \\ \sin \theta_{vn} \end{bmatrix} \tag{M.2}
\end{aligned}$$

N. DERIVATION OF SCP FOR ISLANDED GFM IN CASE OF SMALL DISTURBANCES

Let a load of S_{L1} power is being fed by the GFM and the terminal voltage phasor is v_1 . A change in power ΔS_L is introduced which causes terminal voltage phasor to v_2 . Referring to Figure 5.1, following expressions for the line current can be derived.

$$\begin{aligned} i_1 &= \frac{E \angle 0 - |v_{1poc}| \angle \theta_{v1}}{Z_{sc} \angle \theta_z} \xrightarrow{S_{L1}=v_1 i_1^*} S_{L1} Z_{sc} \angle -\theta_z = E |v_{1poc}| \angle \theta_{v1} - |v_{1poc}|^2 \\ i_2 &= \frac{E \angle 0 - |v_{2poc}| \angle \theta_{v2}}{Z_{sc} \angle \theta_z} \xrightarrow{S_{L2}=v_2 i_2^*} S_{L2} Z_{sc} \angle -\theta_z = E |v_{2poc}| \angle \theta_{v2} - |v_{2poc}|^2 \end{aligned} \quad (\text{N.1})$$

The final load power can be presented in the form of initial load power plus the change in load power.

The updated expressions are given below.

$$\begin{aligned} \therefore S_{L2} &= S_{L1} + \Delta S_L \\ (S_{L1} + \Delta S_L) Z_{sc} \angle -\theta_z &= E |v_{2poc}| \angle \theta_{v2} - |v_{2poc}|^2 \\ \Delta S_L Z_{sc} \angle -\theta_z &= E |v_{2poc}| \angle \theta_{v2} - |v_{2poc}|^2 - S_{L1} Z_{sc} \angle -\theta_z \\ \therefore S_{L1} Z_{sc} \angle -\theta_z &= E |v_{1poc}| \angle \theta_{v1} - |v_{1poc}|^2 \\ \Rightarrow \Delta S_L Z_{sc} \angle -\theta_z &= E |v_{2poc}| \angle \theta_{v2} - |v_{2poc}|^2 - E |v_{1poc}| \angle \theta_{v1} + |v_{1poc}|^2 \\ \Rightarrow \Delta S_L Z_{sc} \angle -\theta_z &= E \left(|v_{2poc}| \angle \theta_{v2} - |v_{1poc}| \angle \theta_{v1} \right) + \left(|v_{1poc}|^2 - |v_{2poc}|^2 \right) \\ \therefore Z_{sc} &= \frac{E^2}{SCP}; \Delta v_{poc} = |v_{2poc}| \angle \theta_{v2} - |v_{1poc}| \angle \theta_{v1} \\ \Rightarrow \left| \frac{\Delta S_L}{SCP} \right| &= \left| \frac{\Delta v_{poc} + \left(|v_{1poc}|^2 - |v_{2poc}|^2 \right) / E}{E} \right| \end{aligned} \quad (\text{N.2})$$

By selecting base voltage equal to 'E' and base power equal to rated of the GFM, the updated expressions are given below.

$$\begin{aligned} \therefore \Delta S_L &= \Delta S_{L,p.u} S_{GFM} \\ \left| \frac{\Delta S_{L,p.u}}{SCP} \right| S_{GFM} &= \Delta v_{poc} / E + \left(|v_{1poc}|^2 - |v_{2poc}|^2 \right) / E^2 \\ \Rightarrow \left| \frac{\Delta S_{L,p.u}}{SCP} \right| S_{GFM} &= \Delta v_{poc} / E + \left(\left(\frac{|v_{1poc}|}{E} \right)^2 - \left(\frac{|v_{2poc}|}{E} \right)^2 \right) \\ \therefore \Delta v_{poc} / E &= \Delta v_{poc,p.u}; |v_{1poc}| / E = |v_{1poc,p.u}|; |v_{2poc}| / E = |v_{2poc,p.u}| \\ \Rightarrow \frac{SCP}{S_{GFM}} &= \left| \frac{\Delta S_{L,p.u}}{\Delta v_{poc,p.u} + \left(|v_{1poc,p.u}|^2 - |v_{2poc,p.u}|^2 \right)} \right| \end{aligned} \quad (\text{N.3})$$

To find the X/R ratio of the short circuit impedance of the islanded GFM, the above equations need to be solved for per unit short circuit impedance and inverse tangent of the calculated angle will result in

X/R ratio. For these calculations, the change in voltage phasor and change in square of the magnitudes of the voltage need to be summed up vectorially.

$$\begin{aligned}
 Z_{sc,p.u} \angle -\theta_z &= \frac{\Delta v_{poc,p.u} + \left(|v_{1poc,p.u}|^2 - |v_{2poc,p.u}|^2 \right)}{\Delta S_{L,p.u}} \\
 \therefore \begin{cases} \Delta S_{L,p.u} = \Delta S_{L,p.u} \angle \theta_{\Delta S_L} \\ \theta_x = \angle \left(\Delta v_{poc,p.u} + \left(|v_{1poc,p.u}|^2 - |v_{2poc,p.u}|^2 \right) \right) \end{cases} & \quad (N.4) \\
 \Rightarrow \left(\frac{X}{R} \right)_{Z_{sc}} &= \tan^{-1} \left(\theta_{\Delta S_L} - \theta_x \right)
 \end{aligned}$$

If the difference of square of voltage magnitude at POC is ignored, the following simplified expression can be derived for the SCP and the X/R ratio of the short circuit impedance.

$$\begin{aligned}
 \frac{SCP}{S_{GFM}} &= \left| \frac{\Delta S_{L,p.u}}{\Delta v_{poc,p.u}} \right| \\
 \left(\frac{X}{R} \right)_{Z_{sc}} &= \tan^{-1} \left(\theta_{\Delta S_L} - \theta_{\Delta v_{poc}} \right)
 \end{aligned} \quad (N.5)$$

O. NUMERICAL EXAMPLE FOR THE CALCULATION OF SCR IN MULTI-CONVERTER SYSTEM

Referring to Figure 5.7, a 500 kVA GFM is connected to a grid with short circuit power of 1 MVA. The line-to-line RMS voltage is 400 V. The line impedances vary from 0 to 1 Ω . The SCP at node 'X' is calculated along with the base power of GFL at node 'X' to keep SCR close to 5. If ' Z_X ' is zero, the same quantities can be referred to POC. The results are given in Appendix Table O.1.

Appendix Table O.1: SCP and base power calculations for different line impedances

<i>Physical arrangement explanation</i>	<i>Calculation Node</i>	<i>Input parameter (Ω)</i>			<i>Output parameters (kVA)</i>	
		Z_2	Z_1	Z_X	SCP	S_b
Directly coupled grid and GFM	POC	0	0	0	1500	300
	X	0	0	1	144	29
Coupling of the local grid with remote GFM	POC	0	1	0	1121	224
	X	0	1	1	140	28
Coupling of the remote grid with local GFM	POC	1	0	0	638	128
	X	1	0	1	128	26
Coupling of the remote grid with remote GFM	POC	1	1	0	260	52
	X	1	1	1	99	20

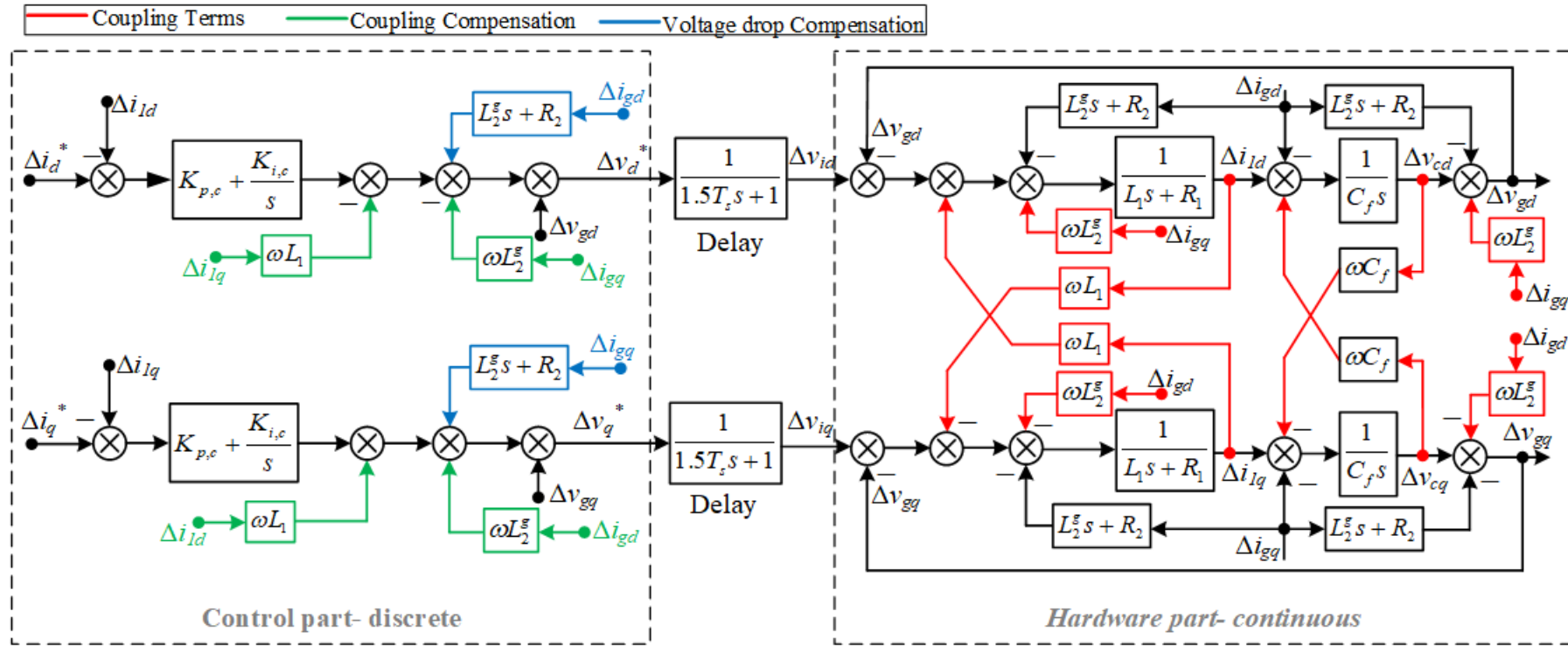
The above table shows that the maximum SCP is recorded if the line impedances are neglected, and it is the sum of the short circuit power of the grid and the rated power of the GFM. The following points can be concluded from the above table.

- If the same line impedance is introduced between GFM and POC (Z_1), grid and POC (Z_2), or between POC and node 'X' (Z_X), the minimum SCP is recorded for $Z_X = 1 \Omega$ among these three cases. The reason for this is the stronger SCP at POC as compared to the short circuit power of the grid or the rated power of the GFM. A strong grid has a lower short circuit impedance, and a small line impedance may cause a noticeable reduction in the SCP for such a source. Similarly, Z_2 has a bigger effect than Z_1 and the reason for this is the stronger source connected to Z_2 as compared to Z_1 .
- The impact of Z_1 is limited for a remote node's SCP calculations.

The minimum SCP is recorded on remote node if the line impedances are not ignored.

P. BLOCK DIAGRAM FOR INNER CURRENT CONTROLLER WITH VOLTAGE LOOP

The complete diagram for the inner current controller with voltage loop is given below.



Appendix Figure P.1: Complete block diagram of the inner current controller with voltage loop